

ABSTRACT

Title of dissertation: NEUTRON DETECTION BY
NOBLE GAS EXCIMER
SCINTILLATION

Amy Elizabeth Beasten, Doctor of Philosophy, 2013

Dissertation directed by: Professor Mohamad Al-Sheikhly
Nuclear Engineering Program
Department of Materials Science and Engineering

The field of neutron detection has many essential applications, from nuclear reactor instrumentation, oil-well logging, radiation safety, and, in recent years, homeland security. Due to the shortage and increasing cost of the neutron absorber used in most conventional gas-filled proportional counters, there has been an increased motivation for the development of alternative methods of neutron detection that do not rely on ^3He . Excimer-based neutron detection (END) is a potential alternative with many advantages, notably the lack of dependence on ^3He . Similar to traditional proportional counters, END operates on the interaction of a neutron with a neutron absorbing nucleus (^{10}B , ^6Li , or ^3He). The energetic charged particles produced in these reactions lose energy in the surrounding gas background and cause ionization and excitation of the noble gas molecules. The difference between END and traditional gas-filled detectors, which collect the ionized charge to produce a detectable signal, is the formation of noble gas excimers (Ar_2^* , Kr_2^* , or Xe_2^*). These excited dimers decay from an excited state back to ground level and emit far-ultraviolet (FUV) radiation in the

form of photons which can be collected using a photomultiplier tube (PMT) or other photon detector. The most important advantage to these potential detectors is the fact that they do not rely on the use of ^3He .

The excimer scintillation yield from rare noble gases following the ^{10}B neutron capture reaction in both ^{10}B enriched BF_3 gas and reticulated vitreous carbon foam (RVC) coated with a layer of B_4C is the focus of this thesis. Experimental data were collected at the National Institute of Standards and Technology (NIST) and on a recently established thermal neutron beamline at the Maryland University Training Reactor (MUTR). The comparison of these data to data from previous thin-film experiments provides the groundwork for the continuation of future END work using these materials, which will be used to develop and optimize a deployable neutron detector based on excimer emission.

NEUTRON DETECTION BY NOBLE GAS EXCIMER
SCINTILLATION

by

Amy Elizabeth Beasten

Dissertation submitted to the Faculty of the Graduate School of the
University of Maryland, College Park in partial fulfillment
of the requirements for the degree of
Doctor of Philosophy
2013

Advisory Committee:

Professor Mohamad Al-Sheikhly, Chair/Advisor

Dr. John Ondov, Dean's Representative

Dr. Gary Pertmer

Dr. Mohammad Modarres

Dr. Tim Koeth

Dr. Rami Kishek

© Copyright by
Amy Elizabeth Beasten
2013

To my family
for their unwavering support, patience, and understanding.

Acknowledgments

The knowledge and inspiration of many contributed to this research. I would like to first thank Dr. Mohamad Al-Sheikhly for bringing me into his research group and being my advisor throughout my graduate education. His enthusiasm for learning is what initially drew me to The University of Maryland, and this dedication has not changed over the years. Secondly, I would like to thank Dr. Michael Coplan for giving me the opportunity to participate in this research project, and for providing the guidance to make it what it is today. It has been a privilege to work with and learn from him.

Thank you to the FUND group, especially to Dr. Charles Clark. Your passion, dedication, and knowledge of this research was inspiring. Thank you to Dr. Alan Thompson for all your patience, especially getting the old Linux machine to communicate with my electronics. Thank you to Rob Vest for all your help, support, and guidance with the photoabsorption experiments, and all your invaluable knowledge on vacuum systems.

A huge thank you must go out to all the people who helped with my experiments. To the Reactor Operators and Senior Reactor Operators, who patiently operated the reactor for me: Slavica Grdanovska, Layla Shahamat, and Dr. Cameron Goodwin. I hope I can return the favor one day. To Dr. Tim Koeth, thank you for trusting me with your cherished toys. Thank you for always being there to answer stupid questions and provide valuable insight into research and life in general. Thank you for being a friend as well as a coworker. Thank you to Vince Adams for teaching me about drill presses and rivet guns, crash courses in electrical wiring, and for always proving that nothing is ever as catastrophic as it first appears. Both Dr. Tim Koeth and Vince Adams work tirelessly on the reactor to keep it

running so every student can continue to work and learn, and for this I am eternally grateful. Thank you, especially, for always being ready to buy me a beer at the end of a hard day. Without you guys, I don't think I would have made it. To Jason Osheroff: thank you dedicating so much of your time to help me finish my experiments. I hope I have provided you with enough of my own wisdom and mistakes that you can successfully continue this line of research.

Thank you to Dr. Eric Burgett for all of your wonderful insight into my research, your help in everything related and unrelated, and for all your support throughout this adventure. Thank you to Dr. Pertmer for imparting all your wisdom, and to Dr. Modarres, for being a valuable part of my committee. Thank you to Dr. Ondov, for stepping in as my Dean's Representative, and for all your valuable insight and assistance.

Thank you to my present roommates, who allowed me to direct my frustrations towards them, and my friends, always ready with a stiff drink and a good laugh after a bad day. To my family for their (mostly) unwavering support and (occasional) patience. I know you all are often the target of my frustration after a bad day. Your patience and understanding are very, very much appreciated.

G.K. Chesterton once said, "Fairy tales are more than true—not because they tell us dragons exist, but because they tell us dragons can be beaten." I want to thank all those dragons, real and imagined, (and the Pagan God of Reactor Mischief) who made my graduate education the experience it was. Without them, I would not have grown into the person I am today.

Contents

List of Tables	viii
List of Figures	x
1 Introduction	1
1.1 Neutron Detection	1
1.2 Early Experiments in Neutron Detection	3
1.3 Applications of Neutron Detection	5
1.3.1 Cosmic Ray Detection	5
1.3.2 Reactor Instrumentation	5
1.3.3 Special Nuclear Material (SNM) Detection	6
1.3.4 Oil Well Logging	7
1.4 Objectives	8
2 Background	11
2.1 Neutron Interactions	11
2.1.1 Scattering	11
2.1.2 Absorption	12
2.2 Neutron Detectors	14
2.2.1 Gas-Filled Detectors	14
2.2.1.1 Ionization Chambers	16
2.2.1.2 Proportional Counters	17
2.2.2 Scintillation Detectors	19
2.3 Excimer-Based Neutron Detection (END)	22
2.3.1 Excimer Scintillation	23
2.4 Advantages to END	26
3 Review of Previous Experiments	28
3.1 NIST Center for Neutron Research	28
3.2 Lyman-Alpha Experiment	30
3.3 END at NIST	31
3.4 Thin-Film Experiments	32
4 Absolute Photoabsorption Cross-Section of $^{10}\text{BF}_3$	35
4.1 Synchrotron Radiation	36
4.2 Photoabsorption Experimental Procedure	39
4.2.1 BF_3 Gas Handling System	39
4.2.2 Stage and Detector Alignment	43
4.2.3 BF_3 Experiment (135-205 nm)	44
4.2.4 BF_3 Experiment (Additional Measurements)	44
4.2.5 Dry N_2 Purge	45
4.3 Data Analysis: Absolute Photoabsorption Cross-Section Determination	46
4.3.1 Beam Current Normalization	47

4.3.2	Monochromatic Scanning Errors	47
4.3.3	Determination of Beam Current Decay Rate	48
4.3.4	Individual Data Point Correction	51
4.3.5	Transmission and Photoabsorption Cross-Section Calculations	53
4.3.6	Determination of Molar Extinction Coefficient	55
4.4	BF ₃ Photoabsorption Cross-Section Results	57
5	FUND Experimental Apparatus Description	62
5.1	MUTR Neutron Beamline	62
5.2	Far Ultraviolet Neutron Detection Experiment	66
5.2.1	Scintillation Cell	66
5.2.2	Photomultiplier Tube Calibration	68
5.2.3	¹⁰ BF ₃ Gas Handling System	73
5.2.4	Carbon Foam Experimental Setup	78
5.2.5	Discussion of Electronics	79
6	Characterization of Incident Neutron Beam	89
6.1	Fluence Measurements	89
6.2	Beam Profile Measurements	96
6.3	Gamma Ray Spectroscopy	98
7	¹⁰ BF ₃ FUND Results	104
7.1	Procedure for ¹⁰ BF ₃ Experiments	104
7.2	Analysis of Results in BF ₃	105
8	Carbon Foam Experiment	120
8.1	Reticulated Vitreous Carbon Foam	120
8.2	Experimental Procedure	123
9	FUND Results	133
9.1	Excimer Scintillation Yield	133
9.1.1	¹⁰ BF ₃ Excimer Scintillation Yield	136
9.1.2	Reticulated Vitreous Carbon Foam Excimer Scintillation Yield	138
9.1.3	¹⁰ B Thin-Film Excimer Scintillation Yield	140
9.2	Conclusions	144
9.3	Contribution	147
9.4	Future Work	148
9.4.1	Neutron Beam Characterization	148
9.4.2	BF ₃	150
9.4.3	Carbon Foam	151
A	Lessons Learned	153
A.1	Pump Failures, 31 May 2011 and 3 June 2011	153
A.2	Viton, 18 May 2011	155

B	O ₂ Photoabsorption Spectra	159
B.1	O ₂ Gas Handling System and Experimental Procedure	159
B.1.1	O ₂ Experimental Procedure	159
B.1.2	O ₂ Absolute Photoabsorption Cross-Section Results	161
C	Photoabsorption Cross-Section Values	163
C.1	¹⁰ BF ₃ Absolute Photoabsorption Cross-Section Data	163
D	Standard Operating Procedure for MUTR Gas Handling System	176
D.1	Introduction	176
D.2	Procedure	177
D.2.1	Stage 1: System Pump Down	177
D.2.2	Stage 2: Introduction of Noble Gas	181
D.2.3	Stage 3: Introduction of BF ₃	183
D.2.4	Stage 4: Dry N ₂ Purge	184
	Bibliography	189

List of Tables

2.2.2-1	Characteristics of several thermal neutron scintillators, including light yield per neutron (Y_n), gamma-ray interaction (Y_γ), emission wavelength (λ_{hv}), and decay times (τ)	21
2.3-1	Properties of noble gases, including density (ρ), peak excimer emission wavelength (λ_{peak}), and peak excimer photon energy (E_{hv}).	22
4-1	Concentration of impurities in $^{10}\text{BF}_3$ gas supplied by Ceradyne [®] , Inc.	35
4.2.1-1	Description of parts used in the SURF III BF_3 Gas Handling System .	40
4.4-1	Comparison of Beam Current Normalization Values between 27 May 2011 and 5-6 July 2011	61
5.2.1-1	Specifications of the Hamamatsu R6835 PMT.	67
5.2.2-1	Intrinsic efficiencies ($\epsilon_{PMT}(\lambda_{Peak})$) of the PMT/ MgF_2 detector package at peak excimer wavelengths and effective intrinsic efficiencies (ϵ_{PMT}).	72
5.2.3-1	Description of valves used in the MUTR BF_3 Gas Handling System .	74
5.2.3-2	Purities of noble gases and contaminant concentrations according to manufacturer data sheet. THC: total hydrocarbons	77
5.2.4-1	Description of valves used in the MUTR Carbon Foam Gas Handling System	79
5.2.5-1	Comparison of peak maxima values from electronics characterization for PMT.	82
5.2.5-2	Comparison of peak maxima values from electronics characterization for PMT-Preamp.	82
5.2.5-3	Comparison of peak minima values from electronics characterization for PMT.	83
5.2.5-4	Comparison of peak minima values from electronics characterization for PMT-Preamp.	83
6.1-1	Thicknesses, macroscopic cross-sections, and transmission values (T) for the materials existing between the fission chamber reference detector and the scintillation cell, used for the determination of μ	92
6.1-2	Average neutron absorption rates for each pressure of BF_3	95
6.1-3	Average neutron absorption rates for each thickness of reticulated vitreous carbon foam with a layer of B_4C	95
7.2-1	Number of pulses observed for a variety of experimental operating conditions. Data is shown for 600 torr Xe. $t = 200$ s	108
8.1-1	Properties of various pore sizes of the carbon foam used in the END experiments. All samples listed are 2.54 cm square with 0.64 cm thickness.	121
8.1-2	Properties of Duocel [®] of 3% nominal density, as claimed by the manufacturer. The tensile strength was determined from edge effects observed on small samples	122

8.1-3	Dimensions of the physical characteristics of RVC foams, as determined from SEM micrographs.	123
8.2-1	Number of pulses observed for a variety of operating conditions. Data is for 45 PPI coated sample (4 μm ^{10}B thickness) in a xenon environment.	124
9.1-1	Uncertainty values for various parameters in Equation 9.1-1.	136
9.1.1-1	Excimer scintillation yield (Y) values for 600 torr Xe	137
9.1.3-1	Concentrations in % and observed energy peaks of surface contaminants in 300-nm thin-film in N_2 environment and exposed to atmospheric pressure for 3.5 months.	141
9.1.3-2	Number of pulses observed for a variety of operating conditions. Data is for 300-nm ^{10}B enriched thin film in a xenon environment.	142
C.1-1	Absolute Photoabsorption Cross-Section (σ) and Uncertainty Values ($u(\sigma)$) for $^{10}\text{BF}_3$ from 135-205 nm, 27 May 2011	163
C.1-2	Absolute Photoabsorption Cross-Section (σ) and Uncertainty Values ($u(\sigma)$) for $^{10}\text{BF}_3$ from 135-145 nm, 5 July 2011	170
C.1-3	Absolute Photoabsorption Cross-Section (σ) and Uncertainty Values ($u(\sigma)$) for $^{10}\text{BF}_3$ from 150-165 nm, 6 July 2011	172
C.1-4	Absolute Photoabsorption Cross-Section (σ) and Uncertainty Values ($u(\sigma)$) for $^{10}\text{BF}_3$ from 190-205 nm, 6 July 2011	174
D.1-1	Description of valves used in the MUTR BF_3 Gas Handling System	177
D.2.1-1	Manual Valves in Initially Closed Position During Pump Down	178
D.2.1-2	Pneumatic Valves in Initially Closed Position During Pump Down	179
D.2.1-3	Manual Valves Changed to the Open Position During Pump Down	180
D.2.1-4	Valves in the Closed Position After Initial Valve Manipulation	180
D.2.2-1	Valves in the Closed Position Prior to Introduction of Noble Gas	181
D.2.2-2	Valves in the Open Position During Noble Gas Introduction	182
D.2.3-1	Valves in the Closed Position Prior to BF_3 Introduction	183
D.2.4-1	Valves in the Closed Position Prior to Dry N_2 Purge	185
D.2.4-2	Valves in the Open Position Prior to Dry N_2 Purge	185
D.2.4-3	Valve logic for BF_3 gas handling system. Initial valve configuration for each stage of experimental procedure.	186
D.2.4-4	Valve logic for BF_3 gas handling system. Final valve configuration for each stage of experimental procedure.	187

List of Figures

1.4-1	Photoabsorption cross-section spectra from various BF_3 photoabsorption experiments. These data range from completely transparent in the FUV region, to completely opaque.	9
2.1.1-1	Elastic scattering of a neutron with a target nucleus.	12
2.1.2-1	$^{10}\text{B}(n,\alpha)^7\text{Li}$ absorption reaction.	13
2.2.1-1	Gas-filled detector	14
2.2.1-2	Pulse height versus applied voltage	15
2.2.2-1	Scintillation detector and photomultiplier tube	19
2.2.2-2	Scintillator detector system	20
2.3-1	Excimer emission for Xe_2^* , Kr_2^* , Ar_2^*	23
2.3.1-1	Rare gas continua observed using a helium discharge tube.	25
3.1-1	NCNR guidehall	29
3.2-1	Lyman- α photons produced per neutron absorbed with ^3He as a function of ^3He pressure.	30
3.3-1	Left-hand scale: Thousands of photons observed per neutron absorbed. Right-hand scale: Thousands of counts observed per neutron absorbed.	31
3.3-2	(a) PMT response to monochromatic UV radiation from SURF III synchrotron taking into account each filter response and PMT efficiency. (b) Relative excimer emission taking into account each filter response and PMT efficiency.	32
3.4-1	Excimer scintillation of argon during irradiation of 600 nm, 900 nm, and 1200 nm substrates.	33
3.4-2	Excimer scintillation of krypton during irradiation of 300 nm, 600 nm, 900 nm, and 1200 nm substrates.	34
3.4-3	Excimer scintillation of xenon during irradiation of 300 nm, 600 nm, 900 nm, and 1200 nm substrates.	34
4-1	Comparison of literature values of the photoabsorption cross-section of $^{10}\text{BF}_3$ in the region 130-180 nm.	36
4.1-1	Acceleration of relativistic electrons in a magnetic field produce a collimated beam of photons perpendicular to the direction of acceleration.	37
4.1-2	Synchrotron Ultraviolet Radiation Facility (SURF III) at NIST	38
4.1-3	SURF III radiant power as a function of operating energies.	38
4.1-4	Diagram of SURF III Beamline 4, with photon path (red) shown. . . .	39
4.2.1-1	NIST SURF III BF_3 gas handling system	40
4.4-1	Absolute photoabsorption cross-section data of $^{10}\text{BF}_3$ from 135 to 145 nm.	57
4.4-2	SURF values compared to literature values of photoabsorption cross section of BF_3	58
4.4-3	Photoabsorption cross-section and molar extinction coefficient of $^{10}\text{BF}_3$ from 135 to 205 nm. Data from all three dates (27 May, July 5-6) are included.	60

5.1-1	Top-down view of the MUTR core configuration.	63
5.1-2	MUTR thermal column access plug	65
5.1-3	3D View of Collimator Plug. Partitions 1 and 4 are filled with a mixture of steel shot, paraffin wax, and boron carbide to attenuate the neutron and gamma radiation from the thermal column leaving only a collimated beam.	65
5.1-4	Collimator shutter assembly in closed (a) and open (b) positions.	66
5.1-5	Scintillation cell with fission chamber beam monitor and ^6Li glass neutron absorber in place.	66
5.2.1-1	Cube and photomultiplier tube (not to scale).	68
5.2.2-1	Net counts from the PMT during an FUV spectral scan at SURF III. Electron beam current $I_{BC} = 10 \mu\text{A}$	70
5.2.2-2	Fractional uncertainties found in $n_{hv}(\lambda)$ from the PMT calibration. Electron beam current $I_{BC} = 10 \mu\text{A}$	71
5.2.2-3	Intrinsic efficiency of the PMT/MgF ₂ detector package in the FUV wavelength region.	71
5.2.2-4	Spectral response of the PMT.	72
5.2.2-5	PMT response as a function of PMT input voltage at $\lambda = 170 \text{ nm}$	73
5.2.3-1	MUTR $^{10}\text{BF}_3$ Gas Handling System	74
5.2.3-2	Typical RGA spectral scan after scintillation cell evacuation	77
5.2.4-1	Gas handling system used for the carbon foam experiments	78
5.2.5-1	Photon counting electronics	80
5.2.5-2	Pulse height distribution data. The triangles represent the PHD with the shutter closed under the same conditions.	81
5.2.5-3	Oscilloscope traces at -1500 V for (a) PMT and (b) PMT and Preamp. Blue lines represent signal from no source and no xenon; red lines represent signal from alpha source and no xenon; green lines represent signal from alpha source and 800 torr xenon; yellow lines represent signal from neutron source and no xenon; black lines represent signal from neutron source and 800 torr xenon.	84
5.2.5-4	Oscilloscope traces at -1700 V for (a) PMT and (b) PMT and Preamp. Blue lines represent signal from no source and no xenon; red lines represent signal from alpha source and no xenon; green lines represent signal from alpha source and 800 torr xenon; yellow lines represent signal from neutron source and no xenon; black lines represent signal from neutron source and 800 torr xenon.	85
5.2.5-5	Oscilloscope traces at -1900 V for (a) PMT and (b) PMT and Preamp. Blue lines represent signal from no source and no xenon; red lines represent signal from alpha source and no xenon; green lines represent signal from alpha source and 800 torr xenon; yellow lines represent signal from neutron source and no xenon; black lines represent signal from neutron source and 800 torr xenon.	86

5.2.5-6	Oscilloscope traces at -2100 V for (a) PMT and (b) PMT and Preamp. Blue lines represent signal from no source and no xenon; red lines represent signal from alpha source and no xenon; green lines represent signal from alpha source and 800 torr xenon; yellow lines represent signal from neutron source and no xenon; black lines represent signal from neutron source and 800 torr xenon.	87
5.2.5-7	Oscilloscope traces at -2300 V for (a) PMT and (b) PMT and Preamp. Blue lines represent signal from no source and no xenon; red lines represent signal from alpha source and no xenon; green lines represent signal from alpha source and 800 torr xenon; yellow lines represent signal from neutron source and no xenon; black lines represent signal from neutron source and 800 torr xenon.	88
6.1-1	NIST-calibrated fission chamber beam monitor.	89
6.1-2	Cross-sections of ^{10}B and ^{235}U over the thermal energy region.	93
6.1-3	Values of η over the thermal energy region.	94
6.2-1	Neutron beam profile immediately behind 4-mm aperture.	97
6.2-2	Neutron beam profile 12 cm behind 4-mm aperture.	97
6.3-1	Gamma ray spectroscopy observed with a mixed neutron beam propagating through the scintillation cell, $t = 200$ s.	99
6.3-2	Gamma ray spectroscopy observed with 2.54 cm Pb brick blocking the scintillation cell, $t = 200$ s.	99
6.3-3	Gamma ray spectroscopy observed with 0.1984 cm boral sheet blocking the scintillation cell, $t = 200$ s.	100
6.3-4	Gamma ray spectroscopy obtained with NaI detector on 31 January 2013. The green line indicates the gamma ray distribution with the shutter open during a mixed beam, the blue line represents the gamma signal with a 0.1984 cm boral sheet immediately in front of the scintillation cell, and the red line represents the gamma signal with a 2.54 cm Pb brick positioned immediately in front of the scintillation cell. $t = 200$ s	101
6.3-5	Gamma ray spectroscopy obtained with NaI detector on 31 January and 5 February 2013. The data show the gamma spectrum with no blocks in front of the scintillation cell, a 0.1984-cm sheet of boral, and a 1" lead brick blocking the scintillation cell.	102
6.3-6	Gamma ray spectroscopy obtained with NaI detector on 5 February 2013. The data show the gamma spectrum with no blocks in front of the scintillation cell immediately prior to, during, and immediately after the exhaust fans were run for fifteen minutes.	103
7.2-1	Counts/s values for 600 torr Xe with different pressures of BF_3	106
7.2-2	C_{Obs} for 600 torr Xe with different pressures of BF_3 , determined from Equation 7.2-1.	107
7.2-3	C_{Obs} for 600 torr Ar, Kr, and Xe with different pressures of BF_3	107

7.2-4	Pulse height distribution data for 0 torr BF ₃ , 100 torr Xe. The triangles represent the PHD with the shutter closed under the same conditions	108
7.2-5	Pulse height distribution data for 20 torr BF ₃ , 100 torr Xe. The triangles represent the PHD with the shutter closed under the same conditions	109
7.2-6	Pulse height distribution data for 200 torr BF ₃ , 100 torr Xe. The triangles represent the PHD with the shutter closed under the same conditions	109
7.2-7	Pulse-height distribution data from ¹⁰ B enriched BF ₃ after bombardment with 3.52 MeV neutrons.	111
7.2-8	Effect of increasing pressures of SO ₂ on a BF ₃ proportional counter.	114
7.2-9	Effect of increasing pressures of SiF ₄ on a BF ₃ proportional counter.	115
7.2-10	Effect of increasing pressures of SF ₆ on a BF ₃ proportional counter.	115
7.2-11	Pulse height distribution data for 600 torr BF ₃ after (a) initial filling following 3 months of “aging” and (b) 3 weeks later.	116
7.2-12	Degradation and recovery of (a) gas multiplication as a result of extended operation in a 10 ⁴ neutron field.	117
8.1-1	SEM micrograph of 30 PPI RVC sample.	122
8.1-2	SEM micrograph of strut of 30 PPI RVC sample.	123
8.2-1	Total pulse values for 45 PPI coated sample (4 μm ¹⁰ B thickness) with increasing pressures of Xe.	125
8.2-2	Total pulse values for 45 PPI coated sample (4 μm ¹⁰ B thickness) with increasing pressures of Ar.	126
8.2-3	Total pulse values for 30 PPI coated sample (8.3 μm ¹⁰ B thickness) with increasing pressures of Xe.	126
8.2-4	Total pulse values for 30 PPI coated sample (8.3 μm ¹⁰ B thickness) with increasing pressures of Ar.	127
8.2-5	Total pulse values for 20 PPI coated sample (8.7 μm ¹⁰ B thickness) with increasing pressures of Xe.	127
8.2-6	Total pulse values for 20 PPI coated sample (8.7 μm ¹⁰ B thickness) with increasing pressures of Ar.	128
8.2-7	Comparison of <i>C_{Obs}</i> .	128
8.2-8	Comparison of coated and uncoated 45 PPI signals as a function of Xe gas pressure.	129
8.2-9	Comparison of coated and uncoated 45 PPI signals as a function of Ar gas pressure.	130
8.2-10	Comparison of coated and uncoated 30 PPI signals as a function of Xe gas pressure.	130
8.2-11	Comparison of coated and uncoated 30 PPI signals as a function of Ar gas pressure.	131
8.2-12	Comparison of coated and uncoated 20 PPI signals as a function of Xe gas pressure.	131
8.2-13	Comparison of coated and uncoated 20 PPI signals as a function of Ar gas pressure.	132

9.1.1-1	Scintillation yield from $^{10}\text{B}(n, \alpha)^7\text{Li}$ in 600 torr Xe with increasing pressure of BF_3	137
9.1.2-1	Scintillation yield from $^{10}\text{B}(n, \alpha)^7\text{Li}$ in different thicknesses carbon foam as a function of Xe pressure.	139
9.1.2-2	Scintillation yield from $^{10}\text{B}(n, \alpha)^7\text{Li}$ in different thicknesses carbon foam as a function of Ar pressure.	139
9.1.3-1	Components of N_{Obs} , determined from Equation 7.2-1, observed for 300-nm ^{10}B enriched thin-film as a function of xenon pressure. Data taken for 200 s at 200 kW reactor power.	142
9.1.3-2	C_{Obs} , determined from Equation 7.2-1, observed for 300-nm ^{10}B enriched thin-film as a function of xenon pressure. Data taken for 200 s at 200 kW reactor power.	143
9.1.3-3	Excimer scintillation yield observed for 300-nm ^{10}B enriched thin film. Reactor power level 200 kW.	143
9.1.3-4	Excimer scintillation yield observed for 300-nm ^{10}B enriched thin film, 20 PPI RVC, and 45 PPI RVC in Xenon environment. Reactor power level 200 kW.	144
A.1-1	NIST SURF III Gas Handling System for 27 May and 2-3 June 2011 Photoabsorption Experiments	154
B.1.2-1	Photoabsorption Cross-Section and Molar Extinction Coefficient of O_2 from 170 to 205 nm	161
B.1.2-2	O_2 Absolute Photoabsorption Cross-Section in Schumann-Runge Bands	162
D.1-1	MUTR $^{10}\text{BF}_3$ Gas Handling System	176

List of Abbreviations

BNCT	Boron Neutron Capture Therapy
CIC	Compensated Ion Chamber
DHS	Department of Homeland Security
END	Excimer-based Neutron Detection
FUV	Far-Ultraviolet
GM	Geiger-Mueller
KF	Kwik-Flange
LAND	Lyman-Alpha Neutron Detection
MUTR	Maryland University Training Reactor
NCNR	NIST Center for Neutron Research
NIST	National Institute of Standards and Technology
NSBR	National Bureau of Standards Reactor
PMT	Photomultiplier Tube
PPI	Pores per Inch
RGA	Residual Gas Analyzer
RPM	Radiation-detecting Portal Monitors
RVC	Reticulated Vitreous Carbon
SEM	Scanning Electron Microscope
SNM	Special Nuclear Material
SURF	Synchrotron Ultraviolet Radiation Facility
TRIGA	Training, Research, Isotopes, General Atomic
XPS	X-ray Photoelectron Spectroscopy

Chapter 1

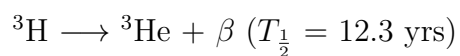
Introduction

The purpose of the research presented in this thesis is to provide an understanding of noble gas excimer scintillation as a new approach to neutron detection. This thesis will detail the incentive for alternative methods of neutron detection, including those methods which form the basis of this research, a discussion of the excimer based neutron detection experiments, and the results presented therein. This introductory chapter reviews the importance of neutron detection and several applications. Later chapters will explore current types of neutron detection methods, previous research that formed the groundwork for this thesis, and the the research itself.

1.1 Neutron Detection

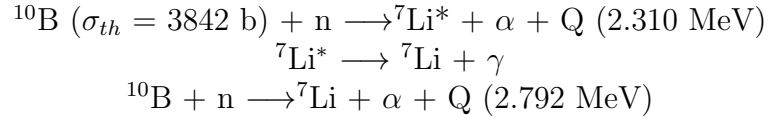
Neutron detection is an important field of study with many applications, including nuclear reactor instrumentation, nuclear materials detection, particle physics, oil well logging, nuclear medicine, nuclear forensics, and radiation biology. Currently, the neutron absorber used in most gas-filled proportional counters, helium-3 (^3He), is costly and in short supply. Other types of detectors, including boron-lined or boron trifluoride proportional counters, lack the sensitivity to neutrons and the gamma-ray discrimination properties of ^3He .

Helium-3 has a low natural abundance and is primarily produced from the radioactive decay of tritium via:



As ^3He has many uses in addition to radiation detection, the demand is very high [1]. In 2010, the supply of ^3He was cited to be 48,000 L, with the demand in excess of 75,000 L [2]. The shortage of ^3He has created an increasing need for alternative methods of detecting neutrons. Excimer based neutron detection (END) is an innovative technique that has several advantages over traditional ^3He filled proportional counters. The most important advantage of these detectors is that they do not require ^3He .

Similar to traditional proportional counters, END is based on a neutron absorbing nucleus, like ^6Li , ^3He , or, in the case of this thesis, ^{10}B , where a neutron combines with a neutron-absorbing nucleus, and the compound nucleus decays into energetic charged particles via one of two reaction pathways:



When thermal neutrons initiate the reaction, the branching ratio with an α and an excited state ^7Li is 93%, and with an α and a ground state ^7Li atom is 7%. The formation of energetic charged particle reaction products causes ionization of the electrons in the gas surrounding the absorber. This reaction is exothermic [3].

The excited state ^7Li atom has a half-life of 10^{-13} s and decays rapidly to the ground state with the emission of a 0.48 MeV gamma ray. Because the Q-values of the reaction (2.310 MeV and 2.792 MeV) are larger than the incoming energy of slow neutrons, the energy transferred to the reaction products is essentially just the Q-value. The energies of the α and the ^7Li atom are 1.47 MeV and 0.84 MeV, respectively, for the excited state ^7Li reaction path, and 1.78 MeV and 1.02 MeV, respectively, for the ground state ^7Li path. Boron-10 is an ideal candidate for the replacement of ^3He gas in neutron detectors due to its large thermal neutron absorption cross-section ($\sigma_{th} = 3842 \pm 8 \text{ b}$), abundance, and large exothermic branching

ratio. The thermal neutron absorption cross-section for ^{10}B is about 72% of the ^3He thermal neutron absorption cross-section ($\sigma_{He} = 5330 \text{ b}$) [3].

In contrast to proportional counters, which collect the ionized charge, END relies on the formation of molecules known as excimers created in a noble gas (Xe, Kr, Ar) background. Excimers are diatomic molecules that are bound only in the excited state (the ground state of an excimer is two unbound ground state atoms). As the excimers return to ground state, they emit far-ultraviolet (FUV) radiation and dissociate. These FUV photons can be collected by a photomultiplier tube or other photon detector. One of the most important advantages to END is the fact that this type of neutron detection does not depend on the use of ^3He .

1.2 Early Experiments in Neutron Detection

Prior to 1930, the neutron remained undetected and undiscovered. The working theory revolved around gamma rays as the accepted type of penetrating radiation. At the time, it was believed that the more energetic the gamma ray, the greater the penetration in a target. In 1930, Bothe and Becker discovered that when light elements such as lithium, beryllium, or boron are introduced in a beam of alpha particles, a penetrating radiation was observed. They concluded that this penetrating radiation was due to 7-15 MeV gamma rays [4].

Curie and Joliet used ionization chambers in 1932 and discovered that when the inner wall had a lining of hydrogenous material, a large current increase was observed. Studies showed that this increase was due to proton recoil from the lining with a maximum energy of 5 MeV. Curie and Joliet now concluded that the gamma rays had unreasonable energies, reaching as high as 50 MeV [4].

Chadwick performed a similar experiment using a wax lining inside an ionization chamber. He used aluminum absorbers to show that the maximum proton recoil energy was 5.7 MeV. He also proved that in order for the gamma ray hypothesis that

Bothe, Becker, Curie, and Joliet postulated, there would need to be gamma rays of energy as far apart as 55 MeV and 90 MeV, which were improbable. In addition, for this to occur, the reaction cross-sections would need to be unreasonably high. Chadwick rejected the working gamma ray theory and instead presented a new one: by assuming that the penetrating radiation was caused by a neutral particle with a mass very similar to that of a proton, all of these issues were avoided. Chadwick was awarded the Nobel Prize in 1935 for the discovery of the neutron [4].

In 1934, Fermi *et al.*, began to study slow, or thermal, neutrons. Fermi discovered that when certain materials are subjected to a neutron beam, these materials became radioactive. When certain materials were surrounded with paraffin wax, this radioactivity increased. This suggested that absorption became more pronounced with thermal neutrons as the neutrons reached thermal equilibrium with the protons in the wax. Moon and Tillman confirmed this theory, and expanded on it by showing that the temperature of the wax changed the efficacy of thermal neutron capture [4].

Dunning used counters lined with boron to prove that the observable cross-sections were the result of absorption as opposed to scattering. Following on this research, Fermi and Amaldi, and others, found that absorption varied inversely with neutron velocity, or with $1/v$ [4].

Early neutron detectors were quite different from today's detectors. Fast neutrons were detected with ionization chambers, or a type of detector known as a cloud chamber. Thermal neutrons were detected with radiation detectors, although the advantages of using the $^{10}\text{B}(n, \alpha)^7\text{Li}$ reaction were recognized early on [4].

1.3 Applications of Neutron Detection

1.3.1 Cosmic Ray Detection

Cosmic rays were discovered around 1912 by Victor Hess [5]. At the time, scientists had been investigating ionizing radiation in the atmosphere. The working hypothesis was that with increasing distance from the source of radiation, the radiation levels decreased. Electroscopes were used to detect and measure the levels of atmospheric radiation, but indicated that radiation levels were greater higher up in the atmosphere. To study this phenomenon, Hess attached modified electroscopes to a hot air balloon and took them up to altitudes of 5.3 km (3.3 mi). He discovered that radiation levels increased up to altitudes of 1 km, and then increased considerably at higher altitudes, almost doubling at 5 km. His conclusion was that there was penetrating radiation coming from outer space [5, 6]. This discovery was confirmed by Robert Andrews Millikan in 1925, who coined the term “cosmic ray.” Compton proved that cosmic rays are charged particles [6].

Particles that strike the upper atmosphere are known as primary cosmic rays and are mainly protons and alpha particles. The primary cosmic rays collide with the nuclei of atmospheric gases to create new subatomic particles like pions and kaons, that ultimately decay into muons. These pions, kaons, and muons fall towards the surface of the earth [7]. Muons are detected by several types of detectors, including cloud chambers and scintillation detectors [8].

1.3.2 Reactor Instrumentation

Different types of neutron detectors are used in nuclear reactors to monitor flux and power levels and have been used in every fission core since Fermi’s Chicago Pile went critical in 1942. These detectors monitor reactor power levels by measuring decades

of neutron flux [12, 13]. In the Maryland University Training Reactor (MUTR), there are three types of neutron detectors: fission chamber, compensated ion chamber, and an uncompensated ion chamber.

The MUTR fission chamber measures ten decades of neutron flux. The detector is a chamber lined with a thin film of ^{235}U and filled with a gas such as Argon. As neutrons enter the detector, they penetrate the lining and may cause fission in the uranium. The fission fragments that are produced travel through the detector and ionize the fill gas. The ion pairs hit the walls of the detector and create pulses, which are converted into an output signal [14].

The gamma compensated ion chamber (CIC) of the MUTR is attached to a linear chart recorder. In addition to the ion chamber lined with ^{10}B , there is a second chamber that is unlined. Both chambers are filled with an inert gas. The second chamber is used to subtract gamma counts from the neutron counts. As the ion pairs are produced in the ^{10}B lined chamber, a current resulting from the gamma and the neutron count rates is produced. As the second chamber is not lined with ^{10}B , the current is only derived from the gamma count rate, so the currents from the two chambers are subtracted to leave only the neutron count rate [14].

1.3.3 Special Nuclear Material (SNM) Detection

Special nuclear material (SNM) includes fissile isotopes of ^{233}U , ^{235}U , and ^{239}Pu . These materials occasionally decay through spontaneous fission, a form of radioactive decay characteristic of heavy elements. The unstable nuclei split into two smaller nuclei of approximately equal mass with the release of one or more neutrons. Special nuclear material could be used in nuclear weapons or dirty bombs, but the release of neutrons from spontaneous fission allows these materials to be detectable using a neutron detector. If a neutron detector is placed close enough to the source of fission, neutrons will interact with the detector lining to produce observable pulses, which

can lead one directly to the source. The Department of Homeland Security (DHS) is especially interested in neutron detection [16].

Special nuclear materials emit gamma rays and neutrons, but because the emission intensities of each are so small, SNM are easy to conceal. Part of the difficulty in detecting SNM is due to the neutron background at sea level from cosmic rays and extraneous solar activity, which has a tendency to overwhelm the emitted flux from nuclear material beyond 7 m from the source [17]. Neutron detectors can be used to detect the neutrons produced through spontaneous fission in a wide variety of homeland security applications, including border crossings, or incoming vessels such as cargo planes or barges, which may be smuggling SNM. Currently, the Department of Homeland Security has more than 1,400 radiation detecting portal monitors (RPMs) located at ports and border crossings with another 2,000 deployed abroad; the DHS, the Department of Energy, and the Department of Defense plan to station an additional 3,500 RPMs at strategic locations in the next six years, so the incentive for neutron detectors that do not rely on ^3He is strong [1, 18, 19].

1.3.4 Oil Well Logging

Well logging is the practice of measuring the properties of geological strata in which a well has been drilled. The data obtained can be used to discover the location of hydrocarbon deposits. The well log is the trace of the data obtained from sensor tools placed in the well, plotted against well depth. In particular, wireline logging is a technique in which these sensors are placed in vessels called “sondes” with electronic circuits and lowered into a borehole. The sensors have the capability of measuring properties such as neutron moderation, thermal neutron absorption, and other sources of radioactivity. A counter and a source of radiation are lowered into a bore, and the counter will measure the different amounts of radiation that scatter back into the detector from the different strata material of the bores [8].

The main neutron source tool used for well logging is neutron moderation (which measures the hydrogen, oxygen, and carbon content and relates it indirectly to porosity). Others include the C/O tool (which measures the ratio of carbon to oxygen and can be used to determine the oil or water content of the well) and the formation neutron cross-section tool (which measures the neutron absorption cross-section inside and outside the well). These typically use an accelerator D-T source because they measure the gamma ray emission resulting from inelastic neutron scattering. The neutron moderation tool measures the slowing down of neutrons by detecting the radiation elastically scattered back into the detector as the neutrons interact with the media inside the detector. In the presence of oxygen and carbon, high energy neutrons inelastically scatter and thermalize, which are observed by the detector. The number of neutrons that are observed can be used to determine the content of oxygen and carbon [20].

1.4 Objectives

The basic nature of this thesis is the development of an excimer-based neutron detection system using a ^{10}B enriched gas or B_4C film deposited on carbon foam mixed with a rare noble gas like Ar, Kr, or Xe. The importance of this research is to lay the groundwork for a new method of neutron detection that does not rely on the use of ^3He as the fill gas. This thesis consists of the investigation of excimer formation through the measurement of FUV photon emission, leading to a determination of the optimum mixture of $^{10}\text{BF}_3$ gas or ^{10}B enriched carbon foam substrate and rare noble gases (Xe, Kr, or Ar), and the measurement of absolute cross-sections for photon production.

This thesis is broken into chapters corresponding to various aspects of the research. A brief background on neutron detection, including traditional methods of detection, the concept of excimer-based neutron detection (END), as well as a discussion of

excimer research is presented in Chapter 2. Previous research that established the basis for the experiments presented in this thesis are discussed in Chapter 3. Chapter 5 discusses the experimental apparatus used in the scintillation experiments on the Maryland University Training Reactor (MUTR), as well as a discussion of detector electronics and a discussion on the photomultiplier tube characterization.

Prerequisite photoabsorption cross-section experiments to determine the viability of $^{10}\text{BF}_3$ are presented in Chapter 4. Current photoabsorption spectra of $^{10}\text{BF}_3$ in the far ultraviolet (FUV) region differ by a factor of 10^3 , where some researchers find that boron trifluoride is transparent and others argue that it is completely opaque (Figure 1.4-1). If BF_3 strongly absorbs in the FUV region (135-205 nm), excimer emission would be attenuated and would not reach the photon detector. This is critical for mixtures of $^{10}\text{BF}_3$ and rare gases, and was the first task undertaken on the project. The results of these experiments are presented in Chapter 4.

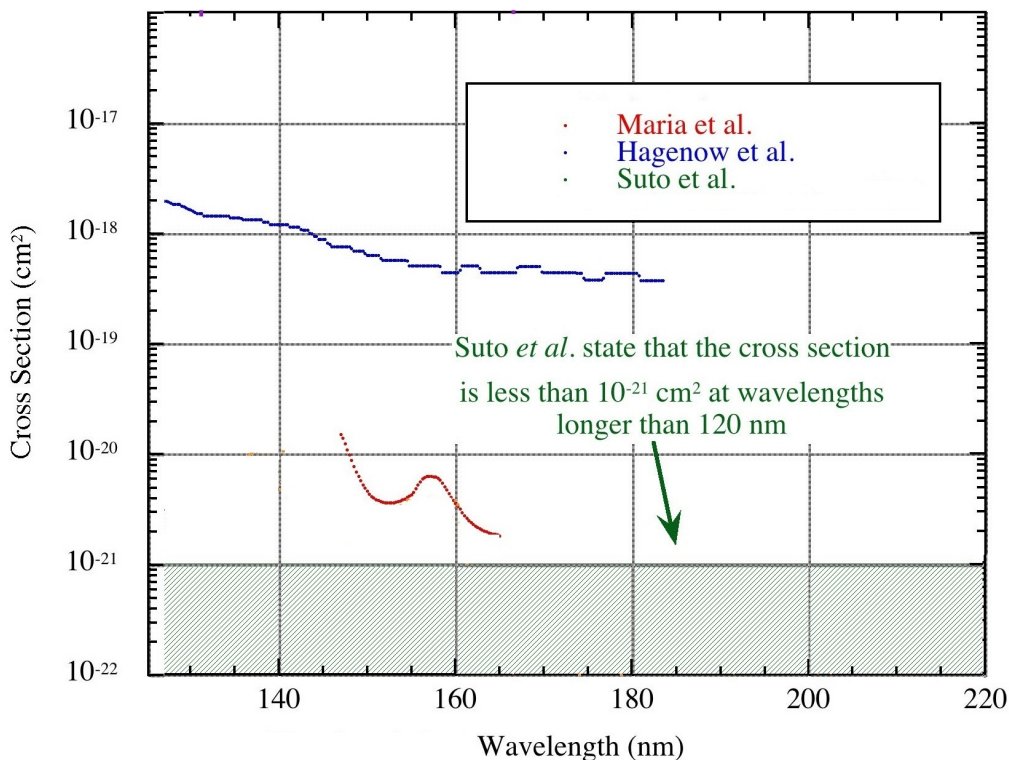


Figure 1.4-1: Photoabsorption cross-section spectra from various BF_3 photoabsorption experiments. These data range from completely transparent in the FUV region [22, 23], to completely opaque [24].

Using the neutron source from the MUTR thermal column, the photon signal from various mixtures and pressures of $^{10}\text{BF}_3$ and rare noble gases was measured. The apparatus and relevant electronics used in these experiments are described in Chapter 5, along with a brief discussion of the photomultiplier tube characterization. The $^{10}\text{BF}_3$ experiments are detailed in Chapter 7. Following the conclusion of the $^{10}\text{BF}_3$ experiments, an opportunity arose to use reticulated vitreous carbon foam (RVC) coated with a layer of B_4C (naturally enriched in ^{10}B to $< 19\%$). As previous experiments demonstrated that thinner films allow for a higher probability of reaction product escape, the open-pore network of the RVC provided an even greater potential while simultaneously increasing the surface area available for neutron interaction. This novel approach is discussed in Chapter 8, and the results of both experiments are presented in Chapter 9. Appendices detailing various problems that were encountered, the results of photoabsorption experiments involving O_2 and the $^{10}\text{BF}_3$, and the operating procedure for the BF_3 gas handling system are also provided following the conclusions of this research.

Chapter 2

Background

Radiation detection is dependent upon the interaction of radiation within a detector medium, the formation of the free charge produced as a result of interaction with the medium, and the collection of this free charge to create a detectable signal [3]. Because neutrons are neutral and have no charge, interaction with matter must occur within the nucleus of an atom, or close enough to the nucleus for nuclear forces to cause a reaction [15]. As a result of the neutrality, neutrons can travel through large thicknesses of matter without interacting. When a neutron does interact with matter, it is with the nucleus of some absorbing material, and the neutron will either undergo a drastic energy change or can even disappear entirely, to be replaced with one or more detectable secondary nuclei or radiation (i.e. beta radiation) [3]. This chapter will touch on different types of neutron interactions with matter, as well as some common neutron detectors. Because excimer-based neutron detection (END) is based on scintillation, traditional scintillation detectors are included in this discussion. Excimer formation and scintillation are discussed as well.

2.1 Neutron Interactions

2.1.1 Scattering

Scattering processes are those in which a neutron is re-emitted. There are two types of scattering reactions, elastic and inelastic [15]. In elastic scattering, all of the energy of the incoming neutron is transferred to the nucleus and the nucleus is left in a stable state. These reactions are called (n, n) reactions. Figure 2.1.1-1 illustrates an elastic

scattering process. Elastic scattering events slow the neutron to thermal energies in equilibrium with the target nuclei prior to a second interaction event [3].

If the energy of the incoming neutron is high enough, inelastic scattering can occur. In inelastic scattering, a fraction of the incoming neutron energy is transferred to the nucleus (more than in an elastic scattering event). A compound nucleus is formed by the interaction of the neutron with the target nucleus, and the nucleus is left in an excited, unstable state. As the nucleus de-excites, ionized particles (alpha particles, fission product, etc.), and/or gamma rays are emitted. These can cause ionization in background gases leading to a detectable electronic signal, however, the cross-sections for inelastic interactions are generally an order of magnitude lower than the cross-section for elastic scattering. Inelastic scattering reactions are, therefore, a less efficient means of detection [3, 15, 26].

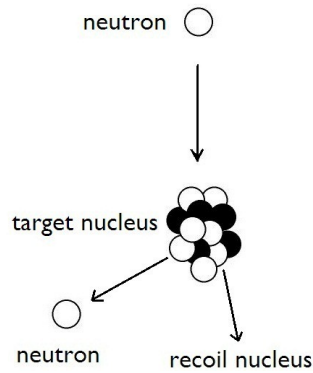


Figure 2.1.1-1: Elastic scattering of a neutron with a target nucleus.

2.1.2 Absorption

Absorption can occur through several processes. With heavy elements, the majority of the binding energy is released through gamma emissions, leaving a stable or unstable isotope. Unstable isotopes will decay and have the potential to emit more gamma rays. With light elements, proton or alpha emission can occur, as in the ${}^3\text{He}(n, p){}^3\text{H}$

or ${}^6\text{Li}(n, \alpha){}^3\text{H}$ reactions, respectively. Secondary reactions are possible with fast neutrons, in a process known as $(n, 2n)$ reactions. Fission can occur with very heavy nuclei, in which the nuclei absorbs neutrons and then splits into two fragments [4].

Figure 2.1.2-1 shows an (n, α) charged particle reaction with ${}^{10}\text{B}$. In this event, an incoming neutron interacts with the nucleus of a ${}^{10}\text{B}$ atom, which forms a compound nucleus. The compound nucleus decays into a ${}^7\text{Li}$ atom and an alpha particle. This is termed an absorption reaction [16]. This reaction is exothermic, releasing up to 2.79 MeV of energy, and readily overcomes the Coulomb barrier [15]. Other charged-particle reactions include (n, p) , (n, d) , (n, t) , and $(n, \alpha p)$ reactions [16].

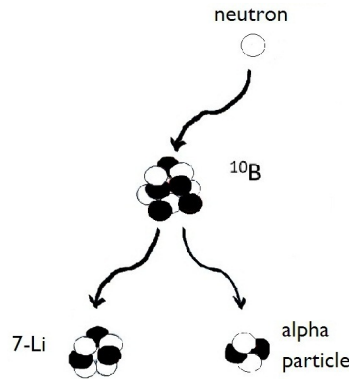


Figure 2.1.2-1: ${}^{10}\text{B}(n, \alpha){}^7\text{Li}$ absorption reaction.

In charged particle reactions, the charged particle must overcome the Coulomb barrier before it can escape the nucleus. The Coulomb barrier is an energy barrier resulting from electrostatic interactions. It is necessary to overcome this barrier before two nuclei can get close enough to interact with each other. Charged particle reactions are common for light nuclides. Other absorption reactions include radiative capture (n, γ) and fission. Radiative capture is very common, and occurs with high probability for many nuclides in the epithermal energy range. When this type of reaction occurs, it is called resonance capture. In fission, a neutron is absorbed by a heavy nuclide like ${}^{235}\text{U}$ or ${}^{239}\text{Pu}$. An unstable compound nucleus forms which splits into two fission fragments and one or more neutrons [16, 15].

2.2 Neutron Detectors

There are several different types of detectors, and each are characterized by the way radiation interacts with the detector material. Ionization is a very common method of detection, in which the movement of charged particles through the detector creates charged particles. Ionization detectors include ion chambers, proportional counters, and Geiger-Mueller (GM) counters.

Other detectors operate through excitation and molecular dissociation, which in combination with the ionization process create the luminescence of scintillation detectors [15]. These will all be discussed.

2.2.1 Gas-Filled Detectors

Traditional gas-filled neutron detectors, shown in Figure 2.2.1-1, include ionization chambers, BF_3 and ^3He proportional counters, gas filled ^{10}B -lined proportional counters, and fission chambers (which detect neutrons that induce fission in fissionable material). In a gas-filled detector, a neutron interacts with a gas or solid coating within the walls of the cathode enclosure and transfers energy to a recoil nucleus or starts a reaction with energetic charged-particle reaction products. In either scenario, the transfer of energy causes ionization in the gas-filled detection medium [3].

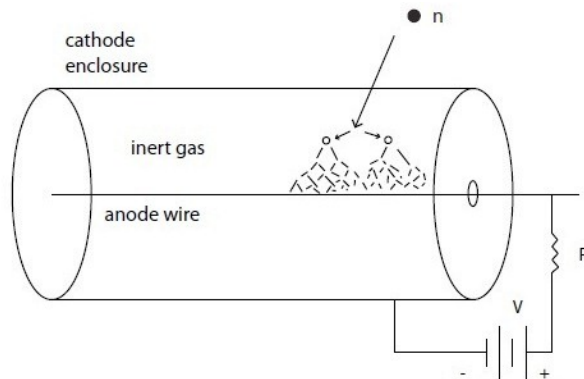


Figure 2.2.1-1: Gas-filled detector

In ionization chambers, a voltage (V) is applied between the wall of the cathode enclosure and the anode wire that is connected to a voltage source through a resistor (R). In ^3He or $^{10}\text{BF}_3$ detectors, the neutrons react with the ^3He or ^{10}B to produce product ions. Positive and negative charges within the detector move toward the chamber wall and central anode wire, respectively. Secondary ionization events may occur as the primary ionization particles travel through the detector. The charge as a function of voltage is shown by Figure 2.2.1-2 [3, 15].

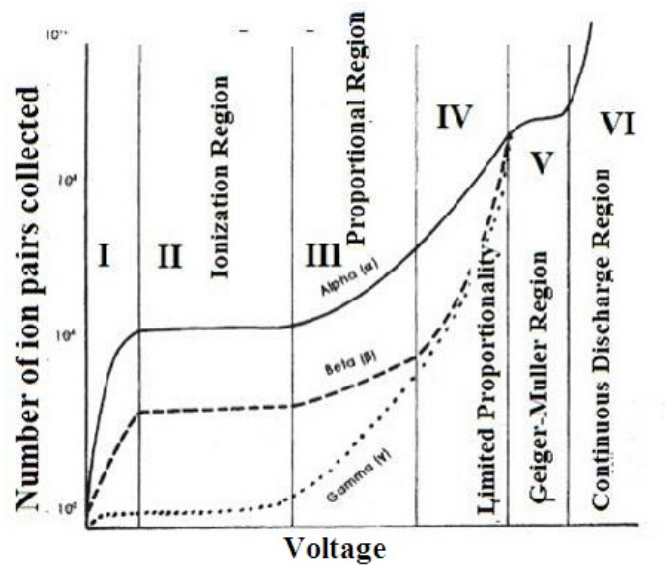


Figure 2.2.1-2: Pulse height versus applied voltage [15]

As seen from Figure 2.2.1-2, there are four distinct regions. In region I, there is competition between the loss of ion pairs through recombination and removal of charge by collection on the electrodes. As the field increases, the ion drift velocity increases, and the recombination time decreases leading to an increase in the fraction of charge collection. Recombination is negligible in region II.

Region III is known as the proportional region where there is a linear relationship between the number of ion pairs collected and the applied voltage of the detector. All collected charge is affected by gas multiplication, and is therefore proportionally increased by a factor of M . Electrons produced in primary ionization are accelerated

to produce secondary ionizations. In region IV, the collected charge is independent of the initiating ionization event. Gas multiplication increases the charge to the point where detector geometry and other limiting characteristics limits charge increase [15].

Typically, the mean free path of electrons in a gas-filled detector is limited to 1-2 μm . Secondary electrons may be collected on the order of 10^{-8} s, but the slow drift velocity of positive ions limits the response time of these detectors. These detectors also require discrimination against gamma signals resulting from non-neutron background events [3, 15].

2.2.1.1 Ionization Chambers

Ionization chambers are the simplest of all gas-filled detectors. Ionization consists of the removal of one or more electrons from a given number of gas molecules to form positive and negative ions. These detectors are based on the direct detection of ionization created by particles passing through a gas. The normal operation of an ion chamber is the collection of charges created by direct ionization in the gas derived from an electric field [3, 15].

As a neutron moves through the gas background, it interacts with a neutron absorbing material such as ^3He , ^{10}B , or ^6Li , and produces charged particle reaction products that move through the gas molecules to produce excited and ionized molecules. The ionization of a neutral molecule results in the formation of a positive ion and a free electron (an ion pair). This is the basic component of the electrical signal derived from an ion chamber. Ions are formed either in the primary interaction with the incident particle, or through secondary processes in which some of the energy of the particle is transferred to an energetic electron [3].

As an electric field is applied, the charged particles will drift in a direction away from their point of origin. This drift creates the steady state ionization current which is a measure of the rate of ion pair formation [3].

2.2.1.2 Proportional Counters

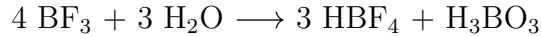
Proportional counters rely on a phenomenon known as gas multiplication to amplify the charge created by gas ionization, in contrast to ionization chambers, which can operate in current or in pulse mode. Gas multiplication occurs with increasing electric field within the gas due to increasing voltage. At low values of the field, electrons and positive ions created through irradiation drift to their respective electrodes. Collisions occur naturally with neutral gas molecules as these positively and negatively charged ions move through the detector volume. Since the drift velocity of these ions is low, there is little transfer of kinetic energy during these collisions. Secondary ionizations are possible if the kinetic energy transfer is greater than the ionization energy of the neutral gas molecule. The probability of secondary ionizations rises exponentially with electric field [4]. The secondary electrons produced will be accelerated by the electric field and collide with neutral gas molecules. This can create even more ion pairs. The process continues as a cascade, which is known as Townsend avalanche. Each free electron created in a collision has the potential to create more free electrons via the same process (10^3 - 10^5 secondary or tertiary electrons) [28]. Townsend avalanche continues until all of the electrons are collected at the anode. This gas multiplication is linear over the electric field, meaning the collected charge is proportional to the number of ion pairs created in the primary ionization event [3, 8].

In the traditional $^{10}\text{BF}_3$ proportional detector, $^{10}\text{BF}_3$ enriched gas acts as both the target for the neutron reaction and the gas that undergoes ionization [3]. The BF_3 gas is enriched in ^{10}B because of the high thermal neutron absorption cross-section ($\sigma_{th} = 3840$ b). These proportional detectors have very good gamma ray discriminating properties. Gamma rays are commonly found in the neutron flux being measured and can react in the detector to create secondary electrons that have the potential to ionize in the gas. As the stopping power for secondary electrons in gases is small, electrons will usually deposit only a small amount of energy in the gas before reach-

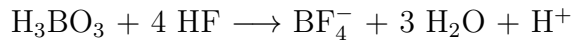
ing the opposite wall. This results in low amplitude pulses that can be discriminated from the rest of the signal [3].

Typically, $^{10}\text{BF}_3$ gas detectors are lined with charcoal to absorb electronegative gases that build up. For instance, for each neutron capture that occurs, three fluorine atoms are released. These fluorine atoms combine with the electrons produced in subsequent neutron capture to produce electronegative fluorine ions. The formation of fluorine ions reduces the electric pulse amplitude of the detector. The charcoal lining of the detector absorbs the fluorine ions created and minimizes the reduction in the electron pulse [28].

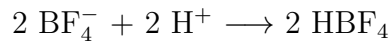
Gaseous BF_3 reacts exothermically with water vapor in the air to produce boric acid and fluoroboric acid:



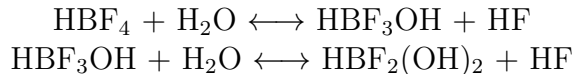
Boric acid (H_3BO_3) acts as a fluoride “scavenger,” preventing the formation of free fluoride ions by reacting with fluorine to produce tetrafluoroborate (BF_4^-), a relatively inert anion.



Tetrafluoroborate can react with the H^+ ion to form fluoroboric acid:



However, under the rare condition that there is no excess boric acid, the fluoroboric acid (HBF_4) may hydrolyze to produce toxic hydrofluoric acid (HF).



The formation of HF or free fluoride ions is highly unlikely, as there will always be free boric acid present in these types of reactions [29].

2.2.2 Scintillation Detectors

The modern scintillator was developed in 1947 by Coltman and Marshall. They successfully used a photomultiplier tube (PMT) to count light produced by alpha, beta, and gamma radiation [15]. An incoming neutron or high-energy particle is absorbed by a neutron absorbing material in an exothermic reaction. Charged particles are emitted and scatter in the scintillation medium, transferring energy to the dopant which causes excitation of the phosphor in the scintillator and produces pulses of light. [8, 28]. These light pulses can be detected by a photomultiplier tube, where the light produced is transmitted to the photocathode of the PMT [15]. A diagram of this detector configuration appears in Figure 2.2.2-1 [3, 28].

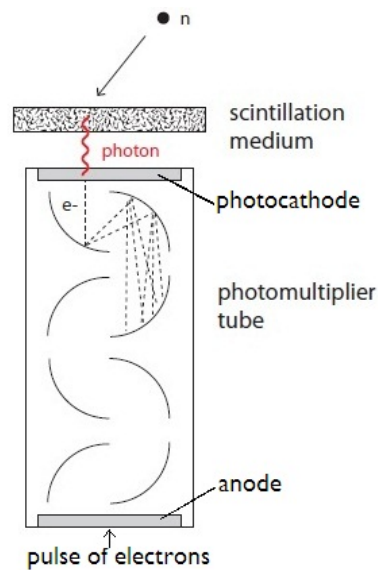


Figure 2.2.2-1: Scintillation detector and photomultiplier tube

The mechanism of scintillation is known as luminescence, wherein a substance absorbs energy and re-emits it as visible or near visible light. Scintillation in neutron detectors results from excitation of the irradiation of the scintillation medium. If the atom is left in a metastable state, the emission of light is delayed. This type of radiation is called phosphorescence [15, 4]. A typical scintillator detection system is shown in Figure 2.2.2-2.

There are several different types of scintillators, usually divided into three main groups: inorganic, organic, and gaseous scintillators. These include organic-crystal, organic-liquid, inorganic-crystal, and gas-filled scintillators [27].

Inorganic scintillators are usually inorganic salt crystals, such as NaI(Tl), CsI(Tl), or CaI(Na), where the element in parentheses is the impurity or activator [27]. These types of detectors are used as gamma ray detectors. Impurities in the salts act as luminescent activators. Ionizing radiation passes through the crystal. An ionization event transfers an electron from the valence band of the crystal lattice to the conduction band and leaves a hole behind in the valence band. The electron-hole pair forms an exciton. Electrons, holes, and excitons move through the lattice of the crystal until they are captured at the activator sites, which are then elevated to excited states. These activator sites de-excite and emit a photon [15, 27].

In organic scintillators, light is produced through molecular transitions. As ionizing radiation passes through the scintillation medium energy can be transferred to the medium molecules and raise them to excited states. Lattice vibrations within the medium may cause the molecules to move to additional excited states. This movement between excited states can result in the emission of a photon [27].

There are several types of organic scintillators, none of which require an activator. Organic-crystal scintillators typically use aromatic hydrocarbons, such as an-

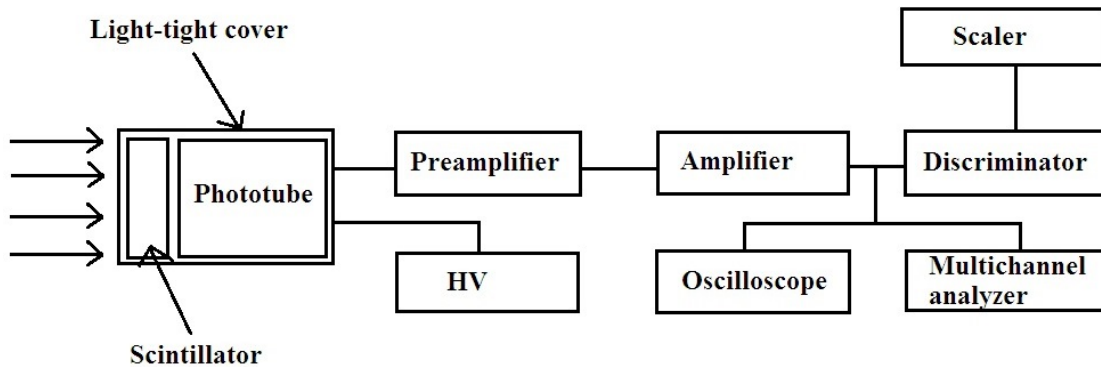


Figure 2.2.2-2: Scintillation detector system [27]

thracene [15]. Organic-liquid scintillators use organic scintillator materials such as *p*-terphenyl, PBO (2-phenyl-5-(4-biphenyl)-oxazole), PBD (2-phenyl-5-(4-biphenyl)-1,3,4-oxadiazole), or POPOP (1,4-di-[2-(5-phenyloxazolyl)]-benzene). The scintillators are usually dissolved in a liquid organic solvent like xylene, toluene, or triethylbenzene. These types of scintillators are typically used for slow neutron detection [4, 15]. Plastic scintillators are mixtures of a solid and one or more solute. The most common solids are polystyrene and polyvinyltoluene. The most common solutes are *p*-terphenyl and POPOP [27].

Gaseous scintillators are mixtures of noble gases, in particular xenon, krypton and argon. As the noble gas background is irradiated, the gas atoms are elevated to an excited electronic state. As they return to ground state, they emit one or more photons to produce a fast light pulse in the UV region [15]. Table 2.2.2-1 illustrates some typical scintillator characteristics.

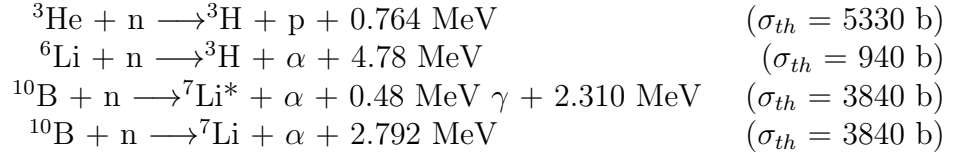
Scintillators have several advantages as neutron detectors. They tend to be transparent to the radiation they produce, have a high conversion efficiency between recoil and fluorescent radiations, and short decay times with fast response times on the order of several hundred nanoseconds. They are, however, very gamma sensitive [3].

Table 2.2.2-1: Characteristics of several thermal neutron scintillators, including light yield per neutron (Y_n), gamma-ray interaction (Y_γ), emission wavelength (λ_{hv}), and decay times (τ) [30].

Host	Dopant	Density (g/cm ³)	Y_n	Y_γ	λ_{hv} (nm)	τ (ns)
⁶ Li-glass	Ce	2.5	6,000	4,000	395	75
⁶ LiI	Eu	4.1	50,000	12,000	470	1,400
⁶ LiF/ZnS	Ag	2.6	160,000	75,000	450	1,000
LiBaF ₃	Ce, K	5.3	3,500	5,000	190-330	1/34/2,100
LiBaF ₃	Ce, Rb	5.3	3,600	4,500	190-330	1/34/2,400
⁶ Li ₆ Gd(¹¹ BO ₃) ₃	Ce	3.5	40,000	25,000	385	200/800
Cs ₂ ⁶ LiYCl ₆	Ce	3.3	70,000	22,000	380	1,000
Cs ₂ ⁶ LiYBr ₆	Ce	4.1	88,000	23,000	389	89/2500

2.3 Excimer-Based Neutron Detection (END)

Excimer-based far-ultraviolet neutron detection utilizes the same nuclear mechanism as gas-filled proportional counters. A nucleus with a high neutron absorption cross-section absorbs a neutron to create an exothermic reaction resulting in two charged particle reaction products. These reactions include:



The exothermicity of the reaction is carried away as kinetic energy of the daughter products. For the ${}^{10}\text{B}$ reaction, the branching ratio is 93% for ${}^7\text{Li}^*$ and 7% for ${}^7\text{Li}$ [3]. In contrast to proportional detectors, END does not rely on the collection of free charge to create an electronic pulse. Instead, an optical signal is produced through scintillation in a noble gas background. The reaction products formed by the neutron reaction cause ionization and excitation to produce noble gas excimers.

Excimers, transient molecules that exist only in an excited state, form when individual excited atoms combine with ground state atoms to form an excited diatomic molecule (excited dimer) [31]. As the excimers return to ground state, they dissociate and emit far-ultraviolet radiation with wavelengths between 120-180 nm that can be collected by an FUV photon detector such as a photomultiplier tube. Figure 2.3-1 illustrates the excimer emission region for Ar, Kr, and Xe excimers [32]. Table 2.3-1 shows the properties of the noble gases used in this research.

Table 2.3-1: Properties of noble gases, including density (ρ), peak excimer emission wavelength (λ_{peak}), and peak excimer photon energy (E_{hv}) [33].

Gas	Z	A (u)	ρ (kg/m ³)	λ_{peak} (nm)	E_{hv} (eV)
Argon	18	39.95	1.761	128	9.57
Krypton	36	83.8	3.696	150	8.42
Xenon	54	131.3	5.897	175	7.02

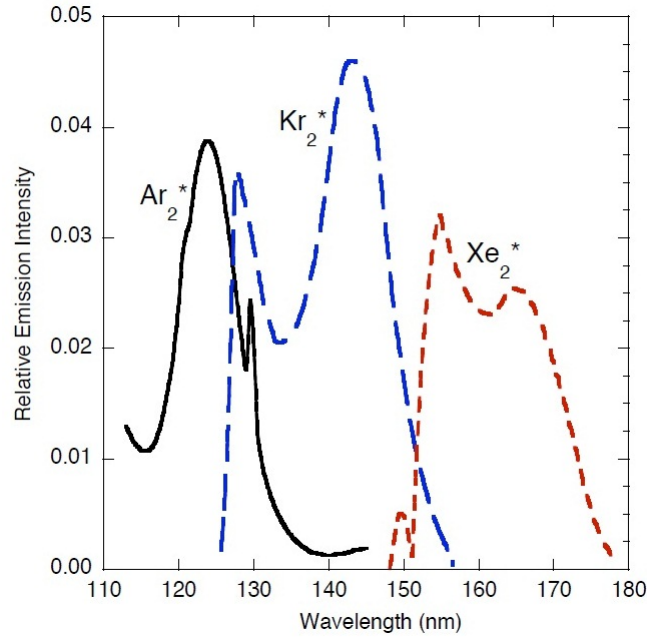
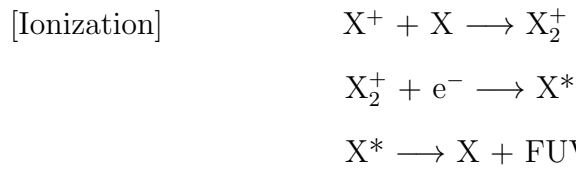
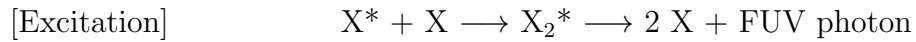


Figure 2.3-1: Excimer emission for Xe_2^* , Kr_2^* , Ar_2^* [32]

2.3.1 Excimer Scintillation

Excimer formation can occur through excitation of an excited noble gas atom, or through ionization of an ionized noble gas atom, followed by diatomic ion formation, electron recombination, and excimer formation [31].

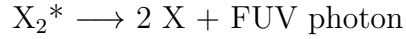


In these reaction equations, X is a noble gas atom, X^* is a noble gas atom in the first excited state, $2X$ is 2 individual noble gas atoms, X^+ is an ionized noble gas atom, X_2^+ is an ionized noble gas diatomic molecule, and X^{**} is a noble gas atom in an excited state above the first excited state [34].

As the noble gas background pressure increases (7-75 torr), the probability of the emitted FUV photon being reabsorbed increases. Additionally, the probability of multiple collisions increases, which leads to the formation of the excimer:



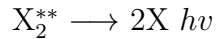
where X_2^* is a noble gas excimer. This reaction occurs very quickly, on the order of 10^{-11} to 10^{-12} s [33]. The excimer then decays and emits a photon:



Excimer formation and rare gas continua have been studied extensively. Figure 2.3.1-1 illustrates the noble gas continua studied by Tanaka, *et al.* [35].

The peak at 170 nm in the Xe continuum is due to the transition from an excited state to ground state, $^3\Sigma_u$ to $^1\Sigma_g^0$. The excited state dissociates to Xe ($5p^6\ ^1S$) + Xe ($5p^5\ 6s^3P$). This behavior can also be used to explain the second continua of Kr and Ar (Figure 2.3.1-1) due to the similarities in the electronic configurations of the excited states of the rare gases. Shorter wavelengths are observed for the lighter rare gases because the excitation energy for the lowest excited state of an atom increases for lighter atoms, which increases the excitation energy and shifts the spectrum to shorter wavelengths [36].

Similar conclusions were drawn by a number of researchers twenty years later. Brodmann claimed the 0_u^+ excimer state decays radiatively, or undergoes vibrational relaxation due to two-body collisions to produce the first continua [37]. Suzuki and Kubota observed that the first continuum emission was due to the transition from a vibrationally unrelaxed and excited state, $0_u^+(^1\Sigma_u^+)$, to the repulsive ground state:



where X_2^{**} is a molecule in the vibrationally unrelaxed excited state [38]. This atom is formed through the three-body collision:



In this equation, X^* is an atom in an (n+1) excited state [37, 38, 39].

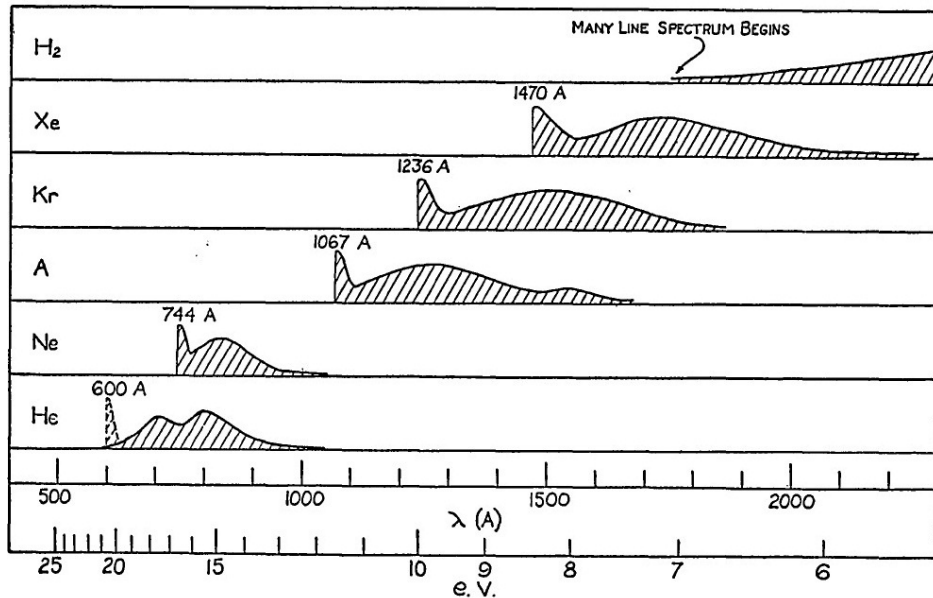
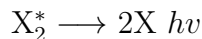


Figure 2.3.1-1: Rare gas continua observed using a helium discharge tube [35].

Suzuki also reported findings for the second continuum emission, citing the transition between vibrationally relaxed and excited molecular states, ${}^1\Sigma_u^+$ to ${}^3\Sigma_u^+$, to the repulsive ground state:



where X_2^* is an atom in the excited vibrationally unrelaxed state formed through:



The conclusion was that rare gas proportional scintillation is due to transitions from an excited state to the ground state:



For pure xenon, the emission wavelength is largely dependent on the gas pressure. Monteiro, *et al.* have observed atomic emission peaks at 130 and 147 nm, for Xe pressures less than 10 torr. As the rare gas pressure increases, excimers form through three-body collisions, and molecular emission peaks are observed at 147 nm and 170 nm (first and second continua, respectively). These continua are the result of radiative decay from a vibrationally excited state to a relaxed excimer state. As

the pressure is increased to 300 torr and higher, only this second peak at 172 nm is observed [40].

Suzuki and Kubota determined the decay times of the $^1\Sigma_u^+$ state is between 4-6 ns. For the $^3\Sigma_u^+$ state, the decay times are 3.2 μs (Ar), 1.7 μs (Kr), and 90 ns (Xe). These experiments were conducted with rare gas pressures on the order of 10^3 torr [38].

There have been numerous studies conducted in an attempt to determine the rise time of the excimer scintillation. Mutterer, *et al.* discovered that the pulse height distributions were different between Ar and Xe, and changed appreciably with increasing rare gas pressure. At 57 torr of Ar, Mutterer *et al.* reported that the rise time was approximately 8 ns with a decay time of 140 ns. For the same pressure of Xe, the rise time was observed to be 20 ns and the decay time was 50 ns. At 300 torr Xe, the rise time is 80 ns, with a decay time of 250 ns [41]. However, these values are in disagreement with other reported values. Conde, *et al.* reported Xe rise times on the order of 2 ns, with 10-20% energy resolution [42]. Nobles reported that the rise time of Xe was 3.5 ns [43]. Conde, *et al.* also observed a delayed secondary Xe scintillation (lag time approximately 12 μs) with a rise time of 10 μs . This secondary scintillation emits additional photons when electrons produced in the primary ionization event collide with the rare gas molecules [42, 44].

Nobles reported the range of α particles at 63 psi (3,258 torr) in Ar (7.3 mm), Kr (5.2 mm), and Xe (4.0 mm). When an 8.1 MeV α is introduced into a Xe noble gas scintillation cell, 3.9×10^5 electrons are produced, resulting in 16 photons emitted per single electron (6.24×10^6 total photons emitted) [43, 45, 46].

2.4 Advantages to END

There are several key advantages to FUV neutron detection. Traditional gas-filled detectors are cylindrical with neutron detection efficiency limited by the size of the

tube. As END does not require a cathode wire, there are no tube size or geometry limitations. These detectors can be as large or small as necessary [47]. Previous experiments have measured high neutron detection efficiency, with as much as 30% of the kinetic energy of the reaction products converted to FUV photons [32].

Noble gas scintillation counters tend to be blind to their own scintillation. They are typically independent of pulse heights to the charge and mass of the exciting particle, allowing good linearity with particle energy [43, 47]. These detectors also have no temperature dependence and may be operated in virtually any environment without being chilled [47].

Chapter 3

Review of Previous Experiments

Prior to the BF_3 and carbon foam END experiments, preliminary excimer scintillation experiments were conducted at NIST to demonstrate the feasibility of noble-gas scintillation. These experiments were conducted at the NCNR, the NIST Center for Neutron Research, between Fall 2008 and Spring 2011.

The Lyman-Alpha Neutron Detection (LAND) and initial END experiments began at the NIST Center for Neutron Research (NCNR) in 2008 [32, 49]. Both experiments have demonstrated the capacity to detect neutrons through far-ultraviolet photon detection. The LAND experiments detected neutrons by means of emission from the excited states of ^1H and ^3H , the reaction products of the $(n + ^3\text{He})$ nuclear reactions. The END experiments use rare gases combined with neutron capture nuclei to produce excimers that decay with the emission of FUV photons. Both the LAND and initial END experiments used cold neutrons from the NCNR, however, the experiments outlined in subsequent chapters used thermal neutrons from the Maryland University Training Reactor (MUTR).

3.1 NIST Center for Neutron Research

The NIST Center for Neutron Research is located at the National Institute of Standards and Technology in Gaithersburg, Maryland. The NCNR is home to nearly 30 scientific instruments utilizing cold and thermal neutrons, including the National Bureau of Standards Reactor (NBSR). The NBSR (Figure 3.1-1) is a heavy-water cooled and moderated reactor with 30 highly-enriched fuel elements. It has a peak

thermal power of 20 MW and an in-core neutron flux of 3.5×10^{14} n/cm⁻²-s⁻¹ [50].



Figure 3.1-1: NCNR guidehall [51]

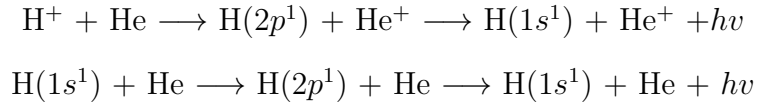
There are nine beamlines extending from the core which supply thermal neutrons to various instruments and experimental stations. A 5-L liquid hydrogen cold source funnels cold neutrons to an additional seven beamlines and experimental stations.

The initial END experiments were conducted on NG-6A and NG-6M, cold neutron beamlines. Each guide tube is coated with Ni-58 to maximize the reflection of low momentum, low angle-of-incidence neutrons through tube distances of 20-60m [52].

Beamline NG-6A has two monochromators, a pyrolytic graphite crystal and cooled slab of beryllium. These monochromators are used to select 0.496 nm wavelength neutrons. Beamline NG-6M consists of a potassium-intercalated graphite monochromator and additional filters for selecting 0.89 nm wavelength neutrons. The nominal flux of the sample locations on each beam was $(2.61 \pm 0.37) \times 10^5$ cm⁻²s⁻¹ [32].

3.2 Lyman-Alpha Experiment

Initial noble-gas scintillation experiments observed Lyman-alpha radiation from the ${}^3\text{He}(n, tp)$ reaction (Q-value 764 keV). This reaction was believed to produce Lyman-alpha photons at $\lambda = 121.5$ nm, through both charge-transfer and excitation. These reactions were believed to occur via:



An experimental scintillation cell was filled with 25-800 torr ${}^3\text{He}$ and irradiated on beamline NG-6A. A photomultiplier tube was used to detect photons at rates up to 46 photons per neutron absorbed [49]. To confirm that the observed signal resulted from Lyman-alpha photons, a single Lyman- α filter was placed between the cell and the photomultiplier tube to block the photons. The results, as a function of ${}^3\text{He}$ pressure, are plotted in Figure 3.2-1. For a more detailed description of these experiments, including the apparatus used, please refer to [49, 53].

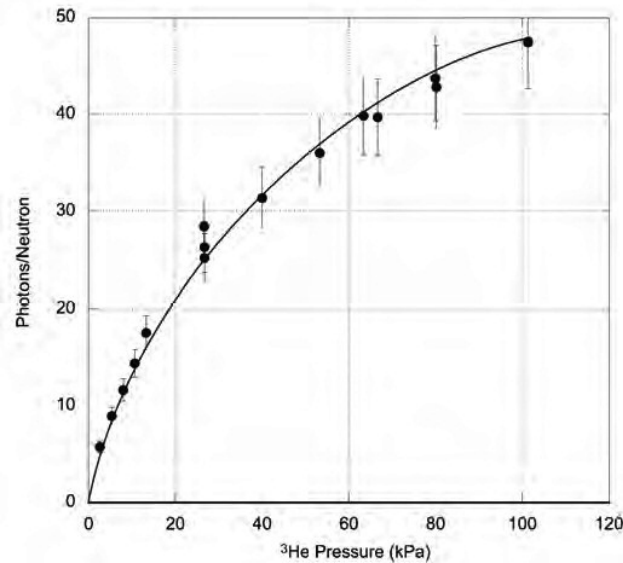


Figure 3.2-1: Lyman- α photons produced per neutron absorbed with ${}^3\text{He}$ as a function of ${}^3\text{He}$ pressure [49].

3.3 END at NIST

Following the initial success of the Lyman-alpha neutron detection (LAND) experiments, attempts were made to amplify the observed photon signal through the introduction of heavier noble gases (Xe, Kr, or Ar). Helium-3 was introduced to the cell at 200 torr, and a select noble gas was added in increments of 25-1000 torr. The excimer emission signal was found to be three orders of magnitude more intense, with tens of thousands of photons observed per neutron absorbed. These results, illustrated in Figure 3.3-1, indicated a conversion efficiency of up to 30% between the Q-value of the neutron reaction and the excimer scintillation emission [32]. In Figure 3.3-1, the left-hand scale illustrates the number of photons produced per neutron reacted with ^3He at 200, 600, and 1200 torr of Ar, Kr, and Xe. The right-hand scale illustrates the number of counts observed per neutron reacted. The error bars correspond to random and systematic uncertainties in the derived photon signal, from counting statistics in the signal and background measurements and detector efficiency calibration.

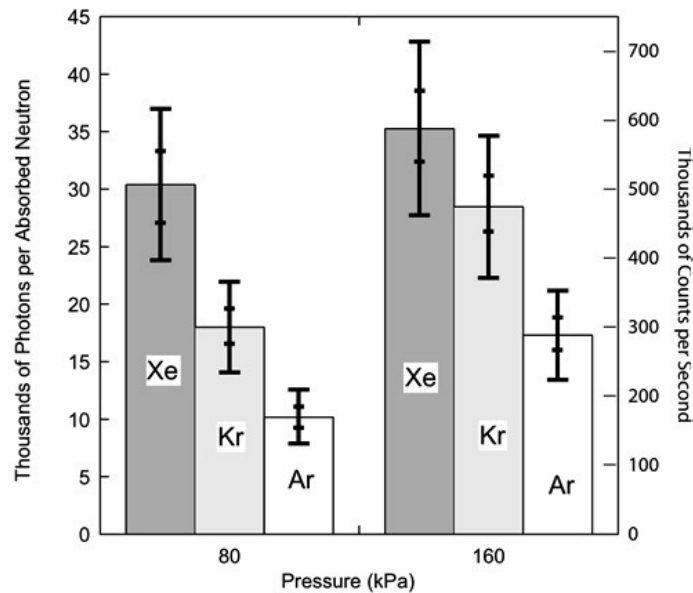


Figure 3.3-1: Left-hand scale: Thousands of photons observed per neutron absorbed. Right-hand scale: Thousands of counts observed per neutron absorbed [32].

Sapphire, fused silica, and CaF_2 spectral filters were used as wavelength filters to identify the radiation as Far-Ultraviolet (FUV) light, characteristic of noble gas excimer emissions. Argon excimers (Ar_2^*) were only detected with the CaF_2 filter at wavelengths around 122 nm. Krypton excimers (Kr_2^*) were detected with CaF_2 and the sapphire filters, with a peak wavelength at 142 nm. Xenon excimers (Xe_2^*) were detected with all three windows, with a peak wavelength around 160 nm. Figure 3.3-2 illustrates the photomultiplier tube response under monochromatic light, with each filter and without any filter, and how this signal changes when noble gases are introduced into the scintillation cell [32].

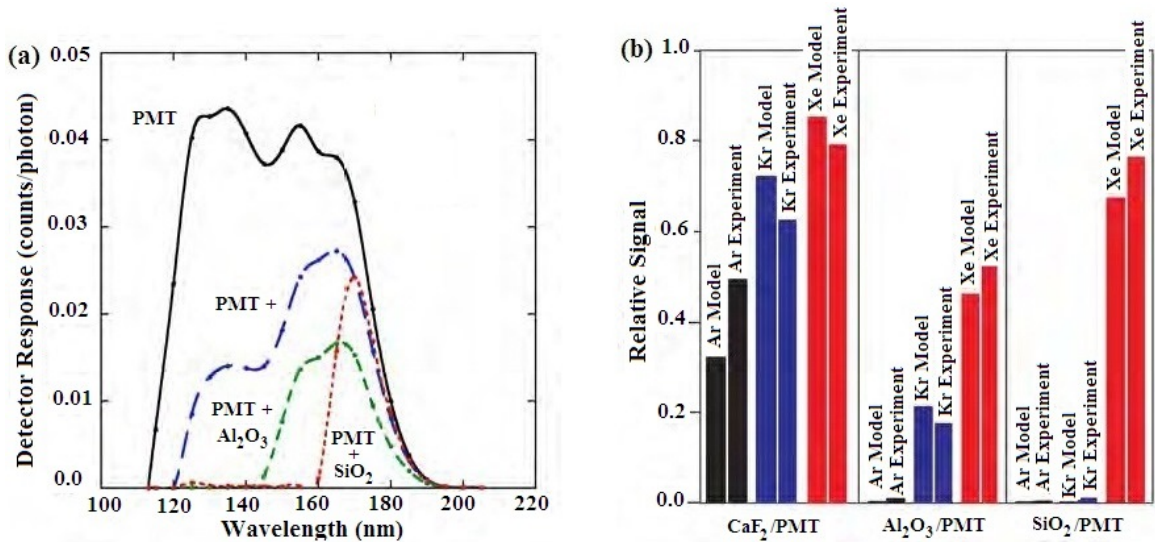


Figure 3.3-2: (a) PMT response to monochromatic UV radiation from SURF III synchrotron taking into account each filter response and PMT efficiency. (b) Relative excimer emission taking into account each filter response and PMT efficiency [32].

3.4 Thin-Film Experiments

Thin-film experiments were conducted using an assembly similar to that of the ^3He experiments (as well as the $^{10}\text{BF}_3$ experiments discussed in Section 5.2.3), replacing the ^3He gas with a ^{10}B enriched thin-film. The ^{10}B film thicknesses ranged from 300 nm to $1.2\ \mu\text{m}$ deposited on silicon substrates and positioned at a 45° angle within

the scintillation cell, with respect to the incident neutron beam. The films were positioned at this angle with a slotted aluminum cylinder approximately 2.54 cm in diameter to increase the path length of the beam by a factor of $\sqrt{2}$. This cylinder was held in place by a groove machined into the bottom and top Conflat[®] flanges. The inner surface of the sample holder cylinder was coated with copper-black oxide (Ebonol C[®]) to minimize the reflection of FUV photons within the cell [54].

Noble gases were added to the scintillation cell in pressures from 50 to 800 torr, and data were collected with and without a small piece of lithium glass, which acted as a block for the neutrons. The data were collected in this manner to discriminate between gamma initiated and neutron initiated events. For more information on these experiments, please refer to [54]. Figures 3.4-1, 3.4-2, and 3.4-3 illustrate the results obtained from the thin-film experiments.

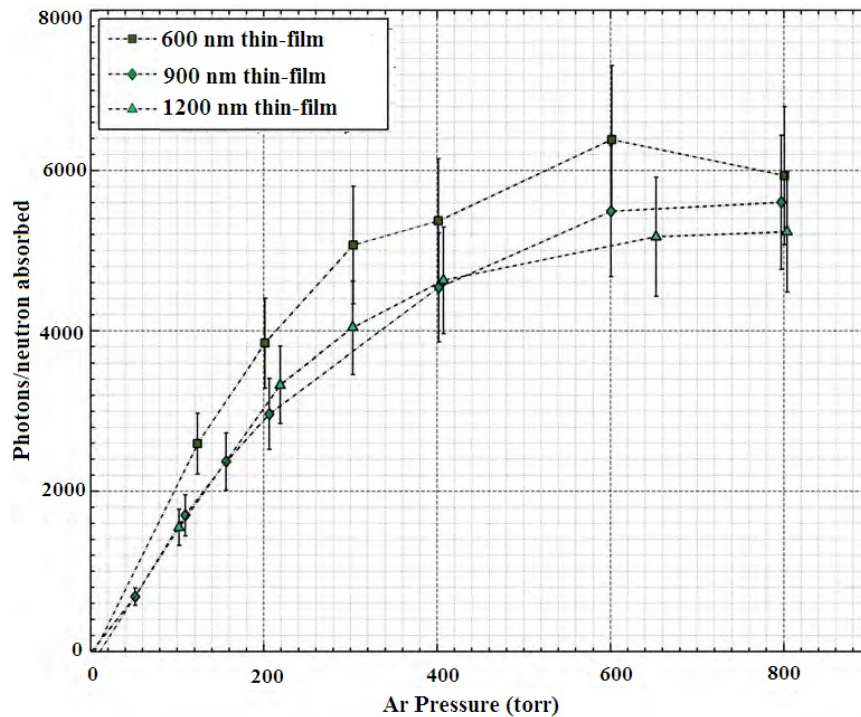


Figure 3.4-1: Excimer scintillation of argon during irradiation of 600 nm, 900 nm, and 1200 nm substrates [54].

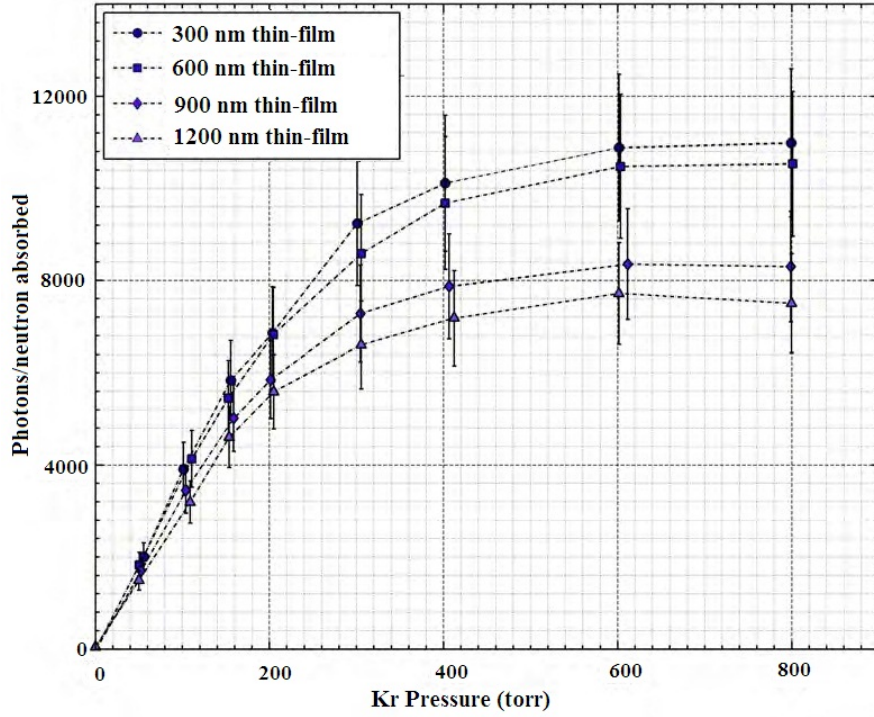


Figure 3.4-2: Excimer scintillation of krypton during irradiation of 300 nm, 600 nm, 900 nm, and 1200 nm substrates [54].

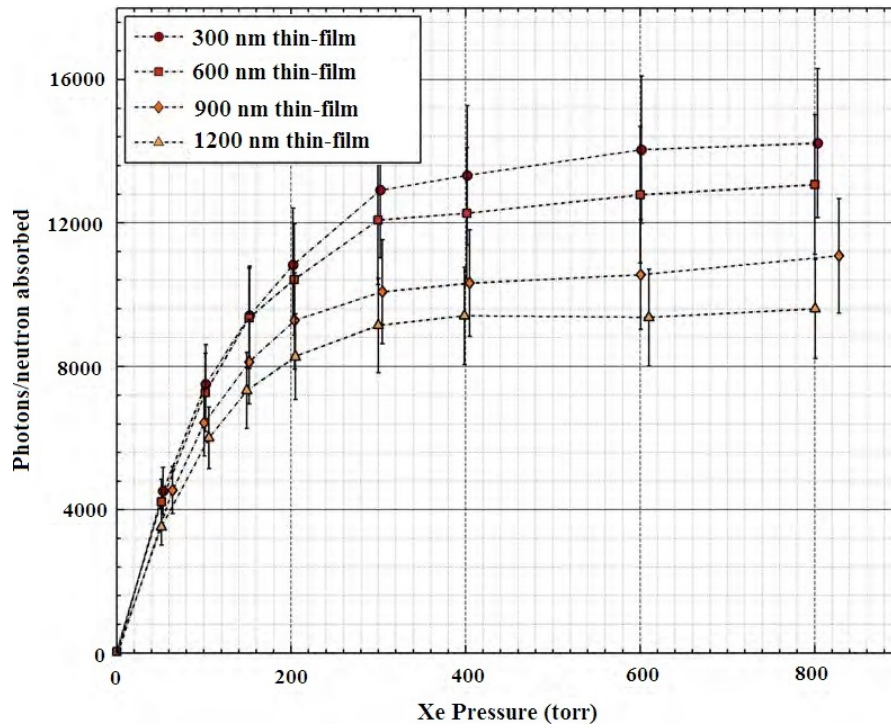


Figure 3.4-3: Excimer scintillation of xenon during irradiation of 300 nm, 600 nm, 900 nm, and 1200 nm substrates [54].

Chapter 4

Absolute Photoabsorption Cross-Section of $^{10}\text{BF}_3$

In order to determine the feasibility of $^{10}\text{BF}_3$ in Far-ultraviolet neutron detectors, a resolution of the absolute photoabsorption cross-section was required for $^{10}\text{BF}_3$ in the region of excimer emission. A comprehensive literature search of $^{10}\text{BF}_3$ in the FUV region (135-205 nm) showed a wide disparity amongst authors in the photoabsorption cross-section of $^{10}\text{BF}_3$ gas, shown in Figure 4-1. This disparity could be the result of impurities in the BF_3 or vacuum system used in the experiments. If $^{10}\text{BF}_3$ strongly absorbs in the FUV region, the excimer absorption will be attenuated and the excimer photons would not reach detector. Beamline 4 at the NIST SURF III (Synchrotron Ultraviolet Radiation Facility) was used to study the photoabsorption spectrum in the wavelength region of interest (135-205 nm).

The ^{10}B enriched BF_3 gas was obtained by Ceradyne[®], Inc., and was $> 99.6\%$ enriched in ^{10}B . The impurities and concentrations, in parts per million per volume (ppmv), are listed in Table 4-1.

Table 4-1: Concentration of impurities in $^{10}\text{BF}_3$ gas supplied by Ceradyne[®], Inc. [55].

Impurity	At %	Wt %	Concentration (ppmv)
^{10}B	99.64	99.6	
^{11}B	0.36	0.4	
N_2			4.62
Air ($\text{O}_2 + \text{Ar}$)			1.33
CO_2			57.57
SO_2			8.6
SiF_4			57.56
HF			< 1

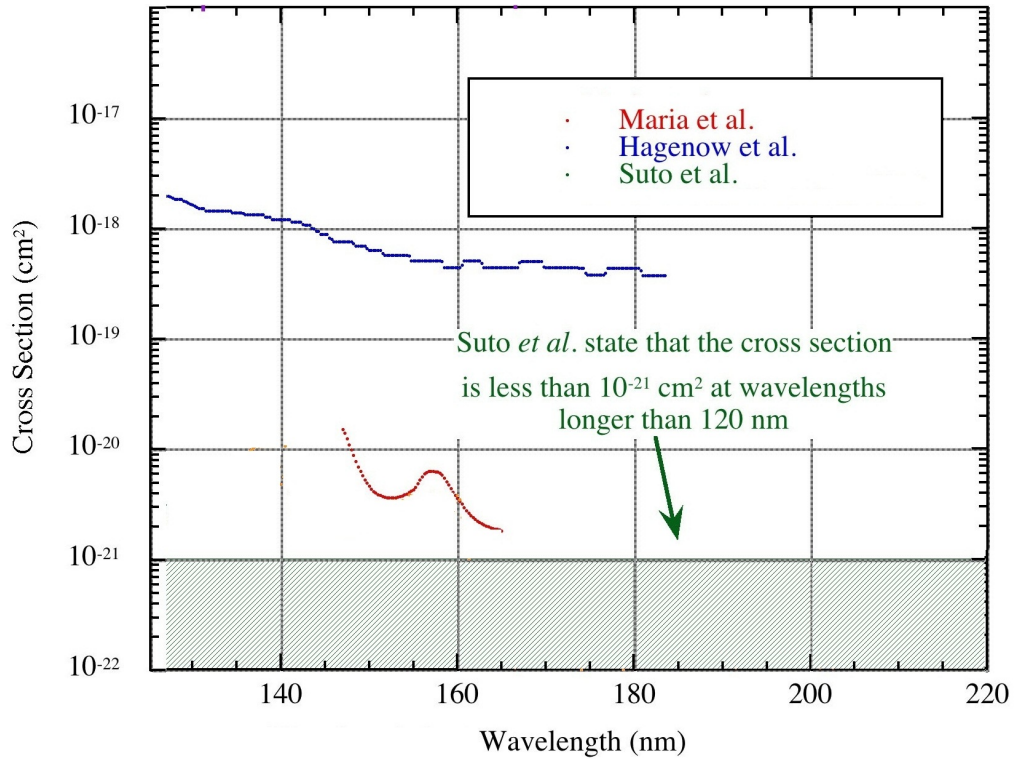


Figure 4-1: Comparison of literature values of the photoabsorption cross-section of $^{10}\text{BF}_3$ in the region 130-180 nm [21, 22, 23, 24].

4.1 Synchrotron Radiation

Synchrotron radiation is bright, broadband, polarized light produced by the electromagnetic radiation emitted as charged particles travel in curved paths. Relativistic electrons are accelerated in a circular orbit and emit electromagnetic radiation in a broad spectral range (Figure 4.1-1) [56]. A magnetic field is employed to turn the circulating electrons and an electric field with electromagnets and radio frequency waves are used to accelerate the electrons. Both the magnetic and electric fields are synchronized with the traveling electron beam [57, 58].

The Synchrotron Ultraviolet Radiation Facility (SURF III) is a compact electron storage ring housed at the National Institute of Standards and Technology (NIST), Gaithersburg, Maryland. It produces a stable source of light from infrared to soft x-ray. The peak output of SURF III is in the extreme ultraviolet (EUV) [54, 60, 61].

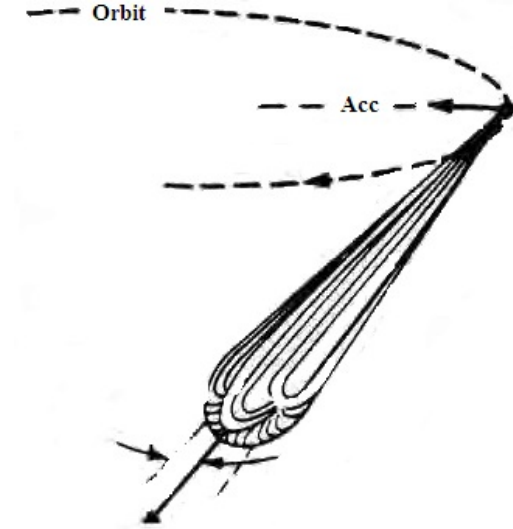


Figure 4.1-1: Acceleration of relativistic electrons in a magnetic field produce a collimated beam of photons perpendicular to the direction of acceleration [57].

Synchrotron light is preferred for photodetector calibration due to the continuous light produced and the ease with which these characteristics can be controlled and manipulated. The photon spectrum and intensity can be changed by altering the electron beam energy or current, respectively [57]. The energies of SURF III electrons range from 10-400 MeV, with currents from 10 pA (1 electron/s) to 1000 A (10^{11} electrons/s) [54, 63]. Figure 4.1-3 shows the wavelength-dependent power at various operating energies.

Beamline 4 (Figure 4.1-4), built for UV experiments and detector calibrations, was used for the photoabsorption experiments. Beamline 4 consists of a 2-m monochromator which is used to disperse the radiation from 115 to 320 nm produced from SURF III [62, 63]. A CaF_2 beamsplitter is incorporated into the optical system on BL-4, which provides an optical beam that can be monitored to provide information on beam current decay. An MgF_2 window installed between the monochromator and the experimental station transmits a wavelength range of 115 nm to 320 nm [54, 59].

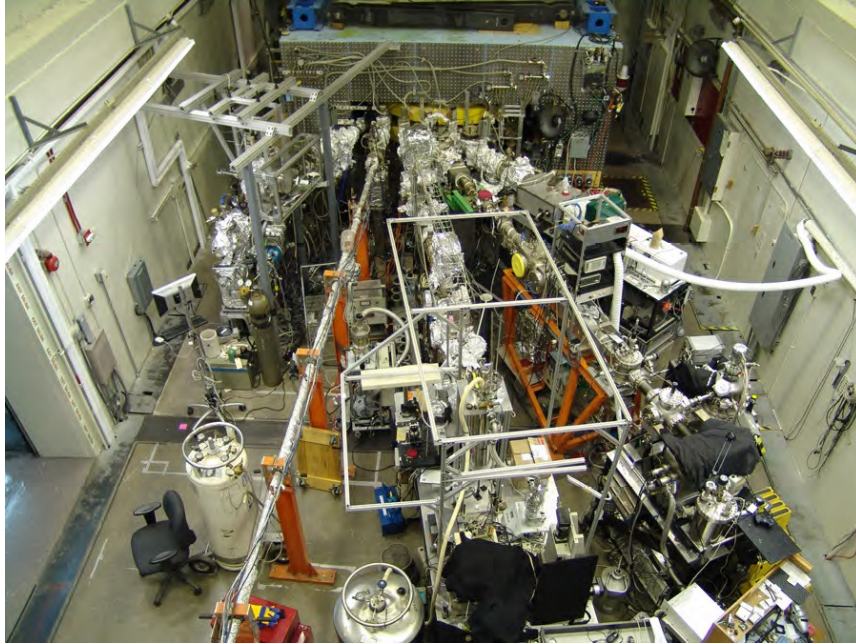


Figure 4.1-2: Synchrotron Ultraviolet Radiation Facility (SURF III) at NIST [56]

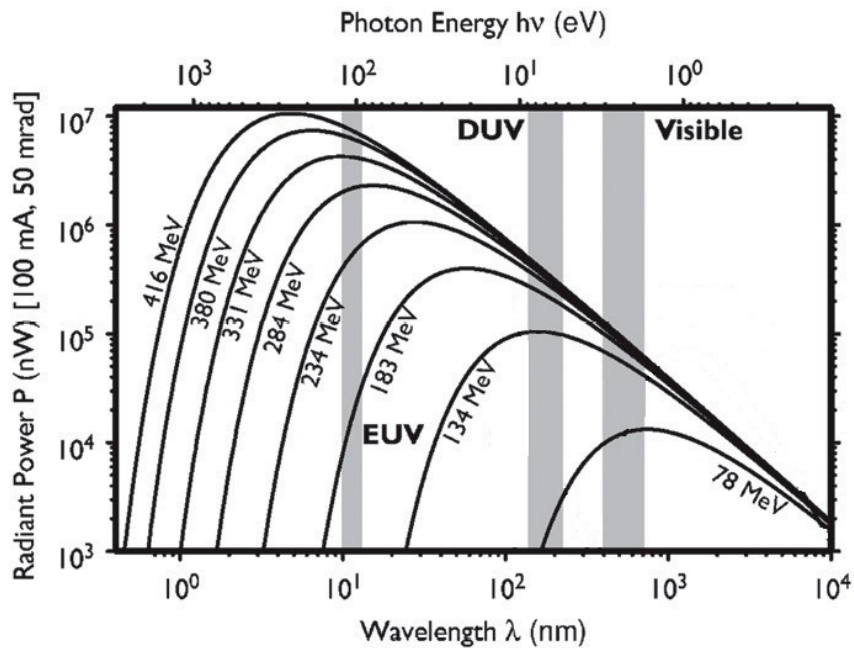


Figure 4.1-3: SURF III radiant power as a function of operating energies [63].

After light leaves the storage ring to enter BL-4, it is focused onto the entrance slit of the 2-m monochromator by two grazing incidence fused silica mirrors. The monochromator has a curved grating with 600 lines/mm and removes all but a small

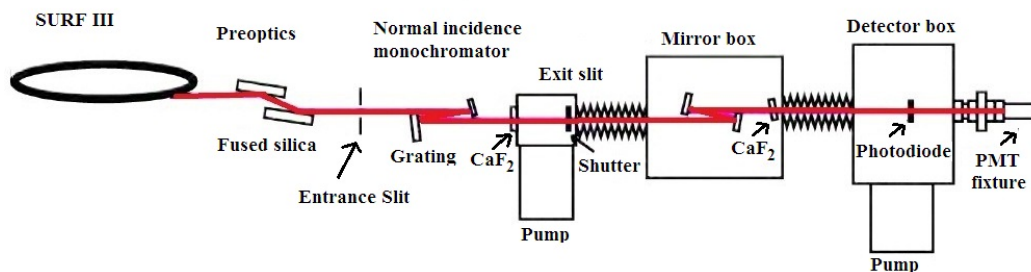


Figure 4.1-4: Diagram of SURF III Beamline 4, with photon path (red) shown [62].

amount of incident radiation (0.7 nm at λ of 200 nm). This allows for very precise wavelength dependent measurements. The monochromator can be rotated and moved along each axis between the entrance and exit slits to perform spectral scans. Once the light passes through the exit slit of the monochromator, two Al-MgF₂ mirrors refocus the light in the mirror box and into the detector box [54, 56, 61].

4.2 Photoabsorption Experimental Procedure

4.2.1 BF₃ Gas Handling System

Because of the corrosive and toxic properties of the BF₃, a system was required that could safely fill and evacuate the experimental apparatus. The system used at SURF III for the photoabsorption cross-section measurements is shown in Figure 4.2.1-1.

The BF₃ monitor hung over the glove box with an emergency alarm set at the established international exposure concentration of 1 ppm [29].

A large N₂ gas cylinder mounted to the BL-4 experimental station served as the source of the dry N₂ purge to force all the BF₃ from the system out through the scrubber, discussed in Section 4.2.5. A shutoff valve (valve D) regulated the flow of N₂ through the rest of the system during the dry N₂ purge. The BF₃ manifold was connected directly opposite the N₂ line.

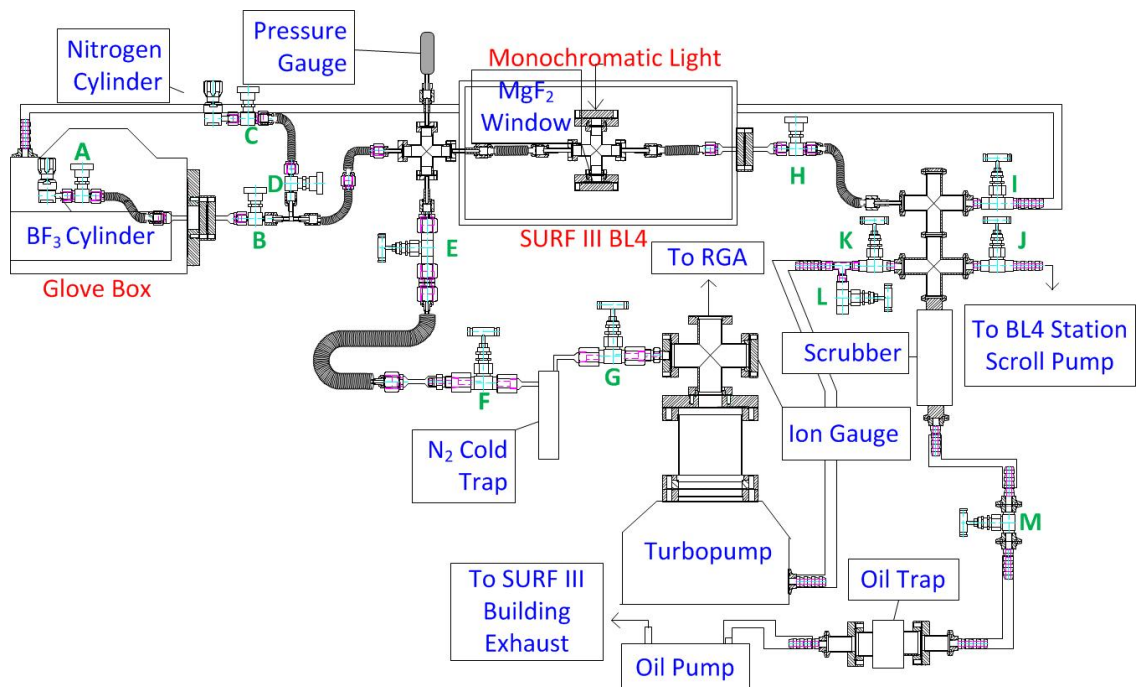


Figure 4.2.1-1: NIST SURF III BF_3 gas handling system

Table 4.2.1-1: Description of parts used in the SURF III BF_3 Gas Handling System

Valve	Description
A	BF_3 Regulator
B	Metering Valve
C	N_2 Regulator
D	N_2 Shutoff Valve
E	Shutoff Valve
F	Cold Trap Inlet Valve
G	Cold Trap Outlet Valve
H	Absorption Cell Isolation Valve
I	Glove Box Exhaust Shutoff Valve
J	BL4 Scroll Pump Exhaust Shutoff Valve
K	Turbopump Exhaust Shutoff Valve
L	Turbopump Exhaust Bypass Valve
M	Scrubber Flush Valve

A metering valve (valve B in Table 4.2.1-1) controlled the amount of BF_3 gas introduced into the system. Extending from this metering valve was a welded flange connected to the exterior of the glove box. This effectively sealed the face of the glove

box. The sealed glove box contained the BF_3 gas cylinder. The glove box exhaust was connected directly to the scrubber with Tygon tubing to allow for the removal of any escaped BF_3 . The valve on the glove box exhaust was closed during the dry N_2 purge to prevent backflow of any residual BF_3 gas back into the glove box (valve I).

The main line of the manifold consisted of a pressure gauge, a cold trap, and the absorption cell located within the BL-4 experimental station. Valve E isolated the manifold from the turbopump. This valve was open only during the initial and final vacuum runs performed immediately prior to and at the conclusion of the pressurized gas runs. During these pressurized gas runs, this valve was closed to isolate the turbopump from the rest of the manifold. Additional protection for the turbopump was provided by the LN_2 cold trap, which included the cold trap inlet and outlet valves (valves F and G, respectively). In the event that the valve failed, these additional cold trap valves prevented BF_3 from entering the turbopump. The continuously cooled LN_2 cold trap condensed the gaseous BF_3 and prevented it from entering the turbopump between experiments. These valves were open during the system pump downs and the initial and final evacuated cell runs. They were closed during the pressurized data collection runs.

Within the beamline station was the BF_3 absorption cell, which consisted of a mini Conflat[®]4-way cross onto which two MgF_2 absorption windows were attached. These windows, which allowed transmission of light through the BF_3 gas in the excimer emission wavelength regions, were mounted in line with the viewports on the walls of the BL-4 experimental station. Monochromatic light was directed through the MgF_2 windows and onto the detector mounted in line with the absorption cell outside of the beamline station. To maintain the pressure of gas within the absorption cell, a shutoff valve (valve H) was connected on the outlet of the experimental station. This valve was closed for the duration of the BF_3 experiments and only opened during the dry N_2 purge through the scrubber.

The exhaust from the glove box connected to one of the ports on one of 2 KF25 4-way crosses mounted on the scrubber. A backflow preventer valve (valve I) was attached to a KF25 pipe barb adapter. This valve was open during normal operation of pressurized experiments and vacuum runs used to normalize the synchrotron beam current. The valve was closed during the dry N₂ purge to prevent the backflow of gas into the glove box.

The turbopump exhaust was also connected to the scrubber in a similar manner. Because the pump was required to continually vent during the entire course of operation, an additional bypass valve (valve L) was connected to the turbopump exhaust. This valve could be opened to the SURF III room atmosphere. During normal operation, this valve was closed, allowing the exhaust to flow directly through the scrubber. During the dry N₂ purge, Valve L was closed off from the scrubber and opened to the atmosphere to allow continued venting without permitting backflow of gas into the pump. Valve K was closed to isolate the pump from the scrubber.

A scroll pump was used to evacuate the beamline endstation. The exhaust from this pump was connected to the KF25 4-way crosses with a single backflow preventer valve (valve J). Only one valve was required to isolate the pump from the manifold during the dry N₂ purge as the pump did not continue to run after the endstation was evacuated.

The scrubber, a CS Clean Systems[®]MiniSorber[®], was connected directly to the SURF III room ventilation system. The scrubber exhausted the BF₃ gas at a concentration of ≤ 0.1 ppm depending on the flow rate. It was found that simply flushing the manifold with dry N₂ for any amount of time did not adequately remove all of the BF₃ gas from the system. A method of forcing the gas through the scrubber was required. Therefore, after the conclusion of the initial dry N₂ purge, a mechanical oil pump was connected to the outlet of the scrubber. Valve M was attached to the rear of the scrubber to control the rate at which the mechanical oil pump worked on

the system. The outlet of the mechanical pump was Tygon[®]tubing, and was easily attached and detached from the SURF III room ventilation system. This setup was only in place during the second phase of the dry N₂ purge, discussed previously. During the course of normal experimentation and the initial dry N₂ purge, this system was removed and the scrubber was connected directly to the SURF III ventilation system.

4.2.2 Stage and Detector Alignment

Prior to data collection, the pressure inside the absorption cell was typically on the order of 10^{-7} torr. The first step in data collection was to align the photodiode with the monochromatic light, and to align the stage within the beamline box to optimize the amount of monochromatic light passing through the absorption cell. These alignments were performed using the LabView[®]software native to BL4. The absorption cell was scanned horizontally and vertically. The alignment was performed at 190 nm, and the mean of the two half-maximum points of the vertical and horizontal scans was taken as the aligned position. The photodiode was aligned in a similar manner. Refer to Figure 4.1-4 for a schematic of BL-4 [64].

Once the detectors and the cross were in the appropriate positions, the beamline experimental station was pumped down. This was done in several stages. The scroll pump lowered the pressure to roughly 10 torr. The cryopump pumped the beamline down even further, and an ion pump was used to finish the task.

Following the pumping down of the beamline box, the gas handling system was pumped down to as low a pressure as possible (on the order of 10^{-7} torr) by slowly opening the valves on the manifold to the rest of the system.

4.2.3 BF₃ Experiment (135-205 nm)

On 27 May, the pressure inside the unit was 3.5×10^{-7} torr. Following an overnight bake at about 100°C, the system was allowed to cool before the foil and tape were removed following the final overnight bake. The stage and photodiode were aligned once more. A vacuum run, and runs at 23, 45, 140, 225, 450, and 760 torr were performed. Each run had a start wavelength of 135 nm, an end wavelength of 205 nm, an interval of 0.25 nm, and 10 data points were collected at each wavelength. Following the run at 800 torr, all the valves on the scrubber connecting to the exhaust from the turbopump, scroll pump, and glove box were closed to prevent backflow during the purging. The metering valve to the BF₃ was closed, and N₂ was introduced into the manifold. The shutoff valve on the rear of the beamline box was opened and the combined mixture of dry N₂ and BF₃ was permitted through the scrubber. The purge lasted about 10 minutes. A residual gas analyzer (RGA) spectral scan showed a prominent peak at 47, which corresponds to BF₂^{*}, indicating a persisting presence of BF₃ in the system. A second flush was performed, although an additional RGA scan still showed the peak at 47 on the order of 10^{-5} torr partial pressure.

4.2.4 BF₃ Experiment (Additional Measurements)

Following the conclusion of the first set of BF₃ photoabsorption data, it was determined that BF₃ exhibited interesting structure in several key regions: 135 to 145 nm; 150 to 165 nm; 190 to 205 nm. It was also determined that the beam current decay had an adverse effect on the transmission data, so smaller wavelength regions were selected, and data were collected over a smaller range of pressures. Beam current decay will be discussed in Section 4.3.1.

The first set of data was collected between 135 and 145 nm, with pressures of 50, 90, 135, 160, 190, 250 torr BF₃, preceded and followed by identical vacuum runs to account for the beam current decay. The second set of data was collected between

150 and 165 nm, with pressures of 250, 340, 468, 570, 675, 750 torr BF_3 , also with two identical vacuum runs before and after data collection. The final set of data was collected between 190 and 205 nm, with pressures of 380, 460, 530, 600, 680, 760 torr BF_3 .

4.2.5 Dry N_2 Purge

The first step of the dry N_2 purge was to close BF_3 regulator to prevent any more BF_3 from entering the system. The BF_3 metering valve was also closed. On the scrubber, the scroll pump exhaust valve and the glove box exhaust valve were closed to the scrubber to prevent any backflow of BF_3 back into these systems that could corrode or damage the vital parts. The backflow preventer on the turbopump exhaust line was closed off from the scrubber and open to the atmosphere of the SURF III room.

The gate valve (Valve E) on the manifold and the valves on the inlet and outlet of the cold trap (Valves F and G) protecting the turbopump were closed to prevent accidental flush of BF_3 into the turbopump. The N_2 regulator was opened, and the N_2 shutoff valve and the rear shutoff valve on the back of the beamline box were also opened. The N_2 was allowed to flow through the system for 10 to 15 minutes.

After this initial purge, the shutoff valve connecting the system to the scrubber on the rear of the beamline box was closed, and the exhaust connecting the scrubber to the building ventilation system was removed. The mechanical oil pump was connected in its place. The rear shutoff valve on the beamline box was reopened following this installation, and the system was evacuated to about 400 torr using the mechanical oil pump. Dry N_2 was introduced to the system to bring it back up to atmospheric pressure, and the system was again evacuated to about 400 torr. This was repeated about a dozen times. At the conclusion of this procedure, the mechanical pump evacuated the system down to about 50 torr.

The mechanical pump was then disconnected and the scrubber exhaust recon-

nected to the scrubber and the building ventilation ductwork. The exhaust valves to the glove box and both pumps were reopened, and the N₂ system was closed and isolated again. The turbopump was turned on at this stage to pump down the system for the second vacuum run.

4.3 Data Analysis: Absolute Photoabsorption Cross-Section Determination

The experimental determination of the absolute photoabsorption cross-section was made by measuring the transmission of ¹⁰BF₃ gas at various pressures from 0 torr to 760 torr. The exponential dependence on pressure of the transmission was used to determine the photoabsorption cross-section. The experimental absorption cell has been previously described.

The experimental procedure began with a series of spectral scans using the BL-4 data acquisition software under different ¹⁰BF₃ pressure conditions. The initial scan was made with the absorption cell evacuated to a pressure of 10⁻⁷ torr. This scan served as the incident signal for the transmission measurements. After the completion of this initial run, the pump was closed off from the absorption cell, a low pressure of ¹⁰BF₃ was introduced into the absorption cell, and spectra was taken. This process was completed for higher gas pressures up to 760 torr. After the final run at 760 torr, the absorption cell was evacuated and a second vacuum spectrum was measured. This second vacuum run was essential for the beam current normalization procedure.

The first part of the data analysis was the correction of the raw data for monochromator scanning errors. The next step was the beam current normalization, which was used in the corrected data to determine the transmission at each pressure. The transmissions were fit to Beers law to determine the absolute photoabsorption cross-section [64].

4.3.1 Beam Current Normalization

SURF III experiences a continual decay in the beam current due to collisions and losses within the circulating electron ring. A CaF_2 beamsplitter incorporated into the beamline optical system is used to provide an optical beam of approximately 10% of the experimental optical power. This can be monitored to provide a measurement of the beam current decay simultaneously with data acquisition. The monochromator resolving power in these experiments has been increased by reducing the size of the exit slit. The reduction in exit slit size reduces the total power in the output beam. Because the optical power delivered to the beam current monitor detector is lower for this experiment, the noise on the optical beam current monitor signal is several percent higher, which introduces a considerable amount of uncertainty into the final photoabsorption cross-section measurements [64].

To overcome this signal to noise limitation, the beam current signal was measured through two identical zero pressure runs, with the only difference being the beam current decay. These vacuum runs were conducted immediately prior to and after the pressurized experimental procedures. The ratio of these vacuum scans was used to determine the correction for beam current decay as a function of elapsed time from the initial vacuum spectrum, which ranged from minutes to hours, and will be discussed in Section 4.3.3 [64].

4.3.2 Monochromatic Scanning Errors

There were several types of errors that occur during data collection which, if uncorrected, would have negatively impacted the observed results. There were always differences between the actual wavelength and the nominal wavelength leading to residual errors. To correct these residual errors, the wavelength values in each data file were replaced with nominal values calculated from the initial wavelength and step

size. These changes were made manually because even though this behavior can be suppressed in the data acquisition software, the feature to suppress this was not available from the front panel [64].

There were also two types of scanning errors that occurred randomly and without known cause. The Zero-Wavelength Scan Error was an apparent scan to zero wavelength in which the monochromator reported a wavelength that was close to but not zero. This error arose from a miscommunication between the monochromator and the data acquisition computer. The wavelength that was reported is incorrect, however the monochromator did actually scan to the desired wavelength. This error was corrected manually by replacing the incorrect wavelength value with the nominal wavelength and the measured values of the signal and relative standard deviations remained unchanged. If these errors remained uncorrected, extreme outliers would have resulted, skewing the data unnecessarily [64].

A more common error is known as the Long-Wavelength Scan Error. This was a real scan to a long wavelength between 250 and 350 nm. This error was not reproducible and has no known cause. The error was corrected manually by replacing the incorrect wavelength with the nominal values. The values of the signal and relative standard deviation were replaced with the mean of the values immediately preceding and following the erroneous data point. The mean is reasonable for the time, wavelength and signal data [64].

4.3.3 Determination of Beam Current Decay Rate

In the determination of the transmission made by comparing the signal observed at each wavelength, there was an implicit assumption that the source intensity is constant. This assumption is not valid for the synchrotron radiation from SURF III as there is a continuous reduction of radiance of the source as a function of time. This decay is the result of losses in the circulating electron beam current. In order to

compensate for this decay, there must be a correction of the data to the value that would have been determined if this beam current decay did not occur. As previously mentioned, the exponential decay rate correction factor was determined from the two vacuum runs. The exponential decay rate was used in conjunction with the change in time between the first vacuum run and the pressurized run to be corrected to determine the correction for each data point [64].

The signal from the photodiode (S) is proportional to the electron beam current (I) of the SURF III accelerator.

$$S = I\alpha \tag{4.3.3-1}$$

where α is a wavelength-dependent constant that accounts for all the variables that affect the optical performance of the beamline, including monochromator throughput, beam splitter transmission, and absorption cell window transmission [64]. If the signal (as a function of wavelength) in the first vacuum run is:

$$S_1(\lambda) = I_1\alpha(\lambda) \tag{4.3.3-2}$$

then the signal (as a function of wavelength) in the second vacuum run is:

$$S_2(\lambda) = I_2\alpha(\lambda) \tag{4.3.3-3}$$

Because the signal, S_1 or S_2 , is the product of two values, the uncertainty in S is the sum of all the relative errors:

$$\frac{u(S)}{S} = \sqrt{\frac{u(I)}{I} + \frac{u(\alpha)}{\alpha}} \tag{4.3.3-4}$$

which, because α is a constant, simplifies to:

$$\frac{u(S)}{S} = \sqrt{\frac{u(I)}{I}} \tag{4.3.3-5}$$

Because the beamline optical performance is constant, a correction factor $C_e(\lambda)$ can be determined:

$$\frac{S_1(\lambda)}{I_1} = \alpha(\lambda) = \frac{S_2(\lambda)}{I_2} \longrightarrow S_1(\lambda) \frac{I_1}{I_2} = S_2(\lambda) C_e(\lambda) \quad (4.3.3-6)$$

where S_1 is the signal from the first vacuum run (as a function of wavelength), and S_2 is the signal from the second vacuum run (as a function of wavelength) [64].

The stored electron beam current decays with an exponential rate factor, R :

$$I(t) = I_0 e^{-Rt} \quad (4.3.3-7)$$

The correction factor from Equation 4.3.3-6 then becomes:

$$C_e(\lambda) = \frac{I_1}{I_2} = \frac{I_0 e^{-Rt_1(\lambda)}}{I_0 e^{-Rt_2(\lambda)}} = e^{R\Delta t_e(\lambda)} \quad (4.3.3-8)$$

where: $t_e(\lambda) = t_2(\lambda) - t_1(\lambda)$ is the elapsed time between vacuum runs. The time between the data points is assumed to be independent of wavelength due to the consistency of the data acquisition software. This means that the correction factor C_e is also independent of wavelength because the wavelength dependent term is contained in $\Delta t_e(\lambda)$ [64]. Therefore, Equation 4.3.3-8 reduces to:

$$C_e = e^{R\Delta t_e} \quad (4.3.3-9)$$

The determination of the value of R uses the mean values of $C_e(\lambda)$ and $\Delta t_e(\lambda)$ taken by averaging these values over all the wavelengths. The standard uncertainties, $u(C_e)$ and $u(\Delta t_e)$ are taken to be the standard deviations of C_e and Δt_e . Because the elapsed time between the initial and final vacuum runs are known, it is possible to determine the value of R to correct any data point for beam current decay [64]. The exponential decay rate R is found from Equation 4.3.3-10:

$$R = \frac{1}{\Delta t_e} \ln(C_e) \quad (4.3.3-10)$$

The uncertainty in R is known by propagating the uncertainties in $u(C_e)$ and $u(\Delta t_e)$ through Equation 4.3.3-10 [64]. The sensitivity coefficients of R are:

$$\frac{\delta R}{\delta C_e} = \frac{1}{\Delta t_e C_e} \quad \text{AND} \quad \frac{\delta R}{\delta \Delta t_e} = \frac{-\ln(C_e)}{(\Delta t_e)^2} \quad (4.3.3-11)$$

The uncertainty in R is given by $u(R)$ in Equation 4.3.3-12:

$$u(R) = \sqrt{\left(\frac{1}{\Delta t_e C_e}\right)^2 u^2(C_e) + \left(\frac{-\ln(C_e)}{(\Delta t_e)^2}\right)^2 u^2(\Delta t_e) + 2\left(\frac{1}{\Delta t_e C_e}\right)\left(\frac{-\ln(C_e)}{(\Delta t_e)^2}\right)u(C_e, \Delta t_e)} \quad (4.3.3-12)$$

The data analysis software is very consistent, so the software takes $u(\Delta t_e)$ to be zero [64]. Therefore, Equation 4.3.3-12 reduces to:

$$u(R) = \frac{1}{\Delta t_e} \frac{u(C_e)}{C_e} \quad (4.3.3-13)$$

4.3.4 Individual Data Point Correction

As previously mentioned, transmission is calculated by dividing the measured signal of a pressurized run, S_P , by the measured signal of the initial evacuated cell, S_1 . As such, the beam current decay correction must be applied to the pressurized cell data points. This is performed using the time elapsed from the data point taken at the same wavelength in the initial evacuated cell run [64]. The corrected signal is:

$$S'_P = S_P C_P = S_P e^{-R \Delta t_P} \quad (4.3.4-1)$$

where Δt_P is the time elapsed between the first vacuum run and the pressure run

in question, and C_P is the correction factor of the pressure run. Equation 4.3.4-1 provides a value of the data point signal corrected for beam current decay which can be used with the signal from the initial evacuated cell signal to determine the transmission values of $^{10}\text{BF}_3$ at a single pressure [64].

Because S'_P is the product of two numbers, its relative uncertainty becomes:

$$\frac{u(S'_P)}{S'_P} = \sqrt{\left(\frac{u(S_P)}{S_P}\right)^2 + \left(\frac{u(C_P)}{C_P}\right)^2} \quad (4.3.4-2)$$

The relative uncertainty, $u(S_P)/S_P$, in the measured signal is assumed to be the relative standard deviation collected and stored in the data file output from the BL-4 data collection software [64]. The uncertainty $u(C_P)$ of the correction factor must be calculated by propagating the uncertainty $u(R)$ found from the beam current decay and the uncertainty in the elapsed time $u(\Delta t_P)$ through:

$$C_P = e^{R\Delta t_P} \quad (4.3.4-3)$$

The BL-4 data collection files store the timestamp data with microsecond (10^{-6} s) resolution. As there is no reason to believe that at this level the computer clock rate is inaccurate, the elapsed time between the timestamps is subject only to the error of the finite resolution, r , in each timestamp [64]. From this knowledge, $u(\Delta t_P)$ is determined from Type B uncertainty evaluation:

$$u(t) = \frac{r}{2\sqrt{3}} = 2.9 \times 10^{-7} \text{s}$$

$$u(\Delta t) = \frac{r}{\sqrt{6}} = 4.1 \times 10^{-7} \text{s}$$

$$\text{where: } r = 10^{-6} \text{s}$$

The sensitivity coefficients of C_P are:

$$\frac{\delta C_P}{\delta R} = (\Delta t_P) e^{R\Delta t_P} \quad \text{AND} \quad \frac{\delta C_P}{\delta \Delta t_P} = R e^{R\Delta t_P} = R C_P \quad (4.3.4-4)$$

Using these sensitivity coefficients, the uncertainty in C_P is found from:

$$\frac{u(C_P)}{C_P} = \sqrt{(\Delta t_P)^2 u^2(R) + R^2 u^2(\Delta t_P) + 2(\Delta t_P) e^{R\Delta t_P} R C_P u(\Delta t_P, R)} \quad (4.3.4-5)$$

The second term in Equation 4.3.4-5 reduces to zero because Δt_P is so small [64]. Therefore, Equation 4.3.4-5 becomes:

$$\frac{u(C_P)}{C_P} = \sqrt{(\Delta t_P)^2 u^2(R) + R^2 u^2(\Delta t_P)} \quad (4.3.4-6)$$

4.3.5 Transmission and Photoabsorption Cross-Section Calculations

The photoabsorption cross-section, σ_{pa} , at each wavelength is dependent upon the pressure dependent transmission. At a single pressure, the transmission, T_P , is found from the corrected signal S'_P , and the initial evacuated cell signal, S_1 [64].

$$T_P = \frac{S'_P}{S_1} \quad (4.3.5-1)$$

As T_P is the ratio of two numbers, the uncertainty $u(T_P)$ is:

$$\frac{u(T_P)}{T_P} = \sqrt{\left(\frac{u(S'_P)}{S'_P}\right)^2 + \left(\frac{u(S_1)}{S_1}\right)^2} \quad (4.3.5-2)$$

The absolute total photoabsorption cross-section, σ_{pa} , is determined by fitting the measured pressure dependent transmission, T_P , to Beers Law which describes the transmission of radiation by an absorbing medium [64]. The pressure dependent transmission is given by Equation 4.3.5-3:

$$T_P = \frac{I}{I_0} = e^{-\sigma_{pa}nl} = e^{-\frac{\sigma_{pa}l}{kT}} = e^{-R_B P} \quad (4.3.5-3)$$

where: I is the transmitted intensity; I_0 is the incident intensity; n is the number density of $^{10}\text{BF}_3$ at a given pressure; l is the path length of light through the absorp-

tion cell; k is the Boltzmann constant ($1.3806503 \times 10^{-23} \text{ m}^2\text{-kg}/(\text{s}^2\text{-K})$); and T is the temperature of the gas, in K. The final expression in Equation 4.3.5-3 is determined from the ideal gas law:

$$PV = NkT \longrightarrow \frac{N}{V} = n = \frac{P}{kT}$$

where N is the number of molecules of $^{10}\text{BF}_3$ and V is the volume of $^{10}\text{BF}_3$ in the absorption cell [64].

The measured transmission data are then fit to Beers Law to determine a value for the exponential rate, R_B .

$$R_B = \frac{\ln(T_P)}{P} \quad (4.3.5-4)$$

Once R_B is known, the photoabsorption cross-section, σ_{pa} , can be determined [64].

Since $R_B = \frac{\sigma_{pa}l}{kT}$, the cross-section can be determined from Equation 4.3.5-5:

$$\sigma_{pa} = -R_B \frac{kT}{l} \quad (4.3.5-5)$$

Because the cross-section is a product of several values, relative uncertainty in the cross-section, $u(\sigma_{pa})/\sigma_{pa}$, is the sum of the standard deviations, given by Equation 4.3.5-6:

$$\frac{u(\sigma_{pa})}{\sigma_{pa}} = \sqrt{\left(\frac{u(R_B)}{R_B}\right)^2 + \left(\frac{u(T)}{T}\right)^2 + \left(\frac{u(l)}{l}\right)^2} \quad (4.3.5-6)$$

The uncertainty in the Boltzmann Constant, k , is negligible due to the fact that k is treated as an exact constant. The uncertainty in R_B , $u(R_B)$, is determined by propagating the uncertainty in the pressure measurement and $u(T_P)$ through Equation 4.3.5-7. The uncertainties in $u(T)$ and $u(l)$ are estimated to state a negligible amount of uncertainty due to the fact that the temperature (T) inside the absorption cell and path length (l) of the cell remained constant for the duration of the

experiments.. The returned value of $u(R_B)$ is the 68% confidence interval, which corresponds to the standard uncertainty (1- σ) [64]. To eliminate confusion, the standard uncertainty will, for the purposes of this discussion, be henceforth referred to as κ .

$$\frac{u(R_B)}{R_B} = \sqrt{\left(\frac{1}{PT_P}\right)^2 u^2(T_P) + \left(\frac{-\ln(T_P)}{P^2}\right)^2 u^2(P)} \quad (4.3.5-7)$$

4.3.6 Determination of Molar Extinction Coefficient

The molar extinction coefficient, ϵ , (in units of L/[mol-cm]) relates to the photoabsorption cross-section, σ_{pa} , by Equation 4.3.6-1:

$$\epsilon cl = \sigma_{pa} nl \quad (4.3.6-1)$$

where c is the molar concentration, l is the path length, and n is the number density of the material, and is determined by $n = \frac{P}{kT}$. The molar concentration, c , is determined from the ideal gas law, shown in Equation 4.3.6-2:

$$PV = NRT \longrightarrow \frac{N}{V} = c = \frac{P}{RT} \quad (4.3.6-2)$$

where R is the ideal gas constant, 8.31447215 m³-Pa/(K-mol). From the value of c determined, Equation 4.3.6-1 can be rearranged to give ϵ , the molar extinction coefficient.

$$\epsilon = \frac{\sigma_{pa} nl}{lc} \longrightarrow \frac{\sigma_{pa} n}{c} \quad (4.3.6-3)$$

The uncertainty, $u(\epsilon)/\epsilon$, is found from Equation 4.3.6-4:

$$\frac{u(\epsilon)}{\epsilon} = \sqrt{\left(\frac{u(\sigma_{pa})}{\sigma_{pa}}\right)^2 + \left(\frac{u(n)}{n}\right)^2 + \left(\frac{u(c)}{c}\right)^2} \quad (4.3.6-4)$$

Because n and c are a function of several variables, the uncertainties of these variables need to be accounted for in the determination of $u(n)$ and $u(c)$. Therefore:

$$\frac{u(n)}{n} = \sqrt{\left(\frac{u(P)}{P}\right)^2 + \left(\frac{u(k)}{k}\right)^2 + \left(\frac{u(T)}{T}\right)^2} \quad (4.3.6-5)$$

and

$$\frac{u(c)}{c} = \sqrt{\left(\frac{u(P)}{P}\right)^2 + \left(\frac{u(R)}{R}\right)^2 + \left(\frac{u(T)}{T}\right)^2} \quad (4.3.6-6)$$

The variables k and R from Equations 4.3.6-5 and 4.3.6-6 are treated as exact constants, so the uncertainties in k and R fall out of Equations 4.3.6-5 and 4.3.6-6. Additionally, the uncertainty in T is considered to be negligible, so $u(T)/T$ also falls away. This leaves the uncertainty in $u(n)$ and $u(c)$:

$$\frac{u(n)}{n} = \sqrt{\left(\frac{u(P)}{P}\right)^2} \quad (4.3.6-7)$$

and

$$\frac{u(c)}{c} = \sqrt{\left(\frac{u(P)}{P}\right)^2} \quad (4.3.6-8)$$

As a result, the uncertainty in ϵ is dependent on the uncertainty in the cross-section, $u(\sigma_{pa})/\sigma_{pa}$, and the uncertainties in $u(n)$ and $u(c)$ found in Equations 4.3.6-7 and 4.3.6-8:

$$\frac{u(\epsilon)}{\epsilon} = \sqrt{\left(\frac{u(\sigma_{pa})}{\sigma_{pa}}\right)^2 + \left(\frac{u(n)}{n}\right)^2 + \left(\frac{u(c)}{c}\right)^2}$$

OR

$$\frac{u(\epsilon)}{\epsilon} = \sqrt{\left(\frac{u(\sigma_{pa})}{\sigma_{pa}}\right)^2 + 2\left(\frac{u(P)}{P}\right)^2} \quad (4.3.6-9)$$

As previously mentioned, the uncertainty in $u(\sigma_{pa})/\sigma_{pa}$ is dependent on the uncertainty in the exponential rate constant, $u(R_B)/R_B$, which was determined in Section 4.3.5.

4.4 BF₃ Photoabsorption Cross-Section Results

Absorption data have been collected at NIST SURF III for gaseous ¹⁰BF₃ over the wavelength region 135-205 nm. Data were taken on 27 May and 5-6 July 2011. Using the procedure detailed in Section 4.2.3, the absolute photoabsorption cross-section results of the 27 May 2011 BF₃ experiments are illustrated in Figure 4.4-1. The uncertainties presented in Figure 4.4-1 are due to the scatter between the data points and were discussed in greater detail in Section 4.3. The uncertainty is in the 68% confidence interval of the standard uncertainty, $1-\kappa$, where κ is the standard deviation of the data points. These data are compared to existing literature data (Figure 4.4-2). Absolute cross-section and uncertainty values are tabulated in Appendix B.1.2.

In the region of 140 to 165 nm, the data are close to the values published by Maria *et al.* Above 165 nm, Maria *et al.* did not acquire any data. Suto *et al.* claim that at

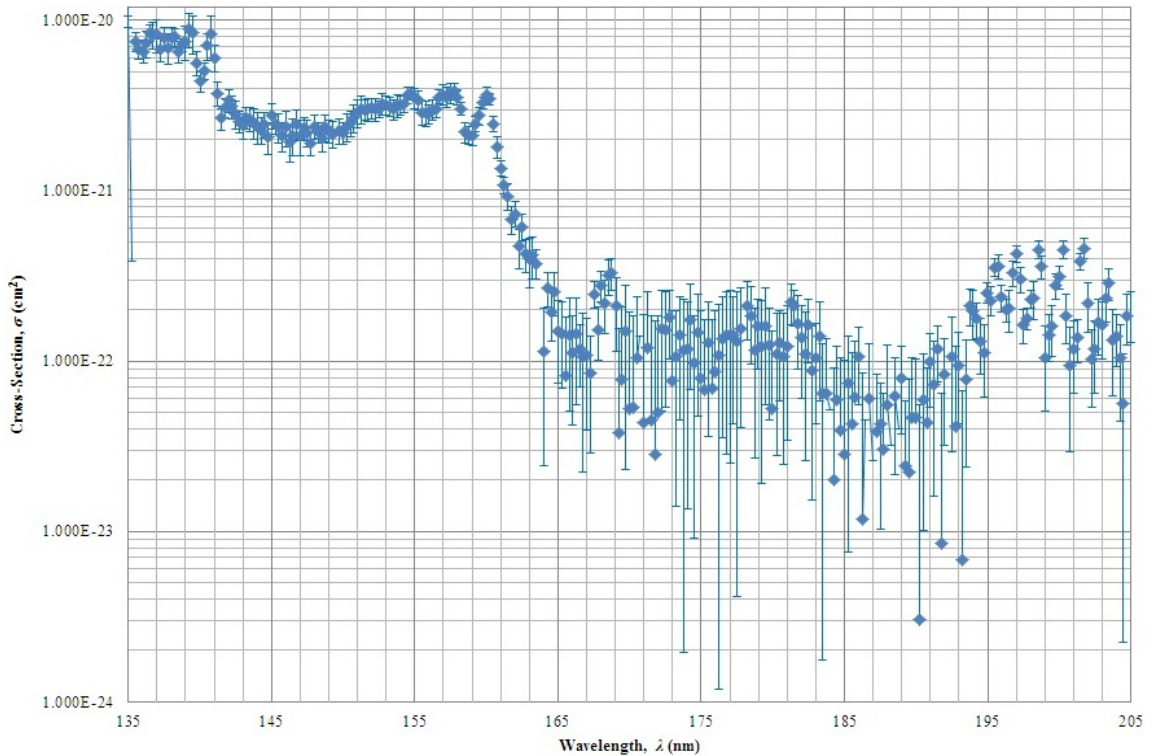


Figure 4.4-1: Absolute photoabsorption cross-section data of ¹⁰BF₃ from 135 to 145 nm.

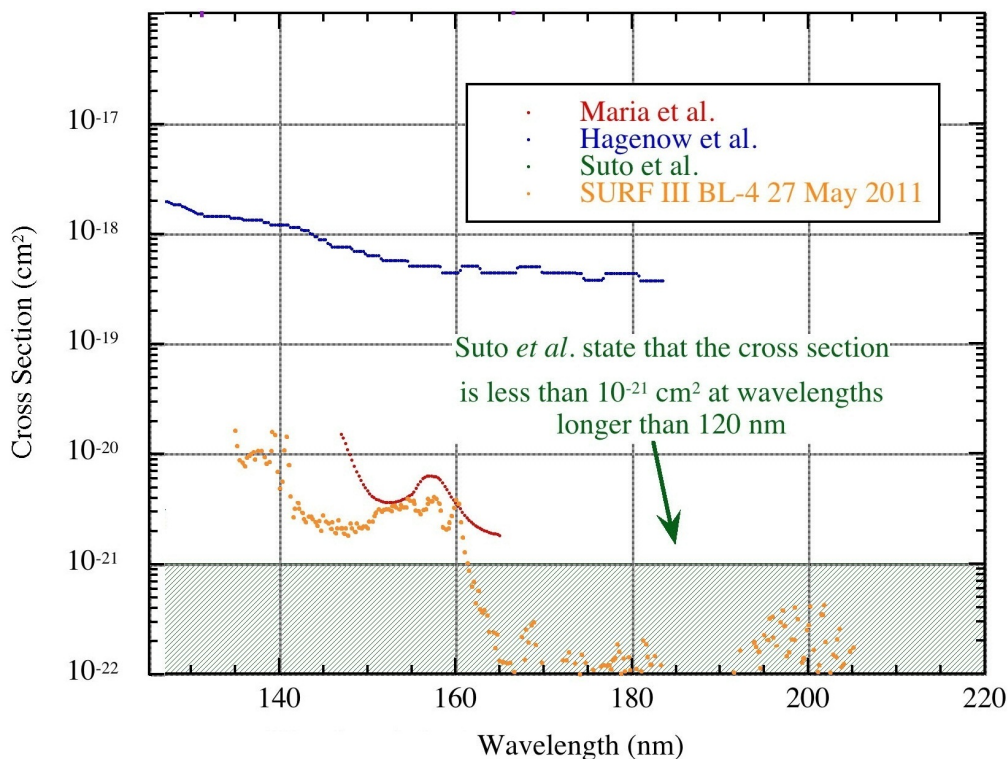


Figure 4.4-2: SURF values compared to literature values of photoabsorption cross section of BF_3 [21, 22, 23, 24].

wavelengths longer than 120 nm, the cross-section is less than 10^{-21} cm^2 , but no data has been published to substantiate this claim [21]. The data obtained from SURF III indicates that the cross-section falls below 10^{-21} cm^2 at wavelengths greater than 160 nm. The data obtained from SURF III do not agree with the data obtained by Hagenow *et al.* [22, 23], although there are similarities to Suto's claim at wavelengths above 160 nm.

There is a difference between the SURF III data and the data published by Maria, *et al.*, however this could be the result of impurities such as water vapor from residual air in Marias system, the system at NIST SURF III, or both. Gaseous BF_3 reacts very strongly with water vapor in the air to produce boric acid and fluoroboric acid (see Section 2.2.1), and any water vapor remaining in the vacuum system could cause an undesired side reaction with BF_3 to produce unwanted contaminants in the system. These contaminants would be strongly electronegative ions that would absorb

electrons to form new complexes that could skew the results of the photoabsorption cross-section measurements. Impurities are listed in Table 4-1. Residual Gas Analyzer (RGA) spectral scans performed on the SURF III system before each BF_3 experimental run indicated that the partial pressures of water vapor, O_2 , CO_2 , and N_2 , the main components of air, were below 10^{-8} mtorr. The purity of Suto's, Maria's, or Hagenow's systems remain unreported, and the cause of the discrepancy between the published photoabsorption cross-section values is unknown. Due to limitations of the MgF_2 windows, the shortest wavelength attainable was 135 nm and data below this wavelength was not obtained for comparison with Suto's and Hagenow's data. Further photoabsorption cross-section work should consider shorter wavelengths.

Structure is evident between 135 and 145 nm, as well as between 150 and 165 nm, and 190 to 205 nm. The cross-sections in these excimer emission regions of interest are low enough to suggest relative transparency of the BF_3 to excimer photons, and from these experiments, it was concluded that excimer emission from rare gases will not be absorbed by $^{10}\text{BF}_3$ (see Figure 2.3-1). The purpose of these experiments were to determine the efficacy of BF_3 absorption in the FUV wavelength regions, so an analysis of the observed structure is not considered as part of this discussion.

Additional data were collected to determine whether BF_3 exhibits structure in the three aforementioned regions, and to determine the repeatability and reproducibility of the experiment. Figure 4.4-3 shows the data from 5-6 July with the 27 May data with the calculated uncertainty values.

The data shown in Figure 4.4-3 provide an indication of the reproducibility of the experiment. The May experiment was run continuously over a period of 4 hours with 280 data points collected at each pressure. Over the long run time, there was a decrease in synchrotron beam current. The beam current decay rate plays a large part in the individual data point correction, which in turn affects the cross-section value at the end of the calculation. Unfortunately, the beam current decay rate is

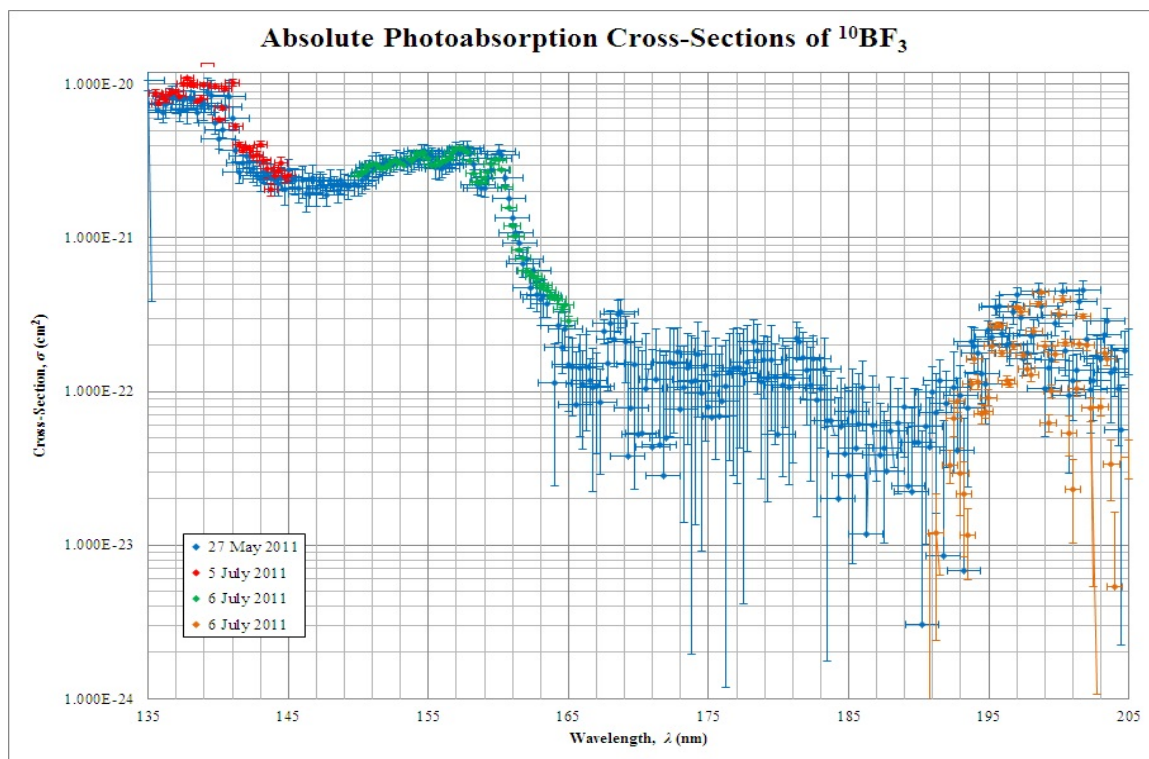


Figure 4.4-3: Photoabsorption cross-section and molar extinction coefficient of $^{10}\text{BF}_3$ from 135 to 205 nm. Data from all three dates (27 May, July 5-6) are included.

an undesired and unavoidable variable in the data calculation and analysis, however, shorter runs would lessen the total beam current decay. Eight sets of data were collected over shorter wavelength regions. An initial vacuum run was performed prior to the introduction of BF_3 gas into the system, and this run was followed by 6-7 pressure runs. After a short dry N_2 purge, a second vacuum run was performed to obtain the second data set for beam current normalization. The wavelength region ranged from 10 to 15 nm, and this resulted in far fewer data points for each pressure run (40 to 60 versus 280). As a result of the fewer data points, the run time for each of the three experiments was significantly shorter, lasting between 90 and 120 minutes rather than 260 to 300 minutes. Thus, the beam current correction factor, $C_e (I_1/I_2)$ was smaller for the subsequent shorter wavelength regions, and this resulted in better resolution of the cross-section data due to the higher accuracy in the beam current decay rate. Table 4.4-1 illustrates the difference in beam current decay rates from

the initial experiment conducted on 27 May 2011 and each of the smaller resolution photoabsorption experiments, conducted across 5 July and 6 July 2011.

As can be seen from Table 4.4-1, the ratio of the beam current decay rates obtained for the 5-6 July 2011 photoabsorption experiments is on average marginally greater than the beam current decay rate obtained for the broader spectrum photoabsorption experiment performed on 27 May 2011.

Table 4.4-1: Comparison of Beam Current Normalization Values between 27 May 2011 and 5-6 July 2011

	27 May 2011	5 July 2011
Elapsed Time between Vacuum Runs (s)	18140 s	5450 s
Correction Factor, $C_e\left(\frac{I_1}{I_2}\right)$	1.49	1.16
Beam Current Decay Rate, R (s^{-1})	2.20E-05	2.65E-05
Uncertainty, $u(R)$	6.85E-08	4.39E-08
	R_1/R_2	1.20
	27 May 2011	6 July 2011
Elapsed Time between Vacuum Runs (s)	18140 s	6310 s
Correction Factor, $C_e\left(\frac{I_1}{I_2}\right)$	1.49	1.17
Beam Current Decay Rate, R (s^{-1})	2.21E-05	2.47E-05
Uncertainty, $u(R)$	6.85E-08	2.62E-07
	R_1/R_3	1.12
	27 May 2011	6 July 2011
Elapsed Time between Vacuum Runs (s)	18140 s	5286 s
Correction Factor, $C_e\left(\frac{I_1}{I_2}\right)$	1.49	1.24
Beam Current Decay Rate, R (s^{-1})	2.21E-05	3.99E-05
Uncertainty, $u(R)$	6.85E-08	2.37E-07
	R_1/R_4	1.80

Chapter 5

FUND Experimental Apparatus Description

Following the conclusion of the $^{10}\text{BF}_3$ photoabsorption experiments, which concluded that the photoabsorption cross-section of $^{10}\text{BF}_3$ was significantly small enough that excimer photons would not be attenuated by the BF_3 gas inside the scintillation cell, the research was moved from NIST to the Maryland University Training Reactor (MUTR). This chapter discusses the MUTR, the experimental apparatus used for both the $^{10}\text{BF}_3$ and reticulated vitreous carbon foam (RVC) experiments. Also included are discussions on all relevant electronics and data collection tools and materials, such as the scintillation cell and the photomultiplier tube calibration.

5.1 MUTR Neutron Beamline

The Maryland University Training Reactor is a 250 kW, open-pool, TRIGA-fueled reactor consisting of 93 fuel elements and three B_4C control rods. The fuel elements are UZrH, 8.5% U, enriched to <19% ^{235}U by weight. The entire core is contained in a 6,000 gallon concrete tank. The core is cooled by natural convection, and water is used as moderator, coolant, and biological shield. The peak neutron flux in the core is approximately 2×10^{12} n/($\text{cm}^2\text{-s}$) [14]. There are five experimental facilities, including a through tube, the East and West beam ports, a pneumatic transfer system (labeled “Rabbit” in Figure 5.1-1), and the thermal column. Two graphite blocks located on the west side of the core act as reflectors. A schematic of the MUTR is illustrated in Figure 5.1-1.

The graphite filled thermal column is composed of water, 0.635 cm aluminum,

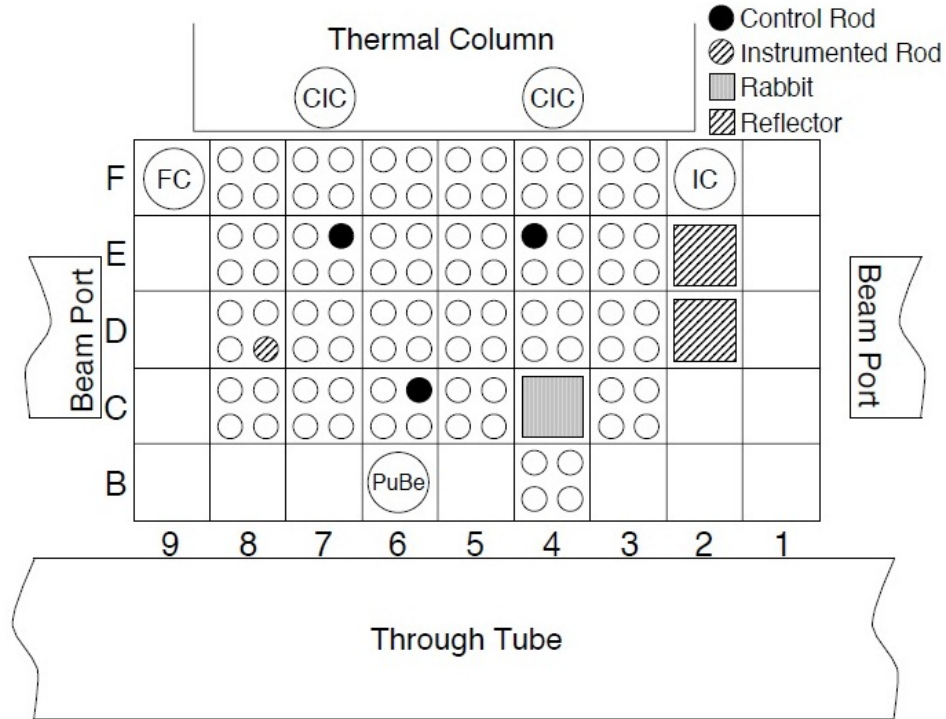


Figure 5.1-1: Top-down view of the MUTR core configuration.

1.5 m of graphite, and 5.08 cm of lead. As neutrons produced from fission diffuse through the thermal column, there is moderation, resulting in a large number of thermal neutrons. To utilize these thermal neutrons, a collimator access plug was designed to fit the thermal column to allow only a narrow beam (5.08 cm diameter) of neutrons to stream out of the core. The collimator access plug was designed using MUTR blueprints and dimensions from an existing Boron Neutron Capture Therapy (BNCT) plug [65]. The 2" pipe down the centerline allows neutrons to stream from the reactor core to the experimental station. The innermost and outermost partitions of the collimator access plug are filled with a mixture of steel shot, paraffin wax, and boron carbide [65]. The thermal column and access plug are illustrated in Figure 5.1-2 and Figure 5.1-3. The characterization of the collimator has been previously performed. Refer to [54] for more information.

The graphite and lead bricks in the thermal column attenuate a significant por-

tion of the gamma radiation produced in the core, however the gamma dose rates measured outside the collimator were 90-100 mR/hr. A remotely controlled beam shutter made of lead and boral was positioned on the outer face of the collimator. This was used to block both neutron and gamma rays when working in the beamline. This shutter is shown in Figure 5.1-4 [54].

The 5.08-cm neutron beam was reduced to 4-mm by a boral aperture located approximately 10-cm in front of the scintillation cell. Behind this aperture, a NIST calibrated fission chamber reference detector was used to monitor the neutron beam. The fission chamber beam monitor will be discussed in Section 6.1.

Additionally, a small piece of ^6Li glass or other shielding could be positioned between the fission chamber beam monitor and the scintillation cell, as required, to isolate the gamma ray contribution to the PMT signal. This glass was demonstrated to absorb approximately 83% of the thermal neutrons coming from the core, but allowed the gamma radiation to stream through. A photograph of the PMT, differential volume, fission chamber, and ^6Li glass is shown in Figure 5.1-5. Other absorbers, such as boral (which was demonstrated to absorb approximately 96% of thermal neutrons from the core) and a 1" lead brick (which absorbed 42% of the thermal neutrons from the core) could also be positioned in front of the scintillation cell.

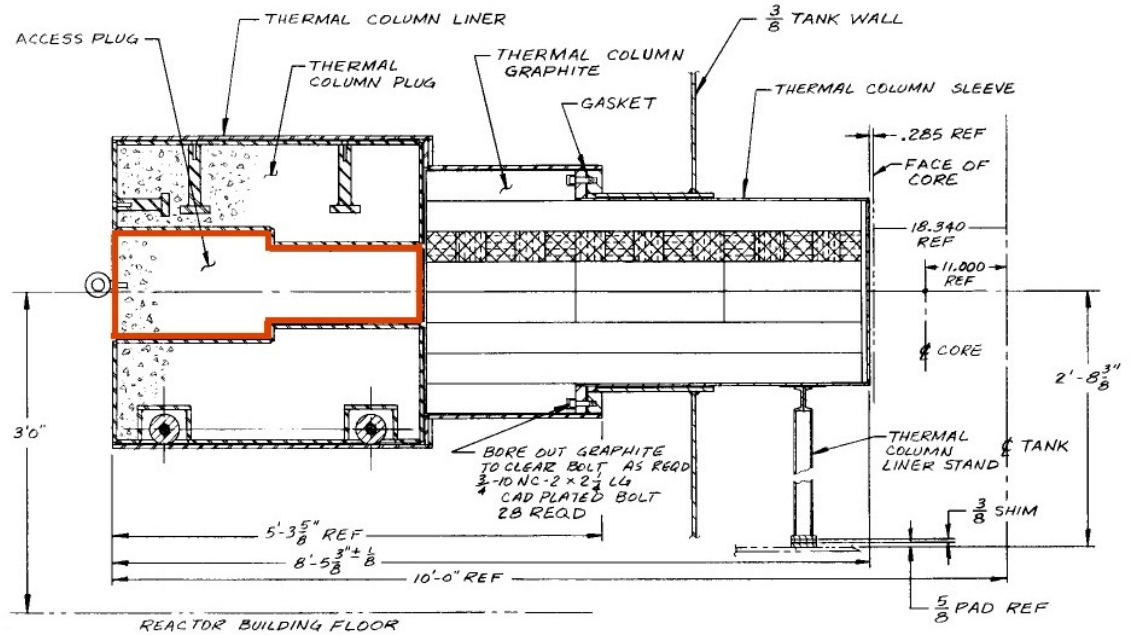


Figure 5.1-2: MUTR thermal column access plug

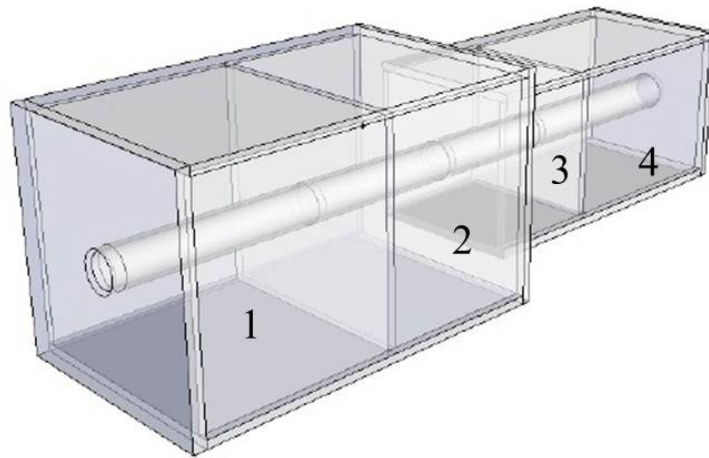


Figure 5.1-3: 3D View of Collimator Plug. Partitions 1 and 4 are filled with a mixture of steel shot, paraffin wax, and boron carbide to attenuate the neutron and gamma radiation from the thermal column leaving only a collimated beam.

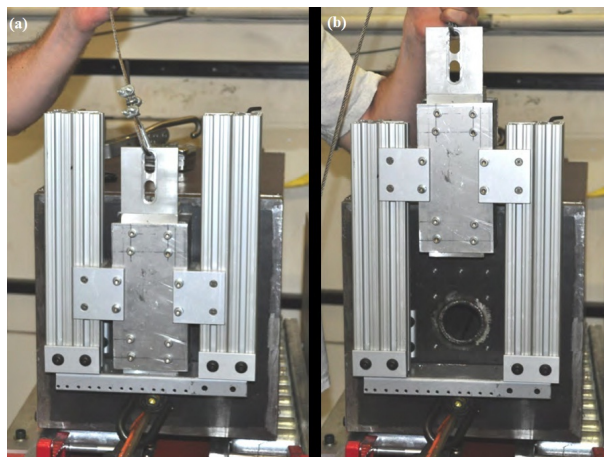


Figure 5.1-4: Collimator shutter assembly in closed (a) and open (b) positions.

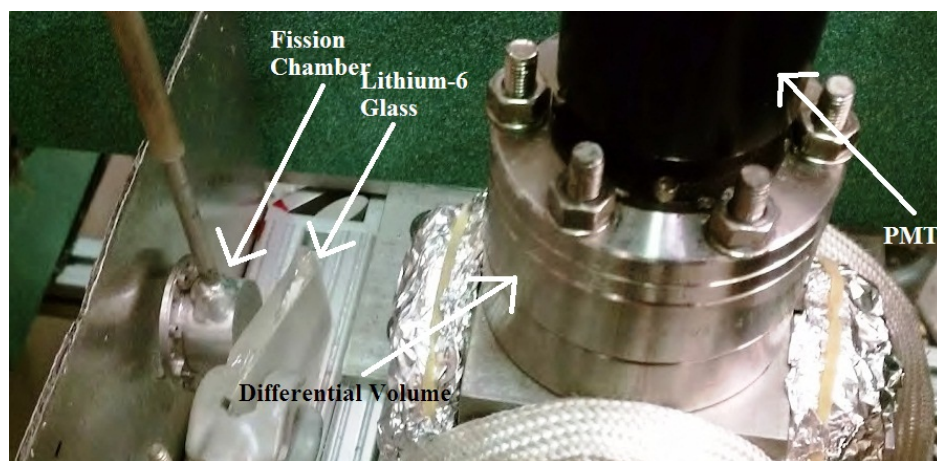


Figure 5.1-5: Scintillation cell with fission chamber beam monitor and ${}^6\text{Li}$ glass neutron absorber in place.

5.2 Far Ultraviolet Neutron Detection Experiment

5.2.1 Scintillation Cell

The purpose of the scintillation cell was to provide a vessel in which high purity noble gases and ${}^{10}\text{B}$ -enriched BF_3 gas could be mixed and subjected to thermal neutrons. The cell was a 70-mm stainless steel Conflat[®] cube with two silica windows (0.5 mm thick) on the front and back to allow neutrons to flow through the cell without being attenuated. The remaining ports were sealed or used as inlet and outlet for the gas

flow. The scintillation cell was connected to a Hamamatsu R6835 photomultiplier tube. This 11-stage PMT has an integrated MgF₂ window and has a spectral response for FUV detection (between 115 and 200 nm) with a wavelength of maximum response at 140 nm [67]. The PMT specifications appear in Table 5.2.1-1.

Table 5.2.1-1: Specifications of the Hamamatsu R6835 PMT [67].

Parameter	Value
Spectral response	115-200 nm
Photocathode material	Cs-I
Photocathode diameter	23 mm
Number of dynodes	11
Anode dark current	0.03 nA
Anode pulse rise time	2.8 ns
Electron transit time	22 ns

The PMT was housed in McPherson 658 end-on housing placed behind a second MgF₂ window. Because of the high gamma dose rates in the beamline (90-100 mR/hr), and the moderate gamma dose rates in the vicinity of the PMT (5-10 mR/hr), an aluminum can filled with lead shot was fitted around the PMT housing to minimize gamma ray interaction with the photocathode and dynodes in the PMT. A movable beam stop made of borated-polyethylene blocks was positioned behind the scintillation cell. A differential volume separated the PMT from the scintillation cell. This volume was continuously evacuated throughout the duration of the experiments.

The calibration of the PMT was performed at NIST SURF III on BL-4. The calibration procedure was not performed as part of these sets of experiments, but the calibration data are briefly discussed in Section 5.2.2.

While the manufacturer specification sheet claims the PMT is solar-blind, it has been shown that the PMT is in fact very sensitive to ambient lighting, especially in the FUV wavelength region, with total observed counts greater than 10⁶ counts in 200

s. The windows of the cell were therefore covered with several layers of aluminum foil and black felt to eliminate the amount of ambient light entering the cube, reducing the observed count rates to 10^3 or less in the same amount of time.

Within the scintillation cell was an aluminum cylinder nested in the center, held in place by grooves in the bottom and top Conflat[®] flanges. The inner surface of this cylinder was layered with black copper-oxide, Ebonol C[®] to reduce FUV photon reflection from the cell. The scintillation cell is shown in Figure 5.2.1-1.

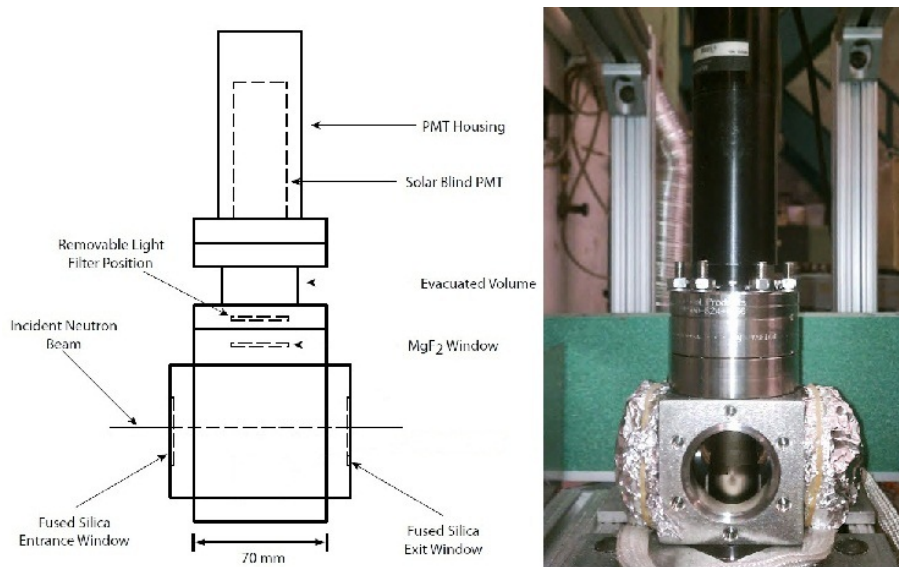


Figure 5.2.1-1: Cube and photomultiplier tube (not to scale).

5.2.2 Photomultiplier Tube Calibration

Calibration of the photomultiplier tube detector package was performed at NIST SURF III, on BL-4, which was also used for the BF_3 photoabsorption cross-section measurements. The PMT was calibrated in a configuration identical to that which was used at the MUTR during the scintillation experiments (PMT attached to the scintillation cell behind an evacuated differential volume and MgF_2 window). The data obtained from calibration provided information on the intrinsic efficiency of the

detector package, including the photoabsorption by the discrete MgF₂ window located on top of the scintillation cell, the photoabsorption by the MgF₂ window on the PMT housing, and the quantum efficiency of the PMT [54].

The intrinsic efficiency of the detector package, $\epsilon_{PMT}(\lambda)$, can be defined by:

$$\epsilon_{PMT}(\lambda) = \frac{n_{hv}(\lambda)}{N_{hv}(\lambda)t} \quad (5.2.2-1)$$

where $n_{hv}(\lambda)$ is the number of observed photon pulses on the PMT at a wavelength λ , N_{hv} is the rate at which photons strike the detector package at a wavelength λ , and t is the time over which pulses were recorded [54]. The number of photon pulses observed is found from:

$$n_{hv} = n_{Tot} - n_{Bkgd} \quad (5.2.2-2)$$

where n_{Tot} is the total number of pulses counted over time t and n_{Bkgd} is the number of pulses resulting from dark current [54]. Figure 5.2.2-1 illustrates the results of $n_{hv}(\lambda)$ for a SURF III beam current of 10 μ A [54].

The uncertainty in n_{hv} is due solely to counting statistics and is therefore the sum of the uncertainties in n_{Tot} and n_{Bkgd} :

$$\sigma_{n_{hv}} = \sqrt{\sigma_{n_{Tot}}^2 + \sigma_{n_{Bkgd}}^2} \quad (5.2.2-3)$$

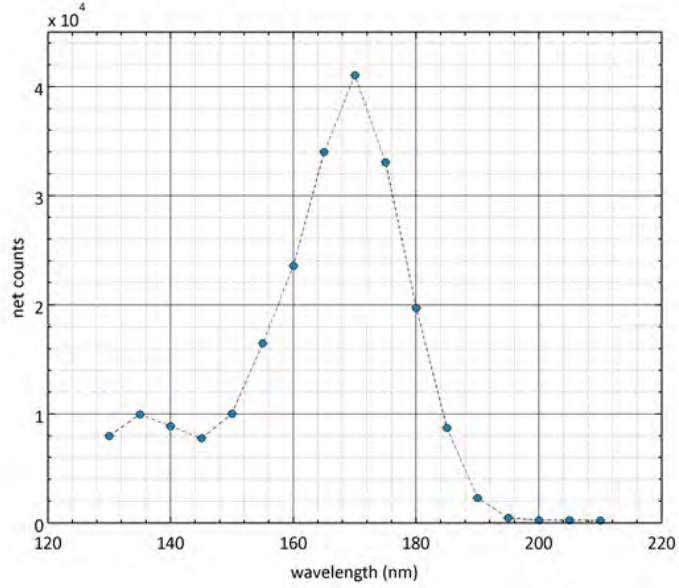


Figure 5.2.2-1: Net counts from the PMT during an FUV spectral scan at SURF III. Electron beam current $I_{BC} = 10 \mu\text{A}$ [54].

Therefore, the fractional uncertainty is defined by the ratio of the uncertainty in n_{hv} over the determined values of n_{hv} :

$$\delta_{n_{hv}} = \frac{\sqrt{\sigma_{n_{Tot}} + \sigma_{n_{Bkgd}}}}{(n_{Tot} - n_{Bkgd})} \quad (5.2.2-4)$$

The fractional uncertainties are shown in Figure 5.2.2-2 [54].

From photodiode measurements of photon flux, values of N_{hv} at each wavelength were extrapolated [54]. To determine the relationship between the SURF III beam current and the BL-4 photon flux, these values were fit by linear regression:

$$N_{hv}(\lambda, I_{BC}) = k(\lambda)I_{BC} \quad (5.2.2-5)$$

where $k(\lambda)$ is the slope of the fit at each wavelength λ and I_{BC} is the SURF III beam current [54].

These regressions were extrapolated to determine the values of $N_{hv}(\lambda)$, and these

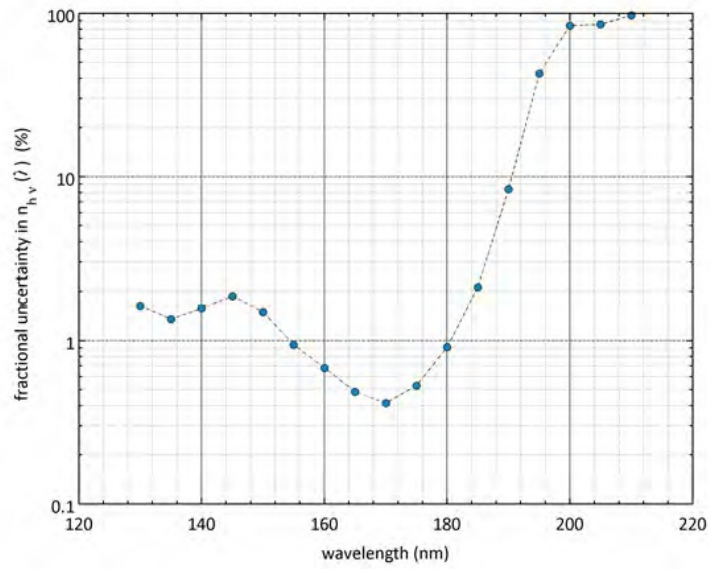


Figure 5.2.2-2: Fractional uncertainties found in $n_{h\nu}(\lambda)$ from the PMT calibration. Electron beam current $I_{BC} = 10 \mu\text{A}$ [54].

values were used to determine the intrinsic efficiency of the PMT detector package using Equation 5.2.2-3 [54]. These values are shown in Figure 5.2.2-3, which can be compared with the spectral response data provided by Hamamatsu in Figure 5.2.2-4.

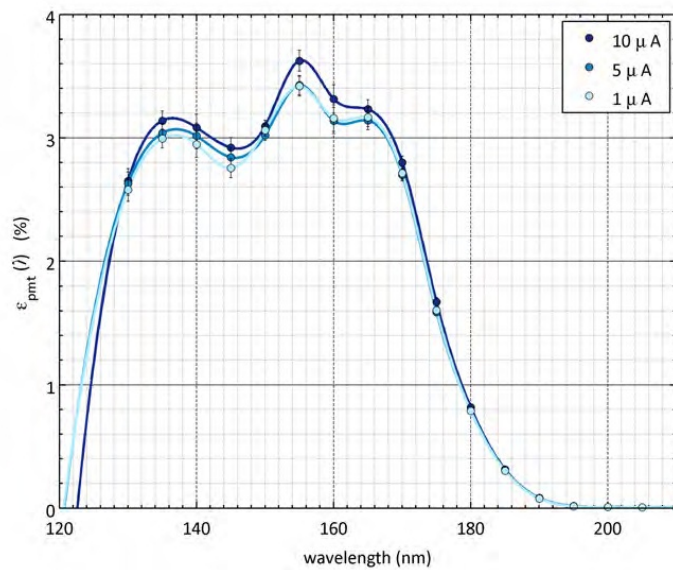


Figure 5.2.2-3: Intrinsic efficiency of the PMT/MgF₂ detector package in the FUV wavelength region [54].

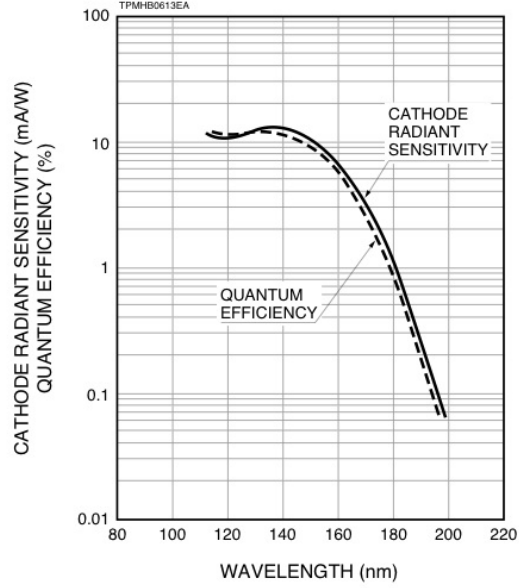


Figure 5.2.2-4: Spectral response of the PMT [67].

These values of the PMT efficiency could not be used for each noble gas used in the excimer scintillation experiments because of the broad continuum of excimer emissions (120-180 nm) [54]. Therefore, an effective PMT efficiency was determined for each noble-gas type using a continuous weighted average:

$$\epsilon_{PMT} = \frac{\int \epsilon_{Fit}(\lambda) s(\lambda) d\lambda}{\int s(\lambda) d\lambda} \quad (5.2.2-6)$$

where $\epsilon_{Fit}(\lambda)$ is a cubic spline fit of the discrete values of ϵ_{PMT} and $s(\lambda)$ is the wavelength distribution of an excimer [54]. Values of ϵ_{PMT} appear in Table 5.2.2-1. Figure 5.2.2-5 shows the response of the PMT as a function of input voltage [54].

Table 5.2.2-1: Intrinsic efficiencies ($\epsilon_{PMT}(\lambda)$) of the PMT/MgF₂ detector package at peak excimer wavelengths and effective intrinsic efficiencies (ϵ_{PMT}) [54].

Gas	λ_{Peak}	$\epsilon_{PMT}(\lambda_{Peak})$ (%)	ϵ_{PMT} (%)
Ar	128	2.2 ± 0.11	1.64 ± 0.06
Kr	150	3.09 ± 0.05	3.14 ± 0.11
Xe	175	1.67 ± 0.03	2.61 ± 0.09

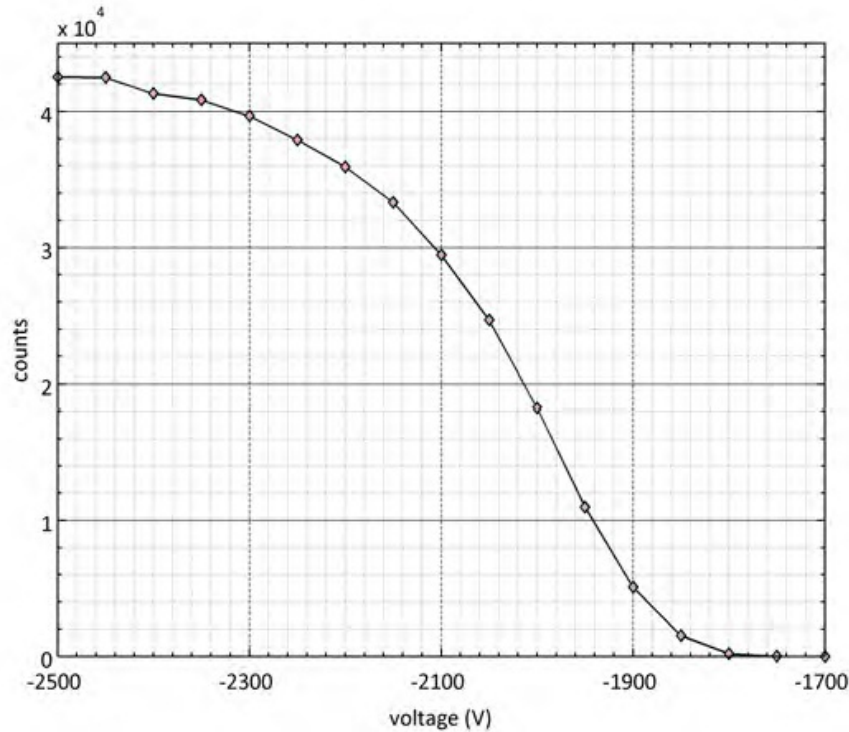


Figure 5.2.2-5: PMT response as a function of PMT input voltage at $\lambda = 170$ nm [54].

5.2.3 $^{10}\text{BF}_3$ Gas Handling System

The gas-handling system used in the neutron experiments was designed to evacuate and fill the scintillation cell with mixtures of $^{10}\text{BF}_3$ and noble gases. The system, connected to an 80/20[®] aluminum frame, included a turbomolecular pump, a roughing pump, noble gas lecture bottles, a pressure gauge, nude ion gauge, two thermocouple pressure gauges, a residual-gas analyzer (RGA), filter, numerous valves, and Conflat[®], VCR[®], and Kwik-Flange[®] connections. A schematic of the gas handling system used on the MUTR Thermal Column beamline is shown in Figure 5.2.3-1. A description of the valves used to control the gas handling system is given in Table 5.2.3-1.

As with the SURF III gas handling system (refer to Figure 4.2.1-1), a number of protective measures were included in the system. These included a liquid nitrogen cold trap before the pump, a glove box to contain the BF_3 gas cylinder, a dry N_2

purge

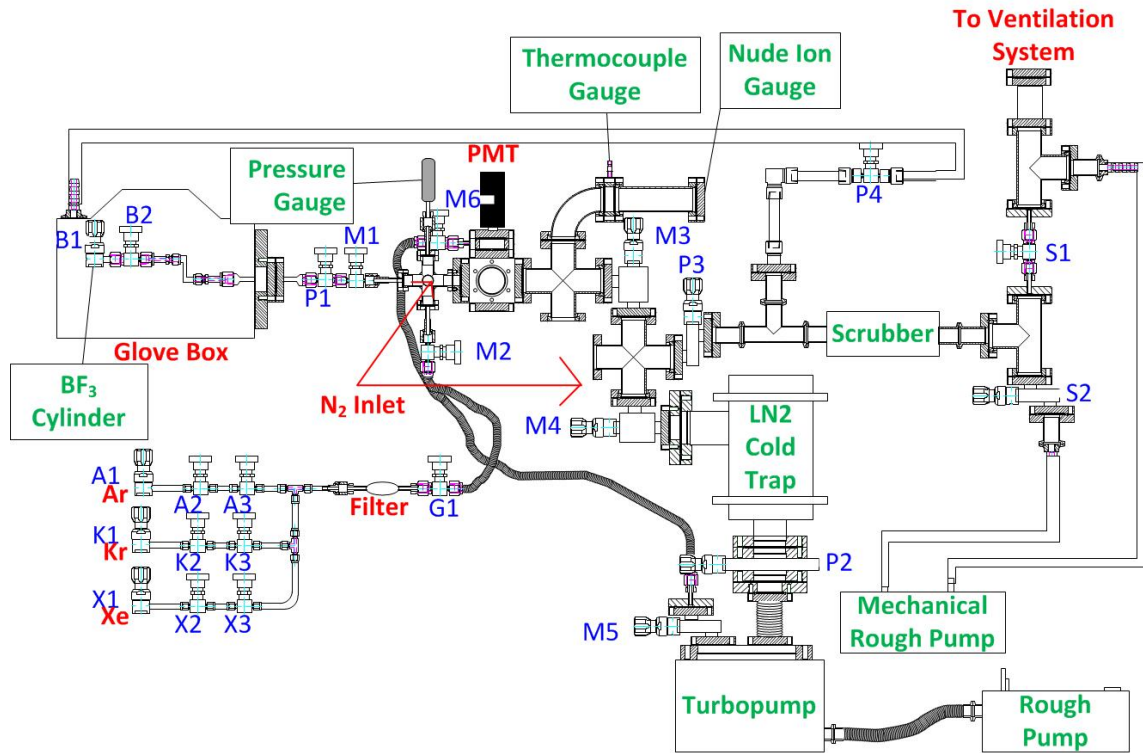


Figure 5.2.3-1: MUTR $^{10}\text{BF}_3$ Gas Handling System. Neutrons flowed in the plane of the page.

Table 5.2.3-1: Description of valves used in the MUTR BF_3 Gas Handling System. Valves with an (M) designation were manually controlled; valves with an (A) designation were controlled by a switchboard.

Valve	Description
Ar	Argon Gas Cylinder (M)
A1	Argon Regulator (M)
A2	Argon Shutoff Valve (M)
A3	Argon Metering Valve (M)
BF3	BF_3 Gas Cylinder (M)
B1	BF_3 Regulator (M)
B2	BF_3 Shutoff Valve (M)
G1	Noble Gas Inlet Control Valve (M)
Kr	Krypton Gas Cylinder (M)
K1	Krypton Regulator (M)
K2	Krypton Shutoff Valve (M)
K3	Krypton Metering Valve (M)
M1	BF_3 Metering Valve (M)

Continued on next page

Table 5.2.3-1 – continued from previous page

Valve	Description
M2	Noble Gas Inlet Shutoff Valve (M)
M3	Cube Outlet Shutoff Valve (M)
M4	Cold Trap Inlet Valve (M)
M5	Differential Volume Isolation Valve (M)
M6	Differential Volume Shutoff Valve (M)
P1	BF ₃ Inlet Valve (A)
P2	Cold Trap Outlet Valve (A)
P3	Scrubber Inlet Valve (A)
P4	Glovebox Exhaust Valve (A)
S1	Ventilation System Isolation Valve (M)
S2	Scrubber Outlet Valve (M)
Xe	Xenon Gas Cylinder (M)
X2	Xenon Shutoff Valve (M)
X3	Xenon Metering Valve (M)

line to flush the experimental gases through a CS Clean Systems[®]BF₃ scrubber, and a mechanical oil pump on the outlet of the scrubber to draw gas through the scrubber and remove the remaining BF₃ from the system. Because these systems were discussed in Chapter 4.2.1, they will not be discussed again.

In addition to the aforementioned protective systems, a ventilation system was constructed to carry the exhaust gas from the scrubber safely out of the MUTR building. This exhaust system was constructed from double layer aluminum duct pipe, with a fan situated approximately halfway up the duct work, and an additional fan at the top to draw the gases out of the scrubber. These fans were wired into a wiring board (which also included all the pneumatic and solenoid valves) in such a way so that if one fan were to fail, an interlock would be activated so that none of the other valves connected to the wiring board would be able to be activated. This was designed to prevent BF₃ from being unsafely exhausted.

Because of the toxicity and highly corrosive nature of BF₃, and the lessons learned during the course of the photoabsorption experiments (refer to Appendix A for a description of these issues), the gas handling system had a number of valves and

interlocks for safe handling and protection of vital equipment. A discussion of these valves can be found in Appendix D.

The experimental procedure began with the cell empty to obtain background count rate data that was subtracted from the observed signal. Once the empty cell background signals were obtained, the cell was filled with a selected noble gas at pressures from 100-800 torr. A fixed pressure of a noble gas (100, 200, 400, or 600 torr) was added to the scintillation cell. Increasing pressures of BF_3 were added to the fixed volume of noble gas (0, 5, 10, 25, 50, 100, 150, and 200 torr BF_3) in the scintillation cell, and photon emission data was collected. Following the conclusion of the data collection of fixed noble gas pressure/incremental BF_3 pressure, the cell was evacuated through the scrubber with a dry N_2 purge, the cell was evacuated, and the next noble gas pressure was added to the scintillation cell and the experimental procedure was repeated.

Prior to the start of each experiment, the turbopump and roughing pump were used to evacuate the gas handling system to 10^{-7} torr. The nude ion gauge (effective range 10^{-10} - 10^{-3} torr) and the thermocouple gauges (effective range 10^{-3} - 10^3 torr) were used to determine the ultimate base pressure in the system, specifically the scintillation cell. After the conclusion of each set of noble gas/ BF_3 experiments, the system was flushed through the scrubber using dry N_2 , then evacuated again. The SRS RGA-100 was used to identify any residual contaminants in the system prior to the introduction of any of the experimental gases. A typical RGA scan is shown in Figure 5.2.3-2.

Before entering the scintillation cell, all three noble gases passed through a Micro-torr MC1-902-F filter to remove any trace contaminants, including trace amounts of water, oxygen, CO, CO_2 , hydrogen, and any hydrocarbons, to <1 ppb. The purities of the gases were research grade, and are shown in Tables 4-1 and 5.2.3-2.

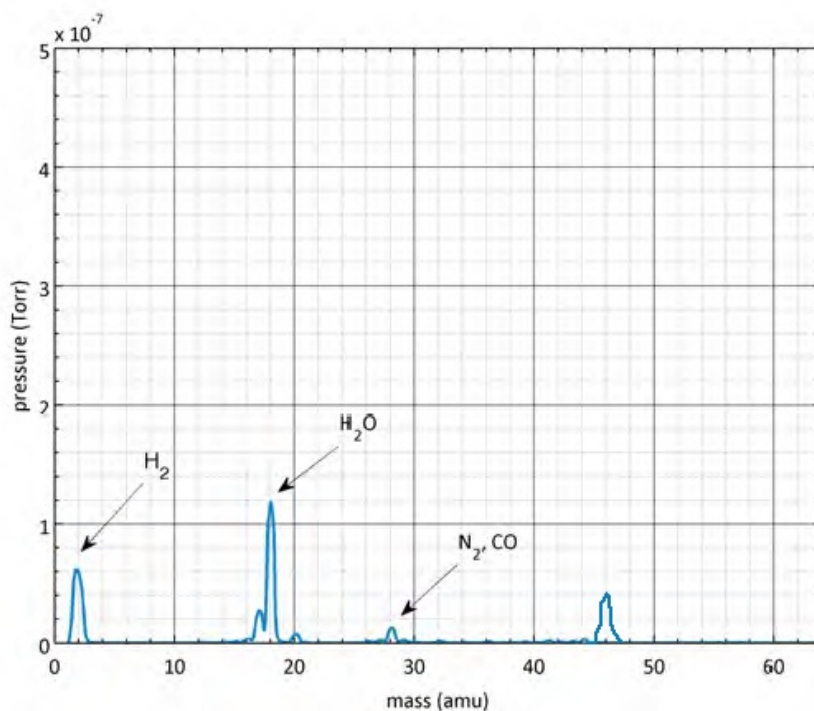


Figure 5.2.3-2: Typical RGA spectral scan after scintillation cell evacuation

Table 5.2.3-2: Purities of noble gases and contaminant concentrations according to manufacturer data sheet. THC: total hydrocarbons

Gas Type	Purity (%)	<n ppm
Ar	99.9995	CO ₂ (0.1), CO (0.1), O ₂ (0.05), THC (0.1), H ₂ O (0.05)
Kr	99.999	Ar (1), CF ₄ (1), CO (1), CO ₂ (1), H ₂ (1), He (1), H ₂ O (4), Xe (10), N ₂ (10), O ₂ (2), THC (0.1)
Xe	99.999	Ar (1), CF ₄ (0.5), CO ₂ (1), H ₂ (2), H ₂ O (0.004), Kr (5), N ₂ (1), O ₂ (0.10), THC (0.5)

Data were collected in 200 s intervals under a variety of experimental conditions, including shutter closed, shutter open with a mixed beam, shutter closed with a 1" Pb brick in front of the scintillation cell, shutter open with a 1" Pb brick in front of the scintillation cell, shutter closed with a 0.1984-cm sheet of boral in front of the scintillation cell, and the shutter open with the same sheet of boral. These experiments were conducted for each gas pressure to determine the contribution of thermal

neutrons and gamma-rays, individually and as a whole, on the excimer scintillation.

5.2.4 Carbon Foam Experimental Setup

Following the completion of the $^{10}\text{BF}_3$ experiment, additional measurements were conducted with carbon foam samples. These sets of experiments will be discussed in Chapter 8. As there were no toxic or corrosive gases used in these experiments, the gas handling system was significantly simplified, with the elimination of supernumerary valves, the ventilation system, cold trap, and glove box. The system used is shown in Figure 5.2.4-1. Table 5.2.4-1 describes the function of each of the valves in the system. All major parts are labeled.

The scintillation cell, PMT, and pumping system used were the same as those in the $^{10}\text{BF}_3$ experiment. These will not be discussed again.

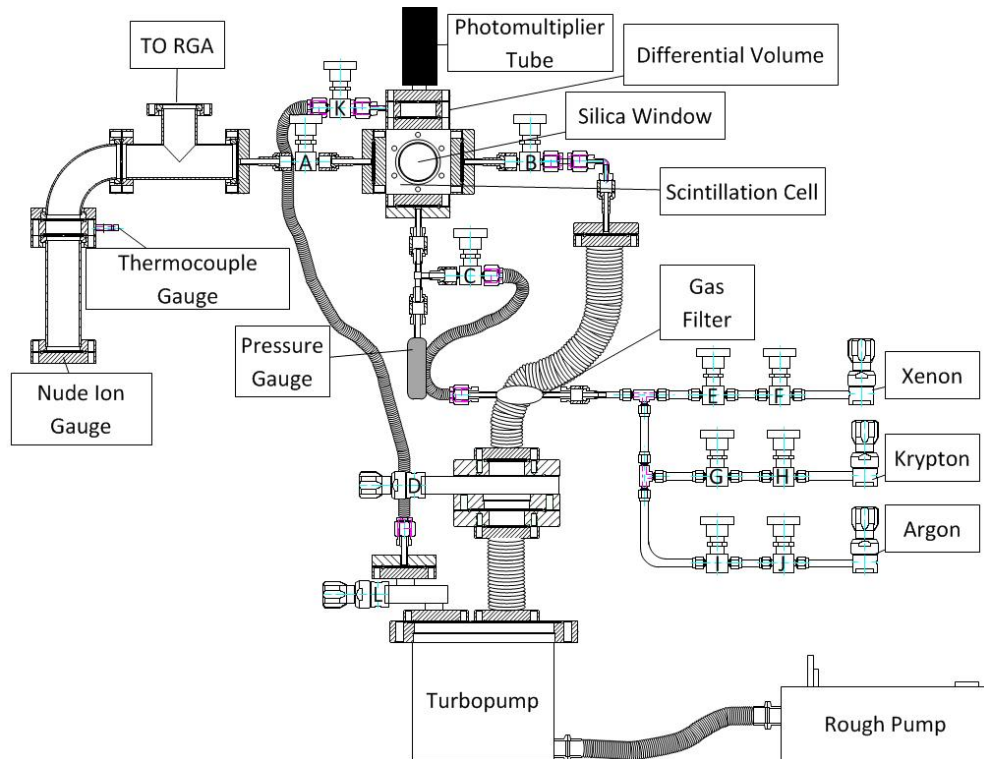


Figure 5.2.4-1: Gas handling system used for the carbon foam experiments

Table 5.2.4-1: Description of valves used in the MUTR Carbon Foam Gas Handling System

Valve	Description
A	Scintillation Cell Isolation Valve
B	Scintillation Cell Isolation Valve
C	Noble Gas Isolation Valve
D	Turbopump Isolation Valve
E	Xenon Valve #1
F	Xenon Valve #2
G	Krypton Valve #1
H	Krypton Valve #2
I	Argon Valve #1
J	Argon Valve #2
K	Differential Volume Isolation Valve
L	Turbopump Isolation Valve

Data were collected under the same experimental operating conditions as those used for the BF_3 experiments.

5.2.5 Discussion of Electronics

When a photon with sufficient energy interacts with a photomultiplier tube photocathode, an electron, known as a photoelectron, may be released due to the photoelectric effect. The photoelectron can be detected using a focusing electrode and aiming it at a series of dynodes of increasing voltages. The signal is amplified through secondary emission until enough charge is collected at the anode to produce an electric pulse. The number of electric pulses can be counted, and using this information, the number of photon events may be determined [27]. Figure 5.2.5-1 illustrates the photon counting electronics.

The PMT pulses were counted using a counter/timer (C/T) and a multichannel analyzer (MCA). The data collected from these electronics were used to calculate the excimer scintillation yield. Throughout the duration of these experiments, the PMT was operated at a voltage of -2300 V, which corresponds to a gain of 3×10^5 [67].

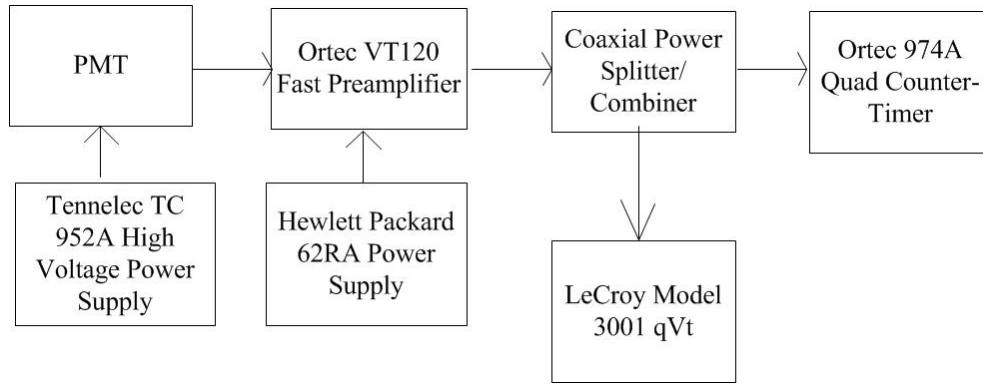


Figure 5.2.5-1: Photon counting electronics

An Ortec[®]VT120A preamplifier amplified the pulses from the PMT. This preamp has a non-inverting gain of 200 and a reported rise time of ≤ 1 ns [68]. A Mini-circuits ZFSC-2-4+ power splitter divided the amplified pulse signal, with one end going into a Lecroy qVt 3001 MCA, and the other going to the C/T. The C/T was an Ortec[®]974A Quad Counter/Timer, equipped with four 8-decade counters. The maximum counting rate is 100 MHz for all negative inputs and 25 MHz for all positive inputs. The time base is 0.1 s or 1 min increments [71].

The MCA, operated in charge (q) mode was used to obtain pulse-height distribution data (PHD). This qVt has 1024 channels and can be operated in one of three modes: charge (Q, area), voltage (V, peak) with analog-to-digital conversion and time-to-digital conversion (T, start/stop). Each mode has high sensitivity (Q = 0.25 pC, V = 1 mV, T = 100 ps) with nanosecond logic functions. It has an integration width of 20 ns with a resolution of 0.25 pC/channel [72]. The data from the qVt were sent via an interface circuit (microcontroller Wiring v1.0 board) to a Dell[®]desktop computer running Linux SUSE, and digitally output to a file using a Perl script. Because the digitization time of the MCA was long, $12 \mu\text{s} + 0.05 \mu\text{s}$ [72], with respect to the decay time of each scintillation event, not every pulse was collected by the MCA, and the PHDs were taken to be a representation of the true distribution. As a result, the data from the C/T were used to determine the absolute number of pulses.

Figure 5.2.5-2 illustrates standard pulse height distribution data obtained during data collection.

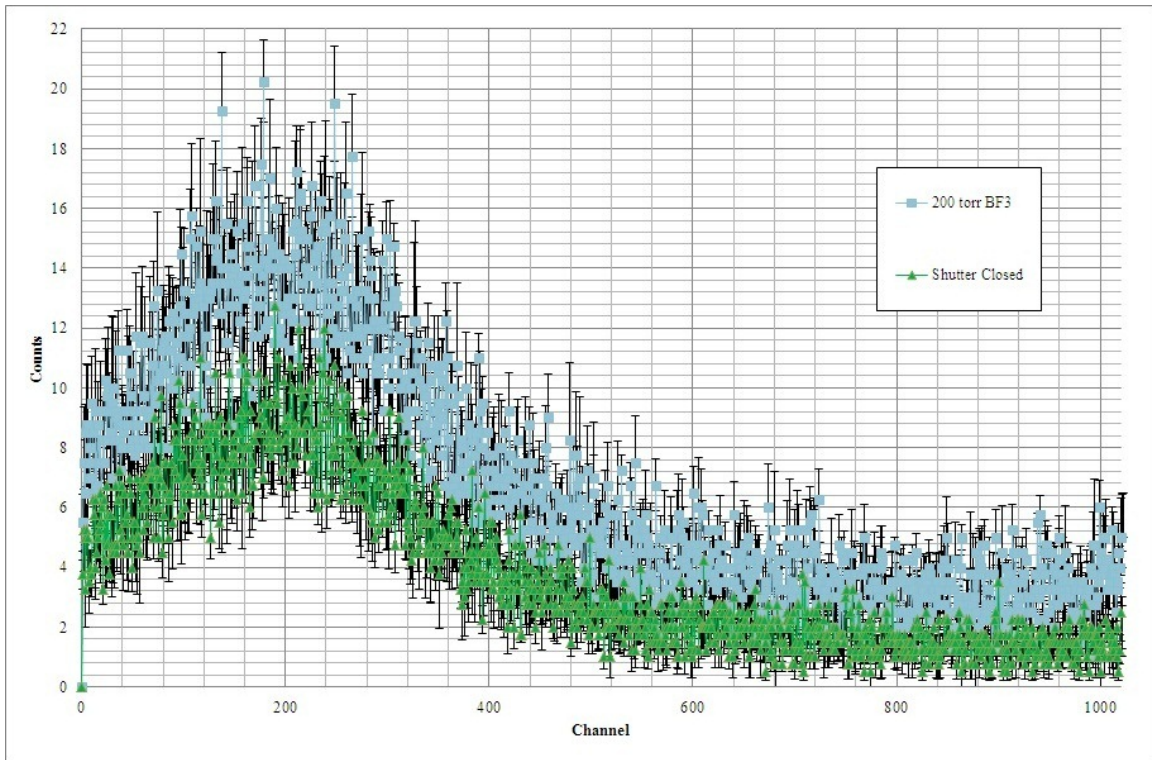


Figure 5.2.5-2: Pulse height distribution data. The triangles represent the PHD with the shutter closed under the same conditions.

The fission chamber beam monitor was operated at +125 V with P-10 gas (90% Ar, 10% CH₄) passing through it. Neutrons that impinge on the ²³⁵U deposit have an 85% chance of inducing fission, and the resulting fission products create ionization within the P-10 gas. The free charge collected on the anode wire and created electronic pulses that were amplified by a Tennelec 2273 charge-sensitive preamplifier and an Ortec[®]671 shaping amplifier. The pulses were then sent to a Tracor Northern 7200 MCA, where the PHDs were digitally transferred to a the Linux SUSE computer using Perl script [54].

While the PMT was operated at a constant voltage of -2300 V, characterization of the PMT and the preamp used in the data collection electronics were performed from -1500 V to -2300 V to demonstrate whether the applied operating voltage was

appropriate for the purposes of these experiments. Data were collected with no neutron source, a small alpha-emitter in the scintillation cell under vacuum and under 800 torr of Xe, and with a neutron source with the scintillation cell under vacuum and with 800 torr Xe. The data were compared for each operating voltage. Comparison of the data are shown in Figures 5.2.5-3 through 5.2.5-7. Values of the peak values are shown in Tables 5.2.5-1 through 5.2.5-4.

Table 5.2.5-1: Comparison of peak maxima values from electronics characterization for PMT.

Voltage	No Source, No Xe	Alpha, No Xe	Alpha, 800 torr Xe	Neutrons, No Xe	Neutrons, 800 torr Xe
1500 V	123.6 μ V	2.587 μ V	458.0 μ V	1.859 mV	1.780 mV
1700V	218.0 μ V	2.598 μ V	530.4 μ V	1.721 mV	1.727 mV
1900 V	155.9 μ V	1.980 mV	6.377 μ V	4.270 mV	13.01 mV
2100 V	340.0 μ V	9.496 mV	1.499 mV	13.60 mV	16.03 mV
2300 V	5.105 mV	3.114 mV	4.617 mV	30.84 mV	324.1 mV

Table 5.2.5-2: Comparison of peak maxima values from electronics characterization for PMT-Preamplifier.

Voltage	No Source, No Xe	Alpha, No Xe	Alpha, 800 torr Xe	Neutrons, No Xe	Neutrons, 800 torr Xe
1500 V	5.617 mV	11.20 mV	18.10 mV	129.6 mV	142.0 mV
1700V	7.325 mV	14.25 mV	24.02 mV	284.0 mV	383.4 mV
1900 V	13.94 mV	17.22 mV	73.81 mV	439.7 mV	759.1 mV
2100 V	9.301 mV	12.20 mV	281.2 mV	839.1 mV	913.7 mV
2300 V	410.1 mV	14.67 mV	445.9 mV	959.7 mV	844.1 mV

Table 5.2.5-3: Comparison of peak minima values from electronics characterization for PMT.

Voltage	No Source, No Xe	Alpha, No Xe	Alpha, 800 torr Xe	Neutrons, No Xe	Neutrons, 800 torr Xe
1500 V	-1.340 mV	-1.331 mV	-1.184 mV	-2.340 mV	-2.169 mV
1700V	-1.481 mV	-1.262 mV	-1.522 mV	-2.366 mV	-2.317 V
1900 V	-1.520 mV	-7.440 mV	-6.288 mV	-31.40 mV	-23.56 mV
2100 V	-1.393 mV	-3.570 mV	-11.20 mV	-94.87 mV	-109.7 mV
2300 V	-34.52 mV	-20.27 mV	-34.61 mV	-148.8 mV	-325.1 mV

Table 5.2.5-4: Comparison of peak minima values from electronics characterization for PMT-Preamp.

Voltage	No Source, No Xe	Alpha, No Xe	Alpha, 800 torr Xe	Neutrons, No Xe	Neutrons, 800 torr Xe
1500 V	-10.03 mV	-18.21 mV	-22.98 mV	-740.0 mV	-370.0 mV
1700V	-11.39 mV	-21.40 mV	-361.9 mV	-740.0 mV	-1.480 V
1900 V	-19.00 mV	-23.80 mV	-895.9 mV	-5.675 V	-9.559 V
2100 V	-13.80 mV	-23.80 mV	-3.820 V	-9.879 V	-10.32 V
2300 V	-3.700 V	-23.90 mV	-5.600 V	-10.36 V	-10.50 V

It was observed that around -2000 V on the PMT, the signal from the PMT-Preamp increased exponentially, with the maxima nearing 1 V, and the minima exceeding -10 V when 800 torr Xe was added to the scintillation cell in the presence of neutrons. This pattern was observed even without the addition of xenon to the scintillation cell, indicating that after a certain voltage (around -2100 V), a cascade effect is present, and the observed signal is amplified by at least an order of magnitude, indicating the operating voltage of -2300 V is likely too high for these experiments. Experiments should be conducted at lower PMT voltages as part of future work.

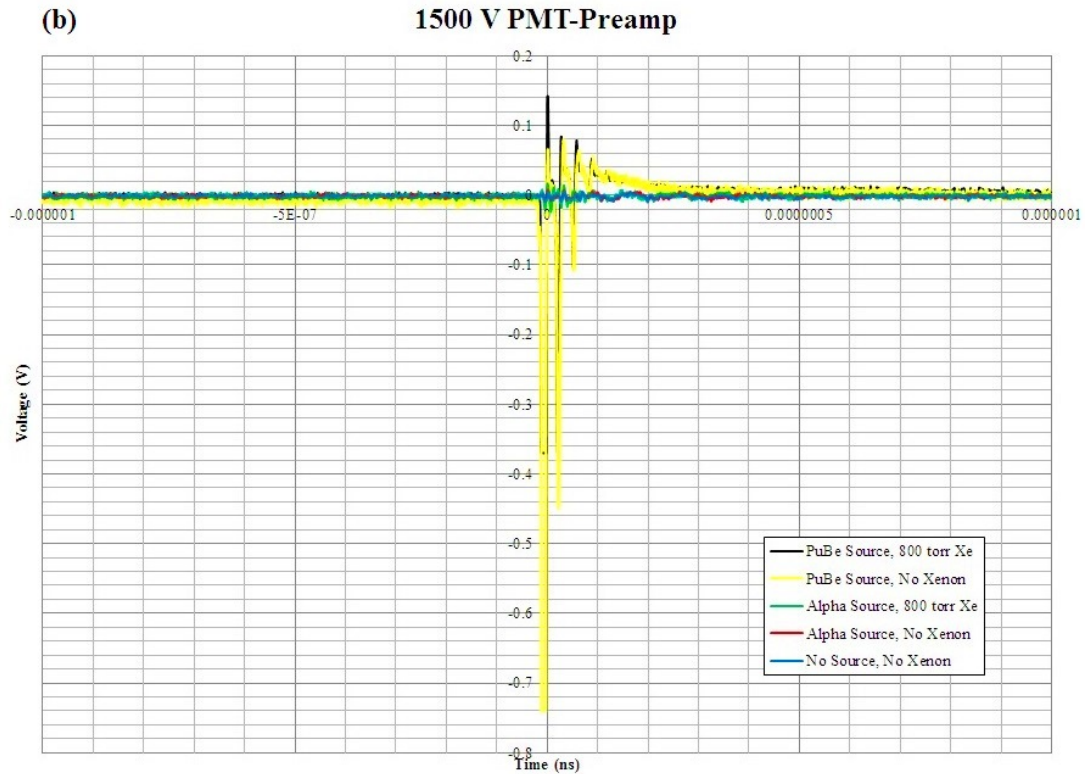
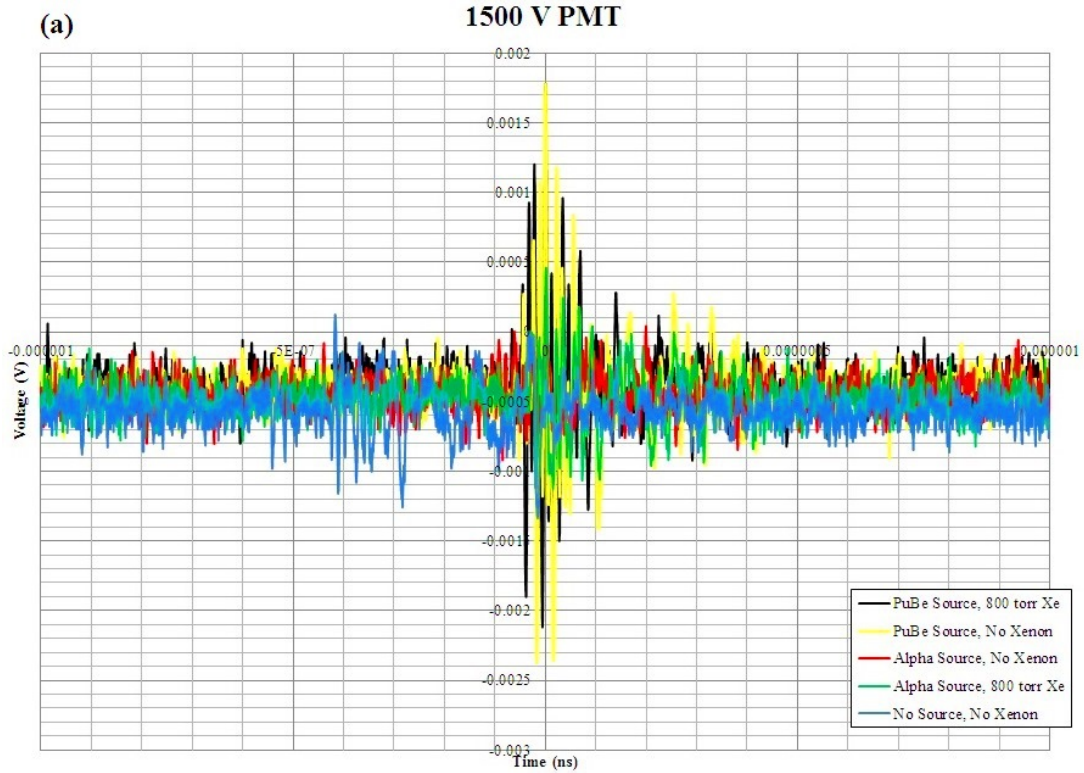


Figure 5.2.5-3: Oscilloscope traces at -1500 V for (a) PMT and (b) PMT and Preamp. Blue lines represent signal from no source and no xenon; red lines represent signal from alpha source and no xenon; green lines represent signal from alpha source and 800 torr xenon; yellow lines represent signal from neutron source and no xenon; black lines represent signal from neutron source and 800 torr xenon.

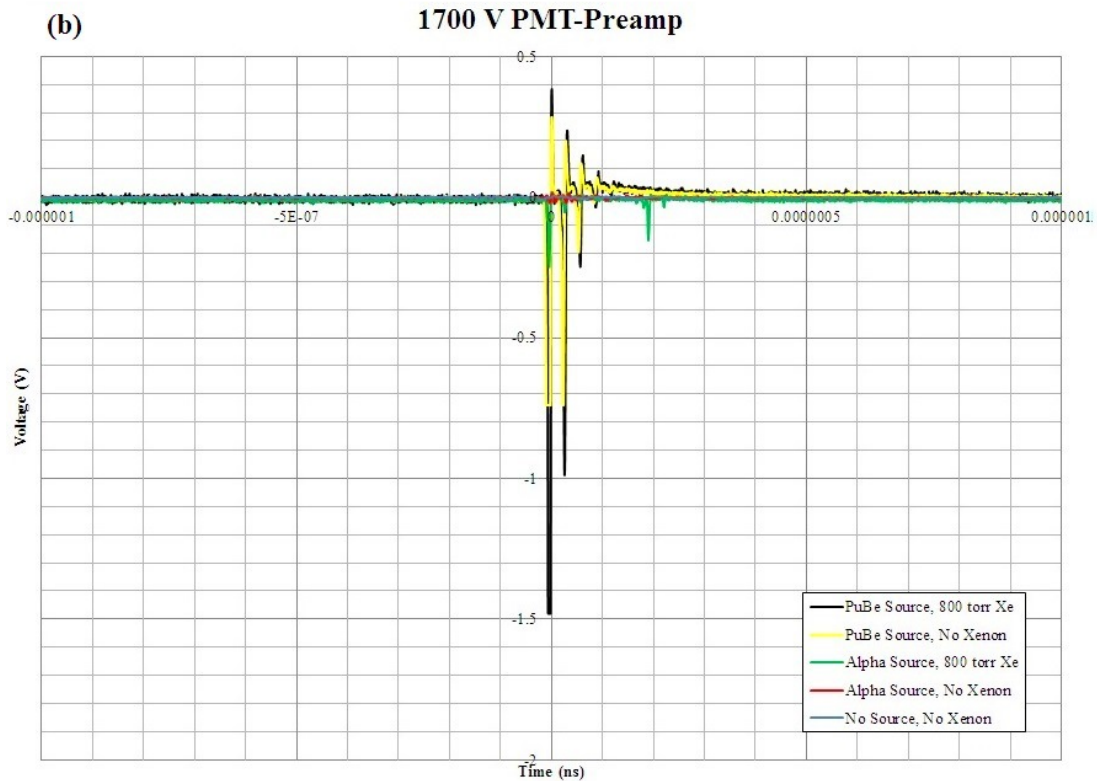
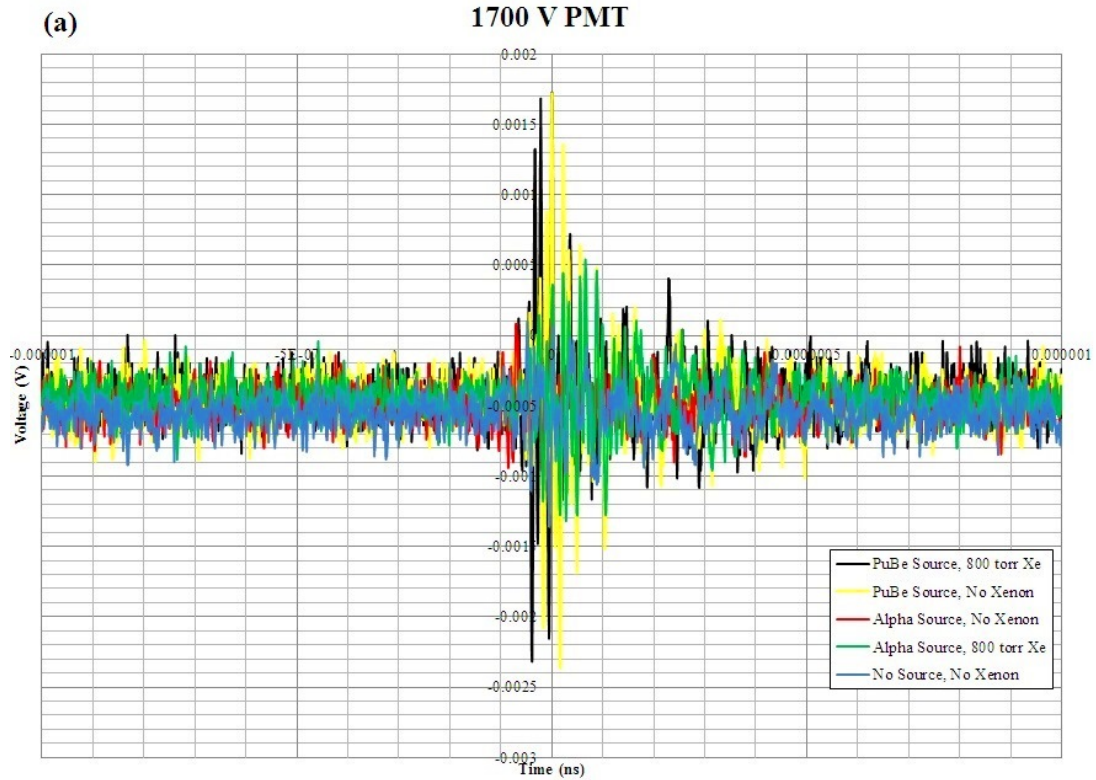


Figure 5.2.5-4: Oscilloscope traces at -1700 V for (a) PMT and (b) PMT and Preamp. Blue lines represent signal from no source and no xenon; red lines represent signal from alpha source and no xenon; green lines represent signal from alpha source and 800 torr xenon; yellow lines represent signal from neutron source and no xenon; black lines represent signal from neutron source and 800 torr xenon.

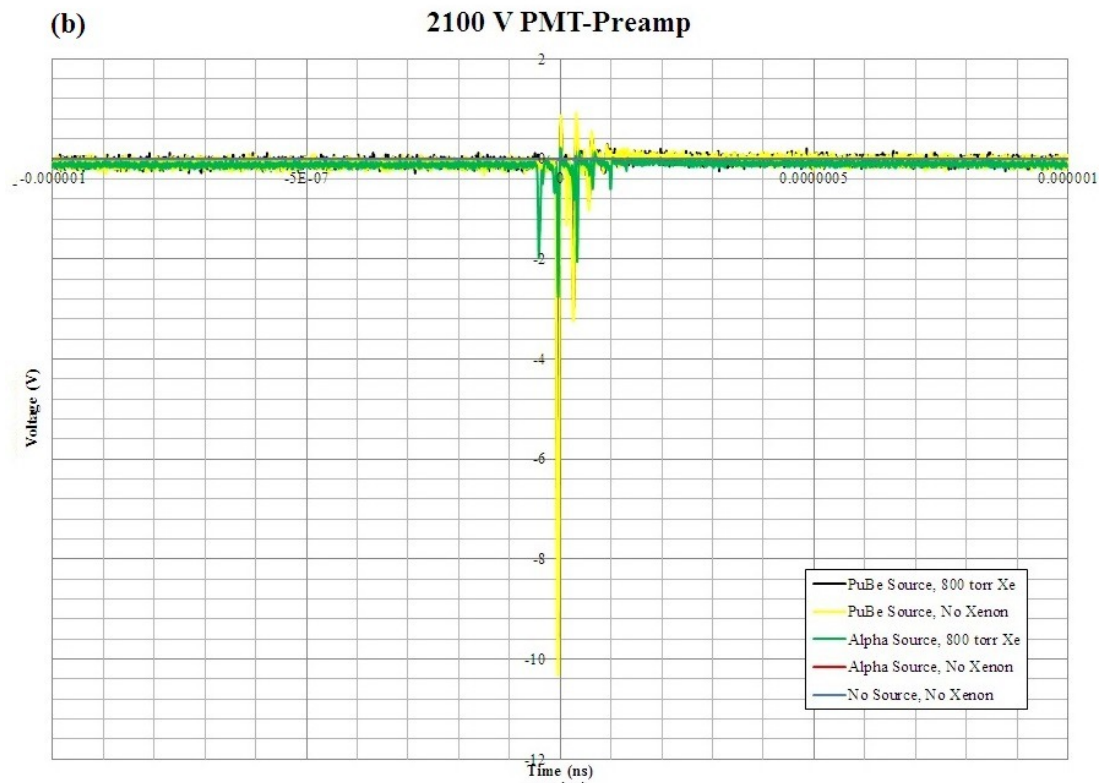
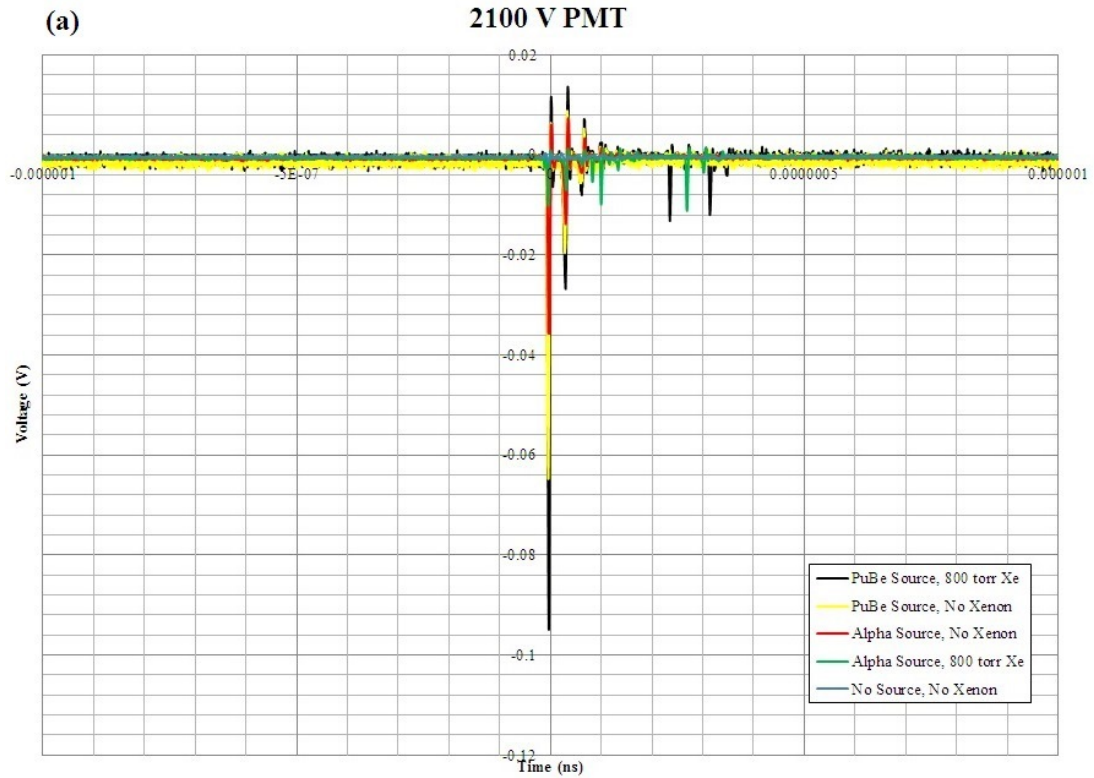


Figure 5.2.5-6: Oscilloscope traces at -2100 V for (a) PMT and (b) PMT and Preamp. Blue lines represent signal from no source and no xenon; red lines represent signal from alpha source and no xenon; green lines represent signal from alpha source and 800 torr xenon; yellow lines represent signal from neutron source and no xenon; black lines represent signal from neutron source and 800 torr xenon.

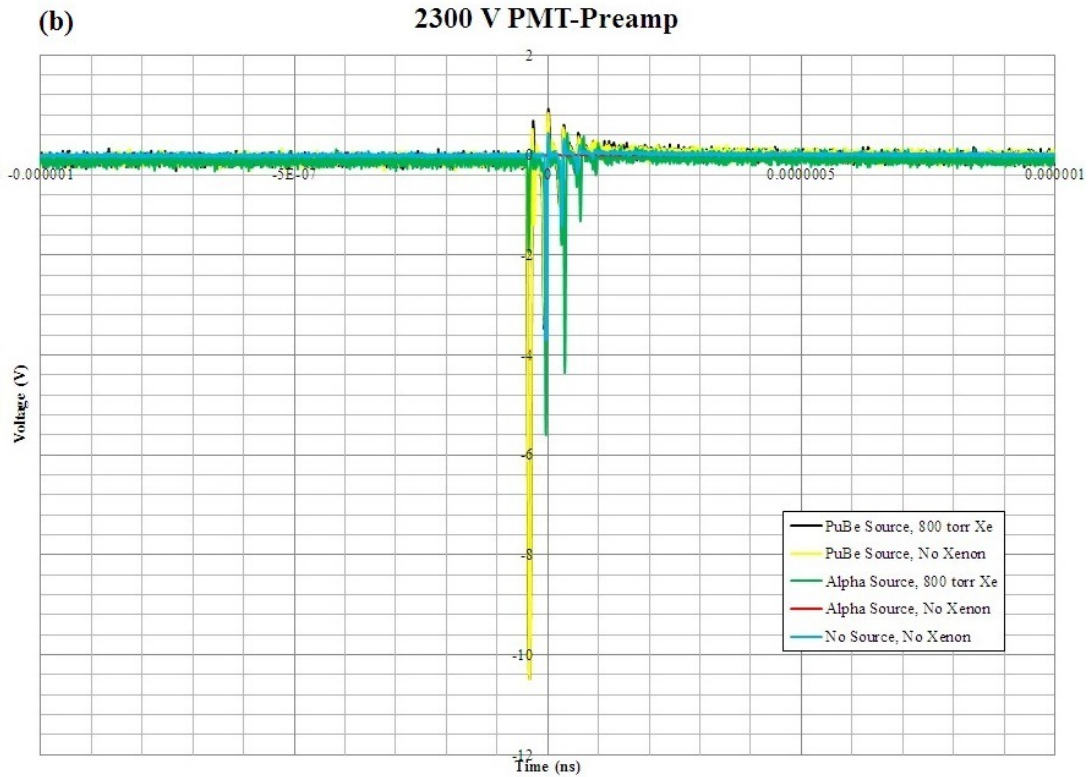
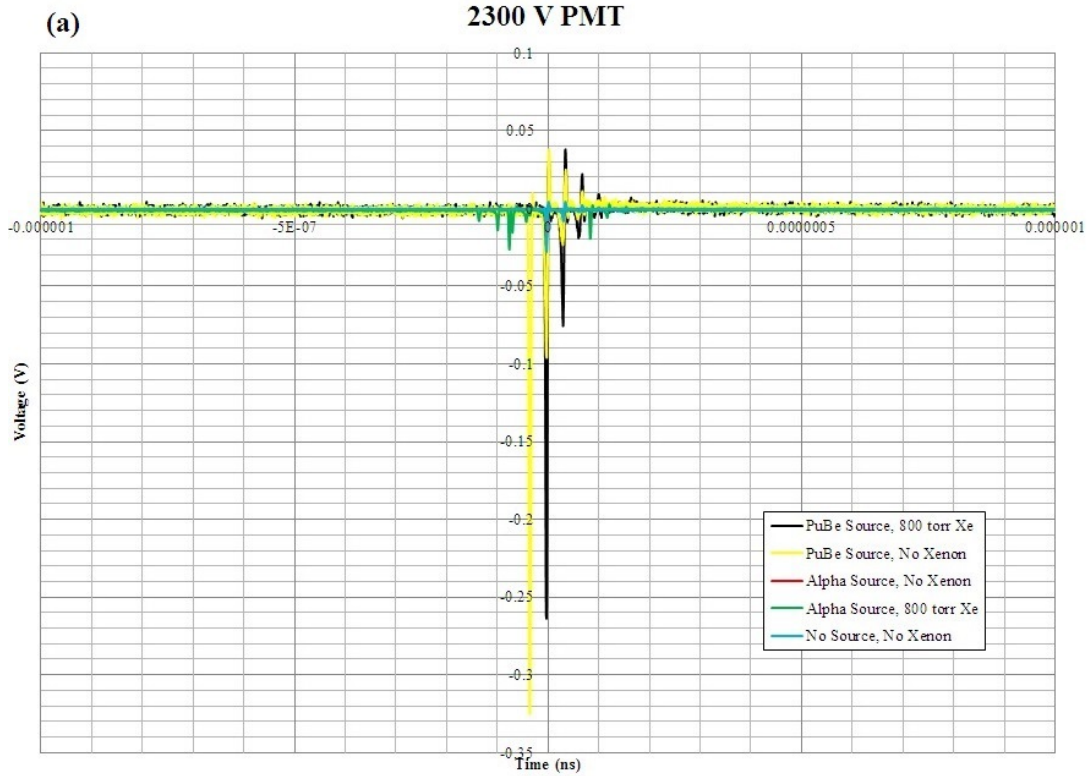


Figure 5.2.5-7: Oscilloscope traces at -2300 V for (a) PMT and (b) PMT and Preamp. Blue lines represent signal from no source and no xenon; red lines represent signal from alpha source and no xenon; green lines represent signal from alpha source and 800 torr xenon; yellow lines represent signal from neutron source and no xenon; black lines represent signal from neutron source and 800 torr xenon.

Chapter 6

Characterization of Incident Neutron Beam

In order to understand the mechanism of the excimer scintillation and draw conclusions on the potential of BF_3 or the reticulated vitreous carbon foam samples, it is important to understand the impact of gamma radiation on the signal detected by the photomultiplier tube. A good neutron detector must have good gamma ray discriminating properties, or it will not function as an ideal neutron detector. Therefore, an understanding of characteristics of the neutron beam is essential. This section will discuss the beam characterizations that have been performed.

6.1 Fluence Measurements

Throughout the duration of the experiments, a NIST-calibrated fission chamber (shown in Figure 6.1-1) was positioned in the neutron beam line in front of the scintillation cell. The beam monitor was used to measure the fluence of the thermal-column neutron beam while the MUTR was operated at a constant power of 200 kW. The fission chamber was positioned behind the 4-mm beam aperture, in front of the scintillation cell (see Figure 5.1-5).



Figure 6.1-1: NIST-calibrated fission chamber beam monitor [54].

This fission chamber has a deposit of ^{235}U which absorbed a small percentage of

the neutrons from the beam at a rate of:

$$F = I_0(1 - e^{-\Sigma_a x}) \quad (6.1-1)$$

where I_0 is the incident neutron beam intensity, Σ_a is the macroscopic absorption cross-section of the ^{235}U sample, and x is the thickness of the ^{235}U [16]. When $\Sigma_a x \ll 1$, Equation 6.1-1 becomes:

$$F = I_0(1 - (1 - \Sigma_a x)) = I_0 \Sigma_a x \quad (6.1-2)$$

In Equation 6.1-2, $\Sigma_a x$ becomes:

$$\Sigma_a x = N \sigma_a x = \rho \frac{N_A}{M} \sigma_a \quad (6.1-3)$$

where N is the atom density of the target, σ_a is the microscopic absorption cross-section of the target, ρ is the mass density of the target, N_A is Avogadro's number ($6.0221 \times 10^{23} \text{ mol}^{-1}$), and M is the molar mass of the target [54].

Substituting Equation 6.1-3 into Equation 6.1-2, F becomes:

$$F = \rho \frac{N_A}{M} \sigma_a I_0 \quad (6.1-4)$$

The rate of neutrons entering the scintillation cell, N_{Beam} , may be found from the fission chamber measurements (n) described in [54]:

$$N_{Beam} = \frac{n}{t} \frac{M_{235}}{\langle \sigma_{235} \rangle \rho_{235} N_A} \zeta \quad (6.1-5)$$

where n is the net counts determined from each fission chamber measurement, t is the length of each neutron count period, M_{235} is the molar mass of the ^{235}U deposit (235.0439 g/mol), $\langle \sigma_{235} \rangle$ is the effective microscopic absorption of ^{235}U , ρ_{235} is the cross-sectional density of the ^{235}U in the fission chamber ($458.073 \mu\text{g}/\text{cm}^2$ [75]), and ζ is the self-absorption correction factor for the fission chamber deposit (1.03756

[52]). This correction factor accounts for any fission fragments that are absorbed before ionizing the P-10 gas [52, 54].

The net counts from the fission chamber measurements, n , are found by:

$$n = n_{Total} - n_{Bkgd} \quad (6.1-6)$$

where n_{Total} is the total number of pulses counted over a given interval, and n_{Bkgd} is the number of pulses attributed to non-neutron events.

The rate at which neutrons are absorbed by the ^{10}B target, N_{Target} (BF_3 or reticulated vitreous carbon foam coated in a layer of B_4C) is given by:

$$N_{Target} = N_{Beam} \frac{\langle \sigma_{10} \rangle \rho_{Target} N_A}{M_{Target}} \mu \quad (6.1-7)$$

where $\langle \sigma_{10} \rangle$ is the effective microscopic absorption cross-section of ^{10}B , ρ_{Target} is the cross-sectional density of the target as a function of pressure or B_4C thickness, M_{Target} is the molar mass of the target material, and μ is the fraction of neutrons transmitted between the fission chamber and the scintillation cell through absorption in fission chamber, loss in through the air gap between the fission chamber and the scintillation cell, the silica entrance window, the aluminum foil covering the windows, and the Ebonol-C[®] coated aluminum cylinder (used only in the BF_3 experiments). Table 6.1-1 lists these materials with various properties. The value of μ was determined to be 0.995 [54].

Using the Ideal Gas Law, the cross-sectional density of the BF_3 gas can be found:

$$\rho = \frac{P M d}{R T} \quad (6.1-8)$$

where P is the pressure of the gas (in torr), d is the depth of neutron travel in the BF_3 gas, R is the Ideal Gas Constant (62.36367 L-torr/K-mol), and T is the temperature in K at STP (293.15 K).

Table 6.1-1: Thicknesses, macroscopic cross-sections, and transmission values (T) for the materials existing between the fission chamber reference detector and the scintillation cell, used for the determination of μ [54].

Material	Thickness (mm)	Σ_a (cm ⁻¹)	T
²³⁵ U	2.41 x 10 ⁻⁴	33.5	0.9992
Al housing	1	0.0139	0.9986
Air	75	3.83 x 10 ⁻⁵	0.9997
Al foil	0.1	0.0139	0.9999
SiO ₂ window	0.5	1.41 x 10 ⁻³	0.9999
Ar, Kr, Xe	35	(1.82, 67.4, 66.3) x 10 ⁻⁵	0.9999, 0.9976, 0.9977

Equations 6.1-5 and 6.1-7 may be combined to determine the neutron absorption rate of the ¹⁰B target:

$$N_{B10} = \frac{n \langle \sigma_{10} \rangle \rho_{Target} M_{235}}{t \langle \sigma_{235} \rangle \rho_{235} M_{Target}} \mu \zeta \quad (6.1-9)$$

Because the MUTR thermal column neutron beam line is not monoenergetic, effective microscopic cross-sections must be used in Equation 6.1-9 [54]. Figure 6.1-2 illustrates the change in ¹⁰B and ²³⁵U microscopic absorption cross-sections over the thermal energy region. To determine these effective microscopic absorption cross-sections, a weighted average may be used:

$$\langle \sigma \rangle = \frac{\int \sigma(E) \phi(E) dE}{\int \phi E dE} \quad (6.1-10)$$

where $\sigma(E)$ is the energy-dependent microscopic cross-section and $\phi(E)$ is the energy-dependent flux of the beam [54]. Because of the $1/v$ nature of both the ²³⁵U deposit in the fission chamber and the ¹⁰B in the BF₃ gas, $\phi(E)$ may be eliminated from Equation 6.1-10, and the effective cross-section now becomes:

$$\langle \sigma \rangle = \frac{\int \sigma(v) n(v) v dv}{\int n(v) v dv} \quad (6.1-11)$$

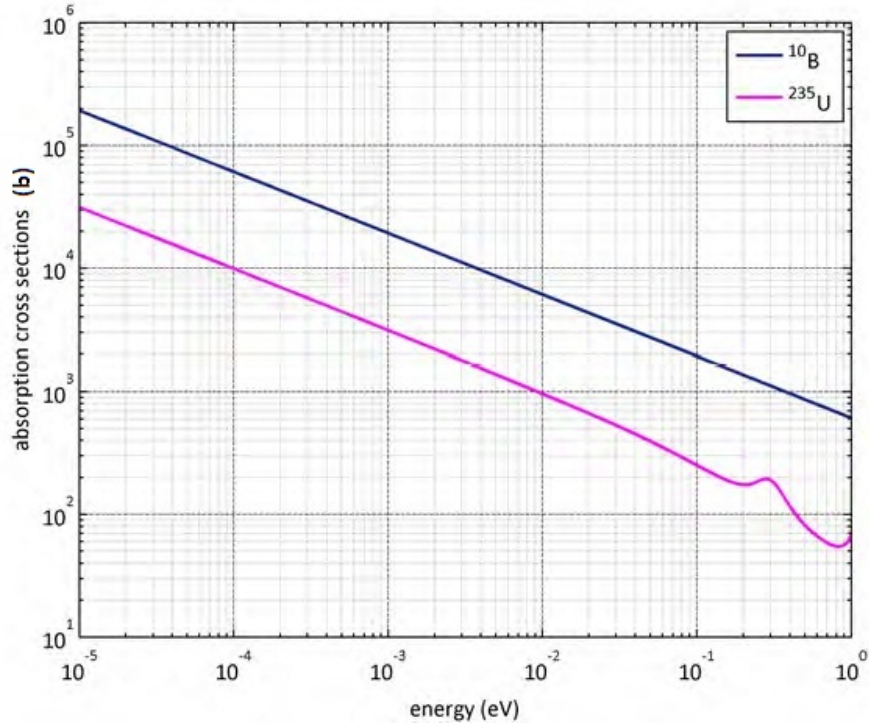


Figure 6.1-2: Cross-sections of ^{10}B and ^{235}U over the thermal energy region.

where $\sigma(v)$ is proportional to $1/v$, and the term σv is constant, reducing Equation 6.1-11 to:

$$\langle \sigma \rangle = \frac{\sigma v \int n(v) dv}{\int n(v) v dv} \quad (6.1-12)$$

The ratio of $\langle \sigma_{10} \rangle$ to $\langle \sigma_{235} \rangle$ becomes:

$$\frac{\langle \sigma_{10} \rangle}{\langle \sigma_{235} \rangle} = \frac{\sigma_{10} v \int n(v) dv}{\int n(v) v dv} \frac{\int n(v) v dv}{\sigma_{235} v \int n(v) dv} = \frac{\sigma_{10}}{\sigma_{235}} = \eta \quad (6.1-13)$$

where η was calculated to be 6.567 at $E = 0.025$ eV (2200 m/s) [54]. Values for η are shown in Figure 6.1-3.

Equation 6.1-9 becomes:

$$N_{Target} = \frac{n}{t} \eta \frac{\rho_{Target} M_{235}}{\rho_{235} M_{Target}} \mu \zeta \quad (6.1-14)$$

Because of the change in the value of n observed over the course of a normal

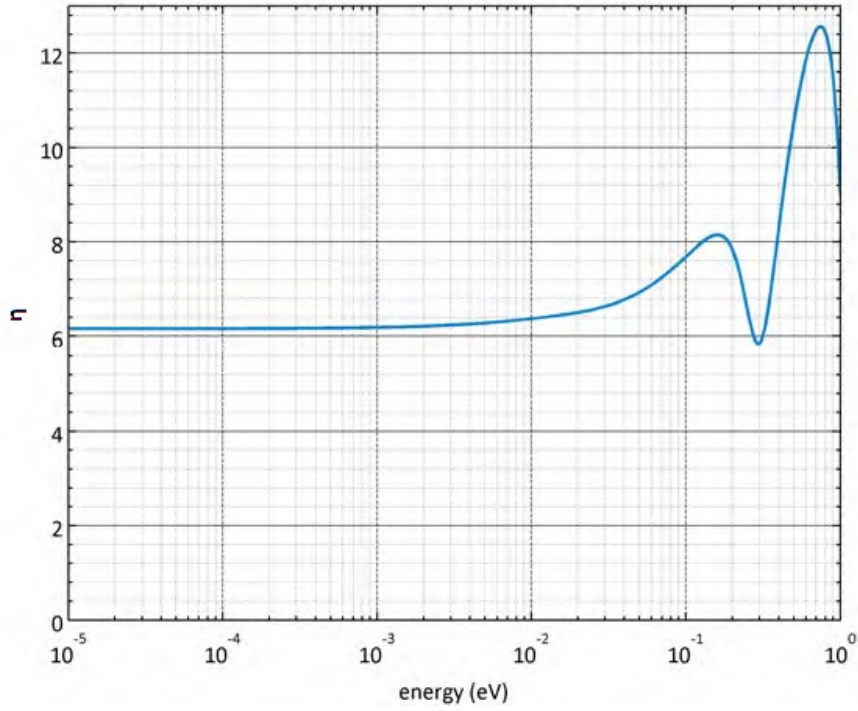


Figure 6.1-3: Values of η over the thermal energy region [54].

operating day, a value of n that corresponded to each photon count were fit by a linear regression:

$$\hat{n}(t) = m_n t + \hat{n}_0 \quad (6.1-15)$$

where $\hat{n}(t)$ represent the fitted values of the neutron count measurements over time t , m_n is the slope of the regression, t is the starting time of each photon count, and \hat{n}_0 is the value of the initial counts [54].

The uncertainty in $\hat{n}(t)$ were found by propagating the uncertainties in m_n and \hat{n}_0 :

$$u(\hat{n}(t)) = \sqrt{\left(\frac{u_{m_n}}{m_n}\right)^2 + (u_{\hat{n}_0})^2} \quad (6.1-16)$$

The standard deviation is then:

$$\sigma_{\hat{n}(t)} = \sqrt{\frac{1}{J-1} \sum_{i=1}^J (n_i - \bar{n})^2} \quad (6.1-17)$$

where \bar{n} is the mean value of the counts from each day of observation, and J is the number of measurements of n [54]. These values were very consistent with those previously determined in [54].

Equation 6.1-18 then reduces to:

$$N_{Target} = \frac{\hat{n}(t)}{t} \eta \frac{\rho_{Target} M_{235}}{\rho_{235} M_{Target}} \mu \zeta \quad (6.1-18)$$

The values of N_{Target} are listed for each pressure of BF_3 in Table 6.1-2 and for each thickness of carbon foam in Table 6.1-3. The value of N_{Target} for the 300-nm ^{10}B enriched thin-film sample was verified as part of the thin-film experiments, and is known to be 73.76 Hz (for a reactor power level of 200 kW) [54].

Table 6.1-2: Average neutron absorption rates for each pressure of BF_3

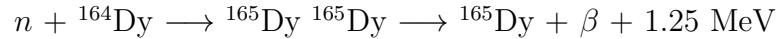
Pressure (torr)	ρ_{BF_3} ($\mu\text{g}/\text{cm}^3$)	N_{BF_3} (Hz)
5	64.92	16.85
10	129.83	33.69
25	324.59	84.25
50	649.19	168.49
100	1298.39	336.99
150	1947.58	505.48
200	2596.77	673.98

Table 6.1-3: Average neutron absorption rates for each thickness of reticulated vitreous carbon foam with a layer of B_4C

Pore Size (PPI)	Thickness (μm)	ρ_{RVC} ($\mu\text{g}/\text{cm}^3$)	N_{RVC} (Hz)
45	4	567.57	563.96
20	8.7	759.84	754.99

6.2 Beam Profile Measurements

Beam profile measurements were used to ensure the divergence of the neutron beam between the fission chamber monitor and the scintillation cell was limited. Dysprosium-164 (isotopic abundance of 28.18%) targets were used because of the large thermal neutron absorption cross-section ($\sigma_{th} = 2981$ b) [76, 77]. When subjected to neutrons, ^{164}Dy undergoes the following reaction:



The half-life of ^{165}Dy is 2.334 h [76].

Dysprosium targets 10 x 10 cm were positioned directly behind the 4-mm beam aperture and 12 cm behind the aperture, at the approximate location of the scintillation cell, and irradiated individually for 45 minutes at 200kW. The areal densities of the foils were 0.0213 g/cm². The activated dysprosium foils were then imaged by exposing an imaging plate (photostimulable phosphor) to the foils. When energetic radiation such as β particles pass through the imaging plate, electrons in the phosphor are excited, some of which become trapped in the lattice of the phosphor. When stimulated with a light source, these trapped electrons de-excite and release photons in a process known as photostimulated luminescence. The imaging plates were measured at NIST using a FujiFilm[®]BAS 1800-II image reader [54, 78].

The neutron beam profiles obtained for each Dy foil location are shown in Figures 6.2-1 and 6.2-2. Figure 6.2-1 illustrates the beam profile directly behind the 4-mm aperture. Figure 6.2-2 shows the beam profile at the location of the scintillation cell, 12 cm behind the aperture [54].

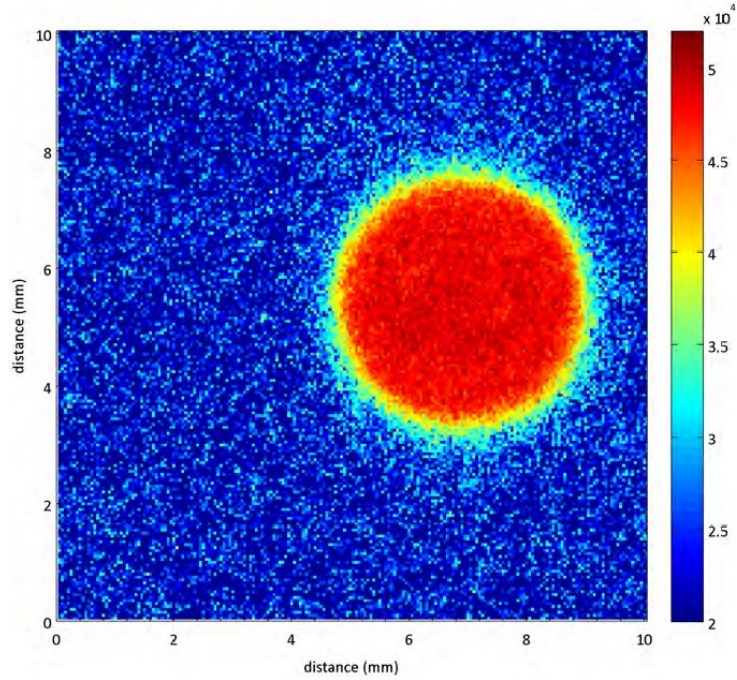


Figure 6.2-1: Neutron beam profile immediately behind 4-mm aperture [54].

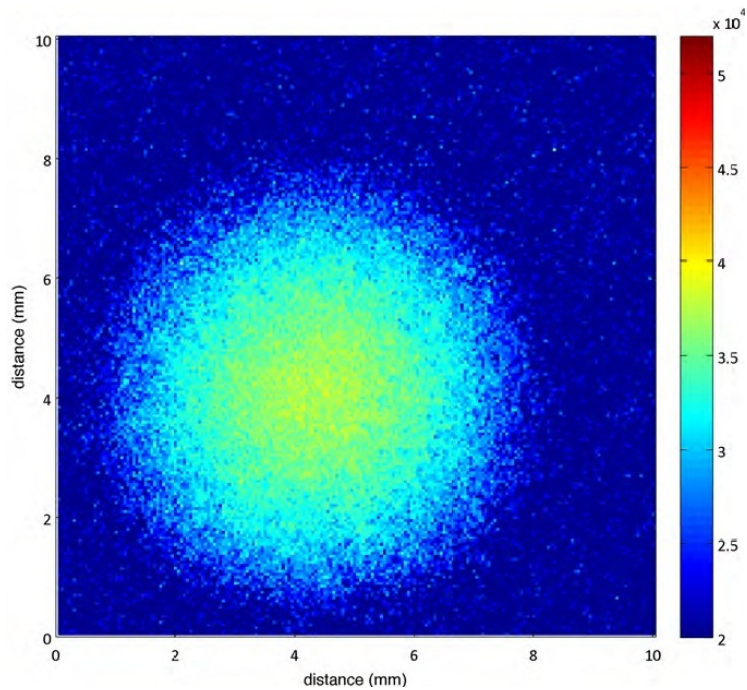


Figure 6.2-2: Neutron beam profile 12 cm behind 4-mm aperture [54].

As can be seen from Figure 6.2-1, the beam spot observed 12 mm from the aperture is larger than the 4-mm aperture itself. This is due to what is known as

“blooming” of the imaging plate, where some of the electrons from β -decay are emitted at glancing angles to the imaging plate. This produces a blurring effect at the boundaries of the image [78]. The beam spot in Figure 6.2-2 is approximately 7 mm in diameter, 3 mm larger than the aperture, indicating a 3-mm spread in the diameter of the beam between the aperture and the scintillation cell [54]. The 7-mm beam size is substantially smaller than the carbon foam target size (25 mm x 25 mm), so when the 4-mm aperture is aligned with the sample, the sample is intercepting the entire beam [54].

6.3 Gamma Ray Spectroscopy

During the course of both the BF_3 and the carbon foam experiments, it became clear that the gamma contribution to the observed signal was significant. A NaI detector was positioned 15” back from the center-line of the scintillation cell in the path of the apertured mixed-neutron beam coming from the thermal column. Data were taken over 200 s intervals for each experimental condition (i.e. shutter closed/open mixed beam, shutter closed/open 2.54 cm Pb brick, shutter closed/open 0.1984 cm boral). The contents of the cell were 800 torr xenon with an uncoated 45 PPI carbon foam sample. The gamma ray data are shown in Figures 6.3-1 through 6.3-4. The NaI detector cutoff was 4 MeV, but the continuum appears to continue well beyond 4 MeV. Spectra beyond 4 MeV is unknown.

As can be seen from Figure 6.3-1, there is a significant gamma contribution with the neutron beam coming out of the thermal column compared to the spectra observed with the shutter closed, and that with the uncoated RVC sample, the observed gamma signal is not the result of gammas being produced in the ^{10}B reaction. The collimator shutter (composed of lead and boral) blocks most but not all of the radiation from the reactor. This has been seen with the increase in signal observed on

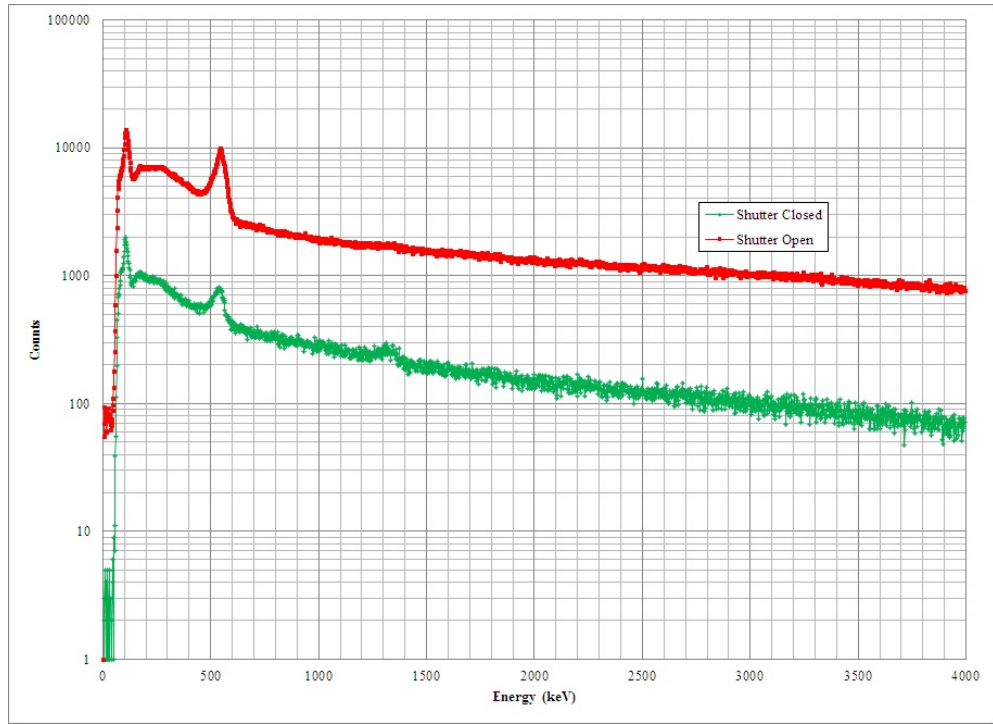


Figure 6.3-1: Gamma ray spectroscopy observed with a mixed neutron beam propagating through the scintillation cell, $t = 200$ s.

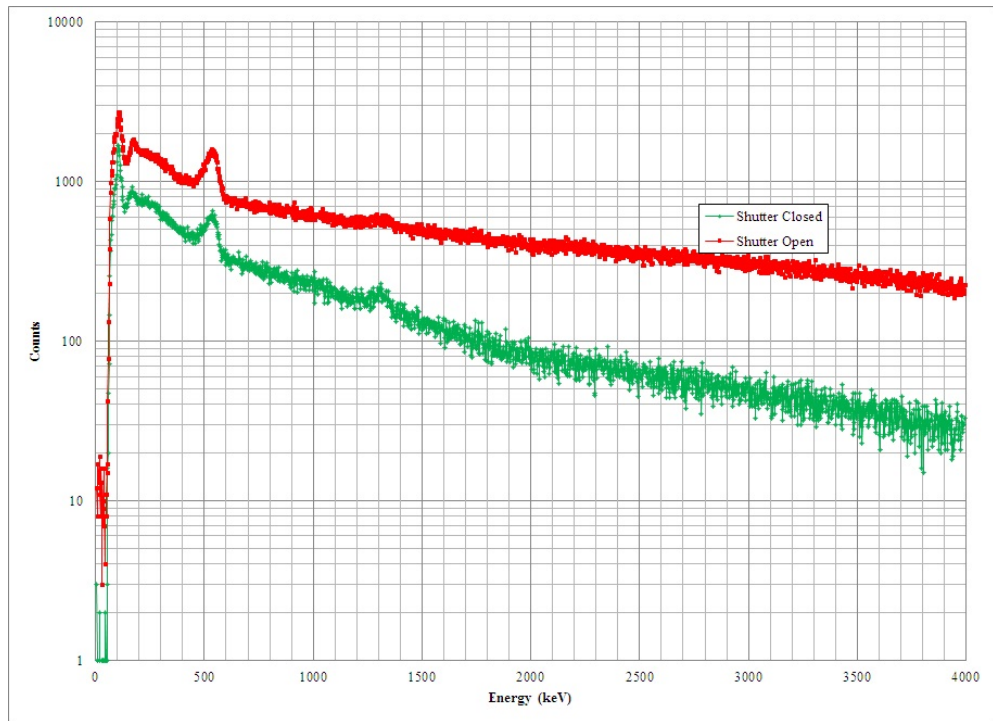


Figure 6.3-2: Gamma ray spectroscopy observed with 2.54 cm Pb brick blocking the scintillation cell, $t = 200$ s.

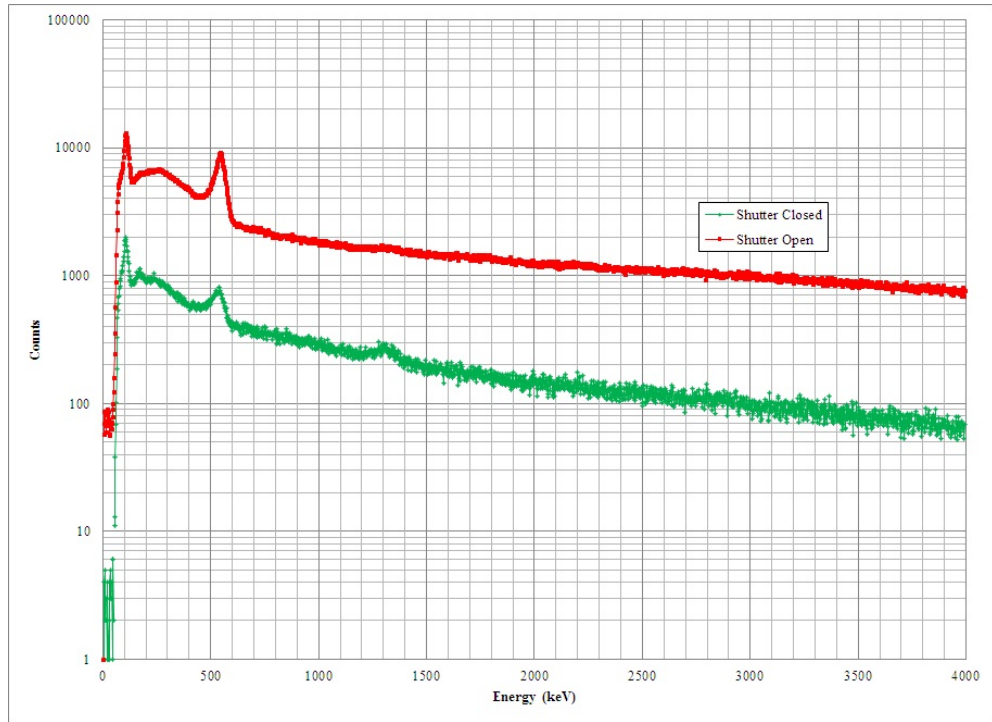


Figure 6.3-3: Gamma ray spectroscopy observed with 0.1984 cm boral sheet blocking the scintillation cell, $t = 200$ s.

the counter/timer from the signal observed with the reactor off. If the shutter blocked 100% of the radiation coming from the thermal column, in theory, the value observed with the reactor off (C_{Null}) and the value obtained with the reactor operating, but the shutter closed (C_{SC}), should be effectively the same. However, the shutter closed values were observed to change not only as a result of reactor power, but also as a result of spectrum hardening, and also as more noble gas is added to the scintillation cell. This indicates that the lead is not blocking all of the gamma rays coming out of the core.

Figure 6.3-4 provides information about the gamma ray spectrum coming out of the thermal column. It can be seen that the gamma signal from the mixed neutron beam and the gamma signal from the 0.1984 cm boral sheet immediately in front of the scintillation cell are nearly identical in intensity and pulse size, as expected. It can also be seen that the 2.54 cm Pb brick drastically reduces the intensity of the gamma rays entering the scintillation cell. This signal reduction is as much as 25%.

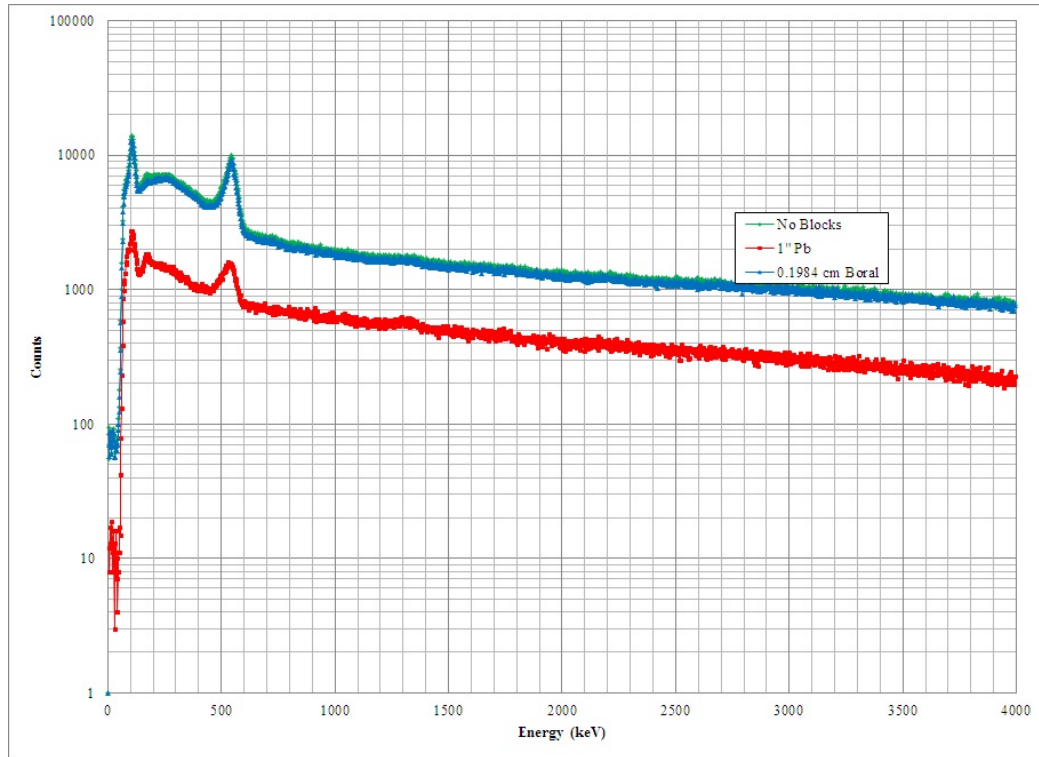


Figure 6.3-4: Gamma ray spectroscopy obtained with NaI detector on 31 January 2013. The green line indicates the gamma ray distribution with the shutter open during a mixed beam, the blue line represents the gamma signal with a 0.1984 cm boral sheet immediately in front of the scintillation cell, and the red line represents the gamma signal with a 2.54 cm Pb brick positioned immediately in front of the scintillation cell. $t = 200s$

The lead brick does not eliminate all of the gammas entering the cell.

It is worth mentioning that, while the neutron spectrum of the reactor hardens throughout extended periods of operation, there is little to no change in the gamma spectrum from day to day operations. This is evidenced in Figure 6.3-5. The data shown was collected under identical reactor operating conditions, with a ^{10}B enriched 300-nm thin-film inside the cell at 800 torr xenon. The data on 31 January was collected as the reactor was being operated at 200 kW, after having been run at 200 kW for eight to ten hours the previous three days. The reactor was shut down in the afternoon of February 1 and remained off until the morning of February 5, when it was brought to 200 kW from cold critical conditions. There is no significant difference between the gamma signal from a reactor with fission product poisons and

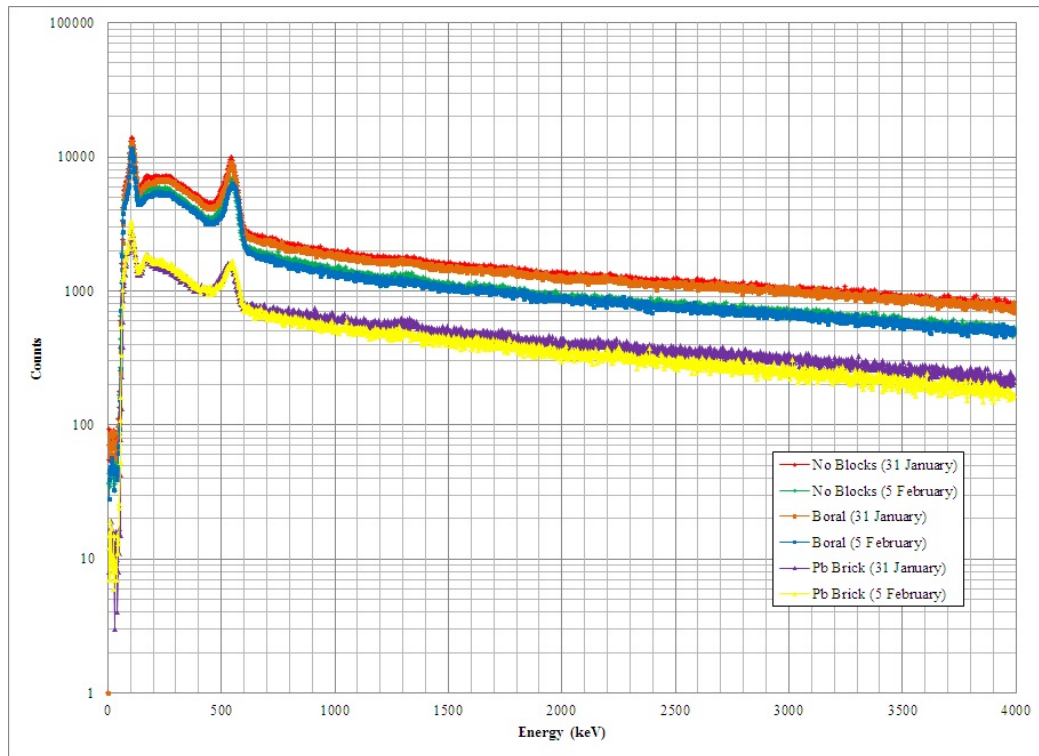


Figure 6.3-5: Gamma ray spectroscopy obtained with NaI detector on 31 January and 5 February 2013. The data show the gamma spectrum with no blocks in front of the scintillation cell, a 0.1984-cm sheet of boral, and a 1” lead brick blocking the scintillation cell.

spectrum hardening and a cold, critical core, or between a ^{10}B enriched thin-film and an uncoated RVC foam sample, indicating that the observed gamma radiation is from the reactor core, and not gammas produced in the ^{10}B reaction inside the scintillation cell. Another important observation is seen in Figure 6.3-6. It was believed that the gamma signal observed was not solely from the thermal column, but due to background radiation in the reactor facility, specifically the accumulation of ^{41}Ar , which is the result of irradiation of ^{40}Ar in the air (Ar being a constituent of air). Evidence of ^{41}Ar appears as a peak at 1293 keV. As ^{41}Ar reaches equilibrium approximately four hours after the reactor first reaches criticality, it accumulates throughout the course of a normal day of operations. Running the exhaust fans for approximately ten minutes every two to three hours before the concentration of ^{41}Ar

reaches equilibrium helps diffuse and disperse the buildup in the reactor building. Figure 6.3-6 shows the change in the gamma signal from three identical runs: one with the shutter open and nothing blocking the scintillation cell immediately prior to the fans being turned on, one with the shutter open and nothing blocking the scintillation cell while the exhaust fans are being run, and one immediately following with the fans off. These results indicate that running the exhaust fans for fifteen to twenty minutes does not change the gamma signal at all, indicating that ambient reactor background radiation has little to no significant contribution on the observed gamma signal coming from the thermal column.

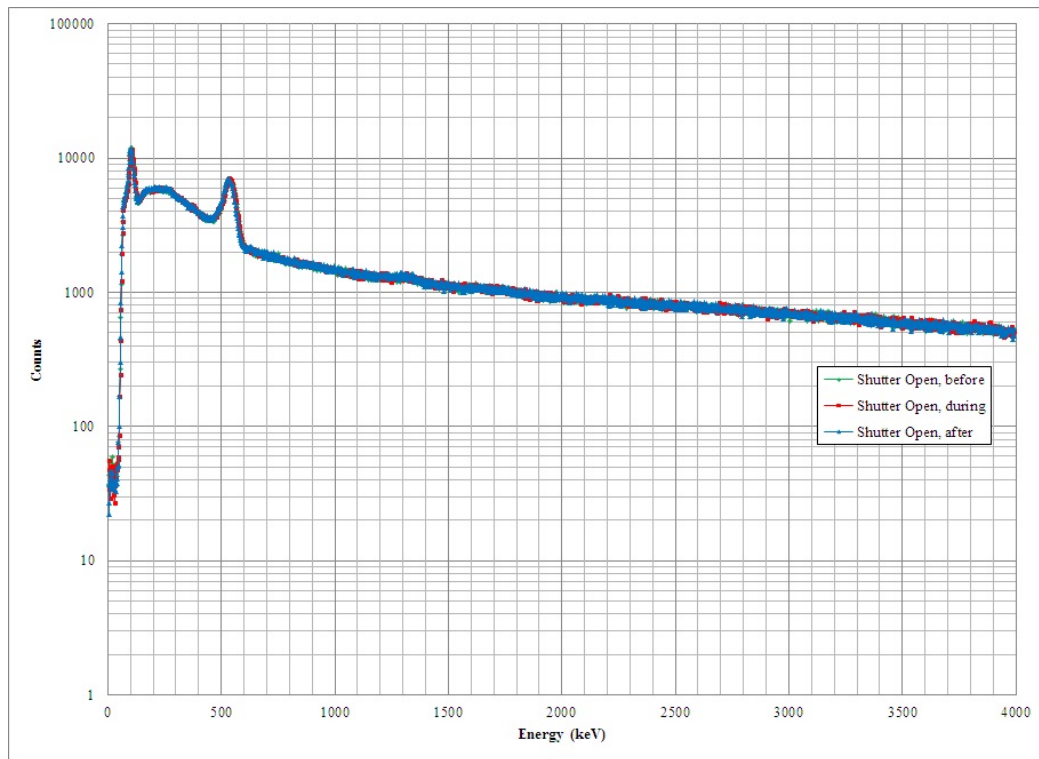


Figure 6.3-6: Gamma ray spectroscopy obtained with NaI detector on 5 February 2013. The data show the gamma spectrum with no blocks in front of the scintillation cell immediately prior to, during, and immediately after the exhaust fans were run for fifteen minutes.

Chapter 7

$^{10}\text{BF}_3$ FUND Results

Following the conclusion of the neutron beam characterization, the focus of this research shifted to the experimental data collection and analysis of the first stage of the research: the ^{10}B enriched BF_3 gas. This chapter will discuss the experimental procedure for data collection, and a discussion of the results obtained from the experiments.

7.1 Procedure for $^{10}\text{BF}_3$ Experiments

The first set of experiments were conducted using mixtures of ^{10}B enriched BF_3 gas and one of three rare noble gases (Xe, Kr, or Ar). The procedure, as previously described, involved mixing BF_3 pressures of 0, 5, 10, 25, 50, 150 or 200 torr with 100, 200, 400, and 600 torr of a noble gas. Pulse-height distribution data, as well as photon count rates, were obtained under a variety of operating conditions. This chapter will describe those experiments and the results obtained.

The scintillation cell was evacuated to a base pressure on the order of 10^{-7} torr. Before the reactor was brought on-line, measurements were collected with the reactor off to obtain background data on PMT noise and dark current, as well as background reaction radiation levels (C_{Null}). As the shroud composed of several alternative layers of black felt and aluminum foil covering the scintillation cell windows was not removed throughout the course of the experiments, these values did not change significantly from day to day.

Once the value of C_{Null} was obtained, the reactor was brought to and maintained

at a power level of 200 kW. Data were then collected with the evacuated scintillation cell. Measurements were conducted with the shutter closed (C_{SC}), the shutter open and a mixed beam of gamma rays and neutrons propagating through the scintillation cell (C_{Tot}), the shutter closed and a 1" thick Pb brick positioned in front of the scintillation cell, the shutter open with the same lead brick in front of the scintillation cell (C_{Pb}), the shutter closed with a sheet of cadmium blocking the scintillation cell, and the shutter open with the same sheet of cadmium in front of the scintillation cell (C_{γ}). These measurements were obtained in order to determine the excimer scintillation yield as a result of neutron events, rather than non-neutron events.

A selected pressure of one noble gas (100, 200, 400, or 600 torr) was then introduced to the scintillation cell, and the measurements to determine C_{Tot} , C_{SC} , C_{Pb} , and C_{γ} were repeated to determine the background due to irradiation of the noble gas background. Once this information was obtained, BF_3 gas was introduced to the cell from 5 to 200 torr. The cell was then purged with dry N_2 through the scrubber, and then evacuated at the conclusion of the experiment. The next pressure of the noble gas was selected, and the process was repeated.

7.2 Analysis of Results in BF_3

In order to determine the number of excimer scintillation events, it was necessary to define a value termed C_{Obs} , which is the total observed pulse value and is defined by:

$$C_{Obs} = C_{Tot} - C_{Null} - C_{\gamma} \quad (7.2-1)$$

where C_{Tot} is the total number of pulses counted over a set period of time, C_{Null} is the number of pulses observed with the reactor at 0 kW prior to the commencement of each day's experiments, and C_{γ} is the number of pulses attributed to dark current and non-neutron events. The value of C_{Tot} is obtained during a 200 s irradiation of the scintillation cell with a mixed neutron beam streaming from the reactor. The

value of C_γ is obtained by placing a boron sheet in front of the scintillation cell to block thermal neutrons from entering the cell. The number of pulses observed can be seen in Figures 7.2-1 and 7.2-2. Table 7.2-1 illustrates an example of the different types of pulse observations conducted for the BF_3 experiments.

A multichannel analyzer (MCA) was used to identify the pulse-height distribution data and to verify that the pulses observed by the counter/timer were not adversely affected by multi-photoelectron events. The PHD data for varying pressures of BF_3 with 100 torr Xe are shown in Figures 7.2-4, 7.2-5, and 7.2-6.

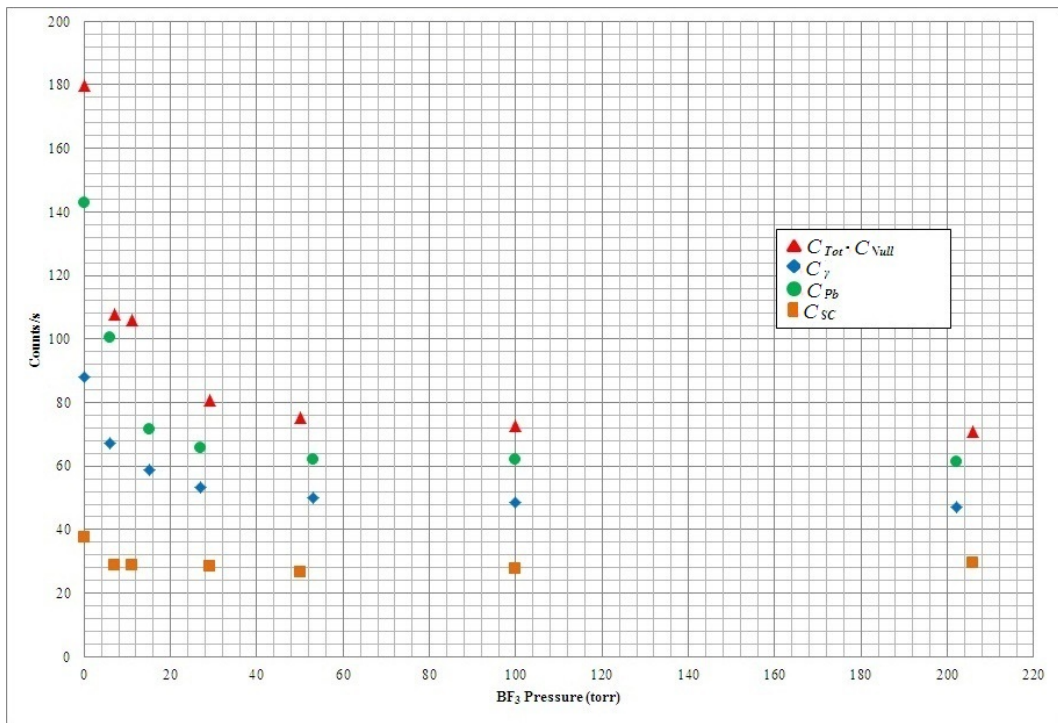


Figure 7.2-1: Counts/s values for 600 torr Xe with different pressures of BF_3 .

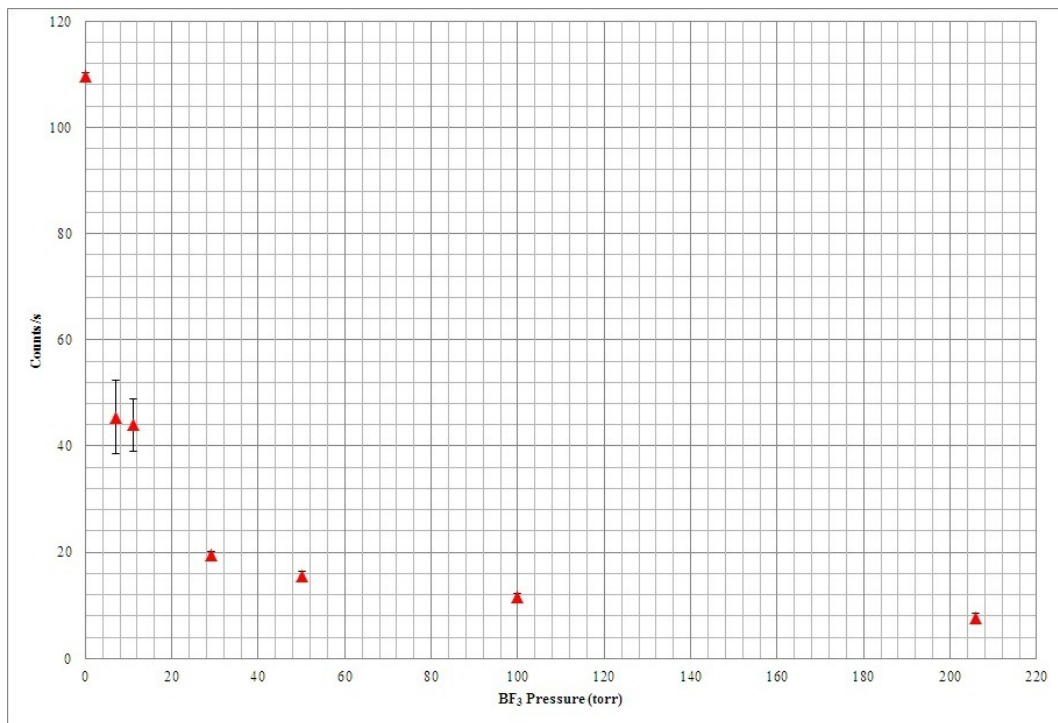


Figure 7.2-2: C_{Obs} for 600 torr Xe with different pressures of BF_3 , determined from Equation 7.2-1.

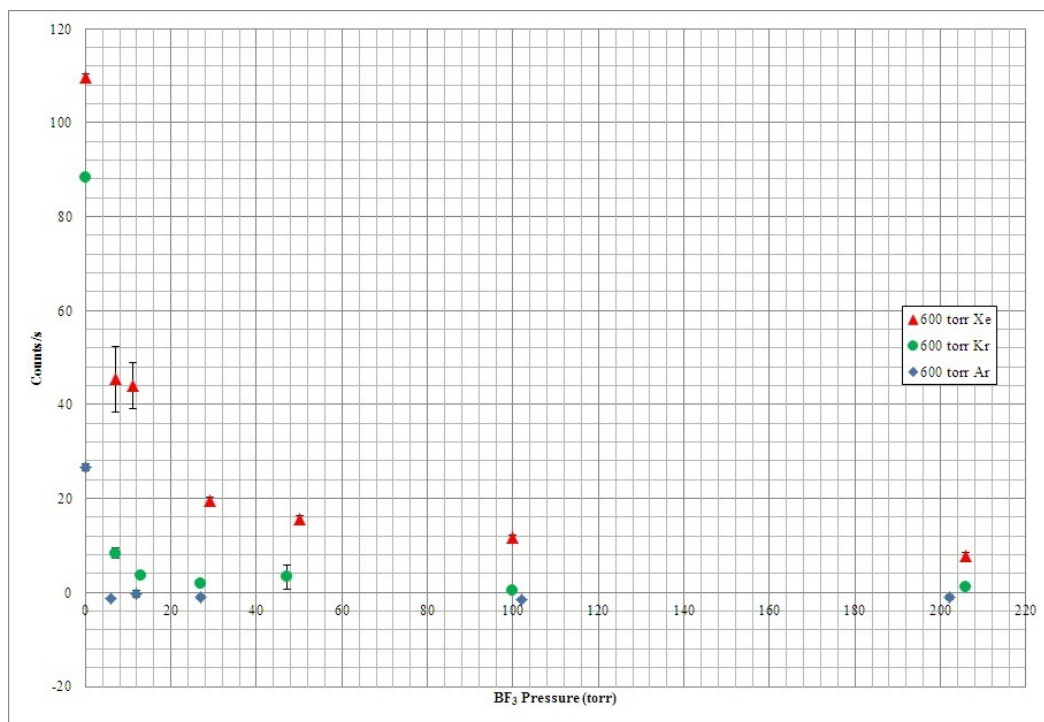


Figure 7.2-3: C_{Obs} for 600 torr Ar, Kr, and Xe with different pressures of BF_3 .

Table 7.2-1: Number of pulses observed for a variety of experimental operating conditions. Data is shown for 600 torr Xe. $t = 200$ s

BF_3 Pressure (torr)	C_{Tot}	C_{SC}	C_{Null}	C_γ	C_{Pb}
0	35990	7492	551	28609	17589
5	21529	5798	551	20105	13470
10	21213	5792	551	14287	11732
25	16146	5667	551	13162	10665
50	15054	5324	551	12390	10003
100	14532	5509	551	12387	9694
200	14154	5928	551	12240	9413

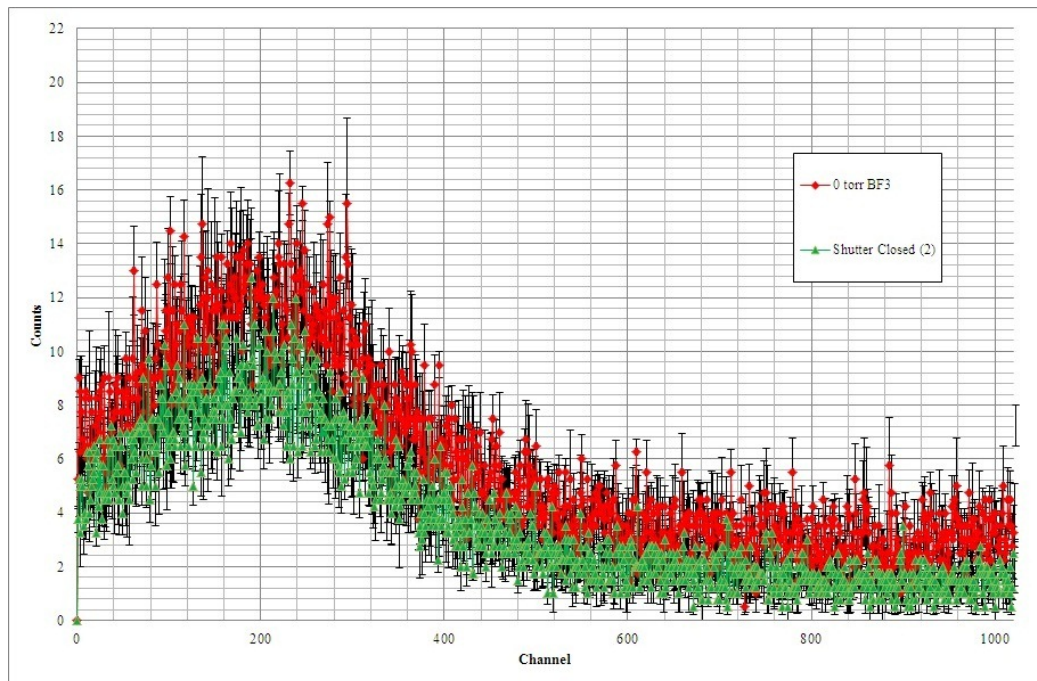


Figure 7.2-4: Pulse height distribution data for 0 torr BF_3 , 100 torr Xe. The triangles represent the PHD with the shutter closed under the same conditions

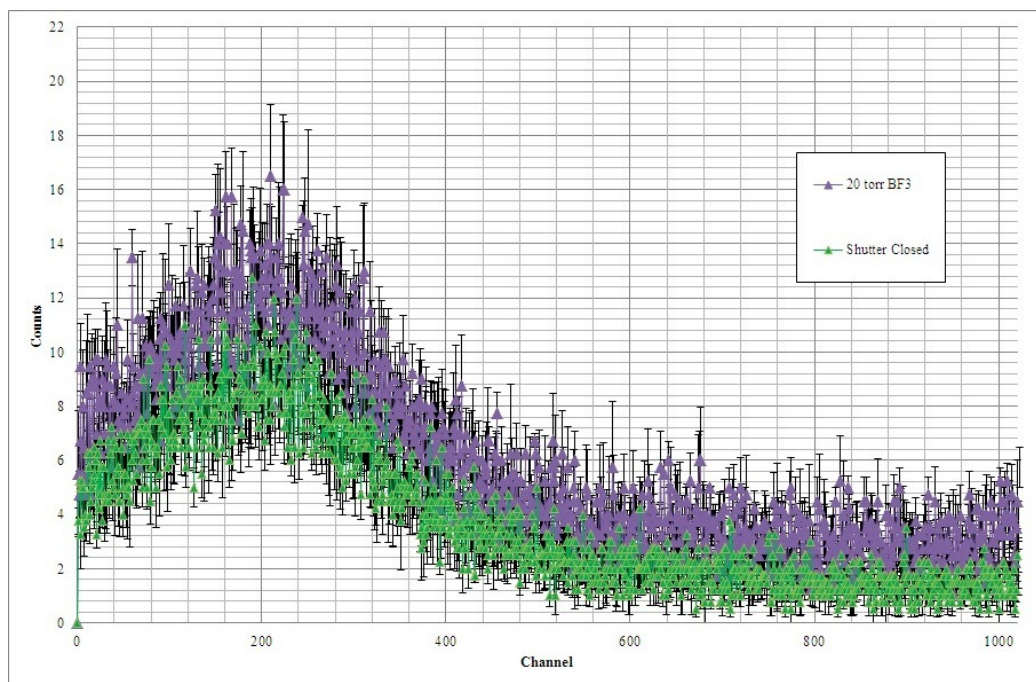


Figure 7.2-5: Pulse height distribution data for 20 torr BF_3 , 100 torr Xe. The triangles represent the PHD with the shutter closed under the same conditions

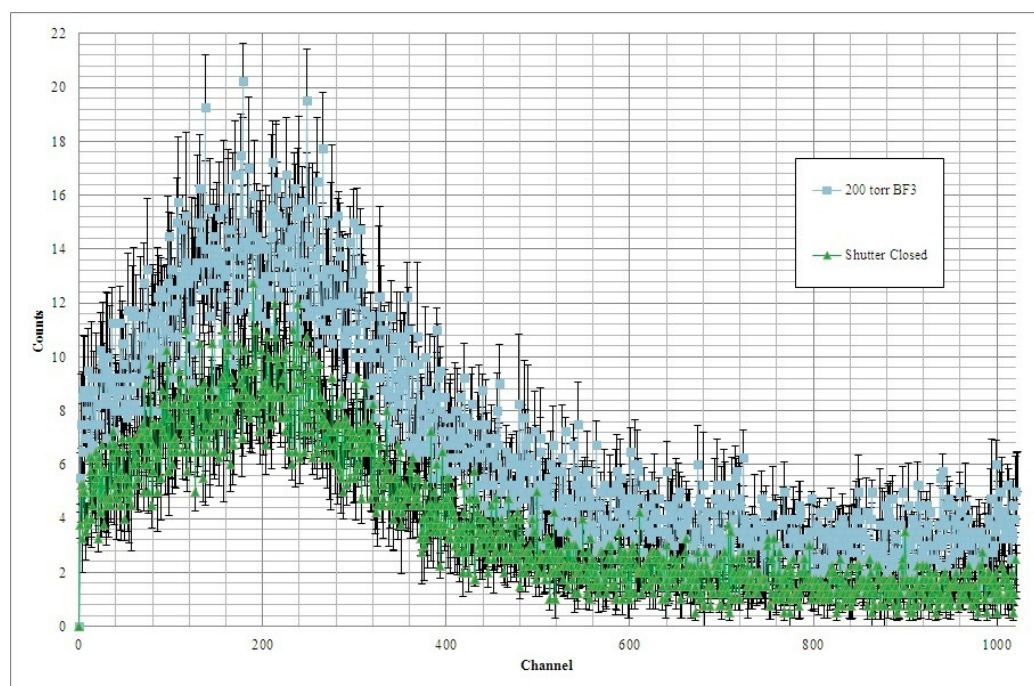


Figure 7.2-6: Pulse height distribution data for 200 torr BF_3 , 100 torr Xe. The triangles represent the PHD with the shutter closed under the same conditions

It is clear from Figures 7.2-1 and 7.2-2 that there is a significant decrease in

C_{Obs} as more BF_3 is added to the scintillation cell. These results were unexpected, and undesirable for the purposes of creating a FUV neutron detector. The exact mechanism of the signal reduction was not investigated. This behavior is not wholly unexpected for BF_3 detectors and many studies have been conducted on identifying the precise mechanism of BF_3 dissociation.

It has been widely shown that BF_3 is highly electronegative and readily dissociates into number of electronegative ions, including BF_2^- and a number of fluorine ions. This is typically why BF_3 proportional counters are lined with charcoal. There have been a number of experiments aimed at determining the mechanism behind BF_3 proportional counter deterioration.

It is common to see charged particle formation in the $^{10}\text{B}(n, \alpha)^7\text{Li}$ reaction as the alpha particles and recoil nuclei ionize in the gases filling the detector. In BF_3 detectors, these electrons attach to impurities in the gases as well as the BF_3 itself and cause recombination and dissociation. The farther electrons travel in the detector, the greater the chance for loss of electrons and more recombination and dissociation. As electrons attach to BF_3 molecules, the increase in negative charge changes the polarity of the BF_3 molecule and causes dissociation and formation of negative ions (especially highly electronegative fluorine atoms). This increase in negative ion formation causes broadening of the pulse height distributions and a decrease in count rate [83]. The more electrons lost in electron capture, the more negative ions formed, causing loss of an even greater number of electrons and resulting in the signal suppression observed in Figures 7.2-1 and 7.2-3.

Cocconi and Bistline, in separate experiments, showed that electron capture is dependent upon the mean free path of travel within the detector volume (λ) and pressure of the BF_3 . As BF_3 pressure increases, the probability of electron survival decreases, as well as the detector efficiency [83, 84].

Davis *et al* observed the deterioration of BF_3 using a mixture of BF_3 (enriched

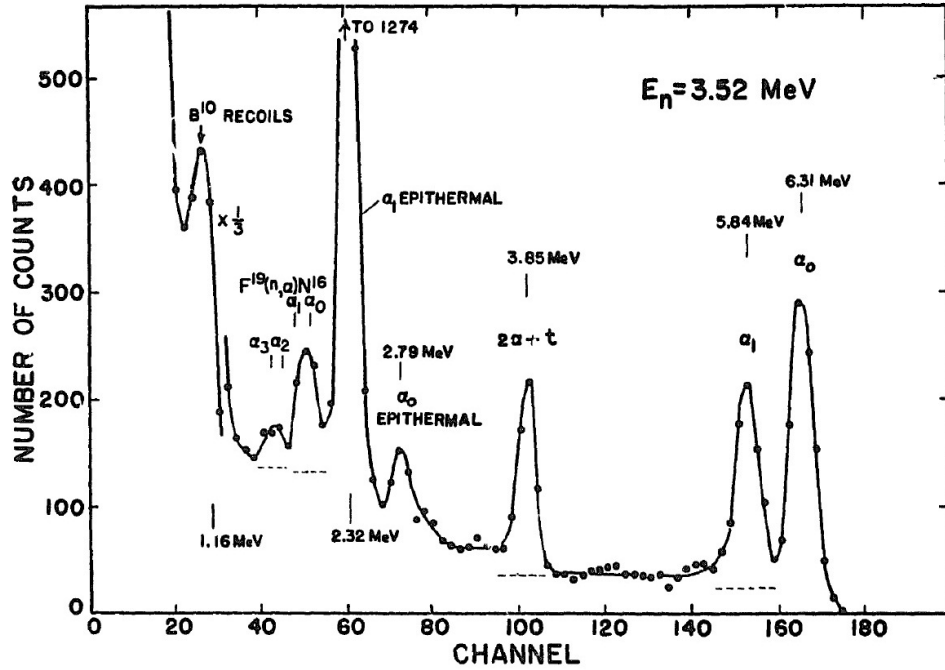
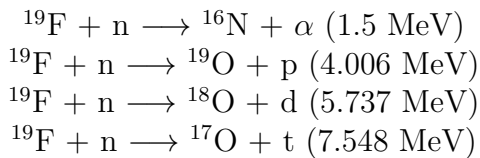


Figure 7.2-7: Pulse-height distribution data from ^{10}B enriched BF_3 after bombardment with 3.52 MeV neutrons [85]

to 96% ^{10}B) in and Argon (160 torr and 1825 torr, respectively) and subjecting it to a neutron field. They postulated that as BF_3 dissociates into ^{10}B and ^{19}F ions, neutrons react with the ^{19}F ions in the following ways:



While all of these reactions are energetically favorable, only the (n, α) and (n, p) reactions have been observed for neutron energies below 9 MeV. Figure 7.2-7 illustrates the results of dissociation with a 3.52 MeV neutron. While this study involved the observation of fast neutrons rather than thermal, these results are interesting and merit discussion.

The peaks around channels 166 and 154 are cited to be the result of ^{10}B disintegration into α particles and ^7Li in the ground state and excited state, respectively. The peaks at channels 74 and 61 correspond to the $^{10}\text{B}(n, \alpha)^7\text{Li}$ and $^{10}\text{B}(n, \alpha)^7\text{Li}^*$

reactions resulting from thermal neutrons. The peaks in channels 43 to 53, corresponding to the $^{19}\text{F}(n, \alpha)^{16}\text{N}$ reactions, show a rapidly rising tail below these peaks. This rising tail is due to the recoil of ^{10}B from elastic scatter of the neutrons. In addition, it was observed that with increasing pressures of BF_3 , the pulse-height distributions rapidly deteriorated [85].

It has been reported that impurities in the BF_3 gas are problematic in BF_3 proportional counters. A list of impurities found in the BF_3 used in the END experiments can be found in Table 4-1. Aponte and Korff has observed that if an impurity in the BF_3 gas is electronegative with an attachment probability larger than 10^{-5} , it will rapidly interact with the BF_3 gas and produce extraneous pulses due to the formation of highly negative ions. As counting rates increase, there is an observable deterioration in BF_3 proportional counters due to the production of F^- ions near the central counter wire. As the F^- ions collect, the electric field changes near the wire resulting in a decrease in pulse size [86].

Inside a glass system, including the one used at the MUTR, there is the possibility of formation of SiF_4 due to the interaction of the BF_3 with SiO_2 , the silica windows used in the MUTR excimer emission experiments [87]. To determine the rate of negative ion formation within a proportional counter (i.e. a BF_3 counter), the number of electrons at any given distance within the counter is given by:

$$n = n_0 \exp\left(\int (\alpha - \eta) dr\right) \quad (7.2-2)$$

where α is a constant, the first Townsend coefficient, and η is the number of attachments/cm made monodirectionally in the field. The number of attachments/cm is further defined as:

$$\eta = \frac{\bar{c}}{\lambda} \frac{1}{v} \frac{p}{P} h \quad (7.2-3)$$

where h is the probability that an electron will bind to the molecule it collides with, \bar{c}

is defined as the average agitational velocity of the electron, λ is the mean free path, v is the drift velocity (making $1/v$ the time needed for the electron to move 1 cm through the field), p is the pressure of the electronegative impurity in the BF_3 gas, and P is the pressure of the BF_3 gas. The term (\bar{c}/λ) is the frequency with which an electron collides in the detector. If Equation 7.2-3 is simplified to:

$$\eta = \epsilon \frac{p}{P} h \quad (7.2-4)$$

where ϵ is the total number of collisions the electrons over the course of 1 cm of travel in the counter and is defined as:

$$\epsilon = \frac{\bar{c}}{\lambda} \frac{1}{v} \quad (7.2-5)$$

The ratio of the impurity pressure to the BF_3 pressure gives the number of collisions that occur within that specific impurity.

It can be seen from Equation 7.2-3 that by increasing the pressure of the BF_3 , the pressure of the impurities within the BF_3 increases, and the number of electrons reaching the counter wire decreases and changes the PHD of the counter and leads to a decrease in the count rate.

Equation 7.2-2 then becomes:

$$n = n_0 \exp\left(\int \alpha dr - h\epsilon\left(\frac{p}{P}r\right)\right) \quad (7.2-6)$$

where n_0 was determined to be 2.93×10^6 [86].

Using the documented values of the impurities contained in the BF_3 gas obtained from Ceradyne, Inc., shown in Table 4-1, the effect of the impurities on the system can be determined. Aponte and Korff measured the effect of the addition of SO_2 into a system filled with BF_3 gas. SO_2 is a common impurity found in BF_3 , and will decompose to SO_2^- , SO^- , and O^- . Figure 7.2-8 illustrates how the addition of SO_2 impacts the efficiency of a BF_3 counter.

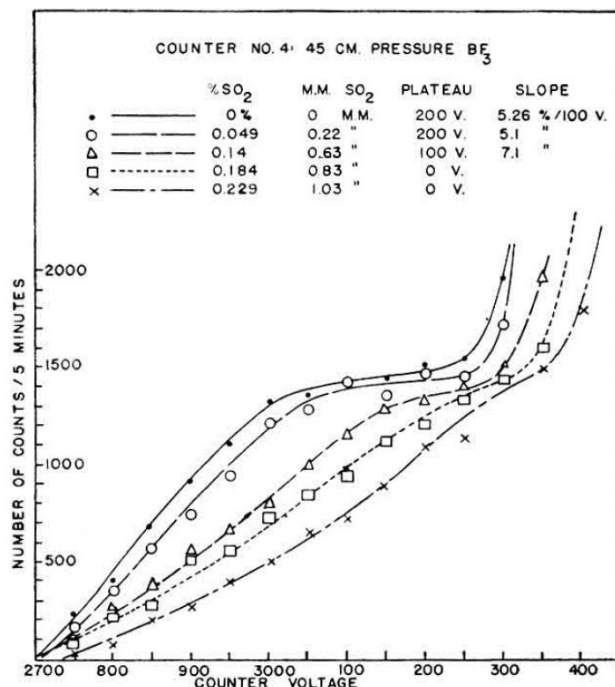


Figure 7.2-8: Effect of increasing pressures of SO_2 on a BF_3 proportional counter [86].

While the impurities in the $^{10}\text{BF}_3$ obtained from Ceradyne list the amount of SO_2 as 8.6 ppmv, it is clear that any amount of SO_2 will cause a change in the shape of the pulse-height distribution data of any BF_3 counter.

Aponte and Korff measured the change in BF_3 counters by adding increasing pressures of SiF_4 and SF_6 , shown in Figures 7.2-9 and 7.2-10 [86].

It is clear from Figure 7.2-9 that only a very small amount of SiF_4 is required to damage a BF_3 counter. Aponte and Korff discovered that as little as 0.2% SiF_4 has a severely detrimental effect on the operation of a BF_3 counter [86]. SiF_4 has a tendency to form from the interaction of BF_3 with glass systems, and it is highly probably that the interaction of the BF_3 used in the MUTR experiments interacted with the silica windows on the front and rear of the scintillation cell to produce SiF_4 [87]. Further study should be conducted to adequately assess the impact of the silica windows on the scintillation experiments.

It has been shown that SF_6 has very strong attachment and electrons with energy as low as 2 eV have been shown to form SF_6^- without causing dissociation. It is

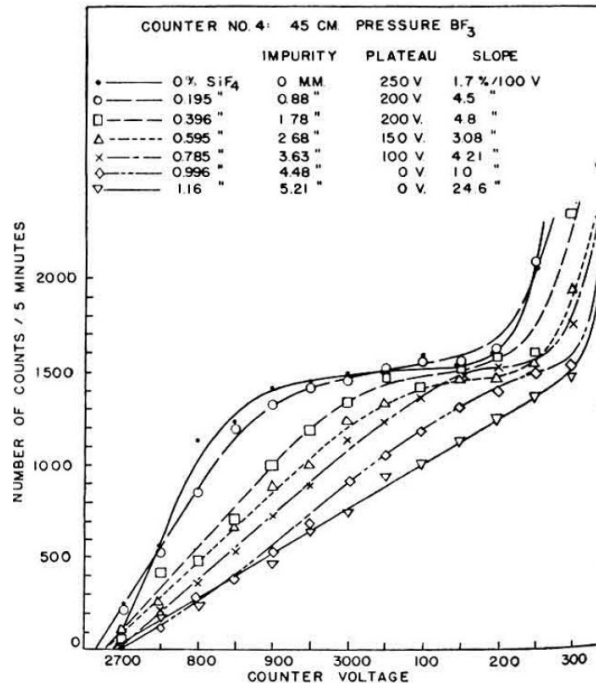


Figure 7.2-9: Effect of increasing pressures of SiF_4 on a BF_3 proportional counter [86].

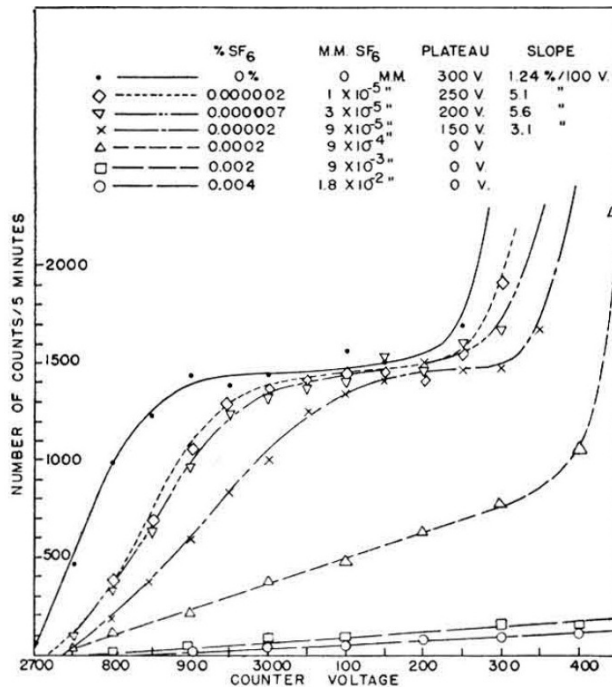


Figure 7.2-10: Effect of increasing pressures of SF_6 on a BF_3 proportional counter [86].

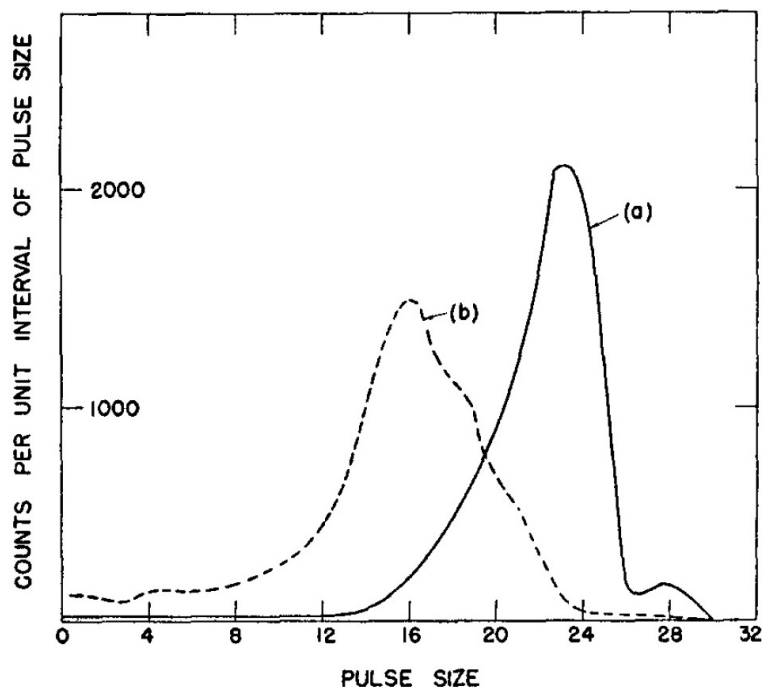
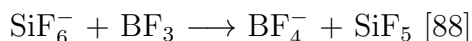


Figure 7.2-11: Pulse height distribution data for 600 torr BF_3 after (a) initial filling following 3 months of “aging” and (b) 3 weeks later[87].

unlikely that electron interaction with SF_6 causes dissociation and that the probability of the formation of SF_5^- is extremely low. Aponte and Korff calculated the value of h to be 0.958, indicating an almost absolute certainty that an electron interacting with SF_6 will attach in the first collision [86]. The probability of SiF_6^- reacting again is high and occurs via:



Fowler and Tunnicliffe have discovered that in order for a BF_3 detector to be extremely efficient, it must have a very high sensitivity which can only be obtained by using high pressures of BF_3 (>150 torr). However, it was also observed that counters with high pressures of BF_3 required “aging” for up to three months with a temporary filling of BF_3 . Without this “aging” process, Fowler and Tunnicliffe observed a marked deterioration in the PHDs that was not observed after a three month “aging” period. This is shown in Figure 7.2-11.

The BF_3 used in the MUTR scintillation experiments was not allowed to soak in

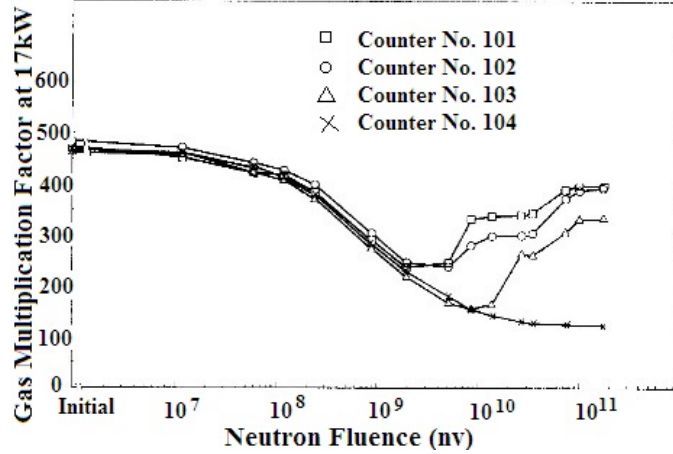
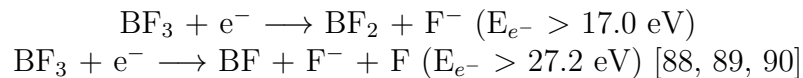


Figure 7.2-12: Degradation and recovery of gas multiplication as a result of extended operation in a 10^4 nv neutron field [89].

the scintillation cell for any amount of time. The BF_3 gas remained in the scintillation cell only as long as data collection required and was immediately flushed from the system. It merits further study to observe whether soaking the system for up to three months has any effect on the pulse-height distribution data.

Tomoda and Fukakusa studied the deterioration of BF_3 counters in intense radiation fields, and while the neutron fluence coming out of the MUTR through the thermal column collimator access plug can by no means be considered intense, it is interesting to note that with increasing neutron fluence, the gas multiplication factor deteriorates (Figure 7.2-12) [89].

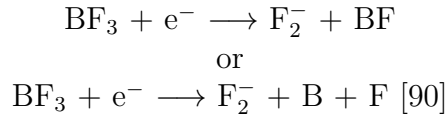
Tomoda and Fukakusa determined that the observed degradation in detector operation was due to the dissociation of BF_3 molecules that occur as the electrons produced through ionization interact with the BF_3 gas and cause recombination and dissociation through:



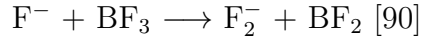
The kinetic energy distributed among the fragments of these two reactions is 3.3 ± 0.2 and 7.9 ± 0.3 eV, respectively, indicating that the second reaction is more probable because it does not require internal excitation [90].

Fluorine atoms have a very strong affinity for electrons and quickly recapture electrons produced in the primary ionization event. The ions produced by the capture of the electrons produce fluorine ions that have a very high probability of recombination with positive ions, forming additional complexes within the detector. These new fluorine complexes are chemically reactive and may be easily removed from the system using a charcoal lining [89].

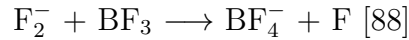
Additionally, F_2^- ions may form as BF_3 interacts with electrons via:



which leaves 3.8 ± 0.3 eV of energy behind, or from the reaction:



The latter reaction is endothermic by 5.6 ± 0.2 eV and unlikely to thermodynamically occur owing to an additional 2 eV more energy required [90]. The F_2^- then reacts with the BF_3 via:



MacNeil and Thynne postulate that in rare instances, it is possible for an electron to interact with a BF_3 molecule, but not cause dissociation. This occurs via:



This reaction has not been definitively observed, however MacNeil and Thynne maintain that it is a possible reaction pathway [90].

Without knowing exactly what is happening inside the BF_3 scintillation cell, it is difficult to accurately provide an explanation for the observed signal suppression. However, it is highly probably that either the BF_3 molecules or the trace impurities, specifically SO_2 and SiF_4 , are dissociating upon interaction with the electrons

produced in the ionization event and are recombining with the electronegative ions formed through dissociation, leading to loss of ionization and the observed decrease in signal. Further experiments should be conducted to identify the mechanism of dissociation within the cell, as well as experimenting with different linings of the scintillation cell, especially charcoal. It should also be investigated as to whether the trace amounts of HF in the BF_3 gas are causing trace etching of the SiO_2 windows, releasing the SiO_2 molecules and further damaging the efficiency of the detector. Unfortunately, those experiments were beyond the scope of this research.

At this time, conclusions cannot definitively be drawn as to the efficacy of $^{10}\text{BF}_3$ as a neutron detector material for excimer scintillation. It is likely that once the dissociation into electronegative ions is understood, it can be controlled, and the potential for BF_3 in these detectors will likely improve.

Chapter 8

Carbon Foam Experiment

Following the conclusion of the BF_3 experiments, an opportunity presented itself to perform experiments on a number of reticulated vitreous carbon (RVC) foam samples coated with natural boron carbide (B_4C). These RVC foams were obtained from Dr. Chris Lavelle at the John's Hopkins University Applied Physics Lab.

Vitreous carbon is a low density material, with low thermal expansion and high resistance to corrosion, which makes it highly favorable as a material in neutron detection [91]. Of particular interest for the END experiments are the open-pore, honeycomb structure and extremely high void volume. This porous structure, in theory, should allow reaction products from the ^{10}B reaction to escape the RVC structure and migrate through the noble gas background, increasing the expected number of excimer photons the photomultiplier tube detects.

8.1 Reticulated Vitreous Carbon Foam

The carbon foam used for the END experiments is developed by Duocel[®]. The properties of various pore sizes (PPI) are shown in Table 8.1-1. Duocel[®] claims the matrix structure “is completely repeatable, regular, and uniform,” and “has a controlled density of carbon per unit volume,” so the uncertainties in the pore density and pore size are considered negligible [92]. For the purposes of all calculations involving the RVC foam, uncertainties lie within reasonable parameters and are limited to known or estimated values. The measured uncertainty in the mass of the B_4C coating on each foam sample is approximately 0.0001 mg, or 0.1 μg . Properties of Duocel[®] carbon

foam of 3% nominal density are shown in Table 8.1-2 [92].

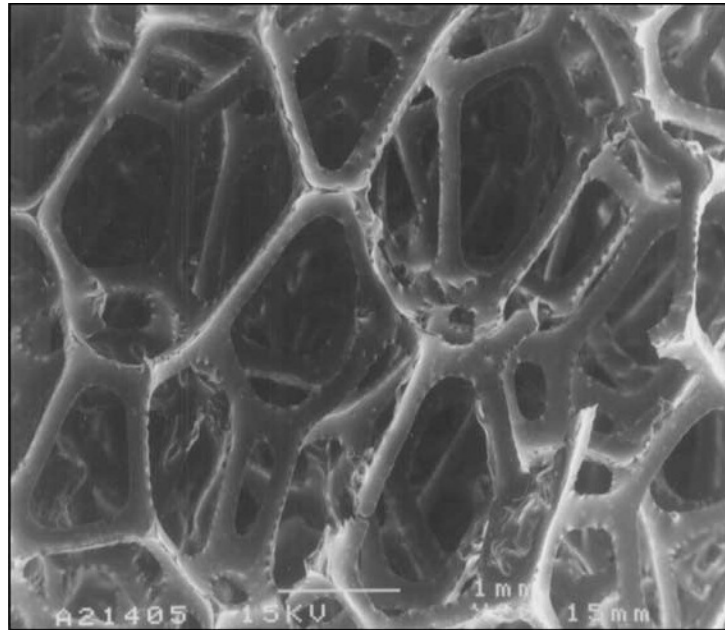
First developed by Chemtronics International in Ann Arbor, Michigan in 1976, the past several decades has witnessed an increased interest in RVC, specifically for electronic applications [93]. Its low density, low thermal expansion, high resistance to corrosion, and high thermal and electrical conductivities make it suitable in a wide variety of applications, from three-dimensional electrodes, high temperature insulation, semiconductor manufacture, and has even been used in reactor shutdown, decommissioning, and decontamination activities of nuclear reactors. In the latter application, RVC is used primarily for the removal of ^{137}Cs [91]. Reticulated vitreous carbon is typically manufactured by polymerization of a resin such as polyurethane or a phenolic resin (occasionally furfuryl and epoxy resins are used) mixed with forming agents. This is followed by drying and curing at 120°C and carbonization at $700\text{-}1100^\circ\text{C}$. The end result is a low volume, disorganized porous carbon with a continuous skeletal structure with approximately 30% linear shrinkage. The low electrical resistance RVC is reported to have between 90% and 97% free void volume depending on the pore size [91, 93, 94]. A Scanning Electron Microscope (SEM) image of a 30 PPI sample is shown in Figure 8.1-1.

Table 8.1-1: Properties of various pore sizes of the carbon foam used in the END experiments. All samples listed are 2.54 cm square with 0.64 cm thickness [95].

Pores per Inch (PPI)	5	10	20	45
Density (g/cm^3)	0.06	0.06	0.06	0.06
RVC mass (mg)	246	246	246	246
RVC Surface Area (cm^2)	18.4	36.9	73.7	111
B_4C Mass (mg)	37	74	148	333
^{10}B Mass (mg)	5.5	14	28	63
RVC + B_4C Total Mass (mg)	288	566	1132	2547

Table 8.1-2: Properties of Duocel[®] of 3% nominal density, as claimed by the manufacturer [92].

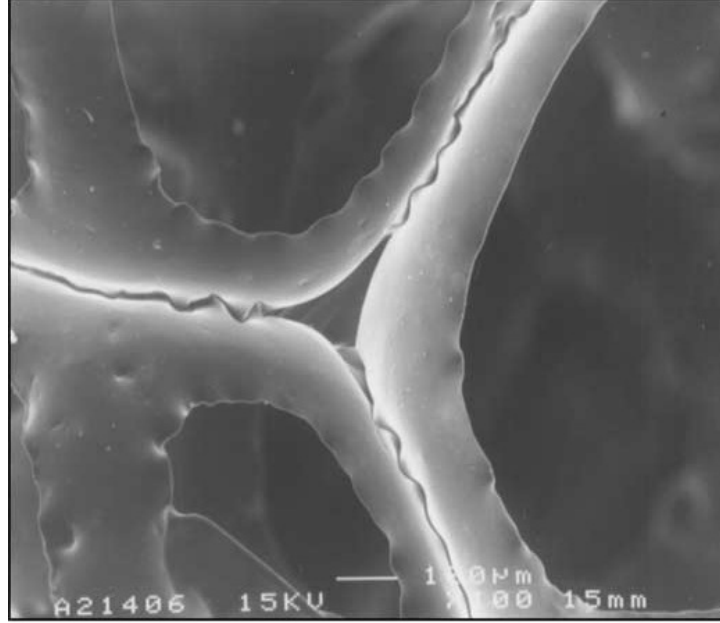
Compression Strength	15-75 psi (775-3878 torr)
Tensile Strength	25-50 psi (1292-2585 torr)
Shear Strength	4.4×10^3 psi (2.27×10^5 torr)
Mohs Hardness	6-7 Mohs



1 mm ———

Figure 8.1-1: SEM micrograph of 30 PPI RVC sample [91].

The honeycomb structure visible in Figure 8.1-1 is composed of tetrahedral strands of carbon known as struts. The replication of this tetrahedral strut arrangement gives the rigidity characteristic to the structure of RVC. Duocel These struts are shown in Figure 8.1-2 for a 30 PPI RVC sample. Imaging from SEM has shown that the struts vary considerably in length and width in any given sample, so uniformity is not completely guaranteed. As the pore per inch (PPI) grade increases, the struts become shorter and thinner. The dimensions of a typical 10 PPI and 30 PPI RVC sample are listed in Table 8.1-3.



100 μm —

Figure 8.1-2: SEM micrograph of strut of 30 PPI RVC sample [91].

Table 8.1-3: Dimensions of the physical characteristics of RVC foams, as determined from SEM micrographs [91].

Pores per Inch (PPI)	10	30
Strut length (mm)	0.810	0.686
Strut thickness (mm)	0.316	0.160
Trigonal strut radius (mm)	0.225	0.157
Trigonal strut area (mm^2)	0.159	0.077

8.2 Experimental Procedure

The experimental procedure was very similar to that of the BF_3 experiments. The carbon foam sample was placed in the aluminum sample holder positioned at a 45° angle with respect to the incident neutron beam to increase the path length of the beam by a factor of $\sqrt{2}$. This cylinder was held in place by a groove in the Conflat flange on the bottom of the cube. The rest of the scintillation cell remained the same.

The sample was positioned in-line with the neutron beam and evacuated to a base pressure on the order of 10^{-7} torr. Before the reactor was brought on-line, measurements were collected with the reactor off to obtain background data on PMT noise

and dark current, as well as background reaction radiation levels (P_{Null}). Because the shroud covering the windows to eliminate ambient light from reaching the PMT

scintillation cell, the shutter open with the same lead brick in front of the scintillation cell (C_{Pb}), the shutter closed with a 0.1984-cm sheet of boral blocking the scintillation cell, and the shutter open with the same sheet of boral in front of the scintillation cell (C_γ). These measurements were obtained in order to determine the excimer scintillation yield as a result of neutron events, rather than non-neutron events.

Table 8.2-1 lists the different pulse observations for the 45 PPI coated carbon foam sample. Plots of C_{Obs} (determined from Equation 7.2-1) and its components are shown in Figures 8.2-1 through 8.2-6 for the coated samples carbon foam samples. A comparison of all the values of C_{Obs} is shown in Figure 8.2-7.

Table 8.2-1: Number of pulses observed for a variety of operating conditions. Data is for 45 PPI coated sample ($4 \mu\text{m } ^{10}\text{B}$ thickness) in a xenon environment.

Noble Gas Pressure (torr)	C_{Tot}	C_{SC}	C_{Null}	C_γ	C_{Pb}
0	10427	6065	535	13733	9656
95	24489	6971	535	16493	13013
200	26207	7012	535	19069	11979
396	37483	8281	535	35271	18023
615	5405	11232	535	45047	23759
805	64357	13080	535	62308	28948

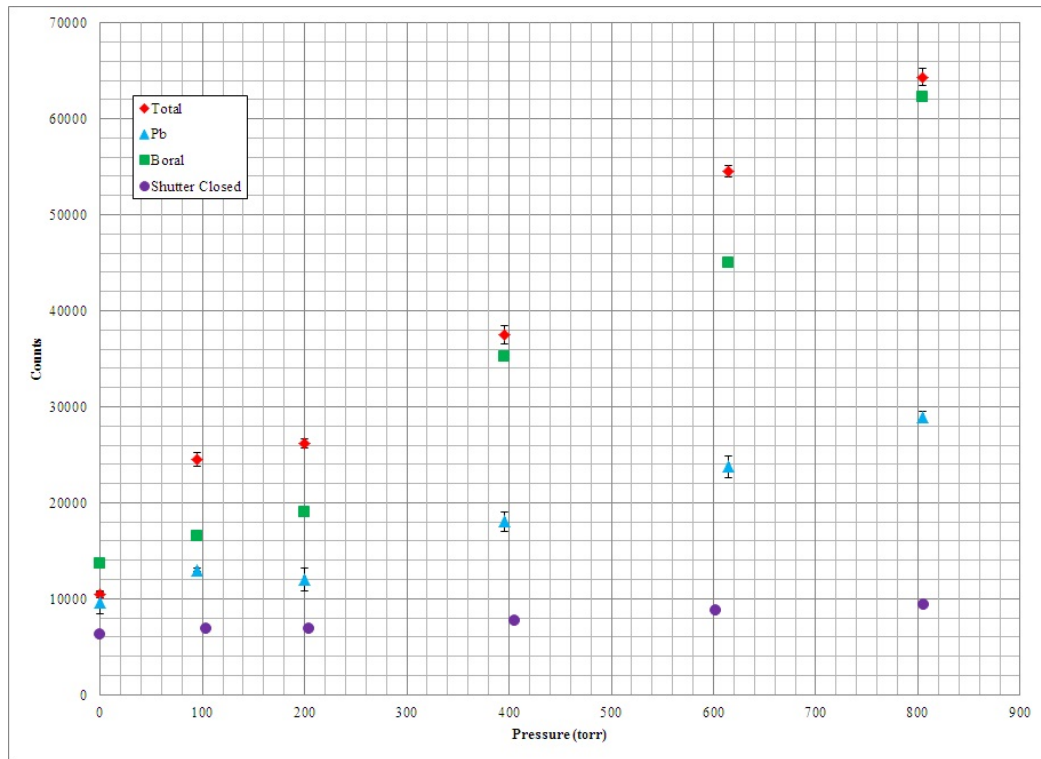


Figure 8.2-1: Total pulse values for 45 PPI coated sample ($4 \mu\text{m}^{10}\text{B}$ thickness) with increasing pressures of Xe.

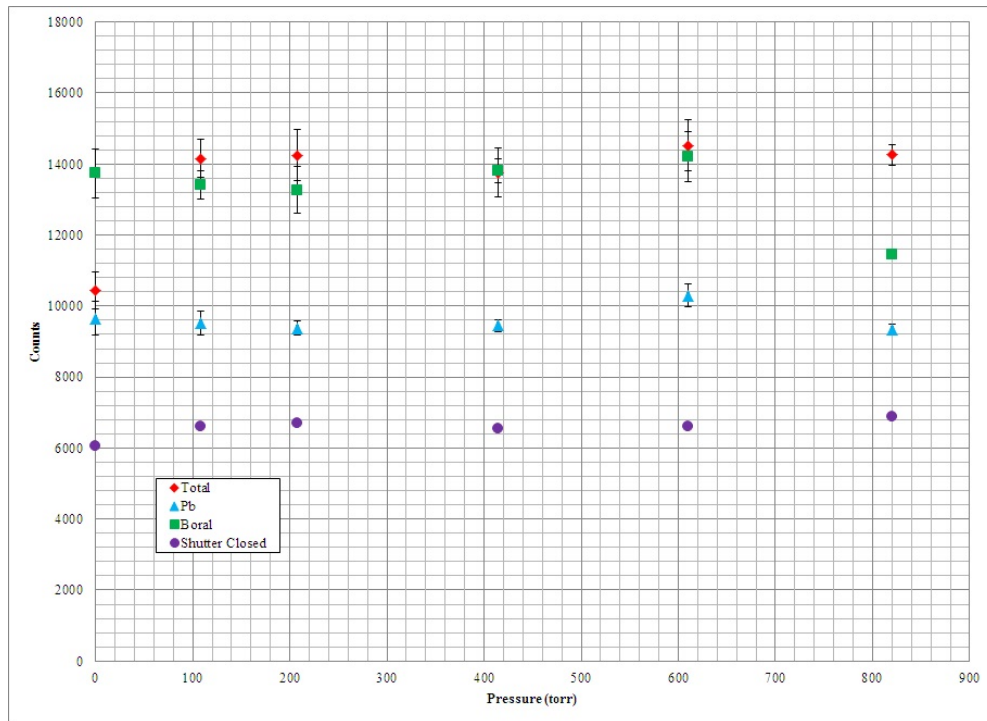


Figure 8.2-2: Total pulse values for 45 PPI coated sample ($4 \mu\text{m}$ ^{10}B thickness) with increasing pressures of Ar.

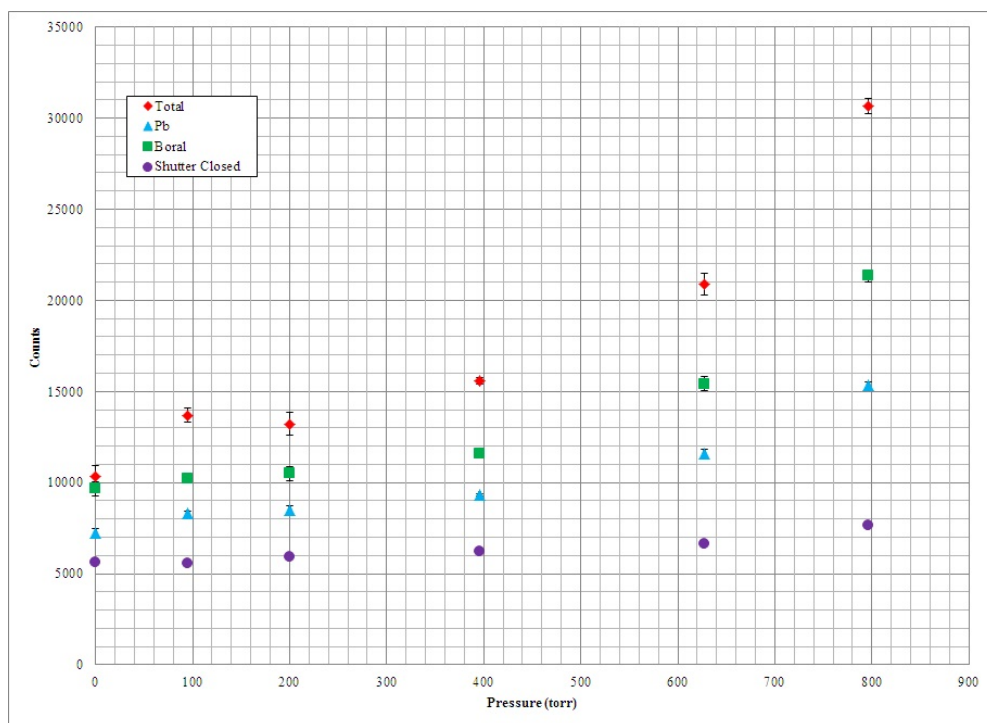


Figure 8.2-3: Total pulse values for 30 PPI coated sample ($8.3 \mu\text{m}$ ^{10}B thickness) with increasing pressures of Xe.

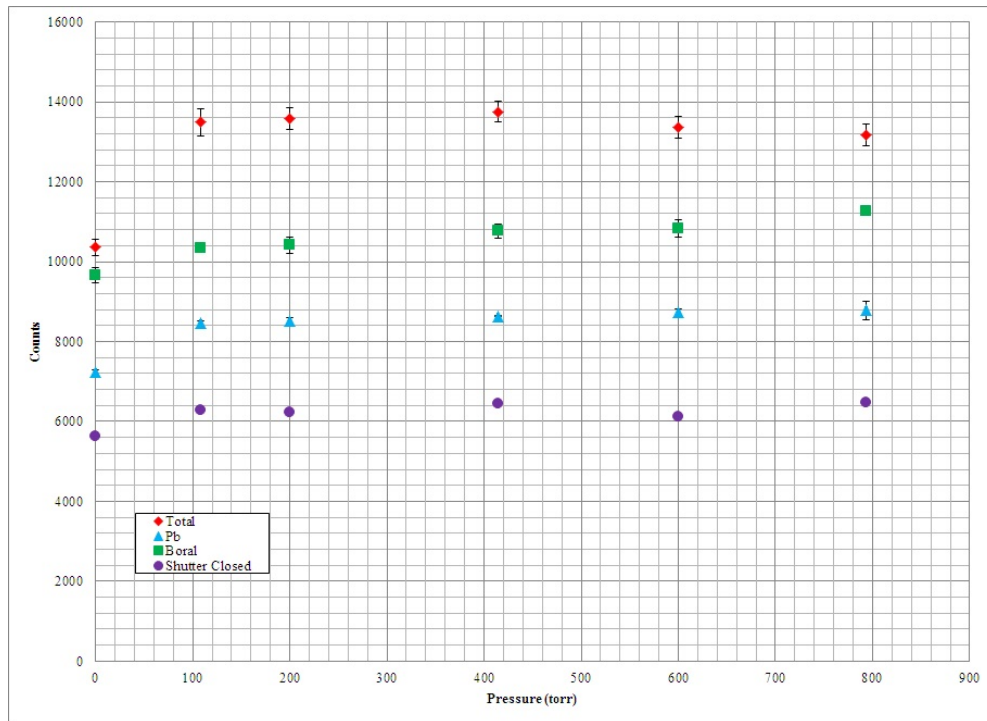


Figure 8.2-4: Total pulse values for 30 PPI coated sample ($8.3 \mu\text{m } ^{10}\text{B}$ thickness) with increasing pressures of Ar.

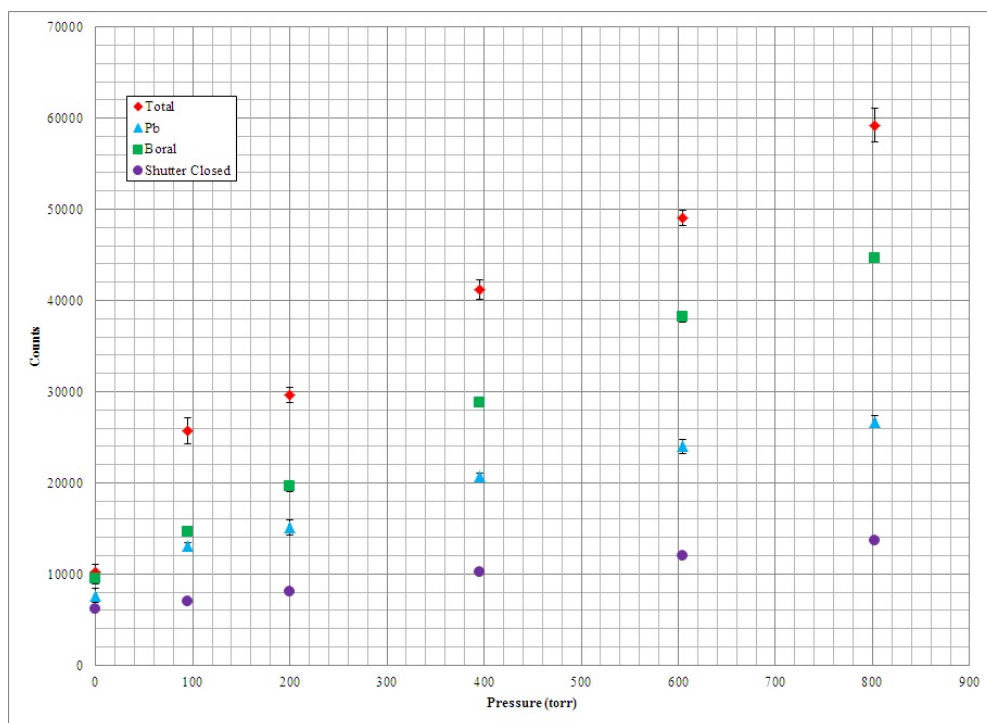


Figure 8.2-5: Total pulse values for 20 PPI coated sample ($8.7 \mu\text{m } ^{10}\text{B}$ thickness) with increasing pressures of Xe.

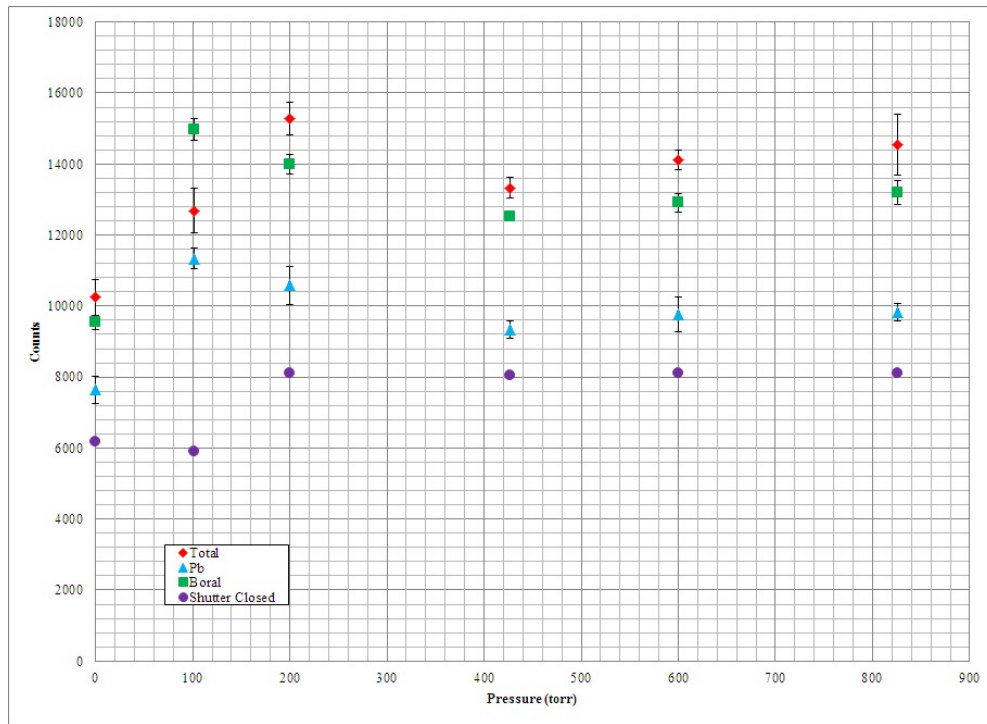


Figure 8.2-6: Total pulse values for 20 PPI coated sample ($8.7 \mu\text{m}$ ^{10}B thickness) with increasing pressures of Ar.

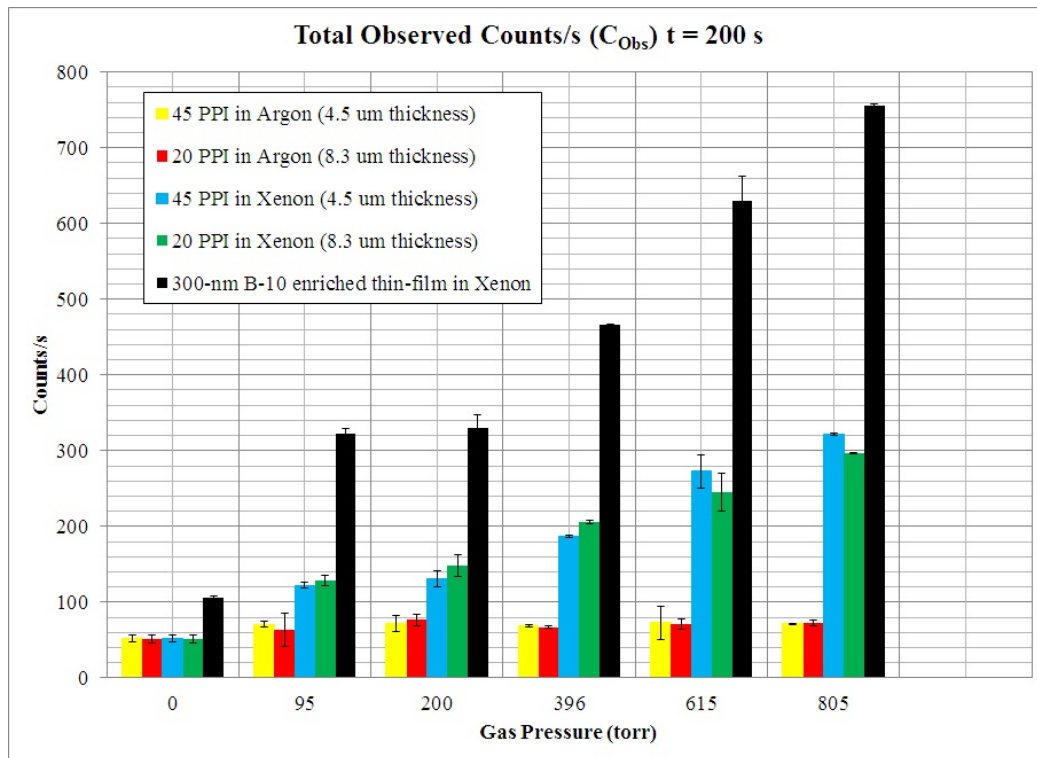


Figure 8.2-7: Comparison of C_{Obs} .

In addition to coated carbon foam samples, uncoated samples of each pore size (45, 30, and 20 PPI) were also irradiated in order to determine the actual signal produced, and potentially determine whether some of the observed gamma signal with the lead brick positioned in front of the scintillation cell was due to internal gamma rays produced as the ${}^7\text{Li}^*$ decays to ground state and emits a gamma ray. The results of C_{Obs} as a result of thermal neutrons for each coated sample compared with the C_{Obs} for each uncoated sample are shown in Figures 8.2-8 through 8.2-13.

It is interesting to observe that, regardless of whether the sample was coated or uncoated, the gamma signal was approximately the same ratio of the total observed signal, indicating that most of the gamma signal observed is due to gamma radiation from the core. There is little evidence to definitively determine that the gamma signal is the result of gamma ray interactions within the cell as a result of the ${}^{10}\text{B}$ reaction.

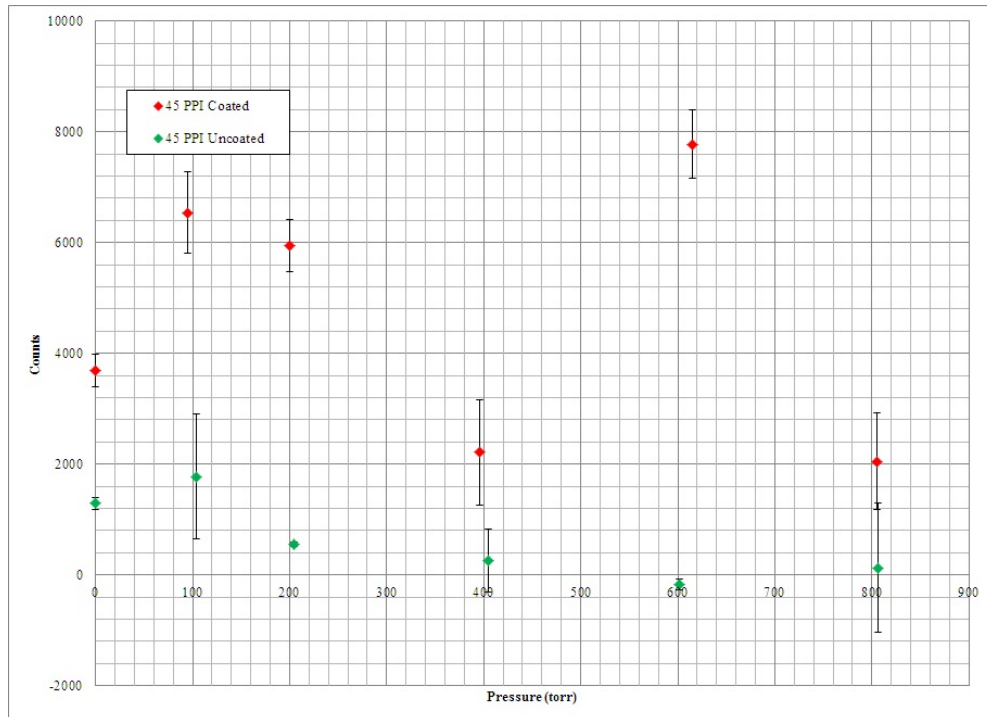


Figure 8.2-8: Comparison of coated and uncoated 45 PPI signals as a function of Xe gas pressure.

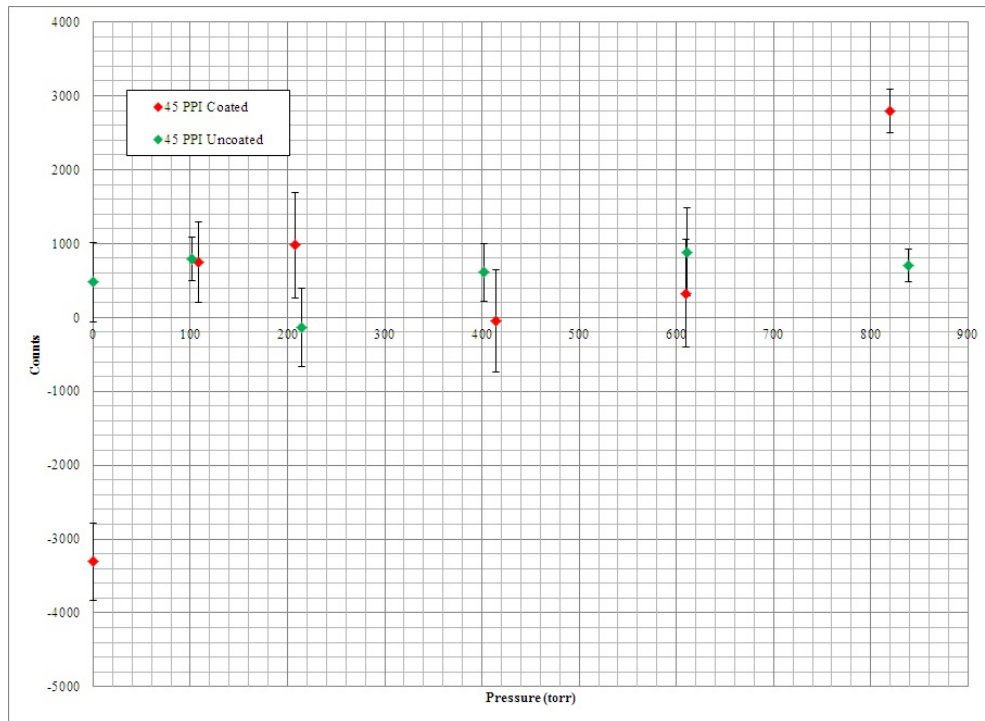


Figure 8.2-9: Comparison of coated and uncoated 45 PPI signals as a function of Ar gas pressure.

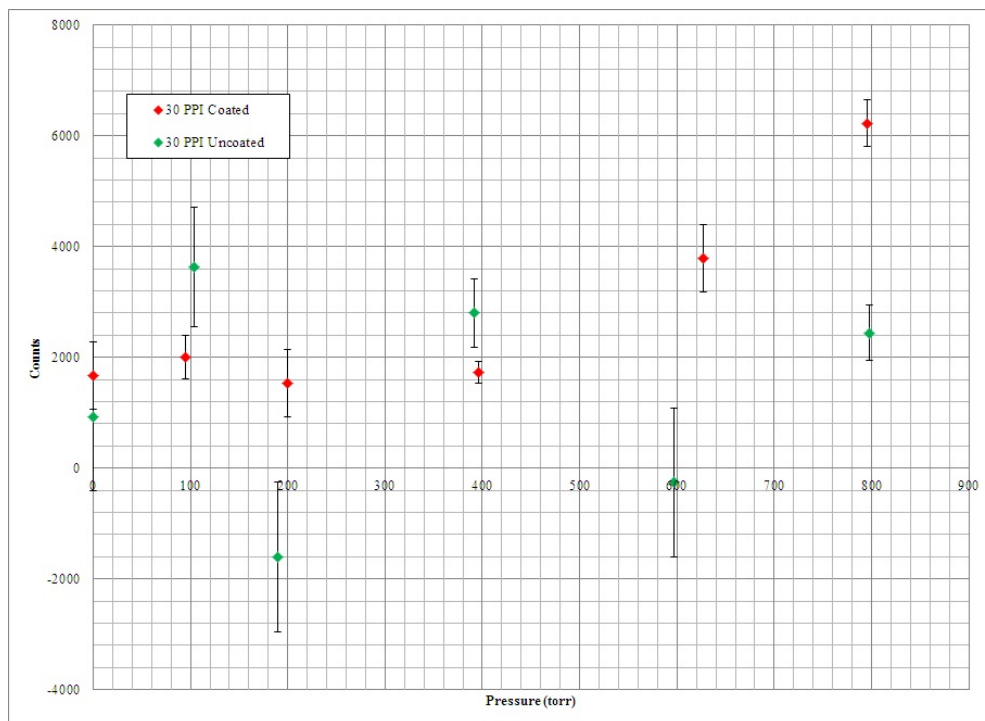


Figure 8.2-10: Comparison of coated and uncoated 30 PPI signals as a function of Xe gas pressure.

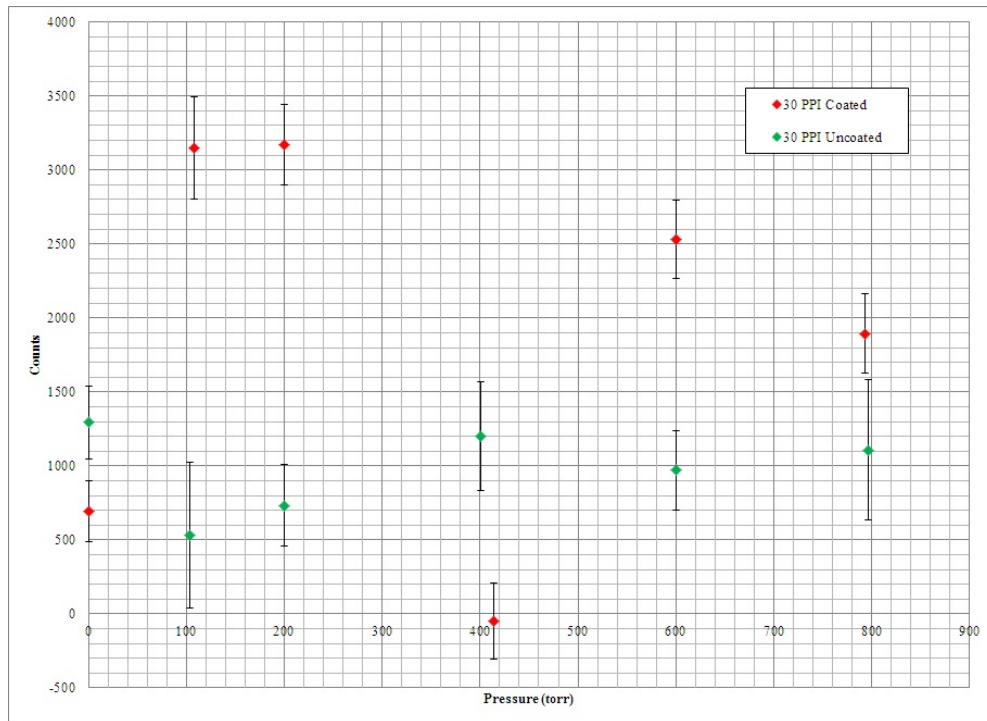


Figure 8.2-11: Comparison of coated and uncoated 30 PPI signals as a function of Ar gas pressure.

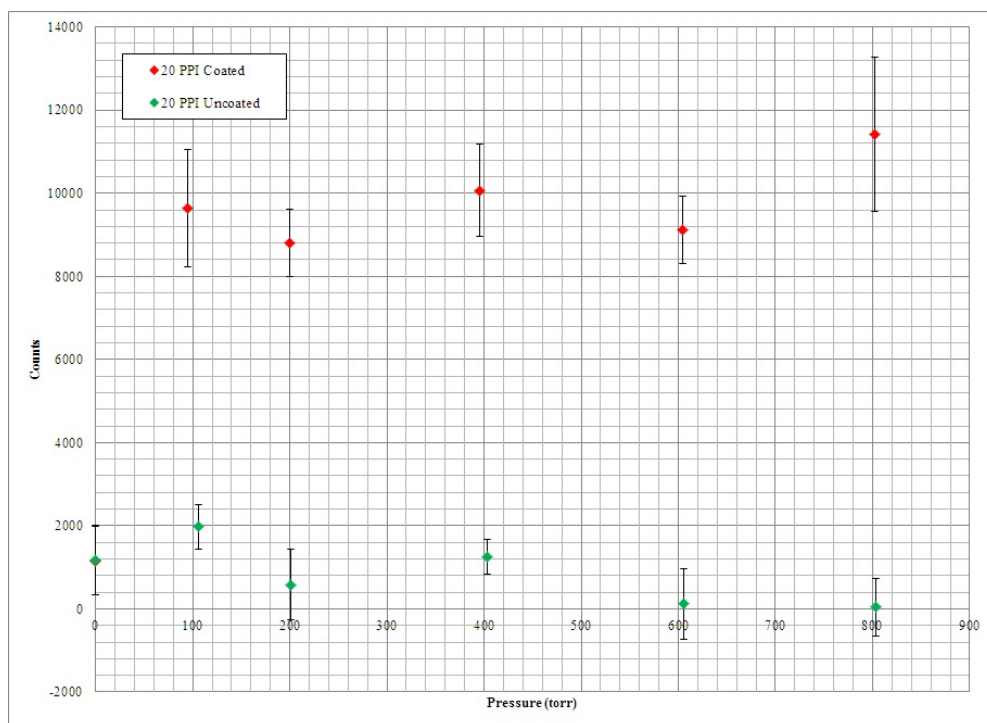


Figure 8.2-12: Comparison of coated and uncoated 20 PPI signals as a function of Xe gas pressure.

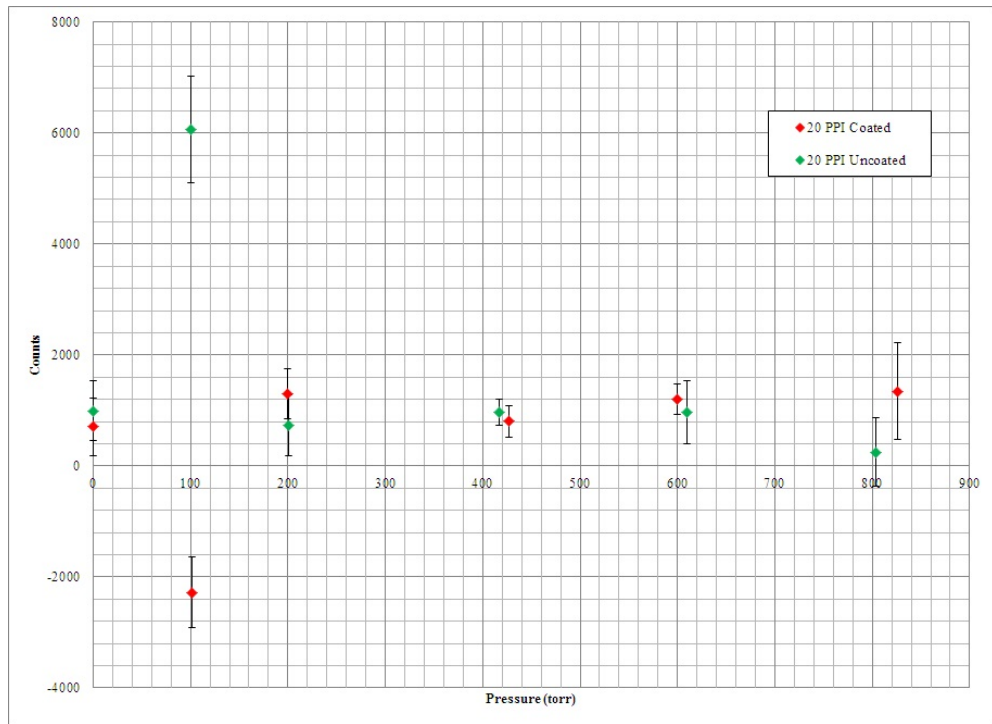


Figure 8.2-13: Comparison of coated and uncoated 20 PPI signals as a function of Ar gas pressure.

Chapter 9 FUND Results

9.1 Excimer Scintillation Yield

Scintillation yield, the number of excimer scintillations detected per neutron absorbed, is an important factor for determining the optimal conditions of a scintillation detector, including geometry, collection efficiency, and ability of the detector to discriminate between different types of radiation (gamma and neutron). The excimer scintillation yield from the $^{10}\text{B}(n, \alpha)^7\text{Li}$ reaction was measured as a function of gas type, pressure, and amount of ^{10}B present. It is defined by the equation:

$$Y = \frac{G_{Cell}}{N_{Target}} \quad (9.1-1)$$

where N_{Target} is the neutron absorption rate in the BF_3 gas or the reticulated vitreous carbon foam (defined by Equation 6.1-18), and G_{Cell} is the excimer photon generation rate within the scintillation cell, defined by:

$$G_{Cell} = \frac{C_{Obs}}{(\epsilon_{PMT})(\epsilon_{Cell})t} \quad (9.1-2)$$

In this equation, C_{Obs} is the number of excimer photons observed as pulses from the PMT, ϵ_{PMT} is the intrinsic efficiency of the photomultiplier tube (1.6% for Ar, 2.2% for Kr, and 3.1% for Xe), ϵ_{Cell} is the collection efficiency of the scintillation apparatus, and t is the photon count rate (200 s) [54]. The PMT efficiency and the scintillation cell collection efficiency define the number of photons generated in the scintillation cell that are detected by the PMT. The scintillation cell collection efficiency has been discussed as part of a previous project and will be discussed briefly [54].

The value of ϵ_{Cell} is based on the collection efficiency of the scintillation cell:

$$\epsilon_{Cell} = \frac{\text{\#radiation incident on detector}}{\text{\#radiation emitted by source}} \quad (9.1-3)$$

This equation takes into account all photons, not just those that produce a detectable pulse. Another assumption that factored into the determination of ϵ_{Cell} was that all photons are emitted isotropically from the exact center of the RVC foam target [54]. This assumption is only valid if all incident neutrons interact with the center of the target and requires that the 4-mm aperture be perfectly positioned with the center of the target. This does, however, allow for the approximation of ϵ_{Cell} as a point source:

$$\epsilon_{Cell} = \frac{\Omega}{4\pi} = \frac{1}{2} \left(1 - \frac{d}{\sqrt{d^2 + a^2}} \right) \quad (9.1-4)$$

where Ω is the solid angle spanned by the detector, d is the distance from the source to the photocathode (8.58 cm), and a is the radius of the photocathode (1.15 mm) [54]. Further assumptions were made to determine the value of $\langle \epsilon_{Cell} \rangle$, including uniformity within the photon emission volume (i.e. approximating it as a hemisphere), uniform distribution of photon emission, the assumption that further reflections within the cell are minimal and therefore insignificant, and that travel through the MgF_2 window to reach the PMT did not alter the path of the photon [54]. Based on this work, it was determined that the value of ϵ_{Cell} was 0.5115% with an uncertainty of 9.69% [54].

This calculated value of ϵ_{Cell} is used with caution in the determination of Y for a number of reasons. The major concerns center around the lack of complete characterization of the carbon foam samples and the sample holder, which is different than the sample holder used in the ^{10}B thin-film experiments. The sample holder for the RVC was an uncoated aluminum cylinder that did not extend to the top of the scintillation cell as the Ebonol C[®] sample holder did. Thus, the reflectivity of the sample holder is expected to change, although this information is unavailable and should be assessed as part of future work. It is also uncertain as to the mechanism of excimer emission from the RVC foam, which is expected to differ from the ^{10}B

thin-films, owing to the large void fraction of the foam compared to the solid-state sample and the lower enrichment of ^{10}B . It is anticipated that the value of ϵ_{Cell} will not change significantly once these unknowns have been accounted for, so this value will be used in all yield calculations, though these yields will simply be considered estimates and will not be asserted to be quantitatively known.

The value of G_{Cell} was determined using the electronics package associated with the photomultiplier tube. Total photon count rates were collected for a period of 200 s, and the number of excimer pulses were determined using a separate series of consecutive measurements, given by Equation 7.2-1.

Because G_{Cell} is the product of several variables, the total uncertainty in G_{Cell} is found by propagating the standard deviations through Equation 9.1-2:

$$u(G_{Cell}) = \sqrt{\left(\frac{u(C_{Obs})}{C_{Obs}}\right)^2 + \left(\frac{u(\epsilon_{PMT})}{\epsilon_{PMT}}\right)^2 + \left(\frac{u(\epsilon_{Cell})}{\epsilon_{Cell}}\right)^2 + \left(\frac{u(t)}{t}\right)^2} \quad (9.1-5)$$

where the values of $u(\epsilon_{PMT})$ and $u(\epsilon_{Cell})$ were quantitatively determined through the photomultiplier tube calibration and simulation of the scintillation cell efficiency, respectively, and $u(C_{Obs})$ is due solely to counting statistics. The relative uncertainty in Y ($u(Y)$) was determined in a similar method:

$$u(Y) = \sqrt{\left(\frac{u(G_{Cell})}{G_{Cell}}\right)^2 + \left(\frac{u(N_{Target})}{N_{Target}}\right)^2} \quad (9.1-6)$$

and $u(N_{Target})$ is found from the uncertainties of each factor in Equation 6.1-18:

$$u(N_{Target}) = \sqrt{\left(\frac{u(\hat{n}(t))}{\hat{n}(t)}\right)^2 + \left(\frac{u(\eta)}{\eta}\right)^2 + \left(\frac{u(\rho_{Tgt})}{\rho_{Tgt}}\right)^2 + \left(\frac{u(M_{235})}{M_{235}}\right)^2 + \left(\frac{u(\rho_{235})}{\rho_{235}}\right)^2 + \left(\frac{u(M_{Tgt})}{M_{Tgt}}\right)^2} \quad (9.1-7)$$

Uncertainty values of the factors in Equation 9.1-7 are listed in Table 9.1-1. The

determined values of $u(Y)$ falls in the 68% confidence interval, which corresponds to the standard uncertainty, $1-\sigma$.

Table 9.1-1: Uncertainty values for various parameters in Equation 9.1-1.

Factor	Description	u (%)	Source
n_{hv}	Excimer photon counts	0.5-7	Scintillation measurements
ϵ_{PMT}	PMT efficiency	3.49	PMT calibration
ϵ_{Cube}	Cell collection efficiency	9.69	Modeling
t_{hv}	Count time	—	
$\hat{n}(t)$	Fitted neutron counts	1.5-5	Fission chamber measurements
η	$^{10}\text{B}/^{235}\text{U}$ thermal cross-section ratio	2.61	Analysis of cross-sections from [77]
ρ_{BF3}	Cross-sectional density of BF_3 target	7.8	
ρ_{B10}	Cross-sectional density of ^{10}B target	10	Neutron imaging
ρ_{RVC}	Cross-sectional density of RVC target	1.5	[92]
ρ_{235}	Cross-sectional density of ^{235}U deposit	0.5	[75]
M_{BF3}	Molar mass of ^{10}B in BF_3	—	
M_{235}	Molar mass of ^{235}U	—	
M_{RVC}	Mass of ^{10}B on RVC sample	1.73	
m_{RVC}	Mass of RVC	3	[92]
$m_{RVC,B4C}$	Mass of B_4C on RVC sample	1.73	Mass of sample before/after coating at APL
ζ	Self-absorption factor	—	[52]
μ	Transmission fraction	—	Transmission calculation

9.1.1 $^{10}\text{BF}_3$ Excimer Scintillation Yield

From Equation 9.1-1, it is possible to determine the excimer scintillation yield as a function of gas type and pressure for the BF_3 experiments. These results are shown in Figure 9.1.1-1 and numerical values appear in Table 9.1.1-1.

Table 9.1.1-1: Excimer scintillation yield (Y) values for 600 torr Xe

BF_3 Pressure (torr)	Y
0	—
5	200
10	75.7
25	25
50	11.6
100	5.1
200	2.7

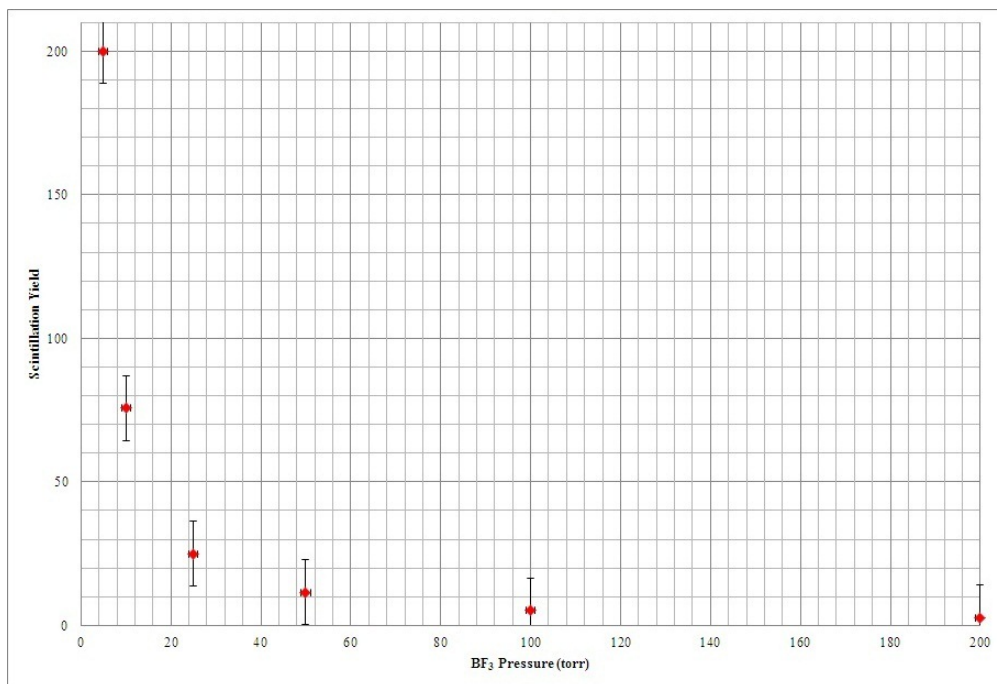


Figure 9.1.1-1: Scintillation yield from $^{10}\text{B}(n, \alpha)^7\text{Li}$ in 600 torr Xe with increasing pressure of BF_3 .

As with the values of C_{Obs} shown in Figures 7.2-2 and 7.2-3, the excimer scintillation yield values decrease with increasing BF_3 pressure. At the time of this writing, the exact mechanism of this signal reduction remains unknown, although it is apparent that with the current detector configuration, the $^{10}\text{BF}_3$ gas will not work as a medium for excimer-based neutron detection.

9.1.2 Reticulated Vitreous Carbon Foam Excimer Scintillation Yield

Better success was had with the carbon foam experiments than with the BF_3 experiments, however, it is clear from the comparison of the components of C_{Tot} that the gamma signal is quite significant. As discussed in Section 6.3, gamma rays up to 4 MeV energy have been observed coming out of the reactor core, and it is known that as gamma ray energy increases, the ability of lead to attenuate the gamma radiation decreases. Lead is sufficient to attenuate up to 2 MeV gamma rays, but drops off significantly at higher energies, so there is incomplete gamma shielding and some higher energy gamma rays are still entering the scintillation cell. The thickness of lead used during the course of these experiments is sufficient to attenuate roughly 60% of the lower energy gamma rays coming out of the thermal column, but it is insufficient to attenuate higher energy gamma rays. Therefore, the value of C_{Pb} is higher than the value obtained from the difference between C_{Tot} and C_γ . Better gamma ray shielding is required to determine the true signal derived from thermal neutron events.

From Equation 9.1-1, it is possible to determine the excimer scintillation yield as a function of gas type and pressure for the RVC foam experiments. The results of RVC foam experiments are shown in Figures 9.1.2-1 and 9.1.2-2.

The excimer emission yields appear to decrease with increasing pore size. It has been demonstrated that charged particle reaction products from the $^{10}\text{B}(n, \alpha)^7\text{Li}$ reaction lose less energy in thin films compared to thick films, enabling a higher probability of detection in thinner films. While the pore sizes are larger in the 20 PPI sample than the 45 PPI sample, the B_4C coating is nearly twice as thick as the 45 PPI sample. The thicker B_4C deposit may simultaneously cause the reaction products from the ^{10}B reaction to lose more energy and not reach the photon detector.

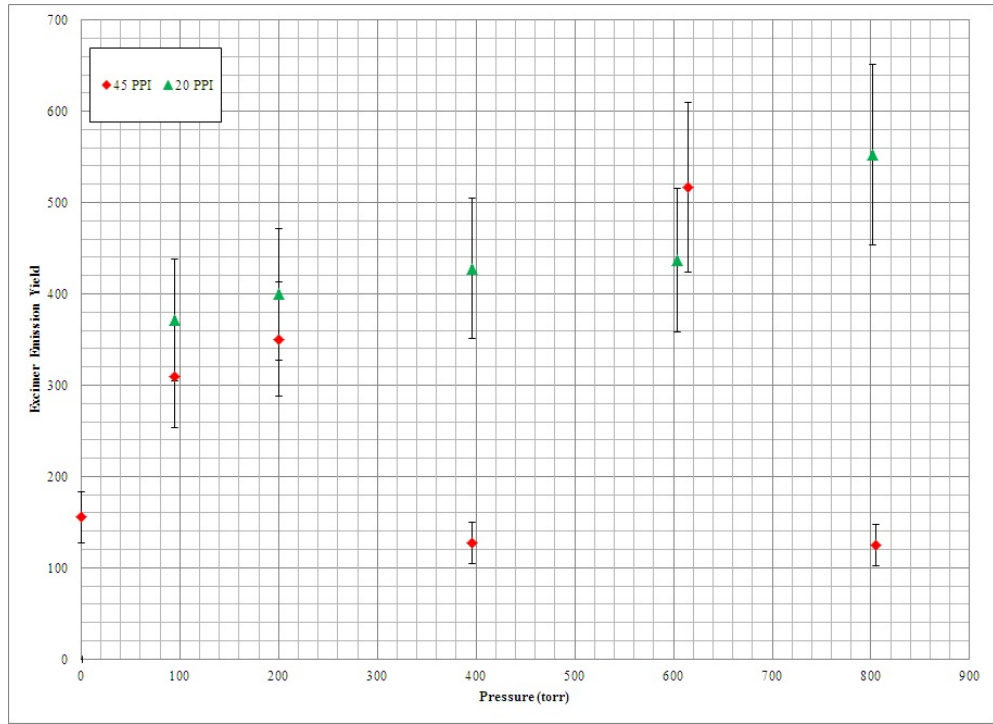


Figure 9.1.2-1: Scintillation yield from $^{10}\text{B}(n, \alpha)^7\text{Li}$ in different thicknesses carbon foam as a function of Xe pressure.

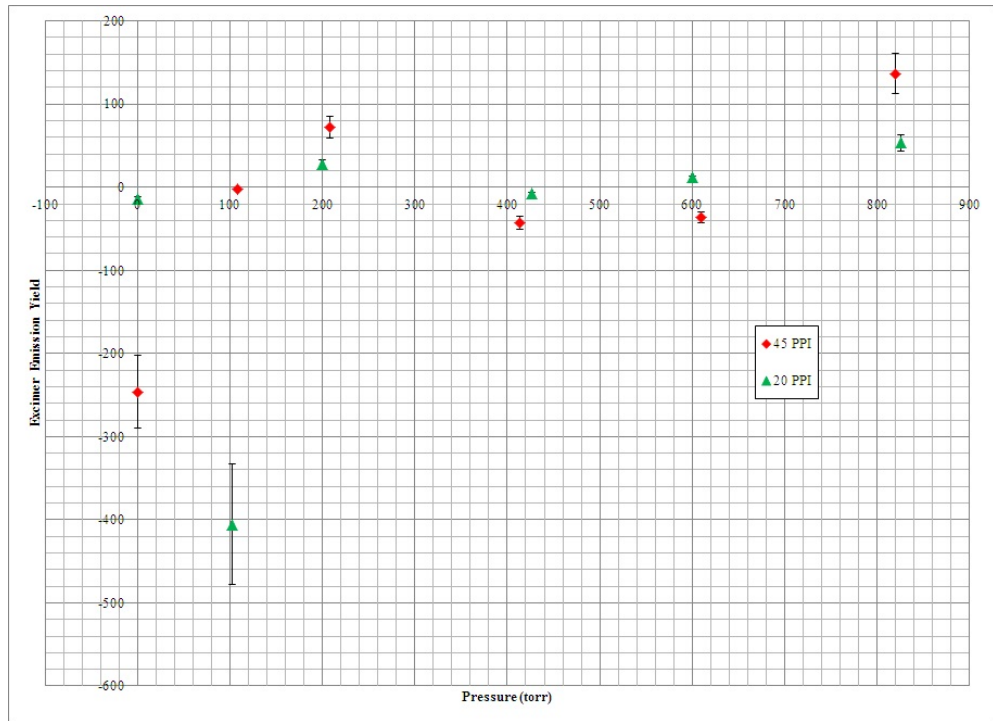


Figure 9.1.2-2: Scintillation yield from $^{10}\text{B}(n, \alpha)^7\text{Li}$ in different thicknesses carbon foam as a function of Ar pressure.

It appears that the yields for Ar are smaller and more inconsistent than for Xe, indicating that Xe is far superior as a noble gas background. Interestingly, the results obtained for the coated and uncoated 30 PPI foam were virtually identical. Attempts were made to re-run the 30 PPI coated sample, however, the sample, after remaining intact through gentle handling and insertion into the scintillation cell, crumbled with no provocation during alignment with the 4-mm aperture. It appears that the sample was either mislabeled (being uncoated as opposed to coated, explaining the similarity between the two samples) or flawed, and no conclusions can be drawn from those results.

9.1.3 ^{10}B Thin-Film Excimer Scintillation Yield

In order to determine the potential efficacy of RVC foam as a neutron detection medium, a 300-nm ^{10}B enriched thin-film was run to compare against the RVC. This film was selected due to a previous set of experiments which indicated that the highest excimer scintillation yield observed for any thin-film and any noble gas pressure was at approximately 300 torr Xe. The ^{10}B enriched thin-films were fabricated as part of a set of previous experiments outlined in [54] and will not be discussed in this writing. The results of this thin-film experiment will not be assessed in relation to the previously defended results, but are instead used to assist in the determination of the viability of RVC foam as a neutron detection medium.

X-ray photoelectron spectroscopy (XPS) was used to assess the chemical composition of the thin-film surfaces to determine the stability and resistance to oxidation [54]. This was performed on samples exposed to atmosphere for 3.5 months as well as a sample kept in an N_2 environment. Slight changes were observed and it was reported that the ^{10}B enriched thin-films were highly resistant to oxidation effects from exposure to atmospheric conditions, however studies did not extend beyond 3.5 months at atmospheric pressure. The 300-nm thin-film was found sitting at atmo-

spheric pressure for a period of time of approximately 9 months, so XPS should be performed again to determine if the content of the nitrogen and oxygen have continued to change. Further increase in the concentration of these surface contaminants could indicate the thin-films are not as stable in atmospheric pressure as previously believed. The results for the 300-nm thin-films are summarized in Table 9.1.3-1.

Table 9.1.3-1: Concentrations in % and observed energy peaks of surface contaminants in 300-nm thin-film in N₂ environment and exposed to atmospheric pressure for 3.5 months [54].

Sample	Boron	Nitrogen	Oxygen	Carbon
300 (N ₂)	78.94/187.7	0.44/401.5	7.03/531.8	13.58/284.8
300 (air)	77.86/187.5	0.72/400.5	8.18/531.7	13.24/284.8

Neutron imaging, originally performed on the samples to determine the consistency of the thermal neutron absorption properties, and X-ray diffraction, performed to assess the crystallinity of the boron thin-films, should be performed again to determine if and how these properties change as the thin-film sample ages. It is not expected that the boron content of the thin-film changes with age, however surface properties like unwanted contaminants or oxidation could change the absorptive properties of the film. The results of the 300-nm ¹⁰B enriched thin-film appear in Table 9.1.3-2. These results are shown in Figure 9.1.3-1.

It is worth noting that again the difference between C_{Tot} and C_{γ} is different than the observed value of C_{Pb} . As previously mentioned, this is likely due to the lack of sufficient attenuation of higher energy gamma rays coming out of the reactor. The value of C_{Obs} , determined from background measurements and the signal from C_{γ} obtained through use of the 0.1984-cm boral sheet is shown in Figure 9.1.3-2 and the excimer scintillation yield is shown in Figure 9.1.3-3. A comparison of the excimer scintillation yield of the RVC foam to the ¹⁰B-enriched 300-nm thin-film is shown in Figure 9.1.3-4.

Table 9.1.3-2: Number of pulses observed for a variety of operating conditions. Data is for 300-nm ^{10}B enriched thin film in a xenon environment.

Noble Gas Pressure (torr)	P_{Tot}	P_{SC}	P_{Null}	P_{γ}	P_{Pb}
0	21210	12056	358	18241	15046
102	64556	13080	358	30099	36540
205	66106	14914	358	40218	38566
401	93177	17573	358	61258	46627
600	126033	21575	358	83512	58604
801	151151	24303	358	105659	69515

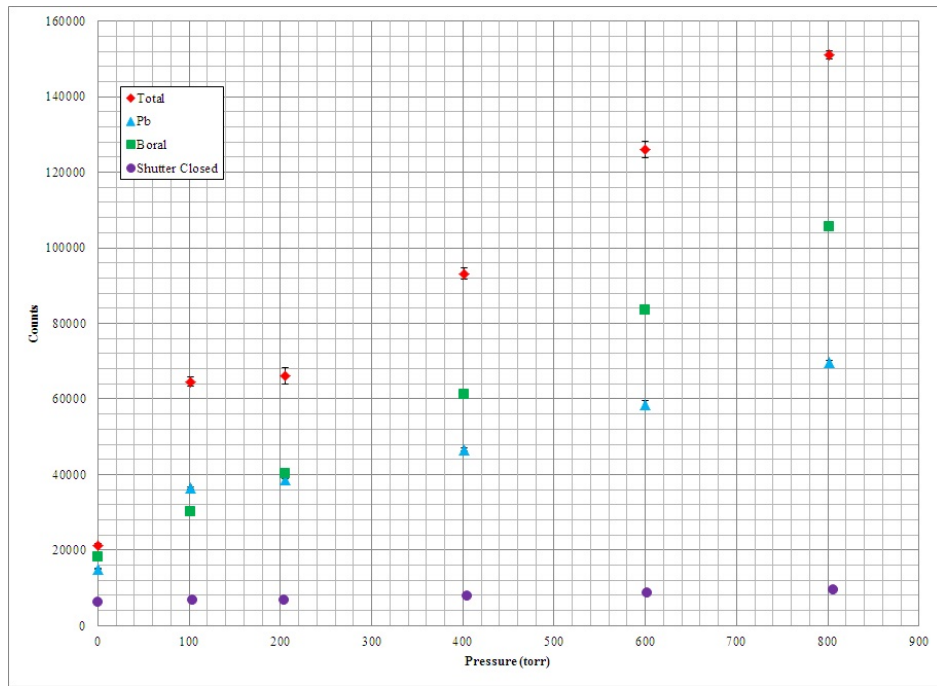


Figure 9.1.3-1: Components of N_{Obs} , determined from Equation 7.2-1, observed for 300-nm ^{10}B enriched thin-film as a function of xenon pressure. Data taken for 200 s at 200 kW reactor power.

The observed yield for the 300-nm thin-film is significantly larger than that observed for either the 20 PPI or 45 PPI coated RVC foam, indicating that carbon foam may not be as ideally suited as a neutron detection medium under current ^{10}B enrichment conditions. The apparent high gamma sensitivity and low excimer yield will likely, at least with the samples studied in this thesis, not create the type of neutron detector that is the goal of Excimer-based Neutron Detection Research.

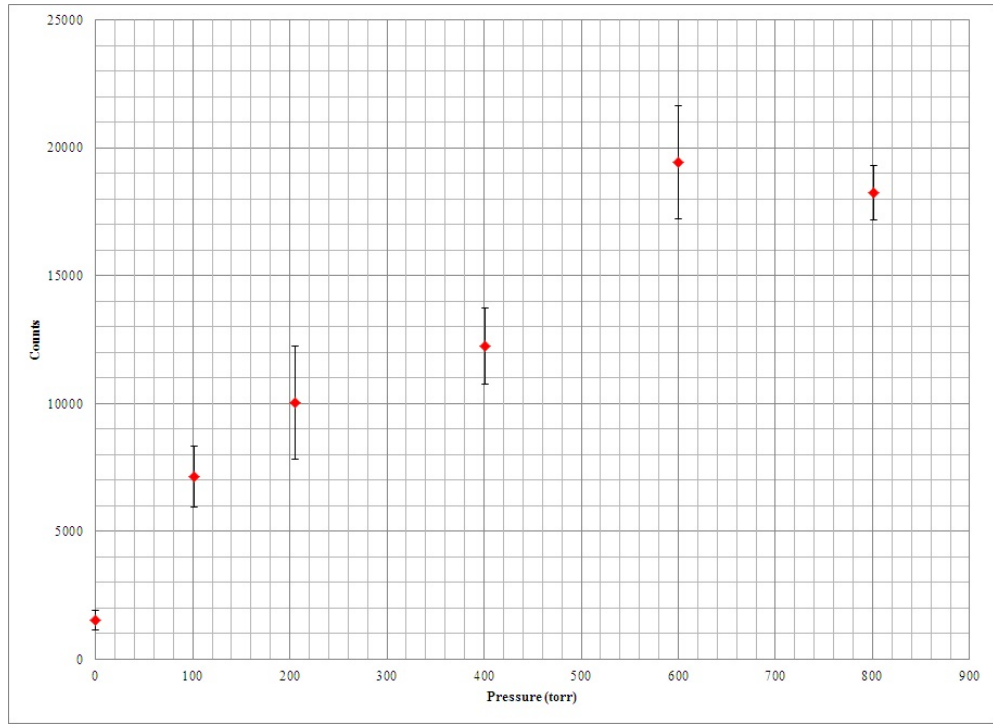


Figure 9.1.3-2: C_{Obs} , determined from Equation 7.2-1, observed for 300-nm ^{10}B enriched thin-film as a function of xenon pressure. Data taken for 200 s at 200 kW reactor power.

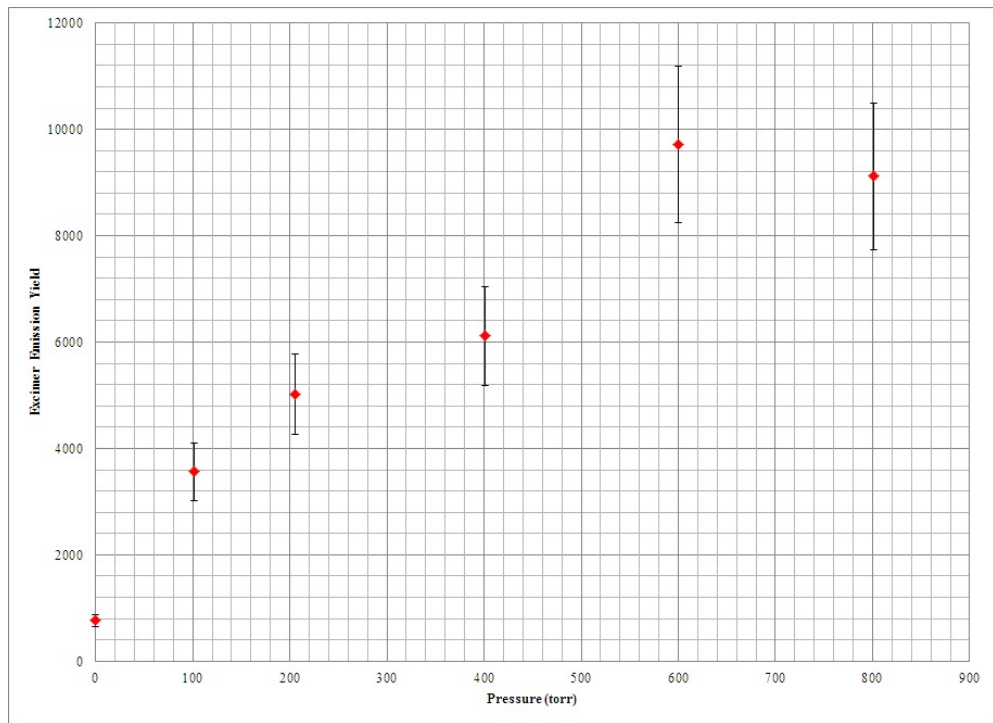


Figure 9.1.3-3: Excimer scintillation yield observed for 300-nm ^{10}B enriched thin film. Reactor power level 200 kW.

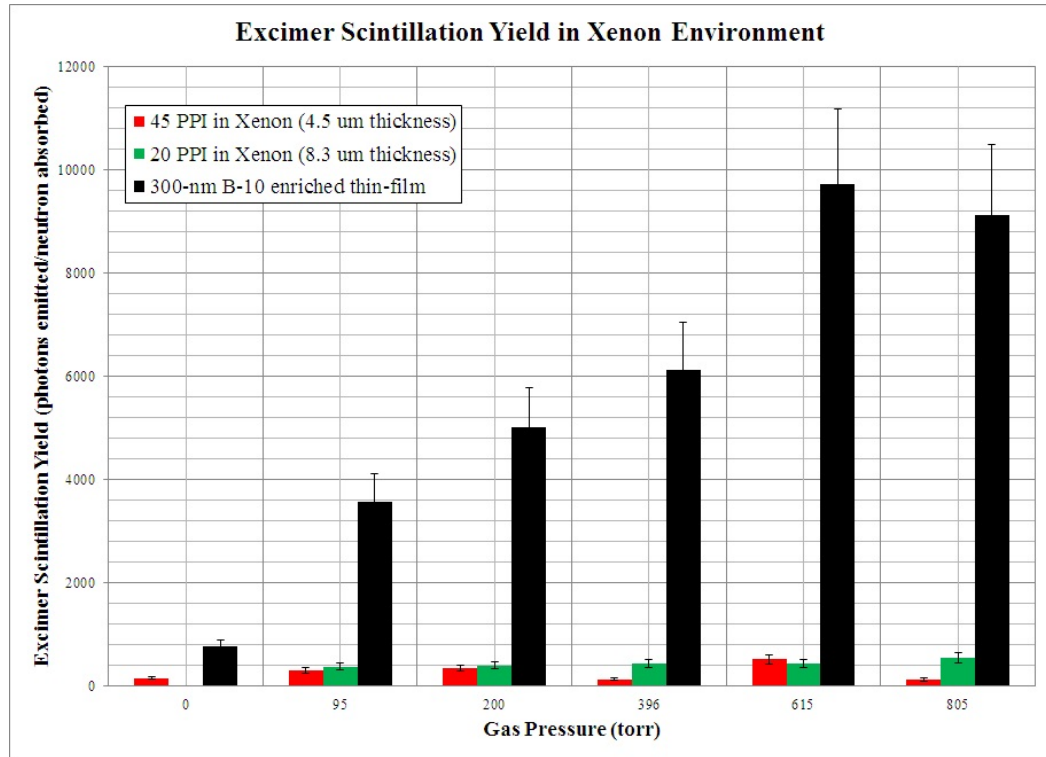


Figure 9.1.3-4: Excimer scintillation yield observed for 300-nm ^{10}B enriched thin film, 20 PPI RVC, and 45 PPI RVC in Xenon environment. Reactor power level 200 kW.

9.2 Conclusions

The results of the Far-Ultraviolet neutron detection experiments provide valuable understanding of the mechanism of noble gas scintillation and its potential for use in neutron detectors. The results discussed here, and all future work related to these experiments, will contribute to the development and optimization of a potentially deployable neutron detector to ease the problems arising from the shortage of ^3He .

The excimer scintillation yields of the carbon foam experiments can be compared to the yields of many of the typical liquid and solid scintillation detectors commonly used (see Table 2.2.2-1). The excimer emission yields for the carbon foam are low compared to the 300-nm ^{10}B enriched thin-film (600-700 photons emitted per neutron absorbed versus 9,500 photons emitted per neutron absorbed, respectively). However, the carbon foam excimer scintillation yields for the carbon foam can still be compared

to the light yields for the LiBaF_3 scintillation detectors doped with either Ce, K, or Ce, Rb. These scintillators have light yields on the order of 3,500 observations per neutron detected, making these detectors nearly five times better at detecting neutrons compared to the carbon foam studied in this research.

Despite the fact that the carbon foam excimer scintillation yields are an order of magnitude lower than the LiBaF_3 scintillation detectors, and between 2 and 3 orders of magnitude lower than other scintillator detectors such as $\text{Cs}_2^6\text{LiTCl}_6$ ($Y_n = 70,000$) or $^6\text{LiF}/\text{ZnS}$ ($Y_n = 160,000$), these preliminary experiments are promising for the use of carbon foam as a neutron detection medium. The carbon foam used in these experiments had a thick layer of a naturally enriched boron material (B_4C). The enrichment in ^{10}B was low ($< 19\%$). The thickness of the B_4C deposit was between 4 and 8 μm , which when compared to the thickness of the ^{10}B enriched thin-film (300 nm) is an order of magnitude different. It has been demonstrated in a previous set of experiments that thinner deposits of boron allow reaction products a higher probability of escape from the surface of the films with less loss of energy, increasing the chances of being detected by the photomultiplier tube. In these previous experiments, the thickest film studied was a 1.2 μm thick film with a ^{10}B enriched deposit. While this film had significantly more ^{10}B than the 300-nm thin-film, the excimer scintillation yield observed was much lower, with approximately 9,000 photons emitted per neutron absorbed compared to almost 15,000 photons emitted per neutron absorbed for the 300-nm thin film sample in an 800-torr Xe environment. Therefore, it can be concluded that by reducing the thickness of the B_4C deposit, the excimer scintillation yield for the carbon foam will increase, perhaps by as much as an order of magnitude. Even though re-characterization of the ^{10}B enriched thin-films has not been fully performed, the efficacy of the thin-films as detector material appears certain. The excimer scintillation yield is high, peaking around 9,000 photons emitted per neutron absorbed (which is not too different from the initial experiments), and

it appears as though any aging that has occurred has not proved to be significantly detrimental to the performance of the film.

Additionally, the enrichment of the ^{10}B in the carbon foams was much lower than that used in the thin-film experiments, which had a ^{10}B isotopic enrichment of approximately 92%. Because ^{10}B has a much higher thermal neutron absorption cross-section than the natural boron isotope, it is understood that the excimer scintillation yield will be much higher for a sample enriched in ^{10}B than a sample with natural boron enrichment. This has been well established in these experiments, when the excimer scintillation yields of the carbon foam and thin-film are compared. Therefore, by increasing the ^{10}B enrichment of the carbon foams, it is highly probable that the excimer scintillation yield will increase dramatically. When paired with a thinner layer of deposit material, the excimer scintillation yield is expected to be much higher by at least an order of magnitude, making them much more viable for use in a neutron detector. Future work could consider either a higher enrichment of ^{10}B in the B_4C , or simply a ^{10}B enriched coating.

With the current detector configuration, it was observed that the excimer scintillation yield decreased with increasing pressures of $^{10}\text{BF}_3$. These results were unexpected, and may be due to dissociation of the BF_3 molecules into electronegative ions which could cause unwanted interactions with the ionization products and noble gas excimers produced. Despite these unexpected results, BF_3 has been successfully used for years in neutron detectors, and it is still highly likely that the potential for use of $^{10}\text{BF}_3$ in these types of detectors still exists. These BF_3 detectors are typically lined with charcoal, or other material, to absorb the electronegative ions that are produced in the dissociation of the BF_3 molecules. The charcoal minimizes the number of free ions available to interact with the ionization products, preventing signal reduction. Once the mechanism behind the BF_3 reaction is understood, steps can be taken to minimize the dissociation of the molecules, and these experiments can be repeated

with potentially different results.

Despite the initial shortcomings of the BF_3 experiment, the carbon foam and ^{10}B enriched thin-film experiments prove to be much more applicable and provide much useful information on the potential of excimer-based neutron detection as an alternative method of radiation detection that is not dependent upon the use of ^3He . The groundwork laid with these experiments will provide invaluable information for the optimization and use of these types of materials in neutron detectors.

9.3 Contribution

The research presented in this thesis set out to establish the groundwork for an alternative method of neutron detection that is not reliant upon ^3He . While noble gas scintillators have been around for several decades, the introduction of a neutron absorbing nucleus (in the case of this research, ^{10}B) is innovative and has proven to have potential for the use in neutron detectors. In the case of this research, the combination of $^{10}\text{BF}_3$ with rare noble gases yielded interesting results, and while the results of that research were unexpected, the potential of these gas mixtures for use in neutron detectors has future potential, if this signal suppression can be understood and minimized.

Reticulated vitreous carbon foam has a wide range of applications, but the potential use of RVC foam as a neutron detection medium has not, as of this writing, been explored or otherwise documented. When previous experiments demonstrated that thinner targets allowed for a higher probability of reaction product escape, the chance to work with B_4C coated RVC foams of various pore sizes was seized. The hypothesis was that the porous structure of the RVC would increase the probability of reaction product escape, and this probability would further increase with increasing pore size while also increasing the surface area available for thermal neutron interaction.

Significant groundwork has been laid for future experiments to continue, and the

viability of the use of Reticulated Vitreous Carbon foam as a material for neutron detectors has been demonstrated through this research. The continued study of these RVC foams, with thinner layers of B_4C , higher enrichments of ^{10}B , and different pore sizes, may lead to the optimization and potential deployment of new types of sensitive, portable neutron detectors that do not rely on 3He .

9.4 Future Work

In order to absolutely quantify and determine the efficacy of the use of reticulated vitreous carbon foam as a medium for neutron detection, a number of future projects exist and should be addressed if Far Ultraviolet Neutron Detector projects are to continue at the MUTR. Wavelength shifters, FUV reflectors, different detector geometry, and increased photomultiplier tube efficiency should be investigated as methods of improving photon collection efficiency. Different types of absorber materials and geometries could be investigated in an effort to improve neutron collection efficiency. In addition to these future experimental topics, further work could be performed on the neutron detection media presented in this thesis. Future experiments will consider the effect of the sample holder on the excimer scintillation signal, as well as determination of the reflectivity of the carbon foam sample. This information will greatly contribute to an understanding of the excimer formation of the carbon foam. This section will address some of these projects.

9.4.1 Neutron Beam Characterization

As demonstrated by the NaI detector, the beam coming out of the MUTR thermal column collimated access plug is not purely thermal neutrons. The beam is a combination of a broad range of gamma radiation as well as thermal neutrons. The groundwork for complete characterization of the incident neutron beam has been

established, however, complete characterization is essential for a well-defined understanding of the characteristics of the excimer scintillation mechanism.

A number of resources are available to characterize the thermal column neutron beam, and investigation of beam characterization was considered. Foil activation, including gold, indium, cadmium, and tungsten, provides invaluable information on a number of properties of the neutron beam. Standard foil techniques require foils fabricated from materials that are activated by an (n, γ) reaction, with a cross-section approximately inversely proportional to the neutron speed in the thermal neutron energy range. The foils are irradiated in the neutron beam, then counted, and compared to foils irradiated in a beam of known fluence. Cadmium foil irradiations are useful to determine the effects of epithermal neutrons, which are always present in a thermal neutron beam [96].

The angular dependence of the neutron beam may also be determined by irradiation indium foils at different angles with respect to the neutron beam. A cadmium foil is placed between two indium foils and irradiated at an angle of 0° with respect to the incident beam. Indium foils of approximately equal mass are then irradiated at angles from 0° to 90° (with another cadmium sandwich irradiated at 45° and 90°). This process is repeated in the opposite direction back down to 0° and spectrum unfolding programs such as SAND is used to determine the angular dependence of the neutron beam. This information provides insight into the fluence and divergence of the beam and is used in conjunction with irradiation of different foils including gold, indium, vanadium, and tungsten (both covered and uncovered) to completely characterize the neutron beam.

9.4.2 BF_3

Interesting results were obtained from the BF_3 experiments, and further study should be given these experiments before it can be safely concluded that $^{10}\text{BF}_3$ gas will not work in excimer-based neutron detection. It has been well established that BF_3 is highly electronegative and has a strong tendency to dissociate into electronegative ions (specifically fluorine ions) which react with the electrons produced in the ionization event and cause signal suppression. For this reason, high purity $^{10}\text{BF}_3$ is used in neutron detectors, which are typically lined with charcoal or some other material that absorbs these electronegative ions and reduces signal suppression. The scintillation cell was not lined with charcoal, presumably leading to an accumulation of electronegative ions and resulting in the observed signal suppression.

In order to combat the signal suppression, it is necessary to understand the precise mechanism of BF_3 behavior in the scintillation cell environment. This includes studying how aging affects the signal, studying the effect of charcoal on the system, and using MgF_2 windows to eliminate the formation of SiF_4 . Additionally, the gas inside the scintillation cell could be periodically sampled and analyzed using Fourier Transform Infrared analysis (FTIR), or Nuclear Magnetic Resonance (NMR) analysis to determine the composition of the BF_3 . These analyses should be performed prior to every irradiation, and prior to combining the BF_3 with any other gas or material, and the initial spectra and composition should be compared to that taken during an excimer scintillation experiment and at the conclusion. These analyses would provide useful information on the behavior of BF_3 during irradiation, and should provide information on the formation of different types of ions such as SO_2 , SiF_4 , or SF_6 that may or may not form. Once this information is obtained, steps can be taken to reduce or eliminate the formation of these charged particles, if indeed that is what is causing the observed signal suppression.

9.4.3 Carbon Foam

To adequately assess the potential for the use of carbon foam in these neutron detectors, it is necessary to obtain more information on the carbon foams used in the excimer scintillation experiments. The 10 PPI samples (coated and uncoated) were studied using neutron imaging at the NIST Center for Neutron Research (NCNR) and the regions of transparency to neutrons were determined. Data are not yet available for the remaining samples.

The carbon foam samples are purported to be very uniform, however, this uniformity should be studied extensively with respect to observed excimer signal. The sample should be rotated in 5° increments within the sample holder and with respect to the neutron beam to determine if the observed signal remains consistent. Larger pore sizes mean more space for the neutrons to travel through without interacting with the B_4C , and if the neutron travels straight through the sample, it may interact with the sample holder and interact or scatter, skewing the observed signal. Rotating the sample, as well as adjusting the 4-mm aperture along the xy-plane from one edge of the sample to the other, would provide useful information on the consistency of excimer formation, as well as the reproducibility of excimer emission. This information would determine the uniformity of the sample and would assist with complete and accurate modeling of the sample, which would contribute greatly to the understanding of excimer formation, lifetime, and energy of formation, and would assist in the optimization of the detector. Reflectivity measurements at various angles and in various locations on the film would also assist in the modeling and understanding of the excimer scintillation mechanism.

It was observed that as the number of pores per inch decreased, the more fragile the samples became. Extreme care was used when handling the samples and placing them in and removing them from the scintillation cell, however, minor sample degradation could not be completely avoided. The mechanical stress/strain of the

samples should be studied in order to determine whether the samples would survive for the projected lifetime of the detector, as well as transport. If the smaller foam pore sizes show promise as a medium for neutron detection, methods of ensuring their survival should be investigated. Failure of the foam during detector operation or during transport would create a costly detector with a short lifespan and would not be as economically efficient or preferable to a ^3He detector.

Thicker samples should be studied as extensively as thinner samples to assist with the optimization of the detector. Stacking the samples should also be investigated in order to study the effect of increased sample thickness or combination of pore sizes on the excimer scintillation.

Appendix A

Lessons Learned

A.1 Pump Failures, 31 May 2011 and 3 June 2011

The first set of BF_3 photoabsorption experiments commenced on 27 May 2011, right before the Memorial Day long weekend. At the conclusion of the day, after the second vacuum run, the pressure of the system was 8.6×10^{-6} torr. The system was left to pump all weekend. Upon the return from the holiday weekend, it was discovered that both the turbopump and beamline cryopump had failed. The causes were unclear. It was assumed at the time that a power glitch due to a spring thunderstorm had caused the pump failures.

The cryopump was replaced with a functional pump and installed on Beamline 4. A replacement turbopump was also obtained and installed on the manifold. The system was baked overnight due to opening the system to the room during the removal of the non-functional turbopump.

On the morning of 2 June 2011, the pressure of the system was 8.6×10^{-7} torr. A second set of BF_3 photoabsorption spectra were collected, however due to an unexpected drop in beam current during the last run, the beam current normalization procedure was unable to accommodate for this change and the data yielded unreliable and inconsistent results. As a result, the plan was to perform a third set of measurements on 3 June 2011.

On the morning of 3 June 2011, Rob Vest, after a successful initial vacuum run, attempted to introduce a small amount of BF_3 into the system. He neglected to close the gate valve on the pump manifold, and did not realize the metering valve was open and so introduced about an atmosphere of BF_3 directly into the pump. The

pump immediately failed due to the extremely corrosive nature of the gas, and it was determined that the failure of the first pump was likely due to insufficient removal of BF_3 from the system.

The two pumps were disassembled, and it was apparent from a visual inspection of the original Pfeiffer pump that there was evidence of BF_3 corrosion on vital parts. This led to the conclusion that the current dry N_2 purge was inadequate in removing all the BF_3 from the system due to a large amount of dead space between the N_2 inlet and the BF_3 metering valve (see Figure A.1-1).

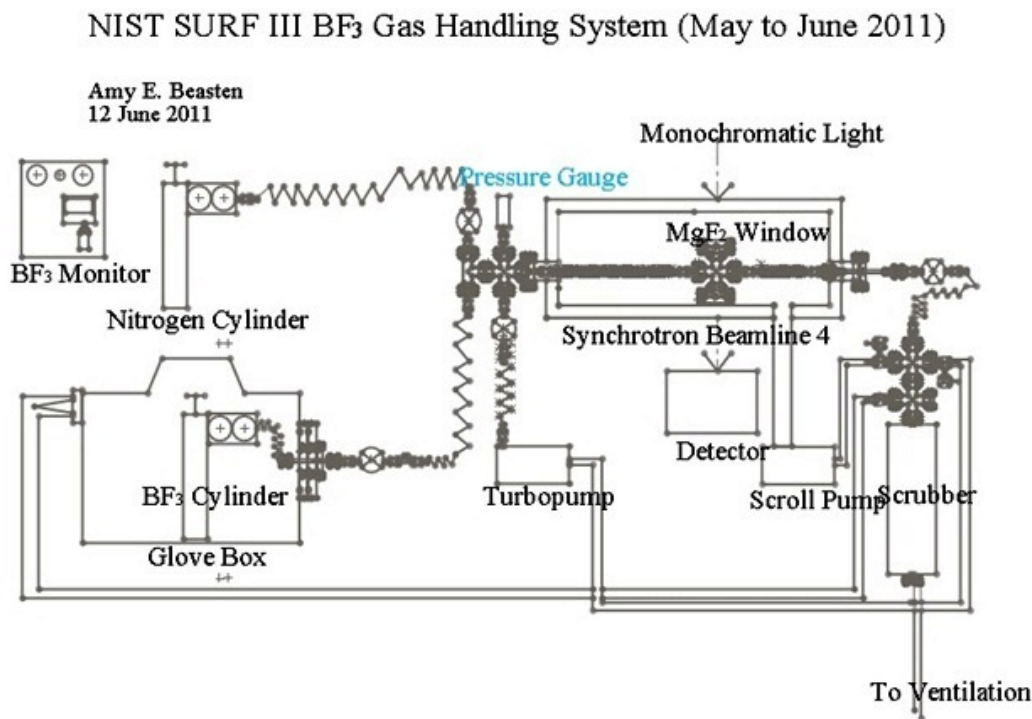


**Figure A.1-1: NIST SURF III Gas Handling System for 27 May and 2-3 June 2011
Photoabsorption Experiments**

The 2-3/4" Conflat[®] "T" was removed, and a 1/4" VCR "T" was installed immediately adjacent to the BF_3 metering valve. Upon removal of the bellows from the metering valve, three wisps of white vapor escaped from the metering valve, a result of residual BF_3 gas reacting with the water vapor in the atmosphere. The vapor fell to the floor and dissipated without major incident, and the BF_3 monitor continued

to register 0.0 ppm. After a safety committee review, it was determined that there was no major hazard, however the complexity of the gas handling system could yield further incident.

The VCR “T” was installed on the manifold, and the N₂ inlet connected immediately opposite the BF₃ metering valve, in the hopes that this would allow for adequate purge.

Additionally, due to the highly corrosive nature of BF₃, and the fact that the gas had clearly destroyed two turbopumps already, it was decided that the best course of action would be to install a liquid nitrogen cold trap on the manifold before the pump. The melting point of BF₃ at 1 atmosphere is 147 K. Even at 10 torr, the melting point of BF₃ is 130-135 K, well above the temperature of liquid nitrogen (77 K). A cold trap was obtained and installed on the system (see Figure 4.2.1-1). In addition, it was decided to attach a mechanical oil pump to the outlet of the scrubber during the dry N₂ purge to assist with the removal of all the BF₃. Previously, the N₂ was expected to force the BF₃ through the scrubber independently of any mechanical assistance. This was likely insufficient for removal of all the BF₃ from the system, for the system would remain at atmospheric pressure prior to the initiation of the next pump down. This could have allowed for copious quantities of un-purged BF₃ mixed with the remaining N₂ gas entering the turbopump as it pumped the system out. Refer to Section 4.2.1 for a complete overview of the gas handling system.

With the installation of the cold trap and the mechanical pump on the outlet of the scrubber, no further pump failures were observed.

A.2 Viton, 18 May 2011

On 17 May 2011, a set of preliminary photoabsorption experiments were performed using 99.999% pure O₂ as a preliminary tool for data collection. These were performed to gain familiarity with the beamline data acquisition software. Refer to Appendix B

for a discussion on the procedure and results.

At the end of the day, the gas handling system was pumped down and wrapped in heating tape covered in aluminum foil from the O₂ regulator to the pressure gauge immediately adjacent to the box on the exterior manifold. The absorption cell inside the beamline box was wrapped in heating tape covered in Aluminum foil as well, from the end of the posterior bellows to the end of the anterior bellows. The Variacs were dialed to 65 V each, and the system was left to bake overnight. It was decided that the system would be baked again to completely replicate the first set of data collection, but was not deemed to be wholly necessary.

When the system was inspected the following morning, 18 May 2011, it was reported that the temperature of the absorption cell within the beamline box had reached in excess of 200 °C. There was no immediate concern for the apparatus at the time, although there did appear to be a large leak in the system that had not previously been in existence.

The system was cooled and the foil and heating tape removed. Upon visual inspection of the absorption cell and the neighboring bellows, it was observed that the stainless steel had turned a bronze-gold color, but no obvious damage. The MgF₂ windows did not appear to have cracked or been damaged under the extreme heat, so the system was pumped on again. The leak detected in the system was very large, and growing, so the apparatus was leak checked to determine the source.

The leak was detected between the 2-3/4" Conflat[®] and the MgF₂ window aligned with the forefront view-port. Tightening the bolts did not seem to help, so it was assumed there was damage to the gasket and the gasket needed to be replaced. Upon removal of the window from the Conflat[®], a large mass of melted black goo was found to have adhered itself to the knife edge of both the Conflat[®] and the MgF₂ window. Cleaning was attempted with a Q-tip dipped in acetone.

The gasket in question was likely Viton, a type of synthetic rubber O-ring. Viton

is fluorinated and rated at temperatures up to 200 °C. As the system was baked at well over 200 °C, the Viton melted to the gasket. The gasket between the rear MgF₂ window and the CF was also Viton, so the absorption cell was dismantled for deep cleaning. The rear MgF₂ window was much easier to clean, as the Viton gasket had not completely melted. The method chosen for cleaning, Q-tip dipped in acetone, was successful in removed the Viton residue from the knife edge of the MgF₂ windows. As for the rest of the system inside the endstation, all the Ni-plated copper gaskets had been adhered to the knife edges of the flanges connecting them. These were easily pried off.

At high temperatures, fluoroelastomers like Viton O-rings break down and release hydrocarbon vapors that re-condense in cooler environments. As the anterior and posterior bellows were not as bronzed as the absorption cell and the MgF₂ windows, it was assumed that the bellows were much cooler than the absorption cell. Because of the bends and kinks in the flexible tubing, the molecules from the hydrocarbon vapors likely collided with the cooler walls of the interior of the tubing and re-condensed on the walls. Due to the need for a high purity environment, the bellows, cross, and flanges were all replaced with equipment that had not been contaminated with hydrocarbons.

When the acetone-dipped Q-tip did not appear to have any significant effect on the removal of Viton from the cross and flanges, these items were placed in an ultrasonic agitator with acetone and heat for 10 minutes. There was no change after 10 minutes, so the agitator was set for another 30 minutes.

On 19 May 2011, the cleaning of the Viton resumed with carbide scribe. The best cleaning method found was apply heat to the flange or window with a heat gun then scrape with the scribe and wipe down with acetone.

When the MgF₂ windows were cleaned as much as possible, they were connected to a vacuum to determine the extent of the damage. There did not appear to be any

leaks from the windows. Replacement parts were obtained for the system.

The next several days were spent at the University of Maryland constructing and wiring a thermocouple interlock that would monitor and regulate the temperature of the systems being baked. Once the threshold temperature was reached, the interlock would shut off the heating tape to prevent overheating again. On 24 May 2011, the preventative system was finished and transported to NIST. The system had in that time been reassembled and was re-wrapped in heating tape and Aluminum foil. The thermocouple element was programmed with an upper limit of 130 °C and left to bake overnight.

An RGA spectral scan indicated peaks at 55, 56, and 57 in the 10^{-9} mtorr range that had not been previously present. It was suspected that this was evidence of hydrocarbon contamination. After baking, the pressure of the system was 3.4×10^{-7} torr. The RGA scan showed that the peaks at 55, 56, and 57 had dropped an order of magnitude to 10^{-10} mtorr, so the system was declared to be ready for the final O₂ transmission run.

There appeared to be some non-uniformity in the MgF₂ windows, however the non-uniformity appeared to have minimal impact on the spectra. This non-uniformity was predicted to be a result of the Viton contamination, but did not have a significantly noticeable negative impact on the data.

Appendix B

O₂ Photoabsorption Spectra

B.1 O₂ Gas Handling System and Experimental Procedure

Prior to the start of the ¹⁰BF₃ photoabsorption experiments, a series of absorption experiments were conducted using 99.999% O₂ gas. This was done to gain familiarity with the BL4 data acquisition software and the data analysis procedure using a well-characterized gas with a known structure. The structure of O₂ is well documented in the wavelength region from 170 to 205 nm, so a series of photoabsorption experiments was conducted in this region to identify the Schumann-Runge bands.

B.1.1 O₂ Experimental Procedure

For the O₂ photoabsorption experiment, the existing BF₃ vacuum apparatus was modified. The N₂ cylinder was removed, the BF₃ manifold was disconnected from the glove box at the metering valve, and the metering valve was attached to the O₂ cylinder. The stage and the photodiode were aligned using the LabView software native to BL4. This method of alignment was described in Section 4.2.2.

The photoabsorption experiments proceeded as follows: an initial vacuum run, with the absorption cell empty, was performed. This run was used as the incident signal for the transmission measurements for the data analysis, as described in Section 4.3. Data were collected from 170 to 205 nm with 0.25 nm increment and 10 samples taken at each data point. Oxygen was introduced to the system at an initial pressure of 36 torr, and another data run was performed. Subsequent pressures of 95, 204, 363, 612, 744, and 813 torr were introduced to the system following the conclusion of the initial vacuum run, and data were collected over the same wavelength range.

Following the conclusion of the final pressurized photoabsorption data collection, the absorption cell was then pumped down and a second vacuum run was performed, this time to take into account the gradual decline in the beam current. The second vacuum run is used in the beam current normalization procedure during data analysis, as described in Section 4.3.

It was intended that an identical O₂ experiment be performed the following day, however difficulties arose when it was discovered that the overnight bake in excess of 200 °C had melted the Viton gaskets between the Conflats[®] and the MgF₂ windows on the absorption cell. The windows were cleaned with a mixture of acetone, heat, and mechanical scraping using a carbide scribe, as described in Appendix A.2. New bellows, 4-way cross, mini Conflat[®] to zero-length adapters, and mini Conflat[®] to VCR-F were obtained due to the fact that the melted Viton likely condensed on the inside of these parts. The parts were replaced to avoid hydrocarbon contamination in future O₂ and BF₃ experiments.

An RGA spectral scan of the system several days later showed very low partial pressures of some compound with molecular weights of 55, 56, and 57 (on the order of 10⁻⁹ mtorr partial pressure). These molecules are assumed to be a hydrocarbon contaminate, but after a controlled bake at 150 °C, the partial pressures decreased an order of magnitude to 10⁻¹⁰ mtorr. The windows do not appear to be adversely affected by either the Viton, cleaning, or the extremely high bake temperatures.

On May 26, the absorption cell and photodiode were both re-aligned using the aforementioned procedure, and a second O₂ experiment was run with an initial vacuum run, and pressures of 56, 115, 221, 450, and 746 torr, and a second final vacuum run. The parameters were the same as the original experiment. This second experiment was conducted to show repeatability and reproducibility of the experiment.

B.1.2 O₂ Absolute Photoabsorption Cross-Section Results

The absolute photoabsorption cross-section and uncertainty values were determined using the same procedure outlined in Section 4.3; this will not be discussed again. Figure B.1.2-1 illustrates the correlation between the two different days of data collection with the calculated uncertainty values.

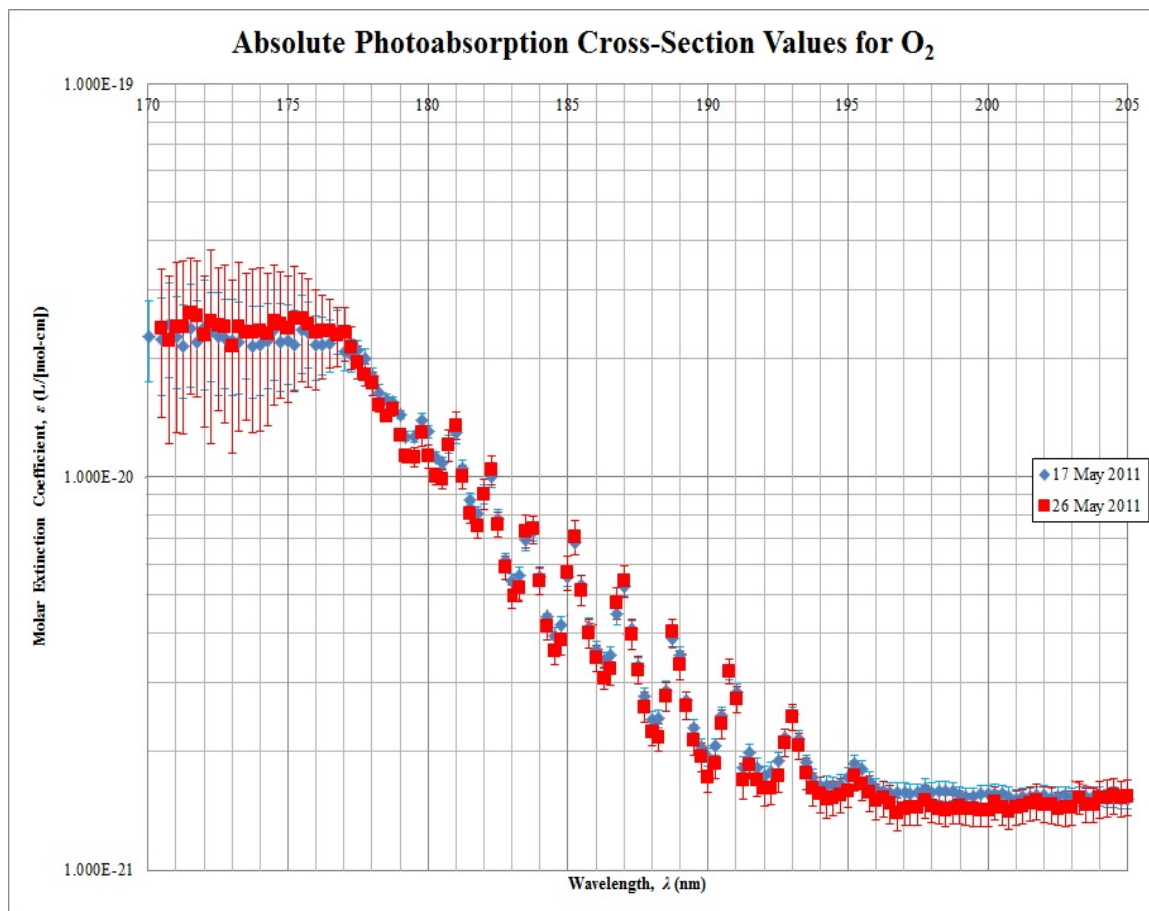


Figure B.1.2-1: Photoabsorption Cross-Section and Molar Extinction Coefficient of O₂ from 170 to 205 nm. The diamonds show the data collected on 17 May and the squares show the data collected on 26 May.

Despite the incident with the melted Viton on the MgF₂ absorption cell windows, it appears from Figure B.1.2-1 that there was no significant effect on the ability of light to pass through the windows. The cross-section and molar extinction coefficient values show very close precision with the initial O₂ photoabsorption experiment.

Additionally, the cross-section values correlate rather well with the documented

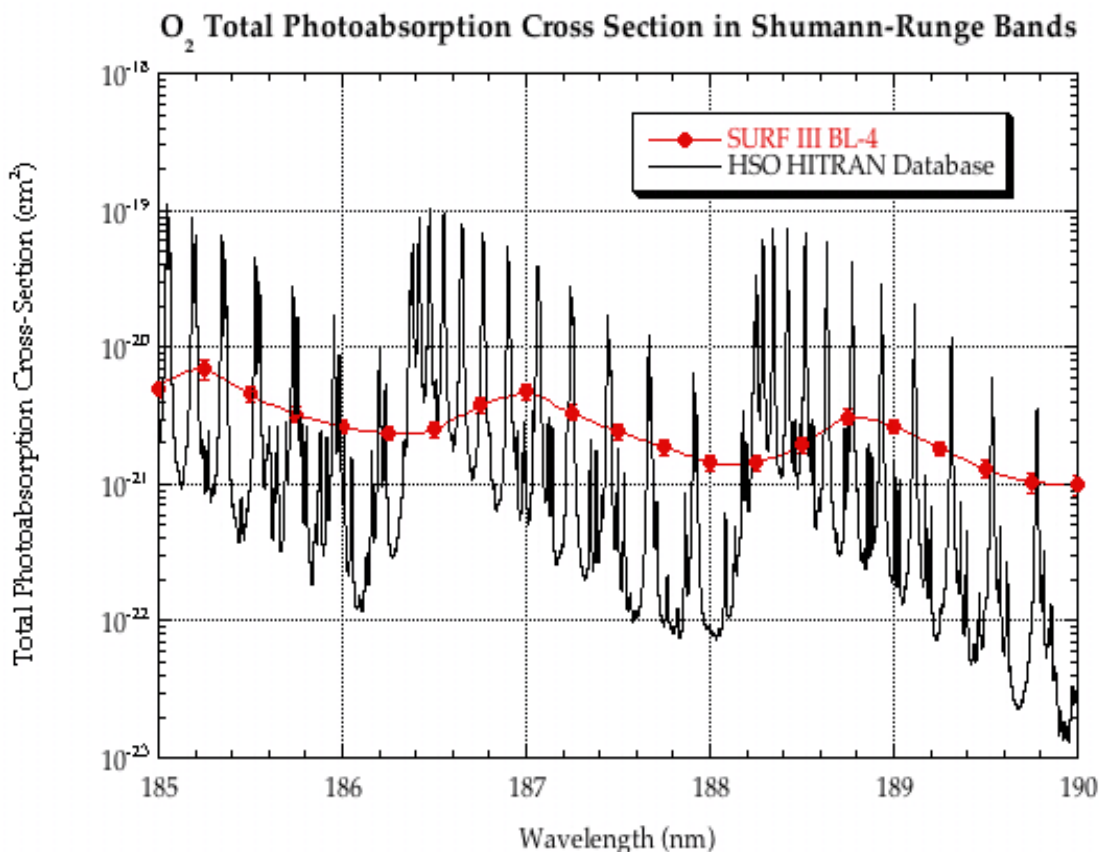


Figure B.1.2-2: O₂ Absolute Photoabsorption Cross-Section in Schumann-Runge Bands [74]

Schumann-Runge bands of O₂ in this region, as shown in Figure B.1.2-2. While the resolution is not as well-defined in the SURF III data, there is a distinct correlation in the shape and location of the peaks between the SURF III data and the documented Schumann Runge bands.

With this information, including the observation that the Schumann-Runge peaks identified through use of SURF III BL4 correlate with the documented literature values of the Schumann-Runge bands of O₂ in the same wavelength region, it was determined that sufficient expertise had been acquired with the BL4 data acquisition software and the cross-section calculation and that the ¹⁰BF₃ photoabsorption experiments could commence.

Appendix C

Photoabsorption Cross-Section Values

C.1 $^{10}\text{BF}_3$ Absolute Photoabsorption Cross-Section Data

Below follow the photoabsorption cross-section and uncertainty values for $^{10}\text{BF}_3$.

Table C.1-1: Absolute Photoabsorption Cross-Section (σ) and Uncertainty Values ($u(\sigma)$) for $^{10}\text{BF}_3$ from 135-205 nm, 27 May 2011

27 May 2011			
Wavelength, λ (nm)	\mathbf{R}_B	σ (cm^2)	$\mathbf{u}(\sigma)$
134.96	-2.9E-05	1.06E-20	1.56E-21
135.25	3.43E-06	-1.2E-21	-1.6E-21
135.51	-2.1E-05	7.49E-21	9.34E-22
135.74	-1.9E-05	6.77E-21	9.06E-22
136.02	-1.8E-05	6.61E-21	1.02E-21
136.25	-2E-05	7.33E-21	1.36E-21
136.51	-2.4E-05	8.5E-21	9.76E-22
136.72	-2.3E-05	8.22E-21	1.44E-21
137	-2.3E-05	8.26E-21	1.81E-21
137.24	-1.9E-05	6.73E-21	1.05E-21
137.5	-2.2E-05	7.88E-21	1.19E-21
137.79	-1.9E-05	6.95E-21	1.43E-21
138.01	-2.2E-05	7.94E-21	1.08E-21
138.25	-2.2E-05	7.98E-21	9.27E-22
138.51	-1.8E-05	6.54E-21	9.55E-22
138.76	-2E-05	7.21E-21	6.21E-22
138.98	-2.1E-05	7.52E-21	1.69E-21
139.23	-2.5E-05	9E-21	2.05E-21
139.49	-2.4E-05	8.49E-21	2.13E-21
139.79	-1.6E-05	5.62E-21	9.13E-22
140.02	-1.2E-05	4.4E-21	6.01E-22
140.27	-1.4E-05	5.05E-21	5.62E-22
140.5	-2E-05	7.12E-21	1.27E-21
140.75	-2.3E-05	8.3E-21	2.26E-21
141	-1.7E-05	6.06E-21	1.08E-21
141.25	-1E-05	3.75E-21	6.02E-22
Continued on next page			

Table C.1-1 – continued from previous page

27 May 2011			
Wavelength, λ (nm)	R_B	σ (cm ²)	$u(\sigma)$
141.51	-7.4E-06	2.66E-21	3.89E-22
141.75	-8.5E-06	3.07E-21	4.07E-22
142	-9.4E-06	3.39E-21	5.23E-22
142.25	-8.7E-06	3.11E-21	4.83E-22
142.5	-7.8E-06	2.81E-21	5.21E-22
142.76	-7.1E-06	2.56E-21	3.76E-22
143	-6.7E-06	2.41E-21	4.06E-22
143.25	-7.5E-06	2.69E-21	3.88E-22
143.5	-7.4E-06	2.65E-21	4.32E-22
143.74	-7E-06	2.52E-21	5.19E-22
144	-6.6E-06	2.39E-21	5.08E-22
144.25	-6.3E-06	2.27E-21	3.99E-22
144.5	-6.8E-06	2.46E-21	4.08E-22
144.76	-5.7E-06	2.06E-21	4.39E-22
144.99	-7.7E-06	2.76E-21	4.72E-22
145.25	-6.9E-06	2.48E-21	3.47E-22
145.47	-6.6E-06	2.38E-21	4.72E-22
145.75	-5.8E-06	2.1E-21	4.19E-22
146.02	-6.6E-06	2.36E-21	5.57E-22
146.27	-5.4E-06	1.95E-21	4.72E-22
146.47	-5.9E-06	2.12E-21	5E-22
146.76	-6.9E-06	2.48E-21	5.12E-22
146.99	-5.9E-06	2.11E-21	5.04E-22
147.25	-6.5E-06	2.33E-21	3.68E-22
147.49	-6.1E-06	2.2E-21	3.92E-22
147.77	-5.3E-06	1.91E-21	3E-22
148.03	-6.6E-06	2.38E-21	3.77E-22
148.25	-6.1E-06	2.21E-21	3.07E-22
148.5	-5.7E-06	2.04E-21	3.48E-22
148.77	-6.6E-06	2.36E-21	4.11E-22
149.03	-6.3E-06	2.26E-21	3.42E-22
149.25	-6E-06	2.16E-21	3.87E-22
149.55	9.54E-06	-3.4E-21	-1.9E-21
149.76	-6.3E-06	2.25E-21	3.82E-22
150.02	-6.1E-06	2.18E-21	3.24E-22
150.25	-6.6E-06	2.38E-21	4.56E-22
150.5	-6.9E-06	2.49E-21	4.21E-22
150.75	-7.5E-06	2.69E-21	4.94E-22
151	-8E-06	2.86E-21	5.29E-22
Continued on next page			

Table C.1-1 – continued from previous page

27 May 2011			
Wavelength, λ (nm)	R_B	σ (cm ²)	$u(\sigma)$
151.25	-8.4E-06	3.02E-21	5.47E-22
151.51	-8.3E-06	2.99E-21	4.05E-22
151.75	-8.4E-06	3.01E-21	4.67E-22
152	-8.5E-06	3.06E-21	4.32E-22
152.25	-8.4E-06	3.02E-21	4.81E-22
152.5	-8.4E-06	3.04E-21	3.41E-22
152.75	-9E-06	3.24E-21	4.62E-22
152.99	-8.9E-06	3.19E-21	3.88E-22
153.25	-8.7E-06	3.13E-21	3.98E-22
153.5	-8.4E-06	3.01E-21	4.17E-22
153.75	-8.8E-06	3.18E-21	4.83E-22
154.01	-8.8E-06	3.16E-21	4.01E-22
154.26	-8.9E-06	3.22E-21	3.54E-22
154.5	-1E-05	3.66E-21	4.23E-22
154.74	-1E-05	3.72E-21	3.38E-22
154.99	-9.8E-06	3.53E-21	4.87E-22
155.25	-9.5E-06	3.4E-21	4.21E-22
155.51	-8.1E-06	2.9E-21	4.64E-22
155.74	-8E-06	2.87E-21	4.96E-22
155.99	-7.8E-06	2.82E-21	3.47E-22
156.25	-8.3E-06	3E-21	3.96E-22
156.51	-8.5E-06	3.04E-21	3.59E-22
156.73	-9.9E-06	3.56E-21	3.35E-22
156.99	-1E-05	3.67E-21	5.05E-22
157.27	-9.9E-06	3.56E-21	4.91E-22
157.5	-1E-05	3.76E-21	5.16E-22
157.74	-1.1E-05	3.83E-21	4.37E-22
157.99	-9.9E-06	3.55E-21	3.6E-22
158.21	-8.5E-06	3.05E-21	2.54E-22
158.54	-6.1E-06	2.2E-21	2.85E-22
158.74	-5.9E-06	2.12E-21	2.67E-22
159.01	-5.9E-06	2.11E-21	2.61E-22
159.22	-6.9E-06	2.47E-21	2.71E-22
159.5	-7.7E-06	2.75E-21	3.19E-22
159.72	-9.2E-06	3.3E-21	2.48E-22
160.02	-1E-05	3.63E-21	3.93E-22
160.25	-9.6E-06	3.46E-21	2.9E-22
160.5	-6.8E-06	2.46E-21	2.48E-22
160.75	-5E-06	1.81E-21	2.55E-22
Continued on next page			

Table C.1-1 – continued from previous page

27 May 2011			
Wavelength, λ (nm)	R_B	σ (cm ²)	$u(\sigma)$
161	-3.8E-06	1.36E-21	1.37E-22
161.25	-3E-06	1.08E-21	1.22E-22
161.51	-2.6E-06	9.29E-22	1.61E-22
161.75	-1.9E-06	6.82E-22	1.3E-22
162	-2E-06	7.34E-22	1.25E-22
162.25	-1.3E-06	4.72E-22	1.22E-22
162.5	-1.7E-06	6.15E-22	1.1E-22
162.76	-1.2E-06	4.24E-22	9.54E-23
163	-1.1E-06	3.99E-22	1.28E-22
163.24	-1.2E-06	4.2E-22	1.16E-22
163.5	-1E-06	3.76E-22	7.36E-23
163.75	1.38E-05	-4.9E-21	-2.2E-21
164.01	-3.2E-07	1.14E-22	9.01E-23
164.24	-7.5E-07	2.69E-22	6.1E-23
164.52	-5.4E-07	1.93E-22	6.24E-23
164.76	-7.2E-07	2.57E-22	7.16E-23
165.03	-4.2E-07	1.5E-22	7.5E-23
165.25	-4.1E-07	1.46E-22	7.65E-23
165.51	-2.3E-07	8.28E-23	9.83E-23
165.79	-4E-07	1.43E-22	9.27E-23
166	-3.1E-07	1.13E-22	7.08E-23
166.25	-4E-07	1.44E-22	8.87E-23
166.51	-3.3E-07	1.17E-22	4.67E-23
166.77	-2.9E-07	1.06E-22	8.37E-23
167.01	-3E-07	1.09E-22	6.95E-23
167.25	-2.3E-07	8.44E-23	5.54E-23
167.52	-6.9E-07	2.48E-22	4.37E-23
167.77	-4.3E-07	1.54E-22	5.24E-23
167.97	-7.8E-07	2.8E-22	5.81E-23
168.23	-6.1E-07	2.21E-22	7.59E-23
168.52	-8.8E-07	3.17E-22	7.55E-23
168.75	-9.1E-07	3.28E-22	6.92E-23
169.04	-5.9E-07	2.11E-22	9.68E-23
169.24	-1.1E-07	3.79E-23	1.19E-22
169.465	-2.2E-07	7.82E-23	1.3E-22
169.69	-4.2E-07	1.51E-22	1.28E-22
170.02	-1.5E-07	5.23E-23	1.41E-22
170.25	-1.5E-07	5.37E-23	1.31E-22
170.5	-2.9E-07	1.04E-22	1.34E-22
Continued on next page			

Table C.1-1 – continued from previous page

27 May 2011			
Wavelength, λ (nm)	R_B	σ (cm ²)	$u(\sigma)$
170.75	1.16E-07	-4.2E-23	-1.8E-22
171	-1.2E-07	4.35E-23	1.45E-22
171.25	-3.3E-07	1.2E-22	1.38E-22
171.5	-1.2E-07	4.48E-23	1.41E-22
171.75	-7.8E-08	2.82E-23	1.45E-22
172	-1.4E-07	5.04E-23	1.33E-22
172.25	-4.3E-07	1.54E-22	1.04E-22
172.5	-4.3E-07	1.53E-22	9.99E-23
172.76	-5E-07	1.8E-22	7.77E-23
173	-2.1E-07	7.62E-23	1.2E-22
173.24	-3E-07	1.06E-22	9.23E-23
173.49	-4E-07	1.42E-22	9.73E-23
173.75	-3.2E-07	1.16E-22	1.14E-22
174.01	-3.3E-07	1.18E-22	1.05E-22
174.25	-4.9E-07	1.75E-22	1.07E-22
174.48	-2.7E-07	9.75E-23	8.83E-23
174.77	-4.1E-07	1.46E-22	9.86E-23
175	-2.2E-07	7.95E-23	1.18E-22
175.25	-1.9E-07	6.83E-23	1.08E-22
175.47	-3.6E-07	1.28E-22	9.25E-23
175.79	-1.9E-07	6.93E-23	1.07E-22
175.98	-2.4E-07	8.64E-23	1.11E-22
176.26	-3E-07	1.09E-22	1.08E-22
176.48	-3.8E-07	1.36E-22	1E-22
176.73	-3.9E-07	1.42E-22	1.14E-22
177.02	-4E-07	1.43E-22	1.18E-22
177.25	-3.9E-07	1.41E-22	9.87E-23
177.46	-3.6E-07	1.3E-22	1.25E-22
177.76	-4.3E-07	1.54E-22	1.13E-22
178.05	1.41E-05	-5.1E-21	-2.3E-21
178.24	-5.9E-07	2.13E-22	7.89E-23
178.53	-5.1E-07	1.85E-22	8.82E-23
178.75	-3.2E-07	1.16E-22	8.95E-23
178.98	-4.5E-07	1.6E-22	7.11E-23
179.23	-3.4E-07	1.23E-22	1.04E-22
179.5	-4.5E-07	1.62E-22	1.07E-22
179.77	-3.5E-07	1.25E-22	7.99E-23
179.98	-1.5E-07	5.29E-23	9.62E-23
180.28	-3.1E-07	1.1E-22	8.19E-23
Continued on next page			

Table C.1-1 – continued from previous page

27 May 2011			
Wavelength, λ (nm)	R_B	σ (cm ²)	$u(\sigma)$
180.5	-3.5E-07	1.28E-22	6.94E-23
180.75	-3E-07	1.07E-22	8.23E-23
181	-3.4E-07	1.23E-22	8.85E-23
181.25	-6.2E-07	2.24E-22	6.02E-23
181.51	-5.9E-07	2.1E-22	5.07E-23
181.75	-4.6E-07	1.65E-22	7.6E-23
182	-3.8E-07	1.37E-22	7.62E-23
182.25	-3E-07	1.09E-22	8.35E-23
182.5	-4.6E-07	1.64E-22	6.75E-23
182.75	-2.5E-07	8.84E-23	7.32E-23
183	-2.9E-07	1.04E-22	6.15E-23
183.25	-3.9E-07	1.4E-22	8.14E-23
183.5	-1.8E-07	6.44E-23	6.27E-23
183.74	-1.8E-07	6.51E-23	7.08E-23
183.99	3.99E-08	-1.4E-23	-6.6E-23
184.25	-5.6E-08	2.01E-23	7.15E-23
184.5	-1.7E-07	5.95E-23	6.34E-23
184.74	-1.1E-07	3.92E-23	6.55E-23
185.01	-7.9E-08	2.83E-23	7.24E-23
185.23	-2.1E-07	7.37E-23	6.62E-23
185.51	-1.2E-07	4.27E-23	7E-23
185.76	-1.7E-07	6.12E-23	6.96E-23
185.98	-3E-07	1.06E-22	5.12E-23
186.25	-3.3E-08	1.18E-23	7.28E-23
186.48	5.36E-08	-1.9E-23	-6.4E-23
186.75	-1.7E-07	6.07E-23	6.62E-23
187.03	5.67E-08	-2E-23	-4.7E-23
187.24	-1.1E-07	3.88E-23	4.45E-23
187.49	-1.2E-07	4.25E-23	3.22E-23
187.75	-8.5E-08	3.06E-23	3.42E-23
187.97	-1.5E-07	5.55E-23	6.89E-23
188.26	7.95E-08	-2.9E-23	-6E-23
188.5	-1.8E-07	6.29E-23	4.15E-23
188.77	5.13E-08	-1.8E-23	-5.8E-23
188.98	-2.2E-07	7.94E-23	4.21E-23
189.26	-6.8E-08	2.45E-23	3.37E-23
189.48	-6.2E-08	2.22E-23	5.53E-23
189.71	-1.3E-07	4.64E-23	5.79E-23
190.01	-1.3E-07	4.67E-23	5.69E-23
Continued on next page			

Table C.1-1 – continued from previous page

27 May 2011			
Wavelength, λ (nm)	R_B	σ (cm ²)	$u(\sigma)$
190.25	-8.4E-09	3.04E-24	5.2E-23
190.5	-1.7E-07	5.98E-23	4.96E-23
190.75	-1.2E-07	4.37E-23	4.78E-23
191	-2.8E-07	9.92E-23	4.56E-23
191.26	-2E-07	7.34E-23	5.74E-23
191.51	-3.3E-07	1.18E-22	4.32E-23
191.75	-2.4E-08	8.6E-24	5.58E-23
192	-2.3E-07	8.36E-23	5.19E-23
192.25	1.4E-05	-5E-21	-2.2E-21
192.5	-2.9E-07	1.05E-22	7.6E-23
192.75	-1.2E-07	4.15E-23	8.06E-23
192.99	-2.6E-07	9.47E-23	5.2E-23
193.24	-1.9E-08	6.86E-24	5.97E-23
193.5	-2.2E-07	7.8E-23	5.43E-23
193.75	-5.9E-07	2.13E-22	5.14E-23
193.99	-5.5E-07	1.98E-22	6.37E-23
194.25	-4.9E-07	1.78E-22	4.18E-23
194.51	-3.6E-07	1.3E-22	4.63E-23
194.77	-3.1E-07	1.12E-22	5.1E-23
194.98	-7E-07	2.53E-22	3.49E-23
195.23	-6.3E-07	2.28E-22	4.41E-23
195.49	-9.9E-07	3.55E-22	4.25E-23
195.73	-1E-06	3.62E-22	5.9E-23
195.97	-6.6E-07	2.37E-22	4.22E-23
196.27	-5.6E-07	2.01E-22	3.1E-23
196.5	-5.6E-07	2.03E-22	5.56E-23
196.76	-9.2E-07	3.29E-22	5.58E-23
197	-1.2E-06	4.26E-22	4.91E-23
197.26	-8.4E-07	3.03E-22	5.19E-23
197.5	-4.5E-07	1.63E-22	3.74E-23
197.72	-5E-07	1.78E-22	2.66E-23
198	-6.4E-07	2.32E-22	2.65E-23
198.24	-6.5E-07	2.34E-22	5.91E-23
198.54	-1.3E-06	4.51E-22	5.48E-23
198.73	-1E-06	3.59E-22	5.46E-23
199.01	-2.9E-07	1.05E-22	5.41E-23
199.25	-4E-07	1.44E-22	4.35E-23
199.5	-4.4E-07	1.59E-22	5.21E-23
199.76	-7.7E-07	2.78E-22	4.8E-23
Continued on next page			

Table C.1-1 – continued from previous page

27 May 2011			
Wavelength, λ (nm)	R_B	σ (cm ²)	$u(\sigma)$
200.03	-8.7E-07	3.13E-22	4.73E-23
200.25	-1.3E-06	4.5E-22	5.41E-23
200.5	-5.2E-07	1.85E-22	5.96E-23
200.75	-2.6E-07	9.43E-23	6.49E-23
201	-3.3E-07	1.18E-22	5.29E-23
201.25	-3.8E-07	1.37E-22	3.93E-23
201.5	-1.1E-06	3.84E-22	4.44E-23
201.75	-1.3E-06	4.61E-22	6.43E-23
202	-6E-07	2.17E-22	7.02E-23
202.25	-2.9E-07	1.03E-22	4.97E-23
202.5	-3.3E-07	1.18E-22	5.35E-23
202.75	-4.7E-07	1.69E-22	6E-23
203	-4.5E-07	1.63E-22	5.99E-23
203.25	-6.5E-07	2.34E-22	6.42E-23
203.49	-8E-07	2.87E-22	6.07E-23
203.75	-3.7E-07	1.32E-22	6.98E-23
203.99	-3.9E-07	1.4E-22	4.82E-23
204.23	-2.9E-07	1.04E-22	5.91E-23
204.49	-1.6E-07	5.63E-23	5.41E-23
204.75	-5.1E-07	1.84E-22	6.08E-23
205.01	-5.3E-07	1.92E-22	6.31E-23

Table C.1-2: Absolute Photoabsorption Cross-Section (σ) and Uncertainty Values ($u(\sigma)$) for ¹⁰BF₃ from 135-145 nm, 5 July 2011

5 July 2011			
Wavelength, λ (nm)	R_B	σ (cm ²)	$u(\sigma)$
135	-4.52619E-05	1.62748E-20	5.89522E-22
135.25	2.28504E-05	-8.21633E-21	-3.06838E-21
135.51	-2.45091E-05	8.81274E-21	4.21773E-22
135.74	-2.09809E-05	7.5441E-21	3.29878E-22
136.02	-2.29981E-05	8.26944E-21	2.83546E-22
136.25	-2.18603E-05	7.86031E-21	2.60793E-22
136.51	-2.3968E-05	8.61817E-21	3.32553E-22
136.72	-2.48676E-05	8.94164E-21	2.57016E-22
137	-2.47346E-05	8.89384E-21	3.98684E-22
137.24	-2.31324E-05	8.31772E-21	2.02978E-22
137.5	-2.77721E-05	9.98602E-21	3.20637E-22
Continued on next page			

Table C.1-2 – continued from previous page

5 July 2011			
Wavelength, λ (nm)	R_B	σ (cm ²)	$u(\sigma)$
137.79	-3.03308E-05	1.09061E-20	3.26143E-22
138.01	-2.8324E-05	1.01845E-20	3.79791E-22
138.25	-2.76379E-05	9.93776E-21	3.46851E-22
138.51	-2.16194E-05	7.77371E-21	2.73848E-22
138.76	-2.23737E-05	8.04491E-21	4.34718E-22
138.98	-2.76628E-05	9.94673E-21	2.07623E-22
139.23	-3.79915E-05	1.36606E-20	2.64748E-22
139.49	-4.11348E-05	1.47909E-20	7.49478E-22
139.79	-2.71186E-05	9.75105E-21	3.42594E-22
140.02	-1.64152E-05	5.90242E-21	1.46231E-22
140.27	-1.95927E-05	7.04496E-21	2.55806E-22
140.5	-2.6081E-05	9.37794E-21	3.58502E-22
140.75	-4.07788E-05	1.46628E-20	5.67478E-22
141	-2.85711E-05	1.02733E-20	5.66646E-22
141.25	-1.47669E-05	5.30976E-21	2.2575E-22
141.51	-1.12655E-05	4.05073E-21	1.61292E-22
141.75	-1.03741E-05	3.73021E-21	1.38305E-22
142	-1.07549E-05	3.86715E-21	1.34436E-22
142.25	-1.06835E-05	3.84149E-21	1.29279E-22
142.5	-9.50941E-06	3.4193E-21	2.59837E-22
142.76	-9.5787E-06	3.44422E-21	2.3109E-22
143	-1.13518E-05	4.08177E-21	1.52475E-22
143.25	-8.85553E-06	3.18419E-21	1.47144E-22
143.5	-7.91462E-06	2.84586E-21	3.68577E-22
143.74	-5.74833E-06	2.06693E-21	1.86191E-22
144	-7.09692E-06	2.55184E-21	3.37166E-22
144.25	-7.59349E-06	2.73039E-21	2.45389E-22
144.5	-8.57956E-06	3.08496E-21	2.82488E-22
144.76	-6.96929E-06	2.50595E-21	2.2477E-22
144.99	-7.05127E-06	2.53543E-21	1.79491E-22

Table C.1-3: Absolute Photoabsorption Cross-Section (σ) and Uncertainty Values ($u(\sigma)$) for $^{10}\text{BF}_3$ from 150-165 nm, 6 July 2011

6 July 2011 (150-165 nm)			
Wavelength, λ (nm)	R_B	σ (cm ²)	$u(\sigma)$
150.02	-7.04124E-06	2.53182E-21	3.41335E-23
150.25	-7.28681E-06	2.62012E-21	3.81451E-23
150.5	-7.64509E-06	2.74895E-21	6.51458E-23
150.75	-8.14446E-06	2.92851E-21	4.55186E-23
151	-8.35365E-06	3.00373E-21	2.44021E-23
151.25	-8.47553E-06	3.04755E-21	4.87439E-23
151.51	-7.98917E-06	2.87267E-21	3.9695E-23
151.75	-7.85427E-06	2.82417E-21	4.1434E-23
152	-8.12958E-06	2.92316E-21	5.69112E-23
152.25	-8.38788E-06	3.01603E-21	2.8185E-23
152.5	-8.79441E-06	3.16221E-21	3.24348E-23
152.75	-8.85794E-06	3.18505E-21	2.66192E-23
152.99	-8.51331E-06	3.06113E-21	2.12362E-23
153.25	-8.30498E-06	2.98623E-21	3.04345E-23
153.5	7.06828E-06	-2.54154E-21	-8.08555E-22
153.75	-8.82072E-06	3.17167E-21	4.37077E-23
154.01	-9.23576E-06	3.32091E-21	4.25337E-23
154.26	-9.81163E-06	3.52797E-21	4.04419E-23
154.5	-9.92125E-06	3.56739E-21	3.2778E-23
154.74	-9.95604E-06	3.5799E-21	1.7973E-23
154.99	-9.17804E-06	3.30015E-21	4.85713E-23
155.25	-8.31319E-06	2.98918E-21	3.3258E-23
155.51	-8.26032E-06	2.97017E-21	1.21723E-23
155.74	-8.3635E-06	3.00727E-21	3.15771E-23
155.99	-8.63699E-06	3.10561E-21	1.66581E-23
156.25	-8.93534E-06	3.21288E-21	2.17954E-23
156.51	-9.28586E-06	3.33892E-21	3.31426E-23
156.73	-9.90931E-06	3.56309E-21	1.43067E-23
156.99	-1.04958E-05	3.77397E-21	1.64525E-23
157.27	-1.07892E-05	3.87949E-21	2.88718E-23
157.5	-1.05642E-05	3.79859E-21	3.0923E-23
157.74	-1.00336E-05	3.60779E-21	2.49957E-23
157.99	-8.85351E-06	3.18346E-21	2.74449E-23
158.21	-7.31058E-06	2.62867E-21	2.05742E-23
158.54	-6.40882E-06	2.30442E-21	2.14431E-23
158.74	-6.37181E-06	2.29112E-21	1.87961E-23
159.01	-6.81141E-06	2.44918E-21	4.09794E-23
159.22	-7.40127E-06	2.66128E-21	1.73914E-23
Continued on next page			

Table C.1-3 – continued from previous page

6 July 2011 (150-165 nm)

Wavelength, λ (nm)	R_B	σ (cm ²)	$u(\sigma)$
159.5	-8.42389E-06	3.02898E-21	2.10817E-23
159.72	-9.06126E-06	3.25816E-21	4.48107E-23
160.02	-8.9566E-06	3.22053E-21	4.62901E-23
160.25	-7.73503E-06	2.78129E-21	4.02907E-23
160.5	-6.01567E-06	2.16306E-21	6.06312E-24
160.75	-4.35362E-06	1.56543E-21	1.2604E-23
161	-3.33922E-06	1.20069E-21	2.99083E-23
161.25	-2.84856E-06	1.02426E-21	2.07199E-23
161.51	-2.306E-06	8.29171E-22	1.46602E-23
161.75	-2.06964E-06	7.4418E-22	1.26559E-23
162	-1.70532E-06	6.13182E-22	2.19177E-23
162.25	-1.642E-06	5.90416E-22	1.58532E-23
162.5	-1.55308E-06	5.58443E-22	1.48426E-23
162.76	-1.50622E-06	5.41593E-22	2.02204E-23
163	-1.35705E-06	4.87956E-22	1.96201E-23
163.24	-1.37105E-06	4.92989E-22	1.60973E-23
163.5	-1.27487E-06	4.58404E-22	1.14869E-23
163.75	-1.18916E-06	4.27588E-22	1.51944E-23
164.01	-1.12787E-06	4.0555E-22	1.61481E-23
164.24	-1.10207E-06	3.96274E-22	2.22846E-23
164.52	-9.46013E-07	3.40158E-22	1.5291E-23
164.76	-1.01771E-06	3.65938E-22	8.83161E-24
165.03	-7.99617E-07	2.87519E-22	2.23931E-23

Table C.1-4: Absolute Photoabsorption Cross-Section (σ) and Uncertainty Values ($u(\sigma)$) for $^{10}\text{BF}_3$ from 190-205 nm, 6 July 2011

6 July 2011 (190-205 nm)			
Wavelength, λ (nm)	R_B	σ (cm^2)	$u(\sigma)$
190.01	8.81112E-08	-3.16822E-23	-1.0553E-23
190.25	1.29237E-05	-4.64697E-21	-4.8327E-22
190.5	1.93952E-07	-6.97395E-23	-1.31107E-23
190.75	-1.52618E-09	5.48768E-25	1.12592E-23
191	9.31757E-08	-3.35032E-23	-9.69042E-24
191.26	-3.3472E-08	1.20355E-23	9.64244E-24
191.51	2.67048E-08	-9.60225E-24	-1.59267E-23
191.75	6.14791E-08	-2.21061E-23	-8.61073E-24
192	5.03393E-08	-1.81005E-23	-1.28786E-23
192.25	-9.25026E-08	3.32612E-23	8.15101E-24
192.5	-1.8737E-07	6.73726E-23	1.64467E-23
192.75	-2.38744E-07	8.58455E-23	1.35345E-23
192.99	-8.11181E-08	2.91677E-23	1.36152E-23
193.24	-5.96936E-08	2.14641E-23	1.31128E-23
193.5	-3.21993E-08	1.15779E-23	5.602E-24
193.75	-3.09515E-07	1.11292E-22	7.80689E-24
193.99	-4.58019E-07	1.6469E-22	1.09743E-23
194.25	-3.21425E-07	1.15575E-22	1.34183E-23
194.51	-2.00347E-07	7.20388E-23	1.05635E-23
194.77	-2.04598E-07	7.35674E-23	6.88748E-24
194.98	-2.55352E-07	9.18172E-23	1.05771E-23
195.23	-5.46228E-07	1.96407E-22	1.79295E-23
195.49	-7.38945E-07	2.65703E-22	1.13831E-23
195.73	-7.51607E-07	2.70256E-22	1.10256E-23
195.97	-4.9157E-07	1.76754E-22	6.6895E-24
196.27	-3.28269E-07	1.18036E-22	8.66896E-24
196.5	-3.13028E-07	1.12556E-22	6.63524E-24
196.76	-5.52441E-07	1.98641E-22	1.22405E-23
197	-9.79694E-07	3.52269E-22	7.79997E-24
197.26	-9.24331E-07	3.32362E-22	1.70501E-23
197.5	-4.76921E-07	1.71487E-22	1.0882E-23
197.72	-3.87257E-07	1.39246E-22	1.01172E-23
198	-3.57771E-07	1.28644E-22	1.23777E-23
198.24	-6.85749E-07	2.46575E-22	1.20691E-23
198.54	-1.02973E-06	3.70261E-22	1.74346E-23
198.73	-1.22326E-06	4.39847E-22	6.78028E-24
199.01	-5.45225E-07	1.96047E-22	1.38718E-23
199.25	-1.74356E-07	6.26932E-23	7.77685E-24
Continued on next page			

Table C.1-4 – continued from previous page

6 July 2011 (190-205 nm)			
Wavelength, λ (nm)	R_B	σ (cm ²)	$u(\sigma)$
199.5	-2.80698E-07	1.00931E-22	9.49042E-24
199.76	-4.90147E-07	1.76242E-22	2.19158E-23
200.03	-8.88838E-07	3.196E-22	2.15227E-23
200.25	-1.11035E-06	3.9925E-22	2.05487E-23
200.5	-5.75795E-07	2.07039E-22	1.03006E-23
200.75	-1.49158E-07	5.36328E-23	1.53708E-23
201	-6.41258E-08	2.30577E-23	1.27463E-23
201.25	-2.88892E-07	1.03877E-22	1.13022E-23
201.5	-5.72588E-07	2.05886E-22	1.35461E-23
201.75	-8.57715E-07	3.08409E-22	1.03347E-23
202	-5.61413E-07	2.01868E-22	1.6917E-23
202.25	-2.15925E-07	7.76401E-23	1.3861E-23
202.5	2.39132E-08	-8.59848E-24	-1.40008E-23
202.75	3.30023E-08	-1.18667E-23	-1.29279E-23
203	-2.21144E-07	7.95168E-23	1.04955E-23
203.25	-4.91016E-07	1.76555E-22	1.33518E-23
203.49	-4.51492E-07	1.62343E-22	1.56674E-23
203.75	-9.36842E-08	3.36861E-23	1.43791E-23
203.99	-1.49075E-08	5.36028E-24	1.11495E-23
204.23	2.04473E-07	-7.35224E-23	-1.41676E-23
204.49	9.79001E-08	-3.5202E-23	-1.29344E-23
204.75	5.35739E-08	-1.92636E-23	-9.94793E-24
205.01	-1.04043E-07	3.74109E-23	1.05377E-23

Appendix D

Standard Operating Procedure for MUTR Gas Handling System

D.1 Introduction

The BF_3 inlet valve, cold trap outlet valve, scrubber inlet valve, and glove box exhaust valve are all automated and operate through the use of a switchboard. The remaining valves must be controlled manually. It is the purpose of this procedure to ensure that the correct sequence of valves are opened and closed throughout the course of the BF_3 FUND experiment. Refer to Figure D.1-1 and Table D.1-1.

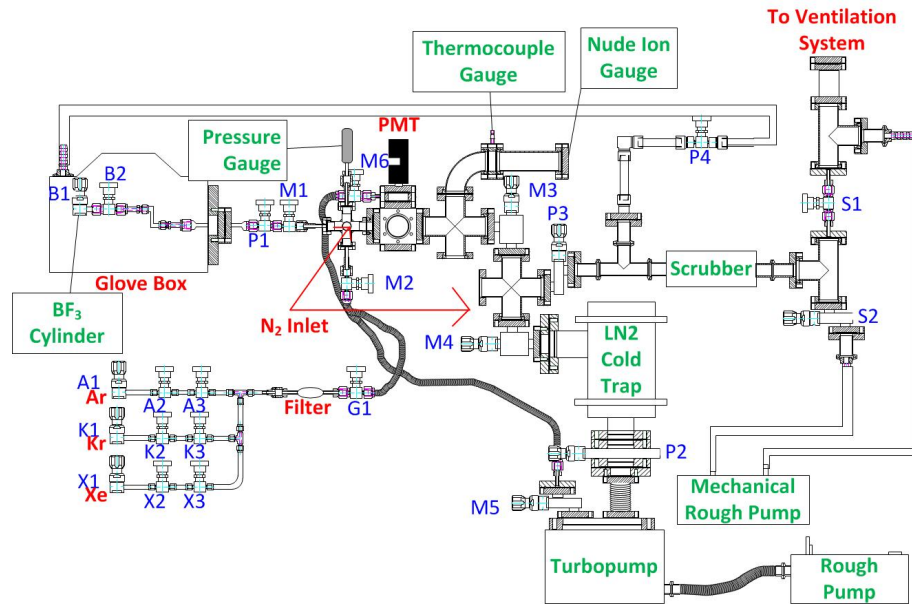


Figure D.1-1: MUTR $^{10}\text{BF}_3$ Gas Handling System. Neutrons flowed in the plane of the page.

Table D.1-1: Description of valves used in the MUTR BF₃ Gas Handling System.
Valves with an (M) designation were manually controlled; valves with an (A)
designation were controlled by a switchboard.

Valve	Description	Valve	Description
Ar	Argon Gas Cylinder (M)	M6	Differential Volume Shutoff Valve (M)
A1	Argon Regulator (M)	Dry N2	Dry Nitrogen Gas Cylinder (M)
A2	Argon Shutoff Valve (M)	N1	Nitrogen Regulator (M)
A3	Argon Metering Valve (M)	N2	Nitrogen Shutoff Valve (M)
BF3	BF ₃ Gas Cylinder (M)	N3	Nitrogen Inlet Valve #1 (M)
B1	BF ₃ Regulator (M)	N4	Nitrogen Inlet Valve #2 (M)
B2	BF ₃ Shutoff Valve (M)	P1	BF ₃ Inlet Valve (A)
G1	Noble Gas Inlet Control Valve (M)	P2	Cold Trap Outlet Valve (A)
Kr	Krypton Gas Cylinder (M)	P3	Scrubber Inlet Valve (A)
K1	Krypton Regulator (M)	P4	Glovebox Exhaust Valve (A)
K2	Krypton Shutoff Valve (M)	S1	Ventilation System Isolation Valve (M)
K3	Krypton Metering Valve (M)	S2	Scrubber Outlet Valve (M)
M1	BF ₃ Metering Valve (M)	Xe	Xenon Gas Cylinder (M)
M2	Noble Gas Inlet Shutoff Valve (M)	X1	Xenon Regulator (M)
M3	Cube Outlet Shutoff Valve (M)	X2	Xenon Shutoff Valve (M)
M4	Cold Trap Inlet Valve (M)	X3	Xenon Metering Valve (M)
M5	Differential Volume Isolation Valve (M)		

D.2 Procedure

D.2.1 Stage 1: System Pump Down

There are several instances in which the entire system will require a total evacuation. These include the initial pump down to evacuate the cell, after the conclusion of each set of experiments, and in the infrequent instances in which the mist eliminator filter needs to be changed (which necessitates breaking the vacuum on the system). Note that in the noble gas line valves X1, X2, K1, K2, A1, and A2 may be in the OPEN

position at any time, so long as valves X3, K3, and A3 are CLOSED unless otherwise specified.

2.1.1 Ensure the system is as free of residual BF₃ gas as possible. For this procedure, please refer to Stage 4: Dry N₂ purge.

2.1.2 Ensure that the BF₃ cylinder is CLOSED.

2.1.3 Ensure that the noble gas cylinders (Xe, Kr, Ar) are all CLOSED.

2.1.4 Ensure that the liquid nitrogen cold trap has been filled with LN₂. If more is required, add to the top of the cold trap. This is REQUIRED to protect the turbopump from any accidental influx of BF₃.

2.1.5 Ensure that the MANUALLY controlled valves listed in Table D.2.1-1 are in the CLOSED position (please refer to Figure D.1-1 for the location of each valve). All valves that have VITALLY important positions are highlighted and in italicized font.

Table D.2.1-1: Manual Valves in Initially Closed Position During Pump Down

Valve Designation	Valve Description	Position
X3	Xe Shutoff	CLOSED
K3	Kr Shutoff	CLOSED
A3	Ar Shutoff	CLOSED
G1	Noble Gas Shutoff	CLOSED
B1	BF ₃ Regulator	CLOSED
M1	BF ₃ Metering Valve	CLOSED
M2	Noble Gas Inlet Shutoff	CLOSED
M3	Cube Outlet Shutoff	CLOSED
M4	Cold Trap Inlet	CLOSED
N1	N ₂ Regulator	CLOSED
N2	N ₂ Regulator Shutoff	CLOSED
N3	N ₂ Inlet to BF ₃ Side	CLOSED
N4	N ₂ Inlet to Scrubber Side	CLOSED

2.1.6 Ensure that the PNEUMATIC valves listed in Table D.2.1-2 are CLOSED. This can be verified by checking the position of each of the switches on the switchboard. If any switch is in the UP position, or there is any colored light illuminated, one or more of the valves are OPEN. Flip the switches to the OFF or NEUTRAL position to CLOSE the valves.

Table D.2.1-2: Pneumatic Valves in Initially Closed Position During Pump Down

Valve Designation	Valve Description	Position
P1	BF ₃ Inlet	CLOSED
P2	Cold Trap Outlet	CLOSED
P3	Scrubber Inlet	CLOSED

2.1.7 Flip switch 1 on the switch board to open the COLD TRAP OUTLET VALVE (P2). The white light will come on and the switch will audibly change states.

2.1.8 SLOWLY open the cold trap inlet valve (M4), cube outlet shutoff valve (M3), and the noble gas inlet shutoff valve (M2). On the noble gas manifold side, the remaining valves may all be opened at this point (G1, X3, K3, and A3). This will open the vacuum system up through the noble gas manifold to the pump. The BF₃ manifold is still isolated from the system. The MANUAL valves listed in Table D.2.1-3 should all now be in the OPEN position. If they are not, ensure they are set to the OPEN position. Anything not listed must be CLOSED. All valves listed in Table D.2.1-4 must be CLOSED.

Table D.2.1-3: Manual Valves Changed to the Open Position During Pump Down

Valve Designation	Valve Description	Position
X1	Xe Regulator	OPEN
X2	Xe Regulator Shutoff	OPEN
X3	Xe Shutoff	OPEN
K1	Kr Regulator	OPEN
K2	Kr Regulator Shutoff	OPEN
K3	Kr Shutoff	OPEN
A1	Ar Regulator	OPEN
A2	Ar Regulator Shutoff	OPEN
A3	Ar Shutoff	OPEN
G1	Noble Gas Shutoff	OPEN
M2	Noble Gas Inlet Shutoff	OPEN
M3	Cube Outlet Shutoff	OPEN
M4	Cold Trap Inlet	OPEN
M5	Differential Volume Isolation Valve	OPEN

Table D.2.1-4: Valves in the Closed Position After Initial Valve Manipulation

Valve Designation	Valve Description	Position
B1	BF ₃ Regulator	CLOSED
P1	BF ₃ Inlet	CLOSED
P3	Scrubber Inlet	CLOSED
M1	BF ₃ Metering Valve	CLOSED
N1	N ₂ Regulator	CLOSED
N2	N ₂ Regulator Shutoff	CLOSED
N3	N ₂ Inlet to BF ₃ Side	CLOSED
N4	N ₂ Inlet to Scrubber Side	CLOSED

2.1.9 When ready, depress the red pushbutton labeled PUMP DLY ON. This will trigger a timer that will automatically open the BF₃ inlet pneumatic valve (P1) after a period of 1 hour.

2.1.10 SLOWLY open the BF₃ metering valve (M1). The entire system is now open to the pump, with the exception of the nitrogen line.

D.2.2 Stage 2: Introduction of Noble Gas

Once the system has been properly evacuated, it is now safe to begin the slow, controlled introduction of gas into the cube. The noble gas will be introduced into the cell before the BF₃ to minimize back flow of BF₃ into the noble gas manifold.

2.2.1 Close the following MANUALLY controlled valves in this sequence: BF₃ metering valve (M1), Noble Gas Inlet Shutoff Valve (M2), Noble Gas Shutoff Valve (G1), Argon Shutoff Valve (A3), Krypton Shutoff Valve (K3), Xenon Shutoff Valve (X3), Cube Outlet Shutoff Valve (M3), Cold Trap Inlet Valve (M4).

2.2.2 Flip the PUMP DOWN switch to the OFF position on the switch board. The valves listed in Table D.2.2-1 should now be CLOSED. All valves that have VITALLY important positions are highlighted and italicized.

Table D.2.2-1: Valves in the Closed Position Prior to Introduction of Noble Gas

Valve Designation	Valve Description	Position
X3	Xe Shutoff	CLOSED
K3	Kr Shutoff	CLOSED
A3	Ar Shutoff	CLOSED
G1	Noble Gas Shutoff	CLOSED
<i>P1</i>	<i>BF₃ Inlet</i>	CLOSED
<i>P2</i>	<i>Cold Trap Outlet</i>	CLOSED
P3	Scrubber Inlet	CLOSED
<i>M1</i>	<i>BF₃ Metering Valve</i>	CLOSED
M2	Noble Gas Inlet Shutoff	CLOSED
<i>M3</i>	<i>Cube Outlet Shutoff</i>	CLOSED
<i>M4</i>	<i>Cold Trap Inlet</i>	CLOSED
N1	N ₂ Regulator	CLOSED
N2	N ₂ Regulator Shutoff	CLOSED

2.2.3 Select the noble gas to be inserted into the cube (Xe, Kr, or Ar) and slowly open the cylinder specific to the gas selected.

2.2.4 Slowly open the selected gas shutoff valve (X3, K3, or A3) and allow the gas to flow through the manifold.

2.2.5 Open the noble gas inlet valve (M2). The valves listed in Table D.2.2-2 should now be OPEN. Anything not listed must be CLOSED.

Table D.2.2-2: Valves in the Open Position During Noble Gas Introduction

Valve Designation	Valve Description	Position
X1	Xe Regulator	OPEN
X2	Xe Regulator Shutoff	OPEN
X3 OR K3 OR A3	Xe/Kr/Ar Shutoff	OPEN
K1	Kr Regulator	OPEN
K2	Kr Regulator Shutoff	OPEN
A1	Ar Regulator	OPEN
A2	Ar Regulator Shutoff	OPEN
M2	Noble Gas Inlet Shutoff	OPEN
M5	Differential Volume Isolation Valve	OPEN

2.2.6 While monitoring the pressure inside the cell on any one of the three pressure gauges (recommended is the digital reader connected to the Swagelok®PTU located just prior to the cube on the 6-way cross), SLOWLY open the noble gas shutoff valve (G1) and inject a carefully controlled amount of gas into the cell.

2.2.7 Close the noble gas shutoff valve (G1) when the prescribed amount of gas has been introduced into the cube.

D.2.3 Stage 3: Introduction of BF₃

Once the noble gas has been introduced into the cell, it is safe to introduce BF₃ into the same cell with the noble gas.

2.3.1 SLOWLY close the following valves in this order: Noble Gas Inlet Shutoff Valve (M2), Noble Gas Shutoff Valve (G1), and X3/K3/A3, depending on which gas was previously introduced into the cell. The valves listed in Table D.2.3-1 must now be CLOSED. All valves that have VITALLY important positions are highlighted and italicized.

Table D.2.3-1: Valves in the Closed Position Prior to BF₃ Introduction

Valve Designation	Valve Description	Position
X3	Xe Shutoff	CLOSED
K3	Kr Shutoff	CLOSED
A3	Ar Shutoff	CLOSED
<i>G1</i>	<i>Noble Gas Shutoff</i>	CLOSED
<i>P1</i>	<i>BF₃ Inlet</i>	CLOSED
<i>P2</i>	<i>Cold Trap Outlet</i>	CLOSED
P3	Scrubber Inlet	CLOSED
<i>M1</i>	<i>BF₃ Metering Valve</i>	CLOSED
M2	Noble Gas Inlet Shutoff	CLOSED
<i>M3</i>	<i>Cube Outlet Shutoff</i>	CLOSED
<i>M4</i>	<i>Cold Trap Inlet</i>	CLOSED
N1	N ₂ Regulator	CLOSED
N2	N ₂ Regulator Shutoff	CLOSED
N3	N ₂ Inlet to BF ₃ Side	CLOSED
N4	N ₂ Inlet to Scrubber Side	CLOSED

2.3.2 Flip the switch labeled BF₃ on the switchboard to the UP position. The green indicator light should be illuminated. This triggers the BF₃ pneumatic inlet valve (P1). The valve DOES NOT CHANGE STATE.

2.3.3 SLOWLY open the BF_3 cylinder (the BF_3 regulator should be OPEN) and allow BF_3 to flow through the line up to the BF_3 pneumatic inlet valve (P1).

2.3.4 Depress the red pushbutton labeled BF_3 DLY OFF. This will momentarily open the BF_3 pneumatic inlet valve (P1) and allow approximately 60 torr of gas between the BF_3 pneumatic inlet valve and the BF_3 metering valve (M1).

2.3.5 While monitoring the pressure inside the cell on any one of the three pressure gauges (recommended is the digital reader connected to the Swagelok[®]PTU located just prior to the cube on the 6-way cross), SLOWLY open the BF_3 metering valve (M1) and allow approximately 20 torr of BF_3 to flow into the cube.

2.3.6 Close the BF_3 metering valve (M1) when the prescribed amount of gas has been introduced into cube.

2.3.7 Repeat steps 2.3.4 through 2.3.6 as necessary.

D.2.4 Stage 4: Dry N_2 Purge

At the conclusion of the BF_3 /noble gas experiments, the cube must be emptied and the entire system purged so the next set of experiments can be conducted.

2.4.1 Flip the switch labeled BF_3 to the DOWN position. This will ensure the BF_3 pneumatic inlet valve (P1) is CLOSED and that no further introduction of BF_3 into the system can occur.

2.4.2 SLOWLY open the BF_3 metering valve (M1) and allow any excess BF_3 still between the BF_3 pneumatic inlet valve (P1) and the BF_3 metering valve (M1) to flow into the cube. The valves listed in Table D.2.4-1 should now be CLOSED. All

valves that have VITALLY important positions are highlighted. The valves listed in Table D.2.4-2 should be OPEN.

Table D.2.4-1: Valves in the Closed Position Prior to Dry N₂ Purge

Valve Designation	Valve Description	Position
X3	Xe Shutoff	CLOSED
K3	Kr Shutoff	CLOSED
A3	Ar Shutoff	CLOSED
G1	Noble Gas Shutoff	CLOSED
P1	<i>BF₃ Inlet</i>	CLOSED
P2	<i>Cold Trap Outlet</i>	CLOSED
P3	Scrubber Inlet	CLOSED
M2	<i>Noble Gas Inlet Shutoff</i>	CLOSED
M3	<i>Cube Outlet Shutoff</i>	CLOSED
M4	<i>Cold Trap Inlet</i>	CLOSED
N1	N ₂ Regulator	CLOSED
N2	N ₂ Regulator Shutoff	CLOSED
N3	N ₂ Inlet to BF ₃ Side	CLOSED
N4	N ₂ Inlet to Scrubber Side	CLOSED

Table D.2.4-2: Valves in the Open Position Prior to Dry N₂ Purge

Valve Designation	Valve Description	Position
X1	Xe Regulator	OPEN
X2	Xe Regulator Shutoff	OPEN
X3 OR K3 OR A3	Xe/Kr/Ar Shutoff	OPEN
K1	Kr Regulator	OPEN
K2	Kr Regulator Shutoff	OPEN
A1	Ar Regulator	OPEN
A2	Ar Regulator Shutoff	OPEN
B1	BF ₃ Regulator	OPEN
P4	Glove Box Exhaust to Scrubber	OPEN
M1	BF ₃ Metering Valve	OPEN
M5	Differential Volume Isolation Valve	OPEN

2.4.3 SLOWLY open the N₂ cylinder.

2.4.4 SLOWLY open the following valves in the following sequence: N₂ Regulator (N1), N₂ Regulator Shutoff Valve (N2), N₂ Inlet to BF₃ Side (N3), and N₂ Inlet to Scrubber Side (N4). This will allow the dry N₂ to fill the entire vacuum system and mix with the BF₃/noble gas mixture inside the cube, and also act as a buffer between the back side of the cube and the pump.

2.4.5 SLOWLY open the Cube Outlet Shutoff Valve (M3) to allow the dry N₂/BF₃/noble gas mixture to flow out of the cube.

2.4.6 Flip the switch labeled PURGE to the UP position to open the scrubber inlet valve. Allow the dry N₂ purge to continue for at least 20 minutes.

2.4.7 At the conclusion of the purge, flip the PURGE switch to the OFF position.

Table D.2.4-3: Valve logic for BF₃ gas handling system. Initial valve configuration for each stage of experimental procedure.

		Pump Down	Introduction of BF₃	Introduction of Noble Gas	N₂ Purge
Designation	Description				
X1	Xe Regulator	OPEN	OPEN	OPEN	OPEN
X2	Xe Regulator Shutoff	OPEN	OPEN	OPEN	OPEN
X3	Xe Shutoff	CLOSED	CLOSED	CLOSED	CLOSED
K1	Kr Regulator	OPEN	OPEN	OPEN	OPEN
K2	Kr Regulator Shutoff	OPEN	OPEN	OPEN	OPEN
K3	Kr Shutoff	CLOSED	CLOSED	CLOSED	CLOSED
A1	Ar Regulator	OPEN	OPEN	OPEN	OPEN
A2	Ar Regulator Shutoff	OPEN	OPEN	OPEN	OPEN
A3	Ar Shutoff	CLOSED	CLOSED	CLOSED	CLOSED
G1	Noble Gas Shutoff	CLOSED	CLOSED	CLOSED	CLOSED

Continued on next page

Table D.2.4-3 – continued from previous page

		Pump Down	Introduction of BF ₃	Introduction of Noble Gas	N ₂ Purge
Designation	Description				
B1	BF ₃ Regulator	OPEN	OPEN	OPEN	OPEN
P1	BF ₃ Inlet	CLOSED	CLOSED	CLOSED	CLOSED
P2	Cold Trap Outlet	CLOSED	CLOSED	CLOSED	CLOSED
P3	Scrubber Inlet	CLOSED	CLOSED	CLOSED	CLOSED
P4	Glove Box Exhaust to Scrubber	OPEN	OPEN	OPEN	OPEN
M1	BF ₃ Metering Valve	CLOSED	CLOSED	CLOSED	CLOSED
M2	Noble Gas Inlet Shutoff	CLOSED	CLOSED	CLOSED	CLOSED
M3	Cube Outlet Shutoff	CLOSED	CLOSED	CLOSED	CLOSED
M4	Cold Trap Inlet	CLOSED	CLOSED	CLOSED	CLOSED
M5	Differential Volume Isolation Valve	OPEN	OPEN	OPEN	OPEN
N1	N ₂ Regulator	CLOSED	CLOSED	CLOSED	CLOSED
N2	N ₂ Regulator Shutoff	CLOSED	CLOSED	CLOSED	CLOSED
N3	N ₂ Inlet to BF ₃ Side	CLOSED	CLOSED	CLOSED	CLOSED
N4	N ₂ Inlet to Scrubber Side	CLOSED	CLOSED	CLOSED	CLOSED

Table D.2.4-4: Valve logic for BF₃ gas handling system. Final valve configuration for each stage of experimental procedure.

		Pump Down	Introduction of BF ₃	Introduction of Noble Gas	N ₂ Purge
Designation	Description				
X1	Xe Regulator	OPEN	OPEN	OPEN	OPEN
X2	Xe Regulator Shutoff	OPEN	OPEN	OPEN	OPEN
X3	Xe Shutoff	OPEN	CLOSED	OPEN	CLOSED
K1	Kr Regulator	OPEN	OPEN	OPEN	OPEN
Continued on next page					

Table D.2.4-4 – continued from previous page

		Pump Down	Introduction of BF₃	Introduction of Noble Gas	N₂ Purge
Designation	Description				
K2	Kr Regulator Shutoff	OPEN	OPEN	OPEN	OPEN
K3	Kr Shutoff	OPEN	CLOSED	OPEN	CLOSED
A1	Ar Regulator	OPEN	OPEN	OPEN	OPEN
A2	Ar Regulator Shutoff	OPEN	OPEN	OPEN	OPEN
A3	Ar Shutoff	OPEN	CLOSED	OPEN	CLOSED
G1	Noble Gas Shutoff	OPEN	OPEN	OPEN	CLOSED
B1	BF ₃ Regulator	OPEN	OPEN	CLOSED	OPEN
P1	BF ₃ Inlet	OPEN	OPEN	CLOSED	CLOSED
P2	Cold Trap Outlet	OPEN	CLOSED	CLOSED	CLOSED
P3	Scrubber Inlet	CLOSED	CLOSED	CLOSED	OPEN
P4	Glove Box Exhaust to Scrubber	OPEN	OPEN	OPEN	CLOSED
M1	BF ₃ Metering Valve	OPEN	OPEN	CLOSED	OPEN
M2	Noble Gas In- let Shutoff	OPEN	CLOSED	CLOSED	CLOSED
M3	Cube Outlet Shutoff	OPEN	CLOSED	CLOSED	OPEN
M4	Cold Trap In- let	OPEN	CLOSED	CLOSED	CLOSED
M5	Differential Volume Isola- tion Valve	OPEN	OPEN	OPEN	OPEN
N1	N ₂ Regulator	CLOSED	CLOSED	CLOSED	OPEN
N2	N ₂ Regulator Shutoff	CLOSED	CLOSED	CLOSED	OPEN
N3	N ₂ Inlet to BF ₃ Side	CLOSED	CLOSED	CLOSED	OPEN
N4	N ₂ Inlet to Scrubber Side	CLOSED	CLOSED	CLOSED	OPEN

Bibliography

- [1] T.M. Persons and G. Aloise. Neutron detectors: Alternatives to using helium-3. tech. rep. GAO-11-753, United States Government Accountability Office, September 2011.
- [2] D. Dixon. Helium-3 shortage could mean nuke detection disaster. *Wired*. April 2010.
- [3] G. F. Knoll. *Radiation Detection and Measurement*. John Wiley and Sons, New York, 1979.
- [4] W.D. Allen. *Neutron Detection*. George Newnes Limited, London, 1960.
- [5] Joseph A. Angelo. *Nuclear Technology* Greenwood Press, 2004.
- [6] V. F. Hess. Observations in low level radiation during seven free balloon flights. *Phys. Z* 13 (1912) 1084.
- [7] [Internet] c2002. The QuarkNet Online Cosmic Ray Detector. [cited 25 February 2012] Available from: <http://quarknet.fnal.gov/cosmics/background.shtml>.
- [8] Serge A. Korff. *Electron and Nuclear Counters: Theory and Use* D. Van Nostrand Company, Inc., 1955.
- [9] [Internet] c2001. Fermilab's CDF Detector. [cited 25 February 2012] Available from: <http://quarknet.fnal.gov/run2/cdf.html>.
- [10] [Internet] c2001. Anatomy of a Detector. [cited 25 February 2012]. Available from: <http://quarknet.fnal.gov/run2/script.shtml>.
- [11] [Internet] c1997. The Detector. [cited 25 February 2012]. Available from: <http://www.hep.man.ac.uk/u/events/detector.html>.
- [12] T.A.J. Jaques, H.A. Ballinger, and F. Wade. Neutron detectors for reactor instrumentation. *Proceedings of the IEE-Part I: General* 100, no. 123 (1953): 110-116.
- [13] [Internet] c.2012. Neutron monitoring Instrumentation. [cited 12 November 2012]. Available from: <http://www.ge-mcs.com/en/nuclear-reactor-instrumentation/neutron-monitoring-instrumentation.html>
- [14] Safety Analysis Report for the Maryland University Training Reactor. tech. rep., University of Maryland, 2000.
- [15] William J. Price. *Nuclear Radiation Detection*. McGraw-Hill Book Company, 1964.
- [16] John R. Lamarsh. *Introduction to Nuclear Engineering*. 2nd ed. Addison-Wesley Publishing Company, Reading, MA, 1983.

- [17] Victor Bom. Fast Neutron Imaging for SNM Detection. Delft University of Technology, Netherlands.
- [18] R.V. Ginhoven, R. Kouzes, and D. Stevens. Alternative neutron detector technologies for homeland security. tech. report PNNL-18471, Pacific Northwest National Laboratory, 2009.
- [19] R.T. Kouzes, E.R. Siciliano, J.H. Ely, P.E. Keller, and R.J. McConn. Passive neutron detection for interdiction of nuclear material at borders. *Nucl. Instrum. Meth. A.* 584, no. 2 (2008): 383.
- [20] Committee on Radiation Source Use and Replacement and the National Research Council. *Radiation Source Use and Replacement*. National Academies Press, 2008. ch 9, pp 147.
- [21] M. Suto, C. Ye, and L.C. Lee. Photoabsorption and fluorescence spectroscopy of BF_3 in the extreme-vacuum-ultraviolet region. *Phys. Rev. A.* 42, no. 1 (1990): 424.
- [22] G. Hagenow, K. Hottmann, H. W. Jochims, and H. Baumgrtel. The photoabsorption of BF_3 in the energy range 6.5-20 eV. *Chem. Phys.* 137 (1989): 287.
- [23] G. Hagenow, K. Hottmann, and H. Baumgrtel. Vibronic couple effects observed in the high-resolution He(I) photoelectron spectra of BF_3 . *Chem. Phys. Lett.* 164, no. 4 (1989): 385.
- [24] H.J. Maria, J.R. McDonald, and S.P. McGlynn. Electronic absorption spectrum of nitrate ion and boron trihalides. *J. Am. Chem. Soc.* 95, no. 4 (1973): 1050.
- [25] A.A. Planckaert, P. Sauvageau, and C. Sandorfy. The vacuum-ultraviolet absorption spectra of boron-trihalides. *Chem. Phys. Lett.* 20, no. 2 (1973): 170.
- [26] S. Mughabghab. *Atlas of Neutron Resonances: Resonance Parameters and Thermal Neutron Cross Sections*. 5th ed. Elsevier, 2006.
- [27] Nicholas Tsoulfanidis. *Measurement and Detection of Radiation*. 2nd ed. Taylor & Francis, 1995.
- [28] T. Crane and M. Baker, *Passive Nondestructive Assay of Nuclear Material*. NRC, 1991.
- [29] Honeywell [Internet]. c2006. Honeywell Boron Trifluoride: Technical Information. [cited 1 September 2011] Available from: http://www51.honeywell.com/sm/bf3/common/documents/FP_BF3_Technical_Information_Manual.pdf.
- [30] C. van Eijk, A. Bessiere, and P. Dorenbos. Inorganic thermal-neutron scintillators. *Nucl. Instrum. Meth. A.* 529 (2004): 260.
- [31] B. Eliasson and U. Kogelschatz. *Appl. Phys. B.* 46, 299 (1988).

- [32] P. P. Hughes, M. A. Coplan, A. K. Thompson, R. E. Vest, and C. W. Clark. Far-ultraviolet signatures of the ${}^3\text{He}(n, tp)$ reaction in noble gas mixtures. *App. Phys. Lett.* 97, no. 23 (2010): 234105.
- [33] E. Aprile, A. Bolotnikov, A. Bolozdynya, and T. Doke. *Noble Gas Detectors*. Wiley VCH, London: 2006.
- [34] A. Sobottka, L. Prganer, L. Drer, M. Lenk [Internet]. c2008. Argon Excimer Lamp [cited 30 August 2011] Available from: [http://www.uni-leipzig.de/~sim\\$iom/muehleithen/2008/sobottka_argon_lamp.pdf](http://www.uni-leipzig.de/~sim$iom/muehleithen/2008/sobottka_argon_lamp.pdf).
- [35] Y. Tanaka, A.S. Jursa, and F.J. LeBlanc. Continuous emission spectra of rare gases in the vacuum ultraviolet region. II. Neon and Helium. *J. Opt. Soc. Am.* 48, no. 5 (1958): 304.
- [36] Y. Tanaka. Continuous emission spectra of rare gases in the vacuum ultraviolet region. *J. Opt. Soc. Am.* 45, no. 9 (1955): 710.
- [37] R. Brodmann and G. Zimmerer. Vacuum-ultraviolet fluorescence under monochromatic excitation and collision processes in gaseous Kr and Xe. *J. Phys. B* 10, no. 17 (1977): 3395.
- [38] M. Suzuki and S. Kubota. Mechanism of proportional scintillation in Argon, Krypton and Xenon. *Nuc. Inst. Meth.* 164 (1979): 197.
- [39] C.M.B. Monteiro, J.A.M. Lopes, J.F.C.A. Veloso, and J.M.F. dos Santos. Secondary scintillation yield in pure argon. *Phys. Lett. B* 668 (2007): 167.
- [40] C.M.B. Monteiro, L.M.P. Fernandes, J.A.M. Lopes, L.C.C. Coelho, J.F.C.A. Veloso, J.M.F. dos Santos, K. Giboni, and E. Aprile. Secondary scintillation yield in pure xenon. *J. Inst.* 2 (2007).
- [41] M. Mutterer, J.P. Theobald, and K.-P. Schelhaas. A low pressure noble-gas scintillation counter for heavy-ion detection. *Nuc. Inst. Meth.* 144 (1977): 159.
- [42] C.A.N. Conde and A.J.P.L. Policarpo. A gas proportional scintillation counter. *Nuc. Inst. Meth.* 53 (1967): 7.
- [43] R.A. Nobles. Detection of charged particles with gas scintillation counters. *Rev. Sci. Inst.* 27, no. 5 (1956): 280.
- [44] C.A.N. Conde, A.J.P.L. Policarpo, and M.A.F. Alves. Gas proportional scintillation counter with Xenon and Xenon mixtures. Laboratório de Física, Universidade de Coimbra, Coimbra Portugal.
- [45] P.E. Thiess and G.H. Miley. New near-infrared and ultraviolet gas-proportional scintillation counters. University of Illinois, Urbana, IL.

- [46] C.A.N. Conde, L. Requiche Ferreira, and M. Fátima. The secondary scintillation output of Xenon in a uniform gas proportional scintillation counter. Laboratório de Física, Universidade de Coimbra, Coimbra Portugal.
- [47] J.A.M. Lopes, J.M.F. dos Santos, R.E. Morgado, and C.A.N. Conde. A Xenon gas proportional scintillation counter with a UV-sensitive large-area avalanche photodiode. *IEEE Trans. Nuc. Sci.* 48, no. 3 (2001): 312.
- [48] J.M.F. Dos Santos, A.C.S.S.M. Bento and C.A.N. Conde. The dependence of the energy resolution of gas proportional scintillation counters on the scintillation region to photomultiplier distance. Physics Department, University of Coimbra, Coimbra, Portugal.
- [49] A.K. Thompson, M.A. Coplan, J.W. Cooper, P.P. Hughes, R.E. Vest, C.W. Clark. Observation of the ${}^3\text{He}(n, tp)$ reaction by detection of far-ultraviolet radiation. *J. Res. Natl. Inst. Stan.* 113, (2008).
- [50] R.E. Williams. "The NIST research reactor and cold neutron source." Presentation. NIST Center for Neutron Research, June 2007.
- [51] [Internet] c.2011. "Competitive Asset: NIST Center for Neutron Research." [cited 12 November 2012]. Available from: http://www.nist.gov/public_affairs/factsheet/ncnr-factsheet.cfm.
- [52] J. Nico, M. Arif, M. Dewey, T. Gentile, D. Gilliam, P. Huffman, D. Jacobson, and A. Thompson. The fundamental neutron physics facilities at NIST. *J. Res. Natl. Inst. Stan.* 110, no. 3 (2005): 137.
- [53] J.W. Cooper and P.P. Hughes. The detection of Lyman-alpha radiation formed by the slowing down of protons and tritons produced by the ${}^3\text{He}(n, tp)$ reaction—a model study. *J. Res. Natl. Inst. Stan.* 114, no. 3 (2009): 185.
- [54] J. McComb. Neutron detection based on far-ultraviolet excimer emission. Thesis Dissertation. 14 August 2012.
- [55] Ceradyne, Inc. Certificate of Lot Analysis for ${}^{10}\text{BF}_3$. Obtained from Elizabeth R. Utley.
- [56] NIST SURF [Internet]. c2010. What is Synchrotron Radiation? [cited 2011 June 13] Available from: <http://www.nist.gov/pml/div699/grp02/updated-what-is-synchrotron-radiation.cfm>.
- [57] James A. Samson and David L. Ederer. *Experimental Methods in the Physical Sciences: Vacuum Ultraviolet Spectroscopy I*. San Diego: Academic Press; 2000.
- [58] Canadian Light Source [Internet]. c2011. What is a Synchrotron Anyway? [cited 2011 June 13]. Available from: <http://www.lightsource.ca/education/whatis.php>.

- [59] NIST SURF [Internet]. c.2010. Beamline 4: Ultraviolet Optical Properties and Calibrations. [cited 2011 June 13]. Available from: <http://www.nist.gov/pml/div699/grp02/beamline4.cfm>.
- [60] U. Arp, C. Clar, A. Farrell, E. Fein, M. Furst, and E. Hagely. Synchrotron ultraviolet radiation facility: SURF III. *Rev. Sci. Inst.* 73, no. 3: 1674.
- [61] U. Arp, R. Friedman, M.L. Furst, S. Makar, and P.S. Shaw. SURF III-an improved storage ring for radiometry. *Metrologia.* 37, no. 5 (2000): 357.
- [62] P.-S. Shaw, K.R. Lykke, R. Gupta, T.R. O'Brian, U. Arp, H.H. White, T.B. Lucatorto, J.L. Dehmer, and A.C. Parr. Ultraviolet radiometry with synchrotron radiation. *Appl. Optics.* 38, no. 1 (1999): 18.
- [63] U. Apr, C. Clark, L. Deng, N. Faradzhev, A. Farrell, M. Furst, S. Grantham, E. Hagley, S. Hill, T. Lucatorto, P. Shaw, C. Tarrío, and R. Vest. SURF III: A flexible synchrotron radiation source for radiometry and research. *Nucl. Inst. Meth. A.* 649 (2010): 12.
- [64] Rob Vest. Data Analysis and Uncertainty Propagation for BL-4 Spectroscopy Experiments. 2011.
- [65] J. McComb. Neutron detection based on far-ultraviolet excimer emission. Thesis Proposal. 5 April 2011.
- [66] J. Ziegler, *Stopping power and range of ions in matter.*
- [67] Hamamatsu Photomultiplier Tube R6835, spec. sheet.
- [68] Ortec, VT120 Fast-Timing Preamplifier, spec. sheet.
- [69] Instruction Manual for TC 952 High Voltage Power Supply, spec. sheet.
- [70] Coaxial Power Splitter/Combiner, spec. sheet.
- [71] Ortec 974A CCNIM Quad 100-MHz Counter/Timer, spec. sheet.
- [72] 3001 Multichannel Analyzer [Internet]. c1995. [cited 2012 June 13] Available from: <http://teledynelecroy.com/lrs/dsheets/3001.htm>.
- [73] M. Berger, J. Coursey, M. Zucker, and J. Chang, *ESTAR, PSTAR and ASTAR: Computer programs for calculating stopping-power and range tables for electrons, protons and helium ions (ver. 1.2.3).*
- [74] HSO HITRAM Database. [Internet]. c2011. Absorption cross-sections in the Schumann-Runge region of oxygen O₂ at 300 K. [cited 6 December 2011] Available from: http://www.atmosphere.mpg.de/spektrum/_image3.php?subkat=\&kat=Oxygen\&file=O2_SchumannRunge\%2812-0\%29+to+\%281-0\%29_log.JPG.

- [75] D. Gilliam. Self-absorption correction factor for fission chamber deposit.
- [76] National Nuclear Data Center. [Internet]. Chart of nuclides database. [cited 2 February 2013]. Available from: <http://www.nndc.bnl.gov/chart/>.
- [77] G. Hale and P. Young. [Internet]. c2006. ENDF/B-VII. [cited 2 May 2013]. Available from: <http://www.nndc.bnl.gov/exfor/endl00.jsp>.
- [78] Z. Chowdhuri. *Absolute Neutron Measurements in Neutron Decay*. PhD thesis, Indiana University (2000).
- [79] D.R. McAlister. Gamma ray attenuation properties of common shielding materials. [Internet] c. 2012. [cited 2 February 2013]. Available from: <http://www.alarasolutions.com/PDF/gamma-ray-attenuation-rev-2.pdf>.
- [80] V.L. McKinney and T. Rockwell, III. Boral: A new thermal neutron shield. Oakridge National Laboratory, 1950.
- [81] Ceradyne. Boral[®]Composite. [Internet]. c2008. [cited 6 February 2013]. Available from: <http://www.ceradyneboron.com/uploads/specSheets/SP-BORA-001enSpecificationBoral.pdf>.
- [82] G.A. Yeo and T.A. Ford. Conformational preferences of the structures, and energetics of the molecular complexes of boron trifluoride with some hydrogen halides, halogens, and interhalogens. *J. Mol. Struct.* 771 (2006): 157.
- [83] V.C. Tongiorgi, S. Hayakawa, and M. Widgoff. High pressure BF₃ proportional counters. *Rev. Sci. Instrum.* 22 (1951): 899.
- [84] J.A. Bistline, Jr. Some properties of BF₃ in ionization chambers. *Rev. Sci. Instrum.* 19, no. 12 (1948): 842.
- [85] E.A. Davis, F. Gabbard, T.W. Bonner, and R. Bass. The disintegration of B¹⁰ and F¹⁹ by fast neutrons. *Nucl. Phys.* 27 (1961): 448.
- [86] J.D. Aponte and S.A. Korff. Effect of gaseous impurities on BF₃ proportional counters. *Rev. Sci. Instrum.* 31, no. 5 (1960): 532.
- [87] I.L. Fowler and P.R. Tunnicliffe. Boron trifluoride proportional counters. *Rev. Sci. Instrum.* 21 (1954): 734.
- [88] J.A. Stockdale, D.R. Nelson, F.J. Davis, and R.N. Compton. Studies of electron impact excitation, negative ion formation, and negative ionmolecule reactions in boron trifluoride and boron trichloride. *J. Chem. Phys.* 56 (1972): 3336.
- [89] T. Tomoda and S. Fukakusa. Deterioration and recovery of BF₃ counters due to operation in intense radiation fields. *Nuc. Instrum. Meth. Phys. Res.* 224 (1984): 557.

- [90] K.A.G. MacNeil and J.C.J. Thynne. Negativ ion formation by boron trifluoride and phosphorus trifluoride. *J. Phys. Chem.* 74, no. 11 (1970): 2257.
- [91] J.M. Friedrich, C. Ponce-de-Léon, G.W. Reade, F.C. Walsh. Reticulated vitreous carbon as an electrode material. *J. Elect. Chem.* 561 (2004): 203.
- [92] ERG Aerospace Corporation [Internet]. c2011. Duocel Carbon Foam. [cited 2 February 2013]. Available from: <http://www.ergaerospace.com/RVC-properties.htm>.
- [93] J. Wang. Reticulated vitreous carbon—a new versatile electrode material. *Electrochimica Acta.* 26, no. 12 (1981): 1721.
- [94] A.G. Chakhovskoi and C.E. Hunt. Reticulated vitreous carbon field emission cathodes for light source applications. *J. Vac. Sci. Technol. B.* 21, no. 1 (2003): 571.
- [95] M.A. Coplan. Proposal to investigate excimer scintillation from reticulated vitreous carbon foam (RVC) targets covered with natural boron carbide using the MUTR thermal column neutron beam. Experimental Proposal. 16 December 2012.
- [96] *Annual Book of ASTM Standards: vol. 12.02, Nuclear (II), Solar, and Geothermal Energy.* ASTM International, Baltimore: 2003.